

Autor:

Pablo Matorras Cuevas

Director:

Luca Scodellaro

Tesis Doctoral

**BÚSQUEDA DE PRODUCCIÓN DE PARES DE
PARTÍCULAS SUPERSIMÉTRICAS EN ESTADOS
FINALES CON DOS LEPTONES DE CARGA OPUESTA Y
GRAN MOMENTO TRANSVERSAL PERDIDO EN
COLISIONES PROTÓN-PROTÓN A 13 TEV**

PhD Thesis

**SEARCH FOR SUPERSYMMETRIC PARTICLE PAIR
PRODUCTION IN FINAL STATES WITH TWO
OPPOSITELY CHARGED LEPTONS AND LARGE
MISSING TRANSVERSE MOMENTUM IN PROTON-
PROTON COLLISIONS AT 13 TEV**



Acknowledgments

Ahora que este período de mi vida acaba, y antes comenzar la siguiente, quiero dedicar unas palabras a todos aquellos sin los cuales este proyecto de cinco años de tesis, que han pasado tan rápido y tan lentamente, no hubiera sido posible. Primero de todo, dar las gracias a Luca, el director de esta tesis, que me ha acompañado y guiado durante todo el camino, y me ha mostrado, una y otra vez, sus inmensos conocimientos tanto de la física como de la política interna de CMS. Luca, *grazie per la tua pazienza, e forza Roma*.

Seguidamente, me gustaría agradecer al grupo de altas energías por su apoyo en este tiempo. A Celso, por darme la oportunidad de participar en el grupo, y por animarme a ir a las conferencias. A Pablo y a Alicia por cuidarme y apoyarme ya desde el TFM. A Brochero, con quien tuve la oportunidad de impartir clase, y que aunque ya no esté en Santander, nunca pierde la oportunidad de aconsejarme. También a mis compañeros, algunos ya doctores (Bárbara, Cédric, Celia, Nicolò, Pedro...) y otros que lo serán en el futuro (Sergio, Rubén, Efrén, Cristian, Antonio, Víctor, Mayra o Diego), con una mención especial a mis compañeros de este cubículo sin ventanas que al final se siente como casa. A Clara, no te agobies, que lo duro de la tesis es hacerla, no escribirla, y a Agustín, a quien al final he ganado a presentar la tesis, pero que estoy seguro de que pronto la terminará.

Así mismo, agradecer al grupo de la Universidad de Oviedo, que aunque sea otra universidad, a menudo se siente como si fuéramos todos de una misma institución. Por un lado, a Javier, que junto a Celso, probablemente sea el “culpable” de los lazos entre ambos grupos, y que a pesar de estar conectado a varias reuniones simultáneas siempre ha estado atento, y por otro a los todos los doctorandos; y por supuesto a las ya doctoras Trapote y Ramón con quienes tanto he compartido estos años. To this last point, I should also include Gorka, Emanuela, Fabian, and all the *team IFIC* I met during TAE.

Por otro lado, tengo que agradecer a mi familia el apoyo, no ya durante la tesis, sino desde siempre. A mi madre, por aconsejarme, apoyarme y aguantarme desde pequeño (y no tan pequeño). A mi padre, por inculcarme el amor a la física. A mis hermanos, Antonio y Francisco, por ayudarme a madurar, por las buenas y por las malas. Y a mi *nonna*, que siempre me pedía que le explicara mi tesis, y siempre me decía, “qué cosas más complicadas estudias”, pero que siempre hablaba con orgullo de su nieto que trabajaba en Ginebra, y que hubiera venido a la defensa encantada.

Finalmente, quiero agradecer a todos mis amigos, tanto a aquellos que viven en Santander (colonia chilena incluida), as well as to all those who don’t, either because they moved out, as close as Bilbao, or as far as Manila, or because I met them abroad, from Sweden to Switzerland passing by the Baltics, the UK or the US and managed to stay in contact, with an especial mention to the Schaf80 gang, whom every time I see, it feels like no time had passed.

Contents

Acknowledgments	iii
Contents	vii
Acronyms	xvi
List of Figures	xxvii
List of Tables	xxx
1 Introduction	1
2 The Standard Model	3
2.1 An overview of the Standard Model	3
2.1.1 Fundamental Particles of the Standard Model	3
2.1.2 Interactions in the Standard Model	5
2.2 Standard model achievements and shortcomings	13
3 Supersymmetry	17
3.1 Origin and common features of SUSY models	18
3.2 Minimal Supersymmetric Standard Model	18
3.2.1 R-Parity and dark matter candidates	19
3.2.2 SUSY particle mass eigenstates	19
3.2.3 Soft supersymmetry breaking of the MSSM and naturalness	20
3.2.4 Phenomenology	21
3.3 Supersymmetry models at the LHC	22
4 Experimental setup	25
4.1 The European Organization for Nuclear Research	25
4.2 The Large Hadron Collider	26
4.2.1 LHC properties and parameters	27
4.2.2 Physics at the Large Hadron Collider	29
4.3 The Compact Muon Solenoid	31
4.3.1 The inner tracker	33
4.3.2 The electromagnetic calorimeter	35
4.3.3 The hadronic calorimeter	36
4.3.4 The solenoid	37
4.3.5 The muon system	38
4.3.6 The trigger system	39
4.4 Event data model and data tiers	40
4.4.1 CMS event data model	40
4.4.2 CMS data tiers	42
4.5 LHC plan and future	43

5	Physics objects reconstruction and identification	47
5.1	Particle flow reconstruction	47
5.2	Muon Reconstruction and identification	49
5.2.1	Muon Reconstruction	49
5.2.2	Muon identification	50
5.3	Electron reconstruction and identification	54
5.3.1	Electron Reconstruction	55
5.3.2	Electron identification	56
5.4	Hadron reconstruction	58
5.5	Jet reconstruction	59
5.5.1	Heavy flavour jet identification	60
5.5.2	Tau lepton reconstruction	63
5.6	Missing transverse momentum	64
6	Monte Carlo simulated samples	65
6.1	The Monte Carlo event Generator	65
6.1.1	Hard Scattering	66
6.1.2	Underlying events	67
6.1.3	Parton Showering	68
6.1.4	Hadronisation	68
6.1.5	Pile-Up Generation	68
6.1.6	Monte Carlo simulation structure at the CMS experiment	68
6.2	Monte Carlo Corrections	69
6.2.1	Commissioning of b-tagging variables in Drell–Yan+Jets events	69
7	Supersymmetric models and main backgrounds	73
7.1	Direct search for supersymmetric particles in this document	73
7.2	Main backgrounds in the dilepton channel	75
7.2.1	Top Backgrounds	76
7.2.2	Z boson backgrounds	78
7.2.3	Diboson backgrounds	79
7.2.4	Triboson backgrounds	80
7.2.5	Higgs backgrounds	81
7.3	Monte Carlo simulated samples used in this analysis	82
8	Event selection and background estimation	83
8.1	Baseline selection	83
8.2	Data taking issues and their treatment	85
8.2.1	2016 Tracker strip occupancy issue	85
8.2.2	2016 and 2017 ECAL trigger primitive prefire	85
8.2.3	2017 ECAL endcaps noise	85
8.2.4	2018 inoperative HCAL sectors	87
8.3	Search strategy	88
8.3.1	Search region optimisation	89
8.4	Background estimation	91
8.4.1	Modelling of $m_{T2}(\ell\ell)$ in $t\bar{t}$, and WW events	91
8.4.2	Normalization and modelling of subleading background processes	98
8.5	Uncertainties	105
8.5.1	Statistical uncertainties	105
8.5.2	Systematic uncertainties	105
8.5.3	Uncertainties in the SR yields	107
9	Results and interpretation	111
9.1	Signal extraction	112
9.2	Observed and expected yields	114
9.2.1	Chargino search regions	114
9.2.2	Top squark search regions	118
9.3	Post-fit Results	125
9.3.1	Fitted values of the rate parameters for the backgrounds’ normalisation	127

9.3.2	Chargino search regions	129
9.3.3	Top squark search regions	132
9.4	Interpretation of results	136
10	Conclusions	141
	References	142
A	Resumen en español	161
B	Triggers	163
B.1	Trigger paths	163
B.2	Measurement of the trigger efficiencies	165
C	Scale factors for additional requirements on lepton selection	167
D	FULLSIM/FASTSIM correction factors for lepton selection efficiencies	173
	Effect of the correction factors on top squark signal samples	177
E	Test of the ML fit in events with $100 \leq p_T^{\text{miss}} < 140$ GeV	181
F	Smoothing of shape variations for uncertainties in JES, JER, and unclustered energy	191
G	Signal and control regions after performing the ML fit by year	195
G.1	Post fit distributions in the signal regions	195
G.1.1	Chargino search regions	195
G.1.2	Top squark search regions	202
G.2	Post fit distributions in the control regions	209
G.2.1	Control regions for chargino/slepton ML fits in 2016 data	209
G.2.2	Control regions for chargino/slepton ML fits in 2017 data	214
G.2.3	Control regions for chargino/slepton ML fits in 2018 data	219
G.2.4	Control regions for top squark ML fits in 2016 data	224
G.2.5	Control regions for top squark ML fits in 2017 data	227
G.2.6	Control regions for top squark ML fits in 2018 data	230

Acronyms

B_n Baryon number. 19

L_n Lepton number. 19

P_R R-Parity. 19

χ^2/\mathbf{dof} goodness-of-fit per degree of freedom. 53

m_T Transverse mass of two leptons. 84

m_T Transverse mass of two particles. Defined in Eq. 8.1. 88

$m_{T2}(\ell\ell)$ Extension of m_T for events with two leptons and two invisible particles. Defined in Eq. 8.2. xix–xxiv, xxix, xxx, 87–91, 98, 99, 105–107, 109–115, 117, 118, 122, 124–126, 129, 131, 132, 181, 182, 191, 192, 195, 196, 198, 202

p_T Momentum measured in the transverse plane. xviii, xix, xxii, xxiii, 32, 37, 39, 50, 51, 53, 54, 56–61, 63, 64, 67, 70, 73, 84–89, 91, 165, 166

p_T^{miss} Missing transverse energy. xii, xix, xx, xxix, 2, 32, 36, 39, 40, 64, 73, 74, 79, 83–86, 88–94, 102, 106–110, 191

\mathbf{H}_T Sum of all jet’s p_T . 85

$Z + \mathbf{jets}$ Production of the Z boson in conjunction with jets. 78

WW Production of a pair of W bosons. 79, 82

WZ Production of a W boson in association with a Z boson. xx, 79, 98–100, 113

ZZ Production of a pair of Z bosons. xx, 79, 82, 100, 101, 113

σ Standard deviation. It determines how data is spread around the mean. Specifically, 95% of data fall within 2σ , 99.7% within 3σ , 99.994% within 4σ and 99.99994% within 5σ , which

-
- is the threshold chosen in particle physics to claim a discovery. 14, 15
- tW** Single top quark production alongside a W boson. 76
- bremstrahlung*** Electromagnetic radiation produced by the deceleration of a charged particle when deflected by another charged particle, typically an electron by an atomic nucleus. 48, 55
- t \bar{t} W** Top-antitop quark pair production in association with W boson. 77
- t \bar{t} Z** Top-antitop quark pair production in association with Z boson. 77, 113
- t \bar{t}** Top-antitop quark pair production. xix, xxix, 76, 82, 87–91, 93
- ALICE** A Large Ion Collider Experiment. 27
- AOD** Analysis object data. 41
- ATLAS** A Toroidal Large AparatuS. xvii, 22, 23, 27, 31, 74, 75
- BDT** Boosted Decision Tree. 57, 62
- BPIX** Barrel section of the pixel detector in the inner tracker. 34
- BSM** Beyond Standard Model theories. xvii, 1, 17, 31, 36, 60
- CERN** Conseil Européen pour la Recherche Nucléaire (European Organization for Nuclear Research). xvii, 25, 26, 31, 42, 44, 141
- CL** Confidence Level. xxii, 125, 136–139
- CMB** Cosmic Microwave Background. 1, 14
- CMS** Compact Muon Solenoid. xvii, xviii, xxix, 1, 22, 23, 25, 27–29, 31–42, 44, 47, 49, 50, 54, 57–60, 62–65, 68–70, 74, 75, 83, 85, 89, 137, 141, 162
- cMVA** Combined Multivariate Algorithm. 62, 63
- CP** Charge-parity. 13, 14, 21
- CR** Control Region. xx, xxv–xxvii, xxix, 88, 90, 91, 98–100, 102, 106, 113, 125, 195, 209–232
- CSC** Cathode strip chambers. xviii, 38, 49

CSV Combined Secondary Vertex. 62

DAQ Data acquisition system. 40, 41

DeepCSV Combined Secondary Vertex using deep neural network. 62, 63

DF Different Flavour. xxii, xxiv–xxvi, xxx, 88, 91, 114, 123, 125, 132, 136, 137, 202, 210, 215, 220

DIGI Involves the conversion of SIM hits into the detector’s response. 69

DM Dark Matter. 1

DNN Deep Neural Network. 62

DT Drift tubes. xviii, 38, 44, 49

DY Drell-Yan. 69, 104

ECAL Electromagnetic calorimeter. xii, xviii, 31, 35–37, 48, 54–58, 85

EE ECAL endcap. xix, 85, 86

EGM EGamma (Electron and photon POG). 58

EOY End of year. 41, 85, 104

EWK Electro weak. 5, 8, 9

FastSim Fast Simulation Monte Carlo Events. 68, 69, 82, 107, 110

FNAL Fermilab National Accelerator Laboratory. 14, 26

FPIX Forward section of the pixel detector in the inner tracker. 34

FSR Final State Radiation. 67

FullSim Full Simulation Monte Carlo Events. 68, 69, 82

GEN Generated Monte Carlo events, with the processing defined in Section 6.1. 69

GIF++ Gamma Irradiation Facility. 45

GSF Gaussian Sum Filter. 56, 57

GUT Grand Unificaiton Theory. 14

H/E Hadron to energy ratio: Proportion of energy deposited in the (HCAL) within a cone of radius $\Delta R = 0.15$ around the direction of the superclusters, divided by the energy deposited in the ECAL by the candidate photon or electron. 57

HB Hadron Barrel. xviii, 36, 37

HCAL Hadronic calorimeter. xii, xviii, 36, 37, 48, 54, 57, 58, 85, 87

HE Hadron Endcap. xviii, 36, 37

HEM A non-conductive mirror-like material called used to construct the HF. 87

HF Hadron Forward. xviii, 36, 37

HL-LHC High Luminosity LHC, an upgrade of the current LHC detector that is expected to start its installation by 2025 and start its operations by 2028. xviii, 43–45

HLT High Level Trigger. 39–41

HO Hadron Outer. xviii, 37, 38

ID Identification. 48, 50, 53, 83

IFCA Instituto de Física de Cantabria. 42

ISR Initial State Radiation. 67, 88, 90, 106, 107

JEC Jet Energy Correction. 60, 64

JER Jet Energy Resolution. xxi, 60, 104–107

JES Jet Energy Scale. 60, 105–107

JME Jet MET (missing transverse energy, or p_T^{miss}) POG. 85

JP Jet Probability. 62

LEP Large Electron Positron collider. 26

-
- LHC** Large Hadron Collider. xvii, xviii, 1–4, 9, 14, 15, 18, 21, 22, 25–27, 31–33, 39, 43–45, 49, 53, 60, 62, 65, 68, 70, 79, 81, 141
- LO** Leading Order. 67, 82
- LS** Long shutdown. 43
- LSP** Lightest Supersymmetric Particle. 1, 2, 19, 21, 73
- MC** Monte Carlo. 40, 41, 60, 65, 68, 82, 114
- ML** Maximum likelihood. xx, xxv–xxvii, 90, 98, 99, 106, 107, 111–113, 125, 195, 209–232
- MPI** multiple parton interactions. 67
- MSSM** Minimal Supersymmetric Standard Model Theory. xxix, 18–21
- MVA** Multivariate Analysis. 57
- NLL** next-to-leading logarithm order. 82, 136, 137
- NLO** Next to Leading Order. 67, 82, 136, 137
- NN** Neural Network. 62
- NNLL** next-to-next-to-leading logarithm order. 67, 82, 137
- NNLO** Next to Next to Leading Order. xvii, 30, 67, 82, 137
- OC** Opposite Charge. xv, xx, 2, 73, 74, 79, 83, 93, 98–100, 104
- PDFs** Parton Distribution Functions. 29, 67, 82, 106, 107
- PDs** Primary Datasets. 40
- PF** Particle Flow. xix, 47, 49, 50, 54, 59, 60, 64, 71
- pMSSM** Phenomenological Supersymmetric Standard Model Theory. 21
- POG** Physics object group. 50, 58, 69, 84, 85, 107, 167
- pp** Proton-proton. 68

PS Proton synchrotron. 26

PU Pile Up. 28, 44, 60, 82

PV Primary vertex. 50, 54, 56, 57

QCD Quantum Chromodynamics. 5–7, 9, 14, 29, 68, 82

QED Quantum Electrodynamics. 5, 8, 10

QFT Quantum Field Theory. 3, 65

RMS Root Mean Square. xviii, 51

RPC Resistive plate chambers. xviii, 38, 49

Run I LHC’s first data taking period that took place between 2010 and 2013, at a $\sqrt{s} = 7 - 8$ TeV. 27, 43, 62

Run II LHC’s data taking period that took place between 2015 and 2018, at a $\sqrt{s} = 13$ TeV. The data collected during this period at the CMS detector was the one used for the analysis presented here. xvii, xviii, xxix, 27–29, 34, 35, 43, 44, 50, 53, 54, 60, 62, 68, 74, 84, 85, 114, 129, 137, 162, 195

Run III LHC’s data taking period that started at 2022 and is expected to finish by 2025, at a $\sqrt{s} = 13.6$ TeV. 27, 43, 44, 62, 69, 70

SCs Superclusters. xxiii, 55, 168

SF Same Flavour. xxii, xxiv–xxvi, xxx, 84, 88, 93, 100, 104, 114, 122, 124, 132, 136, 137, 202, 209, 214, 219

SIM Includes the information about the energy depositions of simulated particles expected within the CMS detector. 69

SM Standard Model of particle physics. xx, xxv–xxvii, xxix, 1, 3–6, 8–10, 12–15, 17–21, 31, 64, 67, 68, 73, 75, 76, 83, 98, 99, 107, 112, 114, 136, 209–232

SMS Supersymmetric models with simplified models spectra. 22, 74, 137

SPD Silicon Pixel Detector. 33, 34

SPS Super Proton synchrotron. 26

- SR** Signal Region. xx–xxii, xxiv–xxvii, xxix, xxx, 73, 83, 88–93, 95, 98, 100, 102, 104, 106, 107, 109, 111–114, 118, 122, 124–126, 129, 131, 132, 195, 196, 198, 202, 209–232
- SR1** First signal region, selecting events with two OC leptons and $160 < p_T^{\text{miss}} < 220 \text{ GeV}$. Slightly different depending on whether the chargino or top squark regions are used (see Table 8.2). xxi, xxii, xxiv, 114, 115, 118, 127–129, 132, 196, 202
- SR2** Second signal region, selecting events with two OC leptons and $220 < p_T^{\text{miss}} < 280 \text{ GeV}$. Slightly different depending on whether the chargino or top squark regions are used (see Table 8.2). xxi, xxii, xxiv, 114, 116, 119, 127, 128, 130, 133, 197, 199, 201, 203, 205, 207
- SR3** Third signal region, selecting events with two OC leptons and $280 < p_T^{\text{miss}} < 380 \text{ GeV}$. Slightly different depending on whether the chargino or top squark regions are used (see Table 8.2). xxi, xxii, xxiv, xxv, 114, 117, 120, 127, 128, 131, 134, 198, 203, 205, 207
- SR4** Fourth signal region, selecting events with two OC leptons and $p_T^{\text{miss}} > 380 \text{ GeV}$. Slightly different depending on whether the chargino or top squark regions are used (see Table 8.2). xxi, xxii, xxiv, xxv, 114, 117, 121, 127, 128, 131, 135, 198, 204, 206, 208
- SSB** Spontaneous Symmetry Breaking. 9–11
- SSD** Silicon Strip Detector. 34
- SUSY** Supersymmetry. xvii, 1, 2, 17–20, 22, 69, 74, 82, 112
- SV** Secondary vertex. xix, 61, 71
- TEC** Tracker End Cap. 34
- TIB** Tracker Inner Barrel. 34
- TID** Tracker Inner Disk. 34
- TOB** Tracker Outer Barrel. 34
- TOD** Tracker Outer Disk. 34
- TP** Trigger Primitives. 85
- udsg jets** Light jets, i.e coming from either the up (u), strange (s) or down (d), or gluons (g). 70
- UE** Underlying events. 67
- UL** Ultra legacy. 41, 85

VBF Vector boson fusion. 78

VFP Feedback bias voltage. 85, 95, 165

WIMP Weakly interacting massive particle. 21

WP Working point. 48, 50, 53, 56, 58

List of Figures

2.1	Fundamental particles of the Standard model and their properties [1]	4
2.2	Measurement of the coupling strength $\alpha_s = \frac{g_c}{4\pi}$ in terms of the energy scale Q for different processes [2].	7
2.3	Shape of the higgs potential depending on the sign of μ . $\mu > 0$ is shown in the left and $\mu < 0$ in the right [3].	11
3.1	Covering of the big open questions with respect to several BSM theories [4]. . . .	17
3.2	Theory cross sections for selected SUSY processes as a function of the particle mass at $\sqrt{s} = 13$ TeV. Taken from [5, 6].	22
3.3	Summary of the mass reach (limits at 95% confidence level) obtained within the framework of simplified models and various final states obtained by several analyses performed by the CMS collaboration. Each line includes arXiv and physics analysis summary numbers that correspond to the analyses yielding relevant results. A more comprehensive information on the models, assumptions, and selection criteria is available in the documentation for each analysis. Results are shown for:	23
3.4	Representation of the mass reach of the various analyses performed by the ATLAS collaboration probing for Supersymmetry. A summary of search outcomes is displayed to represent the available data. Results are expressed in terms of the nominal cross-section, focusing on both an area of almost-maximum mass coverage and a contrasting illustrative scenario, showcasing the phase space to which each search is sensitive to. It must be noted that certain limitations are based on extra hypotheses regarding the mass of intermediary states, which are highlighted through darker bands, which represent varying model parameters [7].	23
4.1	CERN complex, showing the LHC with its four main experiments, its injection chain, and other experiments	26
4.2	Summary of the integrated luminosity collected by the CMS collaboration, by year.	28
4.3	Distribution of pile-up during each of the Run II data taking period at the CMS collaboration.	29
4.4	Schematic representation of the interaction between two partons in a proton-proton collision.	30
4.5	Parton distribution values at Next to Next to Leading Order (NNLO), calculated by the NNPDF collaboration [8]	30
4.6	Schematic view of the CMS detector, with its main components and characteristics [9].	31
4.7	Schematic representation of the CMS coordinate system.	32
4.8	Schematic view of the CMS tracker in the r-z plane [10]. In the strip tracker, every line corresponds to a silicon strip detector. In the pixel detector, the lines represent the ladders and petals that hold the detectors in the barrel and endcaps, respectively.	33
4.9	Layout of the CMS Phase-1 (top), compared to the original detector layout (bottom), in a longitudinal view.	34

4.10	Tracker reconstruction for muons measured during the Run II data taking and produced via $Z \rightarrow \mu\mu$ events, measured in terms of:	35
4.11	Schematic representation of the CMS ECAL [11]:	35
4.12	Geometric view of one quarter of the ECAL [12] in the rz -plane.	36
4.13	Geometric view of one quarter of the HCAL [12] in the $r - z$ plane, with each parts of the detector are shown: the hadron barrel HB, endcap HE, forward HF and outer HO [13].	37
4.14	One quadrant of the CMS detector, with all subdetectors shown, as well as a bigger detail shown for each of the muon subdetectors, showing each of the DTs in orange, the CSC in green and the RPC in blue [14].	38
4.15	Scheme for CMS' Level-1 trigger system, with each sub detectors involved [15]. . .	39
4.16	Main data formats and objects involved in them [16].	41
4.17	Detector data flow with each of the tiers and its function [17].	42
4.18	General LHC and high luminosity LHC(HL-LHC) plans, where for each Run, its working energy, year and designed luminosity are shown.	43
4.19	Expected fluence at the CMS detector for a luminosity of 300fb^{-1} in the R-Z plane [18].	44
4.20	Expected contribution to the fluence at HL-LHC conditions for each of the particles with, in terms of the radius from the beam pipe. Results are presented at the collision point (solid line) and at a distance from the collision point of 250 cm (dashed line) [18].	45
5.1	Section of CMS viewed from the transverse plane, with each of the subdetectors labelled and represented in a different colour. Also represented is how the various particles identified by the particle flow reconstruction are expected to interact with the detector [19].	48
5.2	Root Mean Square (RMS) of two muon tracker (red) and global muon (red) algorithms in terms of the transverse momentum p_T for cosmic rays recorded in 2015 [20].	51
5.3	Reconstruction efficiency of the displaced global algorithm (black filled circles) compared to the global and tracker algorithms (blue empty circles and red empty squares, respectively). The efficiency was measured using simulated events where the Higgs boson decays to two long-lived S-bosons, where each of them decays into a pair of muons [21].	52
5.4	Muon identification efficiencies in terms of η for:	54
5.5	Schematic representation of how the cone used for lepton reconstruction in: . . .	55
5.6	Relative energy electron resolution versus electron p_T in 2016 simulations, as measured by the ECAL ("corrected SC"), by the tracker, and seen in the E-p combination, for:	56
5.7	Electron identification efficiency measured in data (top panel) and efficiency ratios between data and simulation (bottom panel), as a function of the electron transverse energy E_T , for the cut-based identification veto working point. The vertical bars on the markers represent combined statistical and systematic uncertainties.	59
5.8	Schematic representation of the differences between b-jets compared to lighter jets. . .	61
5.9	Misidentification probabilities for c and light jets versus b jet efficiency for several jet taggers. The performance curve for c jets is shown in dashed, while the one for light jets is shown in solid lines.	63
5.10	Example of the calculation of the missing transverse momentum in an event with two jets.	64
6.1	Diagram showing the structure of a proton-proton collision, with each of the colours representing a different stage of the Monte Carlo event generator [22]. The hard process is represented in black, with the pink blob representing the underlying events. The parton shower is shown in green, while the hadronisation is shown in blue.	66
6.2	Observed and simulated distributions in Drell-Yan +jets events. Left: Jet p_T (top), and η (bottom). Centre: Reconstructed Z bosons' p_T (top) and η (bottom). Right: DeepJet discriminant of the first jet against b-jets (top) and c-jets (bottom):	70

6.3	Observed and simulated distributions in Drell–Yan +jets events. Left: Measured distance a particle travels in the transverse plane (2D flight distance) for the most energetic secondary vertex SV (top) and its significance (bottom). Right: Measured distance a particle travels in the 3-D space (3D impact parameter) for the most energetic charged PF particle (top) and its significance (bottom): . . .	71
7.1	Simplified-model diagrams of chargino pair production with two benchmark decay modes:	74
7.2	Simplified-model diagrams of top squark pair production with two benchmark decay modes of the top squark:	75
7.3	Simplified-model diagram of charged slepton pair production. The analysis is focused on a scenario where each slepton decays into a charged lepton and a neutralino.	75
7.4	Feynman diagrams portraying the leading $t\bar{t}$ production Feynman diagrams via: .	76
7.5	Top quark pair decay chain into a b quark pair and W boson pair	76
7.6	Leading-order Feynman diagram for single top quark production in:	77
7.7	Leading order diagrams for the production of a single top quark in association with a W boson	77
7.8	Primary Feynman diagrams for:	77
7.9	Production of the Z boson via:	78
7.10	Production of the Z boson via the Drell–Yan process involving jets	78
7.11	Representative Feynman diagram for the production of a pair of W bosons at the LHC.	79
7.12	Representative Feynman diagram for the production of a pair of Z bosons at the LHC.	79
7.13	Production of pair of W and Z bosons via:	80
7.14	Representative Feynman diagrams for the production of three SM bosons at the LHC	80
7.15	Higgs boson production via gluon fusion	81
7.16	Representative Feynman diagram for the production of a Higgs boson in association with other bosons at the LHC	81
8.1	Observed and expected distributions of the p_T^{raw} for jets in the pseudorapidity region affected by the EE noise ($2.650 < \eta < 3.139$)	86
8.2	Azimuthal separation between the p_T^{miss} and the high- p_T (> 50 GeV) jets with $p_T^{\text{raw}} > 50$ GeV	86
8.3	Sum of the jet’s p_T for all jets with $2.650 < \eta < 3.139$ and $p_T^{\text{raw}} < 50$ GeV. . . .	87
8.4	Observed and expected $m_{T2}(\ell\ell)$ distributions for events in the 2018 dataset with $100 \leq p_T^{\text{miss}} < 140$ GeV, on events with:	87
8.5	Distributions of $m_{T2}(\ell\ell)$ in DF events with $100 < p_T^{\text{miss}} < 140$ GeV and at least one b-tagged jet for 2016 (left plot), 2017 (middle), and 2018 (right) data. The last bin includes the overflow entries. In the bottom panel, the ratio of data and SM expectations is shown. The hatched band represents the total uncertainty, including the sources discussed in Section 8.5.	92
8.6	The same distributions of $m_{T2}(\ell\ell)$ as Fig. 8.5, but in events with at least one jet but no b-tagged jets.	92
8.7	The same distributions of $m_{T2}(\ell\ell)$ as Fig. 8.5, but in events with no jets.	92
8.8	Left: distributions of $m_{T2}(\ell\ell)$ in $WZ \rightarrow 3\ell 1\nu$ events with $p_T^{\text{miss}} > 160$ GeV after the WW emulation. Data from all the data-taking years have been merged to increase statistics. The last bin includes the overflow entries. In the bottom panel, the ratio of data and SM expectations is shown. The hatched band represents the total uncertainty, including the sources discussed in Section 8.5. Middle: same as the left plot for events with $p_T^{\text{miss}} > 100$ GeV. Right: linear fit of the ratio of the (background-subtracted) observed events to the expected WZ events with $p_T^{\text{miss}} > 100$ GeV.	93
8.9	Impact of the $m_{T2}(\ell\ell)$ tail correction on the expected (blinded) exclusion regions for:	94

8.10	Left: observed and expected distributions of the minimum azimuthal distance between the p_T^{miss} and any lepton in the event in $WZ \rightarrow 3\ell 1\nu$ events with $p_T^{\text{miss}} > 380$ GeV after the WW emulation. In the bottom panel, the ratio of data and SM expectations is shown. The hatched band represents the total uncertainty, including the sources discussed in Section 8.5. Right: fit of the ratio of the (background-subtracted) observed events to the expected WZ events with $p_T^{\text{miss}} > 380$ GeV.	94
8.11	Impact of the additional $\Delta\phi^{\text{min}}(\ell, p_T^{\text{miss}})$ uncertainty on the expected (blinded) exclusion regions for:	95
8.12	Examples of the observed distributions for different selection variables in the same-charge CR with $p_T^{\text{miss}} > 160$ GeV: p_T^{miss} in 2016 pre-VFP events (top left plot), jet multiplicity in 2016 post-VFP events (top right), leading jet p_T in 2017 events (bottom left), and b-tagged jet multiplicity in 2018 events (bottom right) data. The last bin includes the overflow entries. In the bottom panel, the ratio of data and SM expectations is shown. The hatched band represents the total uncertainty, including the sources discussed in Section 8.5.	96
8.13	Distributions of $m_{T2}(\ell\ell)$ computed after swapping one of the leptons by a third one, passing the veto lepton requirements but failing the analysis lepton selection. Events from the three data-taking years have been merged. The last bin includes the overflow entries. In the bottom panel, the ratio of data and SM expectations is shown. The hatched band represents the total uncertainty, including the sources discussed in Section 8.5.	97
8.14	Distributions of p_T^{miss} in events with exactly three leptons and no b-tagged jets. The same binning used to define the SRs is shown. The last bin includes the overflow entries. In the bottom panel, the ratio of data and SM expectations is shown. The hatched band represents the total uncertainty, including the sources discussed in Section 8.5. Results are shown for:	98
8.15	Same as for Fig. 8.14 but for jet multiplicity. Results are shown for:	98
8.16	Expected contributions of the WZ background to the search region, divided by leptons' flavour and origin.	99
8.17	Left: Distributions of $m_{T2}(\ell\ell)$ in events with exactly three leptons, no b-tagged jets, and $p_T^{\text{miss}} > 160$ GeV. The $m_{T2}(\ell\ell)$ observable is computed using OC lepton pairs where both leptons come from the candidate Z boson. Data from all the data-taking years have been merged to increase statistics. WZ expectations are normalized to data for each data-taking year in the same CR bins described in the text for the ML fit. The last bin includes the overflow entries. In the bottom panel, the ratio of data and SM expectations is shown. The hatched band represents the total uncertainty, including the sources discussed in Section 8.5. Right: same as in the left plot, when the $m_{T2}(\ell\ell)$ observable is computed using OC lepton pairs where just one lepton comes from the candidate Z boson, and the other comes from the candidate W boson.	99
8.18	Distributions of p_T^{miss} in $ZZ \rightarrow 4\ell$ events after the $ZZ \rightarrow 2\ell 2\nu$ emulation. The same binning used to define the SRs is shown. The last bin includes the overflow entries. In the bottom panel, the ratio of data and SM expectations is shown. The hatched band represents the total uncertainty, including the sources discussed in Section 8.5. Results are shown for:	100
8.19	Same as for Fig. 8.18 but for jet multiplicity. Results are shown for:	100
8.20	Distributions of $m_{T2}(\ell\ell)$ in $ZZ \rightarrow 4\ell$ events with $p_T^{\text{miss}} > 160$ GeV after the $ZZ \rightarrow 2\ell 2\nu$ emulation. Data from all the data-taking years have been merged to increase statistics. ZZ expectations are normalized to data for each data-taking year in the same CR bins described in the text. The last bin includes the overflow entries. In the bottom panel, the ratio of data and SM expectations is shown. The hatched band represents the total uncertainty, including the sources discussed in Section 8.5.	101
8.21	Distributions of p_T^{miss} in $t\bar{t}Z \rightarrow 4\ell$ events after the $t\bar{t}Z \rightarrow 2\ell$ emulation. The same binning used to define the SRs is shown. The last bin includes the overflow entries. In the bottom panel, the ratio of data and SM expectations is shown. The hatched band represents the total uncertainty, including the sources discussed in Section 8.5. Results are shown for:	102

8.22	Distributions of $m_{T2}(\ell\ell)$ in $t\bar{t}Z \rightarrow 4\ell$ events with $p_T^{\text{miss}} > 160$ GeV after the $t\bar{t}Z \rightarrow 2\ell$ emulation. Data from all the data-taking years have been merged to increase statistics. $t\bar{t}Z$ expectations are normalized for each data-taking year in the same CR bins described in the text. The last bin includes the overflow entries. In the bottom panel, the ratio of data and SM expectations is shown. The hatched band represents the total uncertainty, including the sources discussed in Section 8.5.	103
8.23	Distributions of $m_{T2}(\ell\ell)$ in SF events with $ m_{\ell\ell} - m_Z < 15$ GeV, $p_T^{\text{miss}} > 160$ GeV, and no b-tagged jets for 2016 (left plot), 2017 (middle), and 2018 (right) data. The last bin includes the overflow entries. In the bottom panel, the ratio of data and SM expectations is shown. The hatched band represents the total uncertainty, including the sources discussed in Section 8.5.	104
8.24	Distributions of $m_{T2}(\ell\ell)$ in SF events with $ m_{\ell\ell} - m_Z < 15$ GeV, $p_T^{\text{miss}} > 160$ GeV, and no b-tagged jets for 2017 data with the EOY (left) and UL (right) productions. The last bin includes the overflow entries. The open blue squares in the EOY plot show the SM predictions with no jet energy resolution (JER) smearing of jet p_T applied. In the bottom panel, the ratio of data and SM expectations is shown. The hatched band represents the total uncertainty, including the sources discussed in Section 8.5.	104
9.1	Observed and expected $m_{T2}(\ell\ell)$ distributions for SM processes and the signal production for a chargino mass of 500 GeV with a neutralino mass of 300 GeV (grey) and 50 GeV (cyan) in the SR1. Distributions corresponding to different flavour events are shown on the left, while same flavour events are presented on the right. The distributions for events with no jets are depicted in the top plots, while the ones for events with jets but no b-tagged jets are shown in the bottom ones. In the bottom panel, the ratio of data and SM expectations is shown. The hatched band represents the total uncertainty, including the sources discussed in Section 8.5.	115
9.2	Equivalent distributions as presented in Fig. 9.1 but for the SR2.	116
9.3	Observed and expected $m_{T2}(\ell\ell)$ distributions for SM processes and the signal production for a chargino mass of 650 GeV with a neutralino mass of 350 GeV (grey) and for a chargino mass of 800 GeV with a neutralino mass of 200 GeV (cyan) for the SR3 and SR4 for events with no b-tagged jets. Distributions corresponding to different flavour events are shown on the left, while same flavour events are presented on the right. The distributions for the SR3 are depicted in the top plots, while the distributions for the SR4 are shown in the bottom ones. In the bottom panel, the ratio of data and SM expectations is shown. The hatched band represents the total uncertainty, including the sources discussed in Section 8.5.	117
9.4	Observed and expected $m_{T2}(\ell\ell)$ distributions for SM processes and the expected signals produced for a top squark mass of 400 GeV with a neutralino mass of 225 GeV (grey) and for a top squark mass of 400 GeV with a neutralino mass of 313 GeV (cyan) for the SR1. Distributions corresponding to different flavour events are shown on the left, while same flavour events are presented on the right. Top plots represent events with no b-tagged jets, whereas events with at least one b-tagged jet are depicted in the bottom plots. For each distribution, the ratio of data and SM expectations is shown in the bottom panel. The hatched band represents the total uncertainty, including the sources discussed in Section 8.5.	118
9.5	Equivalent distributions as presented in Fig. 9.4 for the SR2.	119
9.6	Equivalent distributions as presented in Fig. 9.4 for the SR3.	120
9.7	Equivalent distributions as presented in Fig. 9.4 for the SR4.	121
9.8	Pulls and impacts of the nuisance parameters for the fit to data in the SRs (only the thirty nuisance parameters with the highest impacts are shown. The results are presented for:	126
9.9	Distributions of the significance of the difference in the fitted values of the rate parameters for each of the data taking years for the chargino/slepton (left) and top squark (right) searches.	128

9.10	Observed and expected $m_{T2}(\ell\ell)$ distributions for SM processes in the SR1 after a background-only fit to the data in the chargino SRs. The $m_{T2}(\ell\ell)$ distributions for a signal hypothesis with a chargino mass of 800 GeV and a neutralino mass of 200 GeV are also shown. The distributions in the SR1 with no jets are shown at the top, and the ones in the SR1 with jets but no b-tagged jets are shown at the bottom, with the plots on the left corresponding to different flavour events and the ones on the right to same flavour events, respectively. In the bottom panel, the ratio of data and SM expectations is shown. The hatched band represents the total uncertainty, including the sources discussed in Section 8.5.	129
9.11	Same as for Fig. 9.10 but for the SR2.	130
9.12	Observed and expected $m_{T2}(\ell\ell)$ distributions for SM processes in the SR3 and SR4 after a background-only fit to the data in the chargino SRs. The $m_{T2}(\ell\ell)$ distributions for a signal hypothesis with a chargino mass of 800 GeV and a neutralino mass of 200 GeV are also shown. The distributions in the SR3 are shown at the top, and the ones in the SR4 are shown at the bottom, with the plots on the left corresponding to different flavour events and the ones on the right to same flavour events, respectively. In the bottom panel, the ratio of data and SM expectations is shown. The hatched band represents the total uncertainty, including the sources discussed in Section 8.5.	131
9.13	Observed and expected $m_{T2}(\ell\ell)$ distributions for SM processes in the SR1 after a background-only fit to the data in the top squark SRs. The $m_{T2}(\ell\ell)$ distributions for a signal hypothesis with a top squark mass of 400 GeV and a neutralino mass of 313 GeV are also shown. Top plots are for DF (left) and SF (right) events with no b-tagged jets. Bottom plots are for DF (left) and SF (right) events with at least one b-tagged jets. In the bottom panel, the ratio of data and SM expectations is shown. The hatched band represents the total uncertainty, including the sources discussed in Section 8.5.	132
9.14	Same as for Fig. 9.13 for the SR2.	133
9.15	Same as for Fig. 9.13 for the SR3.	134
9.16	Same as for Fig. 9.13 for the SR4.	135
9.17	Upper limits at 95% CL on the chargino pair production cross section as a function of the chargino and neutralino masses. The thick dashed red line shows the expected exclusion region in the plane $(m_{\tilde{\chi}_1^\pm}, m_{\tilde{\chi}_1^0})$. The thin dashed (dotted) red lines show the $1(2)\sigma$ variation of the expected exclusion region due to the experimental uncertainties. The thick black line shows the observed exclusion region, while the thin black lines show the variation of the observed exclusion region due to the theoretical uncertainties on the production cross section. Limits are shown for a signal model where:	138
9.18	Upper limits at 95% CL on the top squark production cross section as a function of the top squark and neutralino masses. The thick dashed red line shows the expected exclusion region in the plane $(m_{\tilde{t}_1}, m_{\tilde{\chi}_1^0})$. The thin dashed (dotted) red lines show the $1(2)\sigma$ variation of the expected exclusion region due to the experimental uncertainties. The thick black line shows the observed exclusion region, while the thin black lines show the variation of the observed exclusion region due to the theoretical uncertainties on the production cross section. Limits are shown for models where:	138
9.19	Upper limits at 95% CL on the slepton production cross section as a function of the slepton and neutralino masses. The thick dashed red line shows the expected exclusion region in the plane $(m_{\tilde{\ell}}, m_{\tilde{\chi}_1^0})$. The thin dashed (dotted) red lines show the $1(2)\sigma$ variation of the expected exclusion region due to the experimental uncertainties. The thick black line shows the observed exclusion region, while the thin black lines show the variation of the observed exclusion region due to the theoretical uncertainties on the production cross section.	139
B.1	Efficiencies for a selected event in the ee (top plots), $e\mu$ (middle) and $\mu\mu$ (bottom) channel to pass the trigger requirements in the data-taking year 2016 for the pre-VFP (left) and post-VFP (right) periods, as a function of the leading and trailing lepton's p_T . The quoted uncertainties are statistical only.	165

B.2	Efficiencies for a selected event in the ee (top plots), $e\mu$ (middle) and $\mu\mu$ (bottom) channel to pass the trigger requirements in the data-taking years 2017 (left) and 2018 (right), as a function of the leading and trailing lepton p_T 's. The quoted uncertainties are statistical only.	166
C.1	Efficiencies for an electron satisfying the cut-based medium ID to pass the additional requirements on the track impact parameters and number of missing hits as a function of its p_T and super-cluster (SCs) η . From top to bottom, the plots correspond to the pre-VFP 2016, post-VFP 2016, 2017, and 2018 data-taking year, for Drell–Yan simulated events (left) and data from single electron triggers (right). 168	
C.2	Same as in Fig. C.1 for muons satisfying the medium ID and $I_{\text{rel}} < 0.15$ requirements. 169	
C.3	Scale factors for the leptons, defined as the ratio between the efficiencies for data and simulations shown in Fig. C.1 and Fig. C.2, for electrons (left) and muons (right). From top to bottom, the plots correspond to pre-VFP 2016, post-VFP 2016, 2017, and 2018 data-taking year.	170
D.1	Upper: the left and middle plots show the efficiencies for an electron to pass our selection requirements as a function of its p_T and supercluster η in 2016 pre-VFP FULLSIM and FASTSIM Drell–Yan events, respectively; the right plot shows the FULLSIM/FASTSIM correction factors, derived as the ratio of the two sets of efficiencies. Uncertainties are statistical only. Second row: same for 2016 post-VFP FULLSIM and FASTSIM Drell–Yan events. Third row: same for 2017 FULLSIM and FASTSIM Drell–Yan events. Lower: same for 2018 FULLSIM and FASTSIM Drell–Yan events.	174
D.2	Same as in Fig. D.1 for muons.	175
D.3	FULLSIM/FASTSIM correction factors measured in $t\bar{t}$ events for electrons (left) and muons (right). Upper to lower plots show the results for 2016 pre-VFP to 2018 simulated samples.	176
D.4	Comparison of the kinematic distributions for the leptons in top squark pair production events simulated with the 2016 setting of FULLSIM (red solid points) and FASTSIM before (blue lines) and after (yellow solid histogram) applying the FULLSIM/FASTSIM correction factors. Left (right) plots are for electron (muon) distributions. Upper to lower, the panels show the leading lepton p_T , leading lepton η , trailing lepton p_T , and trailing lepton η	177
D.5	Same as in Fig. D.4 for 2017 samples.	178
D.6	Same as in Fig. D.4 for 2018 samples.	179
E.1	Distributions of $m_{T2}(\ell\ell)$ after the fit to 2016 data in the CR with $100 \leq p_T^{\text{miss}} < 140$ GeV. The distributions are shown in events with no jets (upper plots), jets but no b-tagged jets (middle), and b-tagged jets (lower) for the DF (left plots) and SF (right) channels. The dark blue dashed line represents the expected total SM contributions before the fit. The last bin includes the overflow entries. In the bottom panel, the ratio of data and SM expectations is shown for the expected total SM contribution after the fit using the background-only hypothesis (black dots) and before any fit (dark blue dashed line). The hatched band represents the total uncertainty after the fit.	182
E.2	Pulls of the nuisance parameters for the fit to 2016 data in the CR with $100 \leq p_T^{\text{miss}} < 140$ GeV (page 1).	183
E.3	Pulls of the nuisance parameters for the fit to 2016 data in the CR with $100 \leq p_T^{\text{miss}} < 140$ GeV (page 2).	184
E.4	Same as Fig. E.1, but for 2017 data.	185
E.5	Pulls of the nuisance parameters for the fit to 2017 data in the CR with $100 \leq p_T^{\text{miss}} < 140$ GeV (page 1).	186
E.6	Pulls of the nuisance parameters for the fit to 2017 data in the CR with $100 \leq p_T^{\text{miss}} < 140$ GeV (page 2).	187
E.7	Same as Fig. E.1, but for 2018 data.	188
E.8	Pulls of the nuisance parameters for the fit to 2018 data in the CR with $100 \leq p_T^{\text{miss}} < 140$ GeV (page 1).	189

E.9	Pulls of the nuisance parameters for the fit to 2018 data in the CR with $100 \leq p_T^{\text{miss}} < 140$ GeV (page 2).	190
F.1	Distributions of $m_{T2}(\ell\ell)$ for events with $160 \leq p_T^{\text{miss}} < 220$ GeV, at least one jet but no b-tagged jets in 2018 simulated data sets. The last bin includes the overflow entries. In the bottom panel, the uncertainties in the expected yields of the SM processes are shown: the gray band represents the statistical uncertainty, while the red (blue) band shows the variation in the $m_{T2}(\ell\ell)$ distribution when varying the JES up (down) by its uncertainty. In the left plot, original MC variations are used, while in the right one, the smoothed variations are shown.	192
F.2	Same as in Fig. F.1 for events with $p_T^{\text{miss}} \geq 380$ GeV and veto on b-tagged jets in 2018 simulated data sets.	192
F.3	Comparison of blinded exclusion regions obtained when using the original MC variations (red curve) and the smoothed ones (black) for chargino (left plot) and top squark (right) pair production.	193
G.1	Observed and expected $m_{T2}(\ell\ell)$ distributions for SM processes in the SR1 after a background-only fit to the data in the chargino SRs for 2016 data. The $m_{T2}(\ell\ell)$ distributions for a signal hypothesis with a chargino mass of 800 GeV and a neutralino mass of 200 GeV are also shown. The distributions in the SR1 with no jets are shown at the top, and the ones in the SR1 with jets but no b-tagged jets are shown at the bottom, with the plots on the left corresponding to different flavour events and the ones on the right to same flavour events, respectively. In the bottom panel, the ratio of data and SM expectations is shown. The hatched band represents the total uncertainty, including the sources discussed in Section 8.5.	196
G.2	Same as for Fig. G.1 but for the SR2.	197
G.3	Observed and expected $m_{T2}(\ell\ell)$ distributions for SM processes in the SR3 and SR4 after a background-only fit to the data in the chargino SRs for 2016 data. The $m_{T2}(\ell\ell)$ distributions for a signal hypothesis with a chargino mass of 800 GeV and a neutralino mass of 200 GeV are also shown. The distributions in the SR3 are shown at the top, and the ones in the SR4 are shown at the bottom, with the plots on the left corresponding to different flavour events and the ones on the right to same flavour events, respectively. In the bottom panel, the ratio of data and SM expectations is shown. The hatched band represents the total uncertainty, including the sources discussed in Section 8.5.	198
G.4	Same as for Fig. G.1 but for 2017 data.	199
G.5	Same as for Fig. G.4 but for the SR2 and 2017 data.	199
G.6	Same as for Fig. G.3 but for 2017 data.	200
G.7	Same as for Fig. G.1 but for 2018 data.	200
G.8	Same as for Fig. G.1 but for the SR2 and 2018 data.	201
G.9	Same as for Fig. G.3 but for 2018 data.	201
G.10	Observed and expected $m_{T2}(\ell\ell)$ distributions for SM processes in the SR1 after a background-only fit to the data in the top squark SRs for 2016 data. The $m_{T2}(\ell\ell)$ distributions for a signal hypothesis with a top squark mass of 400 GeV and a neutralino mass of 313 GeV are also shown. Top plots are for DF (left) and SF (right) events with no b-tagged jets. Bottom plots are for DF (left) and SF (right) events with at least one b-tagged jets. In the bottom panel, the ratio of data and SM expectations is shown. The hatched band represents the total uncertainty, including the sources discussed in Section 8.5.	202
G.11	Same as for Fig. G.10 for the SR2.	203
G.12	Same as for Fig. G.10 for the SR3.	203
G.13	Same as for Fig. G.10 for the SR4.	204
G.14	Same as for Fig. G.10 for the 2017 data.	204
G.15	Same as for Fig. G.10 for the SR2 and 2017 data.	205
G.16	Same as for Fig. G.10 for the SR3 and 2017 data.	205
G.17	Same as for Fig. G.10 for the SR4 and 2017 data.	206
G.18	Same as for Fig. G.10 for the 2018 data.	206
G.19	Same as for Fig. G.10 for the SR2 and 2018 data.	207

G.20	Same as for Fig. G.10 for the SR3 and 2018 data.	207
G.21	Same as for Fig. G.10 for the SR4 and 2018 data.	208
G.22	Observed and expected yields of events in the CRs for the normalization of the top background in 2016 data after a background-only ML fit to the chargino/slepton SRs. From top-left clockwise, the SF events in CR1_{tags} , CR2_{tags} , CR4_{tags} , and CR3_{tags} are shown. In the bottom panel, the ratio of data and SM expectations is shown. The hatched band represents the total uncertainty after the fit.	209
G.23	Observed and expected yields of events in the CRs for the normalization of the top background in 2016 data after a background-only ML fit to the chargino/slepton SRs. From top-left clockwise, the DF events in CR1_{tags} , CR2_{tags} , CR4_{tags} , and CR3_{tags} are shown. In the bottom panel, the ratio of data and SM expectations is shown. The hatched band represents the total uncertainty after the fit.	210
G.24	Observed and expected yields of events in the CRs for the normalization of the WZ background in 2016 data after a background-only ML fit to the chargino/slepton SRs (Table 8.5). Top row shows the events with $160 < p_{\text{T}}^{\text{miss}} < 220$ GeV and no jets (left) or at least one jet but no b-tagged jets (right). The middle row shows the same but for events with $220 < p_{\text{T}}^{\text{miss}} < 280$ GeV. Bottom row shows events with $280 < p_{\text{T}}^{\text{miss}} < 380$ GeV (left) with $p_{\text{T}}^{\text{miss}} > 380$ GeV (right), both with no b-tagged jets. In the bottom panel, the ratio of data and SM expectations is shown. The hatched band represents the total uncertainty after the fit.	211
G.25	Observed and expected yields of events in the CRs for the normalization of the ZZ background in 2016 data after a background-only ML fit to the chargino/slepton SRs (Table 8.5). Top row shows the events with $160 < p_{\text{T}}^{\text{miss}} < 220$ GeV and no jets (left) or at least one jet but no b-tagged jets (right). The middle row shows the same but for events with $220 < p_{\text{T}}^{\text{miss}} < 280$ GeV. Bottom row shows events with $280 < p_{\text{T}}^{\text{miss}} < 380$ GeV (left) with $p_{\text{T}}^{\text{miss}} > 380$ GeV (right), both with no b-tagged jets. In the bottom panel, the ratio of data and SM expectations is shown. The hatched band represents the total uncertainty after the fit.	212
G.26	Observed and expected yields of events in the CRs for the normalization of the $t\bar{t}Z$ background in 2016 data after a background-only ML fit to the chargino/slepton SRs (Table 8.5). From top-left clockwise, the events with $160 < p_{\text{T}}^{\text{miss}} < 220$ GeV, $220 < p_{\text{T}}^{\text{miss}} < 280$ GeV, and $p_{\text{T}}^{\text{miss}} > 280$ GeV are shown. In the bottom panel, the ratio of data and SM expectations is shown. The hatched band represents the total uncertainty after the fit.	213
G.27	Observed and expected yields of events in the CRs for the normalization of the top background in 2017 data after a background-only ML fit to the chargino/slepton SRs. From top-left clockwise, the SF events in CR1_{tags} , CR2_{tags} , CR4_{tags} , and CR3_{tags} are shown. In the bottom panel, the ratio of data and SM expectations is shown. The hatched band represents the total uncertainty after the fit.	214
G.28	Observed and expected yields of events in the CRs for the normalization of the top background in 2017 data after a background-only ML fit to the chargino/slepton SRs. From top-left clockwise, the DF events in CR1_{tags} , CR2_{tags} , CR4_{tags} , and CR3_{tags} are shown. In the bottom panel, the ratio of data and SM expectations is shown. The hatched band represents the total uncertainty after the fit.	215
G.29	Observed and expected yields of events in the CRs for the normalization of the WZ background in 2017 data after a background-only ML fit to the chargino/slepton SRs (Table 8.5). Top row shows the events with $160 < p_{\text{T}}^{\text{miss}} < 220$ GeV and no jets (left) or at least one jet but no b-tagged jets (right). The middle row shows the same but for events with $220 < p_{\text{T}}^{\text{miss}} < 280$ GeV. Bottom row shows events with $280 < p_{\text{T}}^{\text{miss}} < 380$ GeV (left) with $p_{\text{T}}^{\text{miss}} > 380$ GeV (right), both with no b-tagged jets. In the bottom panel, the ratio of data and SM expectations is shown. The hatched band represents the total uncertainty after the fit.	216

- G.30 Observed and expected yields of events in the CRs for the normalization of the ZZ background in 2017 data after a background-only ML fit to the chargino/slepton SRs (Table 8.5). Top row shows the events with $160 < p_T^{\text{miss}} < 220$ GeV and no jets (left) or at least one jet but no b-tagged jets (right). The middle row shows the same but for events with $220 < p_T^{\text{miss}} < 280$ GeV. Bottom row shows events with $280 < p_T^{\text{miss}} < 380$ GeV (left) with $p_T^{\text{miss}} > 380$ GeV (right), both with no b-tagged jets. In the bottom panel, the ratio of data and SM expectations is shown. The hatched band represents the total uncertainty after the fit. 217
- G.31 Observed and expected yields of events in the CRs for the normalization of the $t\bar{t}Z$ background in 2017 data after a background-only ML fit to the chargino/slepton SRs (Table 8.5). From top-left clockwise, the events with $160 < p_T^{\text{miss}} < 220$ GeV, $220 < p_T^{\text{miss}} < 280$ GeV, $p_T^{\text{miss}} > 380$ GeV, and $280 < p_T^{\text{miss}} < 380$ GeV are shown. In the bottom panel, the ratio of data and SM expectations is shown. The hatched band represents the total uncertainty after the fit. 218
- G.32 Observed and expected yields of events in the CRs for the normalization of the top background in 2018 data after a background-only ML fit to the chargino/slepton SRs. From top-left clockwise, the SF events in CR1_{tags}, CR2_{tags}, CR4_{tags}, and CR3_{tags} are shown. In the bottom panel, the ratio of data and SM expectations is shown. The hatched band represents the total uncertainty after the fit. 219
- G.33 Observed and expected yields of events in the CRs for the normalization of the top background in 2018 data after a background-only ML fit to the chargino/slepton SRs. From top-left clockwise, the DF events in CR1_{tags}, CR2_{tags}, CR4_{tags}, and CR3_{tags} are shown. In the bottom panel, the ratio of data and SM expectations is shown. The hatched band represents the total uncertainty after the fit. 220
- G.34 Observed and expected yields of events in the CRs for the normalization of the WZ background in 2018 data after a background-only ML fit to the chargino/slepton SRs (Table 8.5). Top row shows the events with $160 < p_T^{\text{miss}} < 220$ GeV and no jets (left) or at least one jet but no b-tagged jets (right). The middle row shows the same but for events with $220 < p_T^{\text{miss}} < 280$ GeV. Bottom row shows events with $280 < p_T^{\text{miss}} < 380$ GeV (left) with $p_T^{\text{miss}} > 380$ GeV (right), both with no b-tagged jets. In the bottom panel, the ratio of data and SM expectations is shown. The hatched band represents the total uncertainty after the fit. 221
- G.35 Observed and expected yields of events in the CRs for the normalization of the ZZ background in 2018 data after a background-only ML fit to the chargino/slepton SRs (Table 8.5). Top row shows the events with $160 < p_T^{\text{miss}} < 220$ GeV and no jets (left) or at least one jet but no b-tagged jets (right). The middle row shows the same but for events with $220 < p_T^{\text{miss}} < 280$ GeV. Bottom row shows events with $280 < p_T^{\text{miss}} < 380$ GeV (left) with $p_T^{\text{miss}} > 380$ GeV (right), both with no b-tagged jets. In the bottom panel, the ratio of data and SM expectations is shown. The hatched band represents the total uncertainty after the fit. 222
- G.36 Observed and expected yields of events in the CRs for the normalization of the $t\bar{t}Z$ background in 2018 data after a background-only ML fit to the chargino/slepton SRs (Table 8.5). From top-left clockwise, the events with $160 < p_T^{\text{miss}} < 220$ GeV, $220 < p_T^{\text{miss}} < 280$ GeV, $p_T^{\text{miss}} > 380$ GeV, and $280 < p_T^{\text{miss}} < 380$ GeV are shown. In the bottom panel, the ratio of data and SM expectations is shown. The hatched band represents the total uncertainty after the fit. 223
- G.37 Observed and expected yields of events in the CRs for the normalization of the WZ background in 2016 data after a background-only ML fit to the top squark SRs (Table 8.5). From top-left clockwise, the events with $160 < p_T^{\text{miss}} < 220$ GeV, $220 < p_T^{\text{miss}} < 280$ GeV, $p_T^{\text{miss}} > 380$ GeV, and $280 < p_T^{\text{miss}} < 380$ GeV are shown. In the bottom panel, the ratio of data and SM expectations is shown. The hatched band represents the total uncertainty after the fit. 224
- G.38 Observed and expected yields of events in the CRs for the normalization of the ZZ background in 2016 data after a background-only ML fit to the top squark SRs (Table 8.5). From top-left clockwise, the events with $160 < p_T^{\text{miss}} < 220$ GeV, $220 < p_T^{\text{miss}} < 280$ GeV, and $p_T^{\text{miss}} > 280$ GeV are shown. In the bottom panel, the ratio of data and SM expectations is shown. The hatched band represents the total uncertainty after the fit. 225

- G.39 Observed and expected yields of events in the CRs for the normalization of the $t\bar{t}Z$ background in 2016 data after a background-only ML fit to the top squark SRs (Table 8.5). From top-left clockwise, the events with $160 < p_T^{\text{miss}} < 220$ GeV, $220 < p_T^{\text{miss}} < 280$ GeV, and $p_T^{\text{miss}} > 280$ GeV are shown. In the bottom panel, the ratio of data and SM expectations is shown. The hatched band represents the total uncertainty after the fit. 226
- G.40 Observed and expected yields of events in the CRs for the normalization of the WZ background in 2017 data after a background-only ML fit to the top squark SRs (Table 8.5). From top-left clockwise, the events with $160 < p_T^{\text{miss}} < 220$ GeV, $220 < p_T^{\text{miss}} < 280$ GeV, $p_T^{\text{miss}} > 380$ GeV, and $280 < p_T^{\text{miss}} < 380$ GeV are shown. In the bottom panel, the ratio of data and SM expectations is shown. The hatched band represents the total uncertainty after the fit. 227
- G.41 Observed and expected yields of events in the CRs for the normalization of the ZZ background in 2017 data after a background-only ML fit to the top squark SRs (Table 8.5). From top-left clockwise, the events with $160 < p_T^{\text{miss}} < 220$ GeV, $220 < p_T^{\text{miss}} < 280$ GeV, $p_T^{\text{miss}} > 380$ GeV, and $280 < p_T^{\text{miss}} < 380$ GeV are shown. In the bottom panel, the ratio of data and SM expectations is shown. The hatched band represents the total uncertainty after the fit. 228
- G.42 Observed and expected yields of events in the CRs for the normalization of the $t\bar{t}Z$ background in 2017 data after a background-only ML fit to the top squark SRs (Table 8.5). From top-left clockwise, the events with $160 < p_T^{\text{miss}} < 220$ GeV, $220 < p_T^{\text{miss}} < 280$ GeV, $p_T^{\text{miss}} > 380$ GeV, and $280 < p_T^{\text{miss}} < 380$ GeV are shown. In the bottom panel, the ratio of data and SM expectations is shown. The hatched band represents the total uncertainty after the fit. 229
- G.43 Observed and expected yields of events in the CRs for the normalization of the WZ background in 2018 data after a background-only ML fit to the top squark SRs (Table 8.5). From top-left clockwise, the events with $160 < p_T^{\text{miss}} < 220$ GeV, $220 < p_T^{\text{miss}} < 280$ GeV, $p_T^{\text{miss}} > 380$ GeV, and $280 < p_T^{\text{miss}} < 380$ GeV are shown. In the bottom panel, the ratio of data and SM expectations is shown. The hatched band represents the total uncertainty after the fit. 230
- G.44 Observed and expected yields of events in the CRs for the normalization of the ZZ background in 2018 data after a background-only ML fit to the top squark SRs (Table 8.5). From top-left clockwise, the events with $160 < p_T^{\text{miss}} < 220$ GeV, $220 < p_T^{\text{miss}} < 280$ GeV, and $p_T^{\text{miss}} > 280$ GeV are shown. In the bottom panel, the ratio of data and SM expectations is shown. The hatched band represents the total uncertainty after the fit. 231
- G.45 Observed and expected yields of events in the CRs for the normalization of the $t\bar{t}Z$ background in 2018 data after a background-only ML fit to the top squark SRs (Table 8.5). From top-left clockwise, the events with $160 < p_T^{\text{miss}} < 220$ GeV, $220 < p_T^{\text{miss}} < 280$ GeV, $p_T^{\text{miss}} > 380$ GeV, and $280 < p_T^{\text{miss}} < 380$ GeV are shown. In the bottom panel, the ratio of data and SM expectations is shown. The hatched band represents the total uncertainty after the fit. 232

List of Tables

3.1	Summarised list of SM particles with their spin and R-Parity and their MSSM equivalent	20
4.1	Space resolution for each of the CMS tracker sub detectors, in terms of the (r, ϕ) plane and along the (z) axis, as defined in Fig. 4.7	34
5.1	Electron identification requirements for the cut-based tight working point in the barrel and in the endcaps. Other cut-based working points apply a looser selection on the same variables.	58
8.1	Baseline selection used for both the chargino and top squark pair production searches. A selection optimised for the full Run II data set is presented in Section 8.3.1.	84
8.2	Definition of the SRs for the chargino, slepton and top squark searches as a function of the p_T^{miss} value, the b-jet multiplicity and jet multiplicity, and the lepton pair channels, as well as the ISR requirement used for the top squark production. Also shown are the CRs with b-tagged jets used for the normalization of the $t\bar{t}$ and tW backgrounds for the chargino and slepton searches. The last row for each search type shows the $m_{T2}(\ell\ell)$ binning used in the ML fit performed to extract the signal.	90
8.3	Definition of the SRs for the 2016 chargino search as a function of the p_T^{miss} value, the b-jet multiplicity and jet multiplicity. Also shown are the CRs with b-tagged jets used for the normalisation of the $t\bar{t}$ and tW backgrounds. Each of the regions is further divided in seven $m_{T2}(\ell\ell)$ bins, as described in the last row.	90
8.4	Definition of the SRs for the 2016 top squark production search as a function of the p_T^{miss} value, the b-jet multiplicity and the ISR jet requirement. Each of the regions is further divided in seven $m_{T2}(\ell\ell)$ bins, as described in the last row.	91
8.5	Preview of the additional CRs included in the ML fit, split according to the same p_T^{miss} and jet multiplicity bins as for the SRs discussed in Table 8.2. Details on the constructions of these CRs are given in Sections 8.4.2 to 8.4.2	91
8.6	Normalisation scale factors for the nonprompt lepton rate for each of the four data-taking periods.	96
8.7	A summary of the sources of uncertainty, the corresponding nuisances in the ML fit data cards, and their correlation across data-taking years and p_T^{miss} bins.	108
8.8	Size of the systematic uncertainties in the predicted yields of SM processes for the chargino search SRs (Top part of Table 8.2). The yields columns show the range of the uncertainties in the global background normalisation across the different data-taking years and SRs, for each p_T^{miss} bin separately. The $m_{T2}(\ell\ell)$ shape columns quantify the effect on the $m_{T2}(\ell\ell)$ shape. This is computed by taking the maximum variation across the $m_{T2}(\ell\ell)$ bins (after renormalising for the global change of all the distribution) in each SR. The range of this variation across the data-taking years and SRs is given for each p_T^{miss} bin separately.	109
8.9	Same as in Table 8.8 for the top squark SRs (Bottom part of Table 8.2).	109

8.10	Same as in Table 8.8 for a representative mass hypothesis of the chargino pair production model ($\tilde{\chi}_1^\pm \rightarrow \tilde{\ell}\nu(\ell\tilde{\nu}) \rightarrow \ell\nu\tilde{\chi}_1^0$, with $m_{\tilde{\chi}_1^\pm} = 800$ GeV and $m_{\tilde{\chi}_1^0} = 200$ GeV).	110
8.11	Same as in Table 8.9 for a representative mass hypothesis of the top squark pair production model ($\tilde{t}_1 \rightarrow t\tilde{\chi}_1^0$, with $m_{\tilde{t}_1} = 400$ GeV and $m_{\tilde{\chi}_1^0} = 275$ GeV).	110
9.1	Observed and expected yields as a function of $m_{T2}(\ell\ell)$ for SM processes and two representative signal mass points. Rows correspond to the chargino SRs for the SF channel.	122
9.2	Same as for Table 9.1 but for the DF channel.	123
9.3	Observed and expected yields as a function of $m_{T2}(\ell\ell)$ for SM processes and two representative signal mass points. Rows correspond to the top squark SRs for the SF channel as defined in the bottom part of Table 8.2.	124
9.4	Same as for Table 9.3 but for the DF channel.	125
9.5	Fitted values of the rate parameters for the normalization of the backgrounds in the chargino/slepton SRs.	127
9.6	Fitted values of the rate parameters for the normalization of the backgrounds in the top squark SRs.	128
9.7	Observed and expected yields of DF (upper half) and SF (lower half) events in the SRs for the chargino/slepton search. The quoted uncertainties in the background predictions include statistical and systematic contributions.	136
9.8	Observed and expected yields of DF (upper half) and SF (lower half) events in the SRs for the top squark search. The quoted uncertainties in the background predictions include statistical and systematic contributions.	137
B.1	Trigger paths used to select events for the 2016 pre-VFP data-taking period. . .	163
B.2	Trigger paths used to select events for the 2016 post-VFP data-taking period. . .	163
B.3	Trigger paths used to select events for the 2017 data-taking period.	164
B.4	Trigger paths used to select events for the 2018 data-taking period.	164
C.1	Summary of the event selection and of the requirements on the tag and probe leptons used in the measurements of the scale factors for the additional requirements on the leptons used in the analysis.	171

Chapter 1

Introduction

Ever since the discovery of the Higgs boson in 2012 [23, 24] the Standard Model of particle physics (SM) is thought to be complete. This model has had a lot of successes, ranging from the prediction of the Higgs boson in 1964, 48 years before its discovery, to the calculation of the value of observables such as the fine structure constant, consistent with a precision of less than 1 part per billion with its measured value [25]. However, despite its multiple successes over several decades, the SM is thought to be incomplete.

One of the more important question not answered by the SM regards the nature of Dark Matter (DM). There are many independent pieces of evidence pointing to its existence, from galaxies' rotational velocities being faster than expected [26, 27], to the anisotropies found in the cosmic microwave background (CMB) [28], or in gravitational lensing cases such as the Bullet cluster [29]. However, despite many independent experimental hints of its existence, its fundamental composition is not known, and instead the only information about its nature is that it interacts gravitationally but does not seem to interact electromagnetically. In addition to that, there are theoretical motivations to consider the SM as incomplete, too. One such reason is that it does not contain a description of the gravitational force, nor an explanation of why the measured mass of the Higgs boson is so much lighter than the Planck scale, the so-called hierarchy problem, which results in the SM not being considered natural.

Several theories, usually referred to as beyond the standard model (BSM), have tried to explain some of these open questions over the years, with no definitive success as of today. Among these theories, the most complete and comprehensive is the supersymmetry (SUSY), devised as an extension of the SM where for each particle in the model there is one supersymmetrical companion [30, 31, 32, 33, 34, 35, 36, 37, 38]. This theory has traditionally been favoured by many particle physicists, since it provides answers to many of the aforementioned problems. For instance, the hierarchy problem is solved, since the large quantum loop corrections to the Higgs boson mass, caused mainly by the top quark, can be counteracted by those coming from the top quark superpartner [39, 40, 41]. In addition to that, if R-Parity is conserved, the lightest supersymmetric particle (LSP) is stable, and, if naturalness is assumed, the LSP particle is expected to be massive [42, 43], making it a good candidate for dark matter.

This thesis presents a search for supersymmetric particles produced in pairs, in events with two oppositely charged leptons (either electrons or muons) and large missing transverse momentum, selected from data collected by the (CMS) detector in proton-proton collisions at $\sqrt{s} = 13$ TeV at the LHC large hadron collider (LHC) in the years 2016, 2017 and 2018, for a total integrated luminosity of 138 fb^{-1} . This search is an extension of a similar analysis performed using only

2016 data [44].

The obtained results are interpreted in several simplified supersymmetric models in final states with two oppositely charged (OC) leptons (ℓ), and missing transverse momentum (p_T^{miss}) from the two LSPs. Results are shown for the pair production of the lightest chargino ($\tilde{\chi}_1^\pm$), of charged sleptons ($\tilde{\ell}$), or of the lightest top squark (\tilde{t}_1) assuming R-parity conservation and assuming the lightest neutralino ($\tilde{\chi}_1^0$) as the LSP. The chargino pair production is studied throughout the whole spectrum of chargino masses experimentally accessible, whereas the top squark search is focused on the compressed spectrum in which the mass difference between the top squark and the LSP is within the masses of the W boson and the top quark. Some of the results presented in this document have already been made public and displayed in international conferences [45], while the full set of results are undergoing their last internal review prior to publication.

The document is organised as follows: the theoretical framework required to understand this document is first presented, first focusing on a review of the main aspects of the standard model, as shown Chapter 2; followed by a brief description of SUSY in Chapter 3. Chapter 4 will focus on the experimental setup, describing how the LHC functions, followed by a description of the CMS apparatus and all its subdetectors. Chapter 5 describes how each of the objects used in the analysis is reconstructed in the CMS detector, followed by a brief description of the Monte Carlo simulated samples, in Chapter 6.

Subsequently, Chapter 7 presents the signal models studied in this document as well as the main standard model backgrounds. It is followed by Chapter 8, where the event selection strategy and background estimation is depicted, as well as the main statistical and systematic uncertainties. In Chapter 9, after explaining how the signal is extracted, the obtained results are shown, both in terms of the distributions and the different interpretations considered in the analysis. Finally, Chapter 10 presents the thesis conclusions. Several appendices are also presented, where a more technical information of the concepts presented in the document core are depicted, including also a summary of the contents presented in the document in Spanish, in Appendix A.

Chapter 2

The Standard Model

Currently, the best description of all known particles and interactions between them lies in a relativistic quantum field theory (QFT), known as the standard model of particle physics (SM). This theory, which covers the electromagnetic, strong and weak forces, has been challenged multiple times ever since its inception, instead providing us with predictions with a great level of accuracy. Due to this fact, nowadays, it is used as the main tool to predict all the known physical processes happening at the LHC (and beyond), and thus, its correct understanding is paramount when searching for new physics, as these kinds of analyses probe for discrepancies in the data with respect to the SM.

This chapter will provide with a general overview of the SM, and it is split in two different sections: Section 2.1 provides a brief description of the model, with a description of each of the forces and particles involved in it, while a list of the achievements and shortcomings of the SM is presented in Section 2.2. More exhaustive and in depth descriptions beyond the scope of this document can be found in the literature [46, 47].

2.1 An overview of the Standard Model

The Standard Model is a renormalisable a relativistic quantum field theory, based on the following group of symmetries:

$$SU(3)_C \otimes SU(2)_L \otimes U(1)_Y \tag{2.1}$$

It describes all the known particles and three out of the four main interactions between them, namely, the weak, strong and electromagnetic interactions, while lacking a description for gravity.

2.1.1 Fundamental Particles of the Standard Model

The fundamental particles of the SM can be divided in two types, including on the one hand the constituents of matter, which are fermions (i.e. particle of half-integer spin), and on the other the mediators of the interactions, which are bosons (i.e. particle of integer spin), as described schematically in Fig. 2.1.

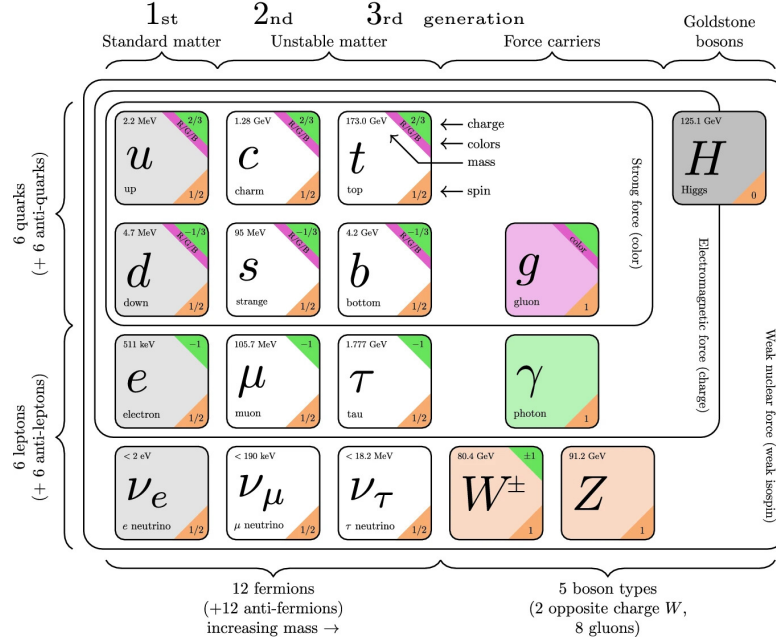


Figure 2.1: Fundamental particles of the Standard model and their properties [1]

Fermions

The fermions describing the matter fields in the SM have spin $1/2$. They are divided in two families of 6 leptons and 6 quarks. Each family is organised in three generations of doublets of increasing masses. The first generation is the one that constitutes ordinary matter, while the particles of the other two generations are unstable and are only generated at high energies. Finally, each fermion in the SM has a corresponding antiparticle with inverted quantum numbers. The lepton doublet is formed by a charged lepton and a neutral one. The charged leptons (generally labelled as ℓ^-) have a charge of -1 and the lightest of them is the electron, while equivalent antimatter leptons (ℓ^+) have $+1$ charge, being the lightest the positron. Of the three charged leptons, only the electron is thought to be stable, while higher generation leptons decay into lighter leptons. Muons (μ) possess a lifespan of approximately $2.2 \mu\text{s}$ [48], albeit due to relativistic effects, the decay lengths of muons produced at the energies reached at the LHC are long enough that they can be considered stable in terms of their reconstruction. Tau (τ) leptons on the other hand have a much shorter lifetime ($\sim 2.9 \times 10^{-13} \text{ s}$) and are typically not observed directly but via their decays, either leptonic ($\sim 35\%$ of the time) or via hadrons ($\sim 65\%$ of the time).

The neutral leptons, known as neutrinos (to distinguish between generations the name of their charged lepton companion is used, i.e. electron-neutrino, ν_e , for the first generation neutrino). They are characterised by having a very low mass¹. Their mass was generally thought to be zero by the SM theory, albeit now it is known to be non-zero due to their flavour oscillations [50, 51, 52]. Neutrinos only interact weakly, whereas the charged leptons are also affected by the electromagnetic force.

Each doublet of quarks is formed by one of an *up* type (up, charm, or top), and one *down* type (down, strange, or bottom), with charges of $+2/3$ and $-1/3$, respectively. Each antiquark (\bar{q}) doublet is similarly formed by a quark of anti-up type, and one of anti-down type, with charges of $-2/3$ and $+1/3$. Unlike the leptons, they carry an additional quantum number, known as colour, which causes them to interact also through the strong force (in addition to the weak and electromagnetic forces). Individual quarks are thought not to be able to exist freely, but instead form part of bound states, collectively known as hadrons. Hadrons are categorised by

¹In fact, its named was coined by the great physicist Enrico Fermi, to reflect that it has the same charge as the neutron, while being much lighter, thus using the diminutive suffix *-ino* from Italian [49].

the number of quarks they contain: mesons are formed by a pair of quarks ($q\bar{q}$) and baryons by a triad of quarks (qqq or $\bar{q}\bar{q}\bar{q}$). Examples of baryons include the protons (formed by two up quarks and one down quark) and neutrons (two down quarks and one up quark) that form the nuclei of the atoms of ordinary matter. In the last years, more exotic compounds have been found, comprising hadrons states of four quarks (known as tetraquarks [53]) or five quarks (known as pentaquarks [54]).

Bosons

Bosons are particles of an integer spin. They can be divided between the force carriers bosons and the Higgs boson. The former are gauge bosons characterised by having a spin 1 and being the force propagators. The most well known of them is the photon, which is the electromagnetic force carrier and is massless and neutral. Also massless and neutral are the strong force carriers, which are known as gluons and interact with the quarks and themselves. Finally, the weak force is carried by three massive bosons: two W bosons, with charge +1 and -1, and the Z bosons, which is neutral.

In addition to these force carrier bosons, an additional boson exists which provides mass to the particles in the SM, via the spontaneous symmetry breaking mechanism [55, 56]. This mechanism is known as the Brout-Englert-Higgs mechanism, or simply Higgs mechanism, while the boson is known as Higgs boson, which, unlike the aforementioned force carrying bosons, has spin 0. This particle was the last fundamental particle to be experimentally observed.

2.1.2 Interactions in the Standard Model

As previously discussed, three forces are included in the SM:

- ◆ The strong interaction, represented by $SU(3)_C$, is responsible for the atomic nuclei stability. It is mediated by gluons at the nucleus length range (~ 1)fm. Its field of study is known as quantum chromodynamics (QCD).
- ◆ The electromagnetic interaction is mediated by the photon and has an infinite range. It is studied by the quantum electrodynamics (QED) theory, which is now part of the electroweak EWK theory.
- ◆ The weak interaction is responsible for the β decay and plays an important role in nuclear fusion. It is mediated by the W and Z bosons, and has a range of $\sim 10^{-3}$ fm. It is described together to the electromagnetic force by the (EWK) theory, which corresponds to $SU(2)_L \times U(1)_Y$.

The general Lagrangian of the SM, namely \mathcal{L}_{SM} , can be thus described as the sum of the Lagrangians of each of the interactions, plus the Higgs Lagrangian:

$$\mathcal{L}_{SM} = \mathcal{L}_{QCD} + \mathcal{L}_{EWK} + \mathcal{L}_H \quad (2.2)$$

Where \mathcal{L}_{QCD} , \mathcal{L}_{QED} and \mathcal{L}_H corresponds to the QCD, the QED and the Higgs Lagrangians, respectively. The whole Lagrangian can be written, in a compact manner, as:

$$\mathcal{L} = -\frac{1}{4}F_{\mu\nu}F^{\mu\nu} + i\bar{\psi}\not{D}\psi + h.c. + \bar{\psi}_i y_{ij} \psi_j \phi + |\mathcal{D}_\mu \phi|^2 - V(\phi) \quad (2.3)$$

Which, it is typically split in four components:

- ◆ The first component $(-\frac{1}{4}F_{\mu\nu}F^{\mu\nu})$ corresponds to the scalar product of the field strength tensor $F_{\mu\nu}$, the kinetic term of the gauge fields, which describes how the gauge fields propagate through space and time.
- ◆ The second component $(i\bar{\psi}\not{D}\psi + h.c.)$ describes the kinetic term of the fermion field ψ , and contains, through the covariant derivative D , the interaction terms between the fermions and the gauge bosons. Likewise, $h.c.$ stands for the hermitian conjugate.
- ◆ The third component $(\bar{\psi}_i y_{ij} \psi_j \phi)$, describes the so-called Yukawa interactions between the fermions and the Higgs field, and contains both the mass terms for the fermions and the interaction terms between the fermions and the Higgs boson.
- ◆ Lastly, the fourth component, $(|\mathcal{D}_\mu \phi|^2 - V(\phi))$ contains the interactions between the Higgs and the other bosons. $|\mathcal{D}_\mu \phi|^2$ gives the mass terms of the weak bosons together with their couplings with the Higgs boson, whereas $V(\phi)$ is the Higgs potential, which includes the Higgs bosons self couplings.

Having defined the general features of the SM, the remaining part of the chapter will focus into providing a more detailed definition of each of the fundamental parts of it, in order to obtain a deeper understanding of each part of the Lagrangian.

Quantum Chromodynamics

QCD is a quantum field theory that describes the interactions between quarks and gluons, which are the fundamental particles involved in the strong nuclear force. It is a non-Abelian gauge theory, meaning it is governed by a non-commutative symmetry group, where the sequence of field transformations affects the result. The mediator particles of the strong force are the gluons, which carry a property known as colour, analogous to how particles in electromagnetism carry electric charge. However, unlike electromagnetic charge, there are three conserved colour charges, namely red (r), green (g), and blue (b), which are orthogonal to each other. Thus, the fermionic fields in QCD are typically represented as:

$$\psi = \begin{pmatrix} \psi_R \\ \psi_G \\ \psi_B \end{pmatrix} \quad (2.4)$$

In QCD, there are eight different types of gluons, each one corresponding to the eight generators of the $SU(3)_C$ symmetry group. Likewise, quarks carry one of the three-colour charges (*red*, *green*, or *blue*), while their corresponding antiquarks carry the opposite charges (namely *anti-red*, *anti-green*, or *anti-blue*). These properties govern how quarks and gluons interact within particles like protons and neutrons, binding them together in the atomic nucleus.

As for the Lagrangian, in the case of the QCD, it is invariant under the transformations of the local gauge symmetry group $SU(3)_C$, and it is defined by:

$$\mathcal{L}_{QCD} = \sum_q \left[\bar{\psi}_{q,i} (\gamma^\mu \mathcal{D}_\mu)_{i,j} \psi_{q,j} - m_q \delta_{i,j} \bar{\psi}_{q,i} \psi_{q,j} - \frac{1}{4} G_{\mu\nu}^a G_a^{\mu\nu} \right] \quad (2.5)$$

Where γ^μ are the Dirac- γ -matrices, $\psi_{q,i}$ the quark field spinor for quark q , and the i, j are the colour indices ($i, j = 1, 2, 3$). \mathcal{D}_μ is the gauge covariant derivative, defined as $\mathcal{D}_\mu = \partial_\mu - ig_c A_\mu^a T_a$, where A_μ^a is the gluon field, g_c the (dimensionless) coupling strength, and T_a are the generators of the non-Abelian group $SU(3)_C$.

Finally, $G_{\mu\nu}^a$ present in the last item in Eq. 2.5, represents the gauge invariant gluon field tensor. Given a structure constant of $SU(3)_C$ f^{abc} , it can be defined as follows:

$$G_{\mu\nu}^a = \partial_\mu A_\nu^a - \partial_\nu A_\mu^a + g_c f^{abc} A_\mu^b A_\nu^c \quad (2.6)$$

This definition of QCD redounds in two interesting properties:

- ◆ **Colour confinement:** This feature, although not proven analytically, is well established both experimentally and in lattice QCD calculations [57], on particles that are not colourless. For instance, if a pair of confined quarks separate from each other, the potential energy of the system will increase until it will become convenient to create of a new pair quark-antiquark to form colour-neutral hadrons with the original quarks. This process, called hadronisation, causes that high-momentum quarks produced in high energy collisions lead to the production of a large amount of collinear hadrons, in what is commonly known as a jet in high energy physics.
- ◆ **Asymptotic freedom:** This phenomenon, discovered for QCD in 1973 [58, 59], implies that the strength of the interactions lowers as the energy increases. A summary of the experimental measurements of the asymptotic freedom is shown in Fig. 2.2.

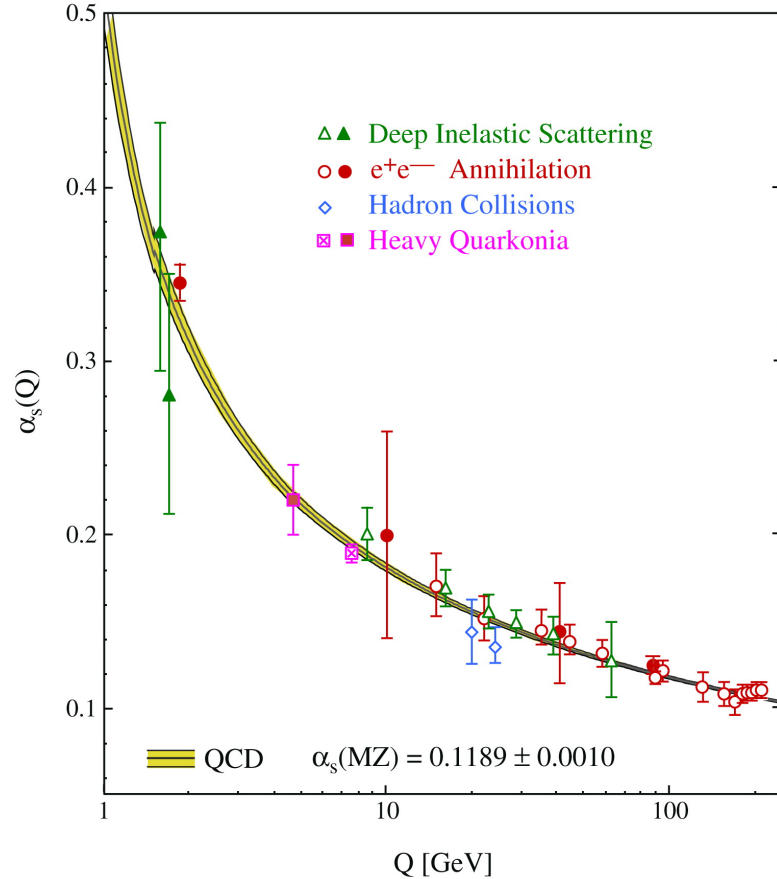


Figure 2.2: Measurement of the coupling strength $\alpha_s = \frac{g_c}{4\pi}$ in terms of the energy scale Q for different processes [2].

Electroweak interaction

Recalling the compact SM Lagrangian presented in Eq. 2.1, two other symmetries besides $SU(3)_C$ can be observed, namely $SU(2)_L \otimes U(1)_Y$. The theory built upon these symmetries is known as the electroweak (EWK) theory. Under this theory, $SU(2)_L$ is represented by the weak isospin (I_W), whose third component is conserved by weak interactions, and $U(1)_Y$ corresponds to the weak hypercharge symmetry. Under this theory, a new fundamental property of the particles arises, known as *chirality*, which only affects fermions, and can take two possible values, typically denoted as left (L) or right (R) handed by analogy to the concept of chirality in classical mechanics.

The term $SU(2)_L$ refers to the group of local phase transformations associated with the weak interaction. These transformations are governed by three generators, corresponding to the three 2×2 Pauli spin matrices. These matrices define the symmetry structure of the weak force in the SM, in particular how particles transform under this interaction. The required gauge invariance is achieved by introducing three spin-1 gauge fields, (W_i , $i = 1, 2, 3$). The weak charged-current interaction couples with different fermions in doublets that differ in one unit of electric charge, and have a weak isospin of $I_W = 1/2$. The interaction eigenstates of these fermion doublets are shown in Eq. 2.7.

$$\begin{pmatrix} \nu_e \\ e \end{pmatrix}_L \quad \begin{pmatrix} \nu_\mu \\ \mu \end{pmatrix}_L \quad \begin{pmatrix} \nu_\tau \\ \tau \end{pmatrix}_L \quad \begin{pmatrix} u \\ d \end{pmatrix}_L \quad \begin{pmatrix} c \\ s \end{pmatrix}_L \quad \begin{pmatrix} t \\ b \end{pmatrix}_L \quad (2.7)$$

with equivalent terms for right-handed antifermions. The right-handed particles and left-handed antiparticles are instead organised in weak isospin singlets with $I_W = 0$ and thus they do not couple to the gauge bosons of this symmetry, since these singlets are unaltered by the $SU(2)_L$ local gauge transformation.

$U(1)_Y$, on the other hand, is a symmetry group analogous to the local gauge group on which the QED theory is formulated. The local phase invariance is satisfied by introducing a neutral field associated to a B boson. In this symmetry, a conserved quantity is defined, known as the weak hypercharge Y_W , which can be defined in terms of the electromagnetic charge Q, and the third component of the weak isospin I_W^3 , as shown in Eq. 2.8:

$$Y_W = 2(Q - I_W^3) \quad (2.8)$$

In order to produce a theory that reunites both weak and electromagnetic forces, a quantum field theory that is invariant under $SU(2)_L \otimes U(1)_Y$ is needed. This translates into the hypercharge needing to have the same value in both components of the isospin doublets. Similarly, if one desires to define such combined theory in terms of its Lagrangian, it can be divided in two components:

$$\mathcal{L} = \mathcal{L}_g + \mathcal{L}_f \quad (2.9)$$

Where \mathcal{L}_g corresponds to the kinetic terms of the three W_i vector bosons and the B boson and it can be written as:

$$\mathcal{L}_g = -\frac{1}{4} (W_{\mu\nu}^i W_i^{\mu\nu} - B_{\mu\nu}^i B_i^{\mu\nu}) \quad (2.10)$$

Where $W_{i\mu\nu}$ (with $i=1,2,3$) and $B^{\mu\nu}$ are the field strength tensors for the weak isospin and hypercharge, respectively. Similarly, \mathcal{L}_f represents the kinetic terms for the fermions and can be written as:

$$\mathcal{L}_f = \sum_f i\bar{\psi}_f \gamma^\mu \mathcal{D}^\mu \psi_f \quad (2.11)$$

Where the sum is extended over all fermions f . \mathcal{D}^μ is the gauge covariant derivative necessary in order to guarantee the Lagrangian gauge invariance, and it is defined as follows:

$$\mathcal{D}^\mu = \partial^\mu + i\frac{g}{2}\sigma_i W_k^\mu + i\frac{g'}{2}Y_W B_\mu \quad (2.12)$$

Where g and g' correspond to the dimensionless coupling constants of $SU(2)_L$ and $U(1)_Y$ respectively. The Pauli matrices σ_i and the weak hypercharge Y_W correspond to the generators of the $SU(2)_L$ and $U(1)_Y$ groups, respectively. Finally, the physical fields can be obtained by performing linear combination of the aforementioned gauge fields, resulting in four fields, two of them neutral, as described in Equation 2.13:

$$A_\mu = \sin\theta_W W_\mu^3 + \cos\theta_W B_\mu, \quad Z_\mu = \cos\theta_W W_\mu^3 - \sin\theta_W B_\mu \quad (2.13)$$

These neutral fields correspond to the two SM neutral gauge bosons, A_μ to the photon (γ), and Z_μ to the Z boson. In addition to these, there are also two charged fields, labelled W^+ and W^- , defined in Eq. 2.14:

$$W_\mu^\pm = \frac{W_\mu^1 \mp iW_\mu^2}{\sqrt{2}} \quad (2.14)$$

Thus retrieving the four electroweak force carriers depicted in Fig. 2.1. However, if the previously mentioned fields were all what there is in the EWK theory, then all the bosons would be massless, which is in clear contradiction with the experimental observation of the W and Z bosons being massive. In addition to that, the fermion mass terms cannot be included in the SM Lagrangian without breaking the gauge symmetry on which the QCD and electroweak terms are based.

The Higgs sector

The gauge symmetry in the electroweak theory ensures the existence of a well-defined and renormalisable Lagrangian, which is crucial for constructing a consistent quantum field theory [60]. However, as we just saw, the very gauge invariance of the theory forbids to introduce in the Lagrangian explicit terms of mass for gauge bosons and fermions, that are nevertheless observed to be massive. A solution for this conundrum was proposed in 1964 by Robert Brout, François Englert and Peter Higgs [55, 56]. In this theory, which became known as the Brout-Englert-Higgs mechanism, symmetries are broken while keeping the Lagrangian gauge invariant. This is done via a spontaneous symmetry breaking (SSB) of the electroweak sector $SU(2)_L \otimes U(1)_Y$, that results in the need for one additional physical scalar particle, the later known as the Higgs boson. This particle would be the visible manifestation of the Higgs field, such that fermions and weak bosons acquire their masses by their interaction with this field. Its search was one of the main reasons for the LHC to be constructed, resulting in the observation of the Higgs boson by the ATLAS [23] and CMS [24] Collaborations in 2012, 48 years after the theory was proposed.

This mechanism is based on the Goldstone theorem [61], which states that if a Lagrangian exhibits an invariance under a continuous symmetry group G , but the ground state of the corresponding potential is only invariant under a subgroup $H \subset G$, then for each broken symmetry generator of G that does not belong to H , a corresponding massless spin-0 particle will exist. The set of states with the lowest energy, which are degenerate, are referred to as Goldstone bosons. These bosons transform as a multiplet under the symmetry group G . This way, if one such state is arbitrarily chosen as ground state of the system, the whole G symmetry is spontaneously broken, either through a real or a complex scalar field.

In the case of the electroweak sector of the SM, with local gauge symmetry $SU(2)_L \otimes U(1)_Y$, SSB is achieved in its minimal form by introducing a new $SU(2)_L$ weak isospin doublet:

$$\phi(x) = \begin{pmatrix} \phi^+(x) \\ \phi^0(x) \end{pmatrix} = \frac{1}{\sqrt{2}} \begin{pmatrix} \phi_1(x) + i\phi_2(x) \\ \phi_3(x) + i\phi_4(x) \end{pmatrix} \quad (2.15)$$

where $\phi^+(x)$ and $\phi^0(x)$ are two complex scalar fields, with positive and null charge, respectively.

Similarly, a new Lagrangian term, gauge invariant under the local transformations $SU(2)_L \otimes U(1)_Y$, is defined as:

$$\mathcal{L} = (\mathcal{D}_\mu \phi)^\dagger (\mathcal{D}^\mu \phi) - V(\phi) \quad (2.16)$$

where \mathcal{D} is the covariant derivative, previously defined in Eq. 2.12, and $V(\phi)$ is the potential of the ϕ field, which takes the form:

$$V(\phi) = \lambda(\phi^\dagger \phi) + \mu^2(\phi^\dagger \phi) \quad (2.17)$$

Where μ and λ are free parameters of the model. λ has to be positive to ensure the existence of a ground state in the potential, whereas the sign of μ^2 would change the shape of the function. A representation of the Higgs potential is depicted in Fig. 2.3, from where it can be extracted that if $\mu^2 > 0$, a single minimum would be found for $\phi = 0$, whereas if $\mu^2 < 0$, a circle of degenerate minima is expected, satisfying:

$$\phi^\dagger \phi = -\frac{\mu^2}{2\lambda} = \frac{v}{2} \quad (2.18)$$

Since the interaction of the electroweak gauge fields with the newly defined field conserves the electric charge, the ground states will be invariant under gauge transformations in the QED symmetry group. Therefore, only the neutral scalar field can have a non-zero value. Under these premises, v is defined as the vacuum expectation value of the Higgs field ϕ :

$$v = \langle 0 | \phi | 0 \rangle = \frac{1}{\sqrt{2}G_F} 246.22 \text{ GeV} [48] \quad (2.19)$$

where G_F corresponds to the Fermi constant. Once the ground state has been defined, the local gauge symmetry $SU(2)_L \otimes U(1)_Y$ gets spontaneously broken into only the QED component, which remains a true vacuum symmetry by construction. Subsequently, if the Goldstone theorem is applied, three massless Goldstone bosons arise, one per as many generators of broken

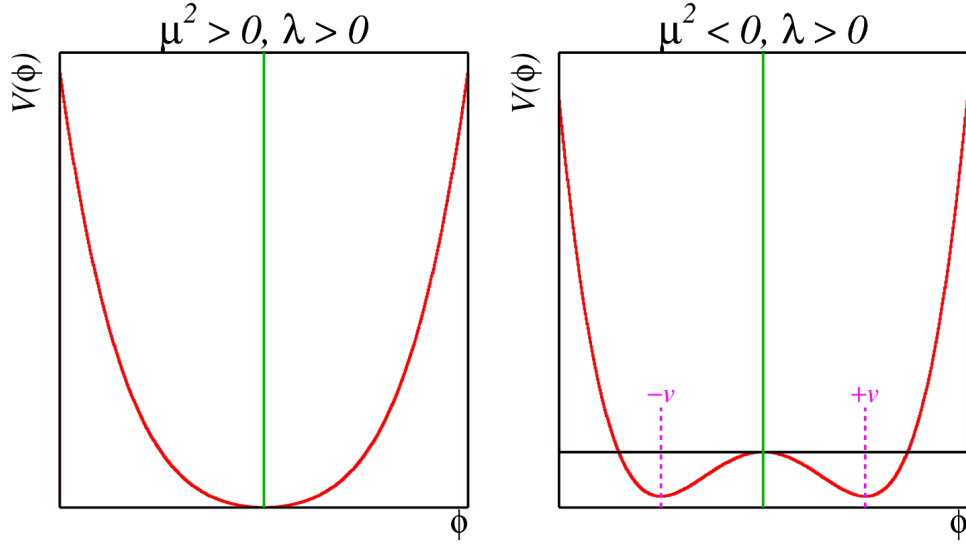


Figure 2.3: Shape of the higgs potential depending on the sign of μ . $\mu > 0$ is shown in the left and $\mu < 0$ in the right [3].

symmetries exist in the theory. These excitations over the ground state can be written in a generalised form:

$$\phi(x) = e^{i\frac{\sigma_i}{2}\theta^i(x)} \frac{1}{\sqrt{2}} \begin{pmatrix} 0 \\ v + H(x) \end{pmatrix} \quad (2.20)$$

where $\theta_i (i = 1, 2, 3)$ are three real fields that correspond to the SSB Goldstone bosons, and $H(x)$ is the Higgs field (sometimes also denoted with non capital h, $h(x)$). With a choice of the gauge value $\theta^i(x) = 0$, the exponential component can be removed, and Higgs field becomes:

$$\phi(x) = \frac{1}{\sqrt{2}} \begin{pmatrix} 0 \\ v + H(x) \end{pmatrix} \quad (2.21)$$

Including this expression for the Higgs field in Eq. 2.16, the new Lagrangian term can be rewritten as shown in Equation 2.22:

$$\mathcal{L}_H = (v + H)^2 \left(\frac{g_w^2}{4} W_\mu^\dagger W^\mu + \frac{g_w^2}{2 \cos^2 \theta_W} Z_\mu Z^\mu \right) + \frac{1}{2} \partial_\mu H \partial^\mu H - \frac{1}{2} M_H^2 H^2 \left(1 + \frac{H}{2v} \frac{H^2}{4v} \right) \quad (2.22)$$

In this equation, the first term corresponds to couplings of gauge bosons to the Higgs field. Here it can be observed that, as expected, there is no photon components since the $U(1)_{QED}$ symmetry is not broken by the Brout-Englert-Higgs mechanism, and thus $m_\gamma = 0$. The W boson's mass is therefore determined from the coupling constant of the $SU(2)_L$ gauge interaction g_W and the vacuum expectation value of the neutral Higgs field, (v , defined in Eq. 2.19):

$$m_W = \frac{1}{2} g_W v \quad (2.23)$$

Whereas the Z boson's mass is obtained in terms of the W boson's:

$$m_Z = m_W \cos \theta_W \quad (2.24)$$

The other two components of Eq. 2.22 explain how a new massive scalar particle, the Higgs boson, interacts with the Higgs field. The last term corresponds to the potential $V(\phi)$, from where the mass term of the Lagrangian can be connected to the vacuum expectation value v and the parameter μ : $v = \frac{\mu^2}{\lambda}$, from where the Higgs boson's mass can be computed to be:

$$m_H = v\sqrt{2\lambda} \quad (2.25)$$

Lastly, given that λ is a free parameter of the theory, it causes the Higgs mass to not be determined by the theory but instead be a parameter that has to be measured experimentally. This causes the electroweak theory to be described by four main parameters: the gauge couplings g_W and g' from $SU(2)_L \otimes U(1)_Y$, and the two free parameters of the Higgs potential, λ and the previously mentioned μ . Once determined these parameters, the couplings of the Higgs boson to the gauge bosons, as well as the masses of the massive gauge bosons W and Z , and of the H boson itself, can be computed.

Fermion masses: In addition to providing an explanation of the origin of the masses of the gauge bosons, the introduction of the aforementioned scalar field doublet provides with a way for the fermions to acquire mass, through an additional Lagrangian term describing the couplings of the fermions to the new scalar particle. The general form of this term is:

$$\mathcal{L} = -G_\ell \psi \bar{\psi} = -G_\ell (\bar{\psi}_R \phi \psi_L + \bar{\psi}_L \phi^\dagger \psi_R) \quad (2.26)$$

Where G_ℓ corresponds to the Yukawa coupling for the fermion ℓ . This Lagrangian can be included in the SM Lagrangian without violating the $SU(2)_L \otimes U(1)_Y$ symmetry. This is because, as previously stated, left-handed fermions form $SU(2)_L$ doublets, and right-handed fermions come in $SU(2)_L$ singlets, so that the second term $\bar{\psi}_L \phi$ of Eq. 2.26 becomes $SU(2)_L$ invariant, while the combination $\bar{\psi}_L \phi \psi_R$ will be invariant under the $SU(2)_L \otimes U(1)_Y$ symmetry. Therefore, the Lagrangian now satisfies the electroweak gauge symmetry, while providing for a mass term for all fermions apart from the neutrinos. For instance, for the case of the electron, the Lagrangian is defined as:

$$\mathcal{L}_e = -G_e \left[(\bar{\nu}, \bar{e})_L \begin{pmatrix} \phi^+ \\ \phi^0 \end{pmatrix} e_R + \bar{e} (\phi^{\dagger+}, \phi^{\dagger 0}) \begin{pmatrix} \nu_e \\ e \end{pmatrix}_L \right] \quad (2.27)$$

where, after the spontaneous symmetry breaking as defined in Eq. 2.22 is applied, the electron Lagrangian becomes:

$$\mathcal{L}_e = \frac{1}{\sqrt{2}}(\nu + H)(g + \bar{e}e) \quad (2.28)$$

where the Yukawa coupling for the electron can be expressed in terms of the electron mass: $g_e = \frac{\sqrt{2}m_e}{v}$, and the Lagrangian can be rewritten as:

$$\mathcal{L}_e = -m_e \bar{e}e - \frac{m_e}{v} \bar{e}eH \quad (2.29)$$

From Equation 2.29 one can infer that the mass of an electron originates from the interaction between left-handed and right-handed massless chiral fermions, coupled with the non-zero expectation value of the Higgs field. This argument can be generalised to all other fermions except for the neutrinos (given that all neutrinos are left-handed, and all antineutrinos right-handed). A general Lagrangian can be thus defined for the first generation fermions as:

$$\mathcal{L}_m = - \left(1 + \frac{H}{\nu} \right) [m_u \bar{u}u + m_d \bar{d}d + m_e \bar{e}e] \quad (2.30)$$

In general, we can define the Yukawa coupling for a given fermion f as $G_f = \frac{\sqrt{2}m_f}{\nu}$.

Lastly, the mass of the neutrinos is not explained by the mechanism explained above, and even though their mass has not been measured, there are strong experimental hints of their mass being non-zero [52, 50, 51]. The current accepted theory to explain neutrinos masses is the Seesaw mechanism, which will not be explained in document, but multiple bibliography has been written covering the topic comprehensively [62].

2.2 Standard model achievements and shortcomings

As already introduced in the Chapter 1, the SM is an incredibly successful theory that has been able to predict the behaviour of particles and has been confirmed by numerous experiments over the past few decades. Some of these achievements include:

- ◆ **The unification of electromagnetic and weak forces:** The SM successfully unified the electromagnetic and weak forces into a single electroweak force [63, 64] discussed in Section 2.1 of this document. Many predictions on electroweak observables made by this theory have been experimentally verified [65].
- ◆ **The prediction of the Higgs boson:** The SM predicted the existence of the Higgs boson, which, as already mentioned, was finally discovered in 2012 at the Large Hadron Collider by the ATLAS and CMS Collaborations [23, 24].
- ◆ **Performing accurate predictions of particle interactions:** The SM has been incredibly successful in predicting the behaviour and interactions of subatomic particles [48]. For instance, it accurately predicts the decay of the neutron, the interactions between quarks, and the production of particles in high-energy collisions.
- ◆ **Mechanism for CP violation:** The Standard Model predicts that certain particles violate the charge parity symmetry (known as CP violation) [66]. This prediction was confirmed by experimentally by the KEK and Belle collaborations [67].

However, as successful as the SM has been, many questions remain to be solved, both from a theoretical and an experimental perspective. These include:

- ◆ **How does gravity behave at microscopic level?** Despite being the most well known and studied fundamental force in the universe at a macroscopic level, gravity is not included in the SM. This is because the interaction is significantly less intense than the other three fundamental forces at the electroweak scale. However, it is expected to play a significant role at the Planck scale, where quantum gravitational effects are expected to become important.
- ◆ **Where is all the antimatter?** The SM fails to explain why, despite the fact that matter and antimatter have almost identical properties, the majority of the universe is formed

by matter. While the CP violation does provide with explanation of the asymmetry, new processes are needed to fully account for it.

- ◆ **What is dark matter made of?:** The existence of dark matter has been inferred from multiple observations, such as the rotation speeds of galaxies [27, 26, 68], gravitational lensing [69] or in the CMB [28]. From these observations, it is estimated that only 5% of the energy of the universe correspond to the “ordinary” matter, 25% correspond to dark matter, and the remaining is associated to dark energy [70]. However, Dark matter could only be a Standard Model particle if neutrinos existed in quantities much greater than empirically observed, which has been ruled out by several cosmological measurements [71, 72]. Thus, in order to explain the existence of dark matter, some extension to the SM is necessary.
- ◆ **Why do neutrinos have masses?:** The SM assumes that neutrinos are massless, but experimental observations have shown that they do have a non-zero mass [52, 50, 51]. The mechanism that gives neutrinos mass is not yet fully understood.
- ◆ **Why are forces different?** It is not well understood at a theoretical level why the couplings of the forces differ so much from one another. One attempt to explain that is via a theory unifying all the forces, named Grand Unification Theory (GUT) [73]. This theory proposes that all three gauge symmetries belong to a larger SU(5) symmetry group, being each a low energy representation of a single fundamental interaction, where all the interactions converge at $\sim 10^{15}$ GeV. Nowadays, despite SU(5) having been rejected as the correct gauge group, the idea of the SM being part of something more fundamental, analogously to how Maxwell laws unified the electric and magnetic forces, remains in the mind of many physicists.
- ◆ **Hierarchy problem and fine-tuning:** The SM is a renormalisable theory, meaning its predictions are expressed as an expansion series. In particular, corrections to the Higgs boson mass due to interactions with fermions can become very large at very high energies, on the order of the Planck scale ($\sim 10^{18}$ GeV). Without the presence of any physics beyond the SM, a precise fine-tuning of these contributions is required to maintain the Higgs boson mass finite and close to the electroweak scale ($\sim 10^2$ GeV). One of the primary motivations for exploring physics beyond the SM is to avoid this fine-tuning. Models that do not require this tuning propose new particles with masses at the order of the TeV, which can therefore be probed at the LHC.

In addition to these arguments, several tensions between experimental measurements and the predictions of the SM currently exist. These include:

- ◆ The measurement of the positive muon anomalous magnetic moment by the g-2 collaboration at the Fermilab National Accelerator Laboratory (FNAL). In 2021, results showed a 3.3 standard deviations (σ) from the SM prediction [74, 75]. The same analysis was improved by a new analysis of the data in 2023, which, if combined with other measurements [76] presents a discrepancy with the SM theoretical value of over 5σ deviations, typically enough to claim a discovery in the particle physics field. However, later theoretical calculations using lattice QCD produce values in agreement with the experimental value. [77].
- ◆ Several measurements of the B hadrons performed by the LHCb or Belle Collaborations among others deviate from the SM by $2-3\sigma$ [78].
- ◆ The latest measurement by the CDF Collaboration² of the W boson’s mass deviates significantly from the SM mass [81]. This measurement also deviates significantly with other measurements of the W bosons [82, 83], most recently by the CMS Collaboration, which show agreement with the SM [84].

²One of the main detectors of the Tevatron particle accelerator, a hadron collider precursor to the LHC that was active until 2011 [79, 80].

All these results need to be taken with a grain of salt, though, as even if the methodology of each analysis is assumed to be correct, and the treatment of systematic uncertainties properly assessed, they all fall short of the standard discovery threshold set for the LHC, where for a result to be claimed as different from the SM, it should deviate by at least 5σ from the expected value.

Chapter 3

Supersymmetry

While widely successful, the SM fails to address multiple open questions, both from a theoretical and an experimental perspective. While there are other BSM theories that try to address some of these open questions, Supersymmetry (SUSY) is perhaps the most complete, as it provides solutions for many of the open questions at the same time. Fig. 3.1 presents a summary of the main BSM theories, and whether they answer the principal open questions in high energy physics.

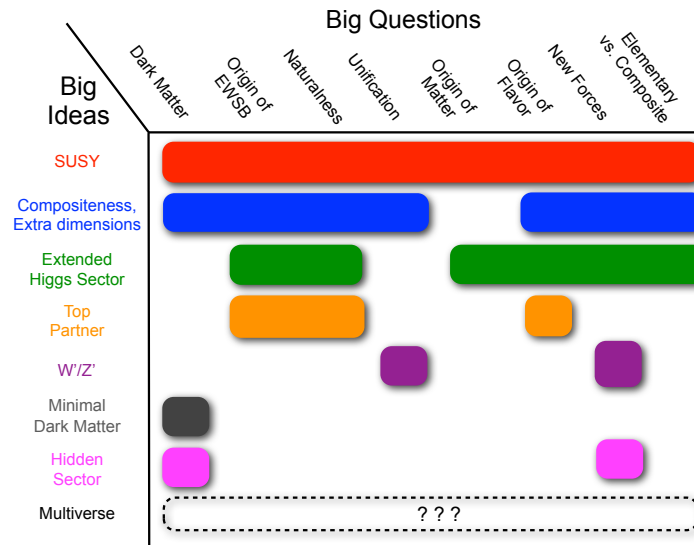


Figure 3.1: Covering of the big open questions with respect to several BSM theories [4].

SUSY is thus defined as a theoretical framework that posits the existence of several additional, yet-to-be-observed particles, called supersymmetric particles or sparticles, related to the known fundamental particles through a symmetry transformation. There exist many different supersymmetric models, having all in common that for each known particle (quarks, leptons, and gauge bosons) there should exist a corresponding supersymmetric partner with different spin quantum numbers. The existence of these superpartners would provide a new symmetry between fermions and bosons. If discovered, they could help address several unresolved questions in particle physics, such as the hierarchy problem and the nature of dark matter. Supersymmetry has been extensively studied both theoretically and experimentally, with searches for supersymmetric particles being a major focus of ongoing experimental efforts at high-energy

particle colliders, both at the CMS and ATLAS Collaborations.

In this chapter, a brief phenomenological description of supersymmetry is given. In Section 3.1 a brief description of its history and the commonalities between the multiple different SUSY models is presented, followed by a brief description of the simplest SUSY model, the minimal supersymmetric standard model (MSSM), in Section 3.2. A succinct description on how models are interpreted from an experimental point of view is given in Section 3.3. This chapter aims at presenting a general overview of the supersymmetric theories, while a precise description of the particular models studied in this document is reserved to Section 7.1 in Chapter 7.

3.1 Origin and common features of SUSY models

The first formulations of the SUSY theory, or more precisely, group of theories, arose shortly after the SM was formulated, once theoreticians realised the existence of the hierarchy problem (discussed in Section 2.2). The first models, proposed in the 70s by Wess and Zumino [34, 35] attempted to solve this problem by proposing a new symmetry between fermions and bosons in a four-dimensional supersymmetric field theory. SUSY theories further evolved in the 80s, when the first MSSM models were proposed, starting from the one proposed in 1981 by Dimopoulos and Georgi [85] building on the works of Fayet [36].

Generally, supersymmetric theories are based on a space-time symmetry that converts fermionic to bosonic states, and vice versa. This transformation is generated by the operator Q (as well as its hermitian conjugate, Q^\dagger), which changes the spin angular momentum of the SM particles by $1/2$:

$$Q|Boson\rangle = |Fermion\rangle, \quad Q|Fermion\rangle = |Boson\rangle \quad (3.1)$$

Particles that undergo such operation are referred to as *superpartners*. Both bosonic and fermionic states, superpartners of each other, are arranged in *supermultiplets*, irreducible representations of the supersymmetric algebra, each of them containing the same number of bosonic and fermionic degrees of freedom. The supersymmetric particles are generally labelled with the same symbol as their SM companion but with a tilde (e.g. $\tilde{\ell}$ would be the SUSY companion of a lepton ℓ). Since the SUSY operators Q and Q^\dagger , shown in Eq. 3.1, commute with the squared mass operator ($-P^2$), particles in the same supermultiplet have the same eigenvalues of $-P^2$, and therefore the same mass value. In addition to that, since Q and Q^\dagger commute with the generators of the gauge transformations, particles in the same multiplet, if they exist, are expected to have the same electric charge, weak isospin, and colour degrees of freedom.

There is no principle under which a SUSY theory needs to only have one supersymmetry. These theories are generally notated as a $\mathcal{N} = i$ theories, with $i = 1, 2, \dots$ being the number of distinct copies of the operators Q and Q^\dagger existing in the theory. Theories commonly known even outside the scientific environment such as many of the string theories are built on $\mathcal{N} > 1$ SUSY theories [86]. However, these theories generally do not provide any phenomenological predictions that can be studied at the LHC, and therefore in this document the focus will be given to $\mathcal{N} = 1$ SUSY theories.

3.2 Minimal Supersymmetric Standard Model

Out of the multiple $\mathcal{N} = 1$ SUSY theories, the minimal supersymmetric standard model is the simplest, as the term “minimal” is a reference to the minimum set of new stable particle and

interactions needed to create a consistent SUSY theory with the known phenomenology. MSSM theories are characterised for having one supersymmetric particle per each SM particle, differing from it by a half unit of spin, doubling also the number of fields.

Lastly, under the MSSM, the Higgs field is actually formed by two doublets, H_u and H_d :

$$h_u = \begin{pmatrix} h_u^+ \\ h_u^0 \end{pmatrix} \quad h_d = \begin{pmatrix} h_d^+ \\ h_d^0 \end{pmatrix} \quad (3.2)$$

Under this theory, the observed Higgs boson is the lightest neutral Higgs, h^0 , while there are other 4, yet undiscovered Higgs bosons: Another neutral boson with a heavier mass (named H^0), two charged Higgs bosons (H^+ and H^- , respectively), as well as a fifth, neutral pseudoscalar Higgs, denoted as A^0 . The supersymmetric companions of these particles, one for each boson, are collectively named higgsinos, as they have a spin 1/2. A summary of the SM particles with their MSSM superpartners is shown in Tab. 3.1.

In addition to the aforementioned particles, others may be created as a mixture of higgsinos and electroweak gauginos, due to the effects of the symmetry breaking. One such example is the mixture of neutral gauginos (\tilde{W}^0 and \tilde{B}^0) with the neutral higgsinos (\tilde{h}_u^0 and \tilde{h}_d^0), whose mixing forms four eigenstates which are known as neutralinos ($\tilde{\chi}_i^0$, where $i = 1, 2, 3, 4$ corresponds to each mass eigenstate). Similarly, the charged gauginos (\tilde{W}^- and \tilde{W}^+) can mix with the charged higgsinos (\tilde{h}_u^\pm and \tilde{h}_d^\pm) to form four mass eigenstates known as charginos ($\tilde{\chi}_i^\pm$, with $i = 1, 2$). In both of these cases, they are generally labelled in terms of increasing mass, meaning that the lightest neutralino is $\tilde{\chi}_1^0$.

3.2.1 R-Parity and dark matter candidates

Similarly to what happens in the SM, in the MSSM models, the conservation of the baryon number (B_n) or of the total lepton number (L_n) is not explicitly required. However, unlike in the former, the MSSM theories do provide for terms that allow for processes that violate B_n or L_n . However, the violation of both lepton and baryon numbers are highly constrained experimentally. The strongest experimental constrain is due to the lack of any observations of the decay of the proton [87], which would violate B_n and L_n in one unit. To solve this conundrum, a new symmetry, named R-Parity (P_R) is added that eliminates all terms of the renormalisable potential that could violate the conservation of B_n and L_n . For a particle of spin s it is defined as:

$$P_R = -1^{3 \cdot (B_n - L_n) + 2s} \quad (3.3)$$

Under this notation, all MSSM particles are expected to have an R-Parity of -1, whereas SM particles, including the Higgs boson, have an R-Parity of +1, as shown in Tab 3.1.

This results in SM particles not mixing with the MSSM ones and in each vertex of an interaction containing an even number of particles with $P_R = -1$. This implies that a supersymmetric particle has to decay in an odd number of supersymmetric particles, being the lightest supersymmetric particle (LSP) stable. As a consequence, if the LSP has no electric charge, it would be a good dark matter candidate. These properties are used in the design of the analysis described in this document.

3.2.2 SUSY particle mass eigenstates

In the MSSM, the mass eigenstates of squarks and sleptons arise from combinations of right-handed and left-handed squarks, sleptons, and sneutrinos, with small mixing angles. These eigen-

SM Particle		spin	R-Parity	Superpartner		spin	R-Parity
Fermions	Quark q	1/2	+1	Squark \tilde{q}		0	1
	Lepton l	1/2	+1	Slepton \tilde{l}			
Gauge bosons	W W^\pm	1	+1	Wino $\tilde{W}^\pm, \tilde{W}^0$		1/2	-1
	B B^0	1	+1	Bino \tilde{B}^0			
	Photon γ	0	-1	Photino $\tilde{\gamma}$			
	Z Z^0	0	-1	Zino \tilde{Z}			
	gluon g	1	+1	Gluino \tilde{g}			
Higgs bosons	Higgs h_u h_d	0	+1	Higgsino $\tilde{h}_u = (\tilde{h}_u^+, \tilde{h}_u^0)$ $\tilde{h}_d = (\tilde{h}_d^-, \tilde{h}_d^0)$		1/2	-1

Table 3.1: Summarised list of SM particles with their spin and R-Parity and their MSSM equivalent

states are obtained by diagonalising 6×6 squared-mass matrices for right-left handed squarks and sleptons, and a 3×3 matrix for sneutrinos. The first and second generations of sfermions typically exhibit softer Higgs couplings and thus each generation can be approximated by the seven interaction eigenstates, the two left and right-handed components of the two squarks and the charged slepton, plus the sneutrino's.

On the other hand, the third generation of sleptons and squarks are known as heavy flavour sfermions, given that they are the SUSY companions of the heavy flavour fermions. They are characterised by having larger couplings to the Higgs field and thus exhibit larger differences in mass, resulting in mass eigenstates that differ from gauge eigenstates.

With respect to the gauginos, as explained before, the mass eigenstates for the charged winos and higgsinos correspond to the charginos ($\tilde{\chi}_1^\pm, \tilde{\chi}_2^\pm$), whereas the neutral wino, bino and higgsino are grouped in the four neutralinos ($\tilde{\chi}_1^0, \tilde{\chi}_2^0, \tilde{\chi}_3^0$ and $\tilde{\chi}_4^0$), as previously explained. Lastly, the gluino, a colour octet fermion, is unique among all sparticles in the MSSM as it cannot mix with any other particle.

In addition to these particles, in MSSM models, as previously stated, five different Higgs bosons are expected, three neutral (two scalar and one pseudoscalar) and two charged. In this way, the experimentally observed Higgs boson is the lightest of the neutral scalars (h^0).

3.2.3 Soft supersymmetry breaking of the MSSM and naturalness

Perhaps the least appealing part of MSSM theories, (or SUSY models in general) is the lack of any experimental evidence to sustain any of the particles they introduce.

On the other hand, all SM particles have been observed with relatively small masses, the largest being the top quark with a mass of ~ 175 GeV. Given the fact that the simplest non-excluded SUSY models propone particles in the \mathcal{O} TeV, the exact symmetry between the MSSM models and the SM is thought to be broken, as MSSM particles' masses would not be of the same order of magnitude as their SM companions.

Nonetheless, in order to preserve naturalness, the SUSY breaking terms should be such that they do not introduce any new divergent contributions to the mass of the scalars such as the Higgs boson. This type of breaking is termed "soft," allowing the effective Lagrangian of the MSSM to be expressed in two distinct parts.

$$\mathcal{L} = \mathcal{L}_{\text{MSSM}} + \mathcal{L}_{\text{soft}} \quad (3.4)$$

Where $\mathcal{L}_{\text{MSSM}}$ corresponds to the MSSM Lagrangian, containing all the gauge and Yukawa interactions and preserving the supersymmetry invariance, and $\mathcal{L}_{\text{soft}}$ is a term that contains those terms that violate supersymmetry, while not introducing quadratic divergences in the theory. This results in the supersymmetric particles receiving two contributions to their masses, one from the electroweak symmetry breaking, and another from the soft supersymmetry breaking.

In general, the masses of the MSSM particles and the mixing details of the gauginos vary a lot on the particular model, a part of the general consensus of the mass of h_0 corresponding to the SM Higgs mass. However, while the quadratic divergences from the SM Higgs mass are removed via the *soft* symmetry breaking, several corrections to the Higgs boson's mass remain, the largest among them being due to the top quark and top squark masses.

This effect, known as the little hierarchy problem, scales as the logarithm of the ratio between the top squark and the top quark masses, and it's typically addressed via naturalness arguments, that is, predicting that at least the masses of the few lightest superpartners would be on the $\mathcal{O}(\text{TeV})$. This assumption, applied to the third generation squarks, namely the top squark, causes its mass to remain relatively close to its SM partner, to avoid big fine-tuning on the models. This argument, albeit not necessarily backed by experimental observations, gives a strong motivation to the search for the production of top squarks at the LHC. One such search, for the top squark produced in final states with two leptons, is presented in this document.

3.2.4 Phenomenology

Once all the gauge and Yukawa couplings, the Higgs sector parameters, and the soft symmetry breaking terms are considered, one is left with more than 100 free parameters in the MSSM Lagrangian. Naturally, not all free parameters can be studied at the LHC, which drive experimentalists to use reduced models with only a relevant set of parameters, known as phenomenological adaptations of the MSSM (pMSSM). In general, pMSSM models are characterised by:

- ◆ Providing for a dark matter candidate, typically the LSP. There are two possible weakly interacting massive particle (WIMP) particles that could make a good LSP candidate, the neutralino and the sneutrino. While some models do consider the sneutrino as the LSP [88], most models, included the ones studied in this document, assume the LSP to be the lightest neutralino, $\tilde{\chi}_1^0$ [89].
- ◆ Not allowing for any R-Parity violating processes. This results in particles being produced in pairs.
- ◆ Not introducing any new sources of CP violation, or flavour changing neutral currents.
- ◆ Assume mass degeneracy. For instance, in the models studied in this document, assuming the degeneracy of the masses of first and second generation squarks and sfermions.

A summary of all the theoretical predictions for the cross sections of the main pMSSM particles is shown in Fig. 3.2.

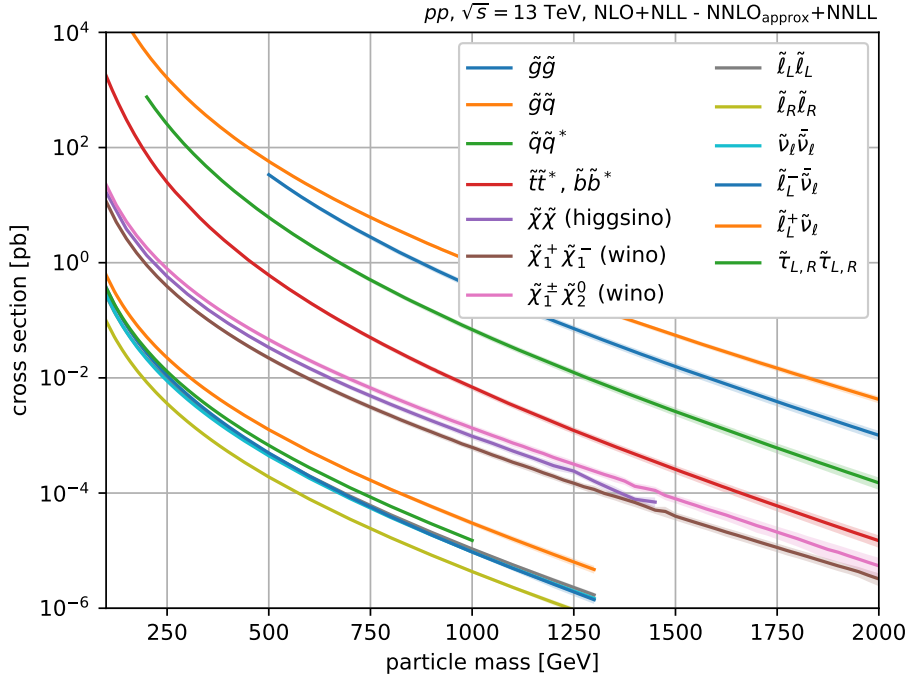


Figure 3.2: Theory cross sections for selected SUSY processes as a function of the particle mass at $\sqrt{s} = 13 \text{ TeV}$. Taken from [5, 6].

3.3 Supersymmetry models at the LHC

Due to the amount of unconstrained parameters obtained in SUSY models, many searches for SUSY are performed utilising simplified models spectra (SMS) which take advantage of effective Lagrangians. These type of Lagrangians typically contain a minimal number of particles and their interactions, drastically reducing the number of free parameters in the theory. The remaining parameters chosen by the model include the branching fractions or the masses of each particle involved, and can be directly related to collider physics observables. In addition to that, the production cross sections shall be calculated, taking into account the fundamental properties of the model, and the accelerator characteristics.

These models provide a general topology that covers a broad range of signal phase space. It is typical to interpret the results of an analysis in the context of multiple SMSs with similar final states.

Multiple analyses have been probed for SUSY models since the inception of LHC, mainly at the ATLAS and CMS Collaborations. The obtained results show no significant excesses compatible with a SUSY signal, and allow the establishment of exclusion limits that in some cases, such as the search of gluinos, reach masses of the order of 2 TeV, reducing the possible values for the free parameters, therefore shrinking the phase space available for new physics. A summary of various analyses searching for SUSY performed at the CMS Collaboration is presented in Fig. 3.3, with its equivalent limits from the ATLAS Collaboration shown in Fig. 3.4.

[illegible]

(b) Simplified models of squark pair production.



Figure 3.4: Representation of the mass reach of the various analyses performed by the ATLAS collaboration probing for Supersymmetry. A summary of search outcomes is displayed to represent the available data. Results are expressed in terms of the nominal cross-section, focusing on both an area of almost-maximum mass coverage and a contrasting illustrative scenario, showcasing the phase space to which each search is sensitive to. It must be noted that certain limitations are based on extra hypotheses regarding the mass of intermediary states, which are highlighted through darker bands, which represent varying model parameters [7].

Chapter 4

Experimental setup

The data set used in this document has been recorded by the CMS detector in three years of proton-proton collisions delivered by the LHC at a centre of mass energy of 13 TeV. This chapter describes how these apparatuses work, starting with a brief introduction of the CERN laboratory as a whole in section 4.1. Section 4.2 will cover the fundamentals of the LHC complex, and the chapter will be concluded with section 4.3, dedicated to the CMS detector and its parts.

4.1 The European Organization for Nuclear Research

The European Organisation for Nuclear Research (CERN) (the acronym comes from the original French name, *Conseil Européen pour la Recherche Nucléaire*), was conceived in 1954 as a pan-European organisation to unite scientists from all over the continent in a non-militaristic manner [90]. Since its inception, multiple discoveries have been made using the CERN facilities, such as the discovery of neutral currents or of the W, Z and Higgs bosons [65, 23, 24], among many others. Many advancements not directly related to particle physics have also been developed at CERN, ranging from applications in medical sciences to the creation of the first webpage.

Nowadays, CERN is a leading laboratory in particle physics, based in Geneva (Switzerland), and an example of international collaboration. It spans 23 member states, with a further 10 associate member states. Non European countries like the United States of America or Japan are also part of CERN, albeit with an observer status. Multiple non-member states have co-operation agreements with CERN. Conversely, the membership of the Russian Federation, a traditional collaborator at CERN, as well as Belarus' is currently suspended since March 2022 due to the conflict in Ukraine [91].

In total, more than 600 universities and institutions worldwide are involved at CERN. The laboratory forms a complex, shown in Fig. 4.1, where the LHC is the largest experiment, but with multiple other experiments in operation, such as antimatter production (AD), or the study of radioactive ion beams (ISOLDE), as well as testing areas for future detectors (namely, the north and east areas). It also serves as a meeting point for scientists worldwide, hosting multiple auditoria where workshops and conferences are performed, as well as multiple office buildings, and other amenities such as restaurants and hotels to host visitors. Similarly, it is designed as an educational hub, hosting various expositions for the general public, the latest of which being the *Porte de science*, inaugurated during the fall of 2023 [92]. It also provides with programs such as the CERN summer student program, which reunites undergraduate/master students worldwide over every summer in a combination of master classes and working on a summer project for 2 to 3 months. [93].

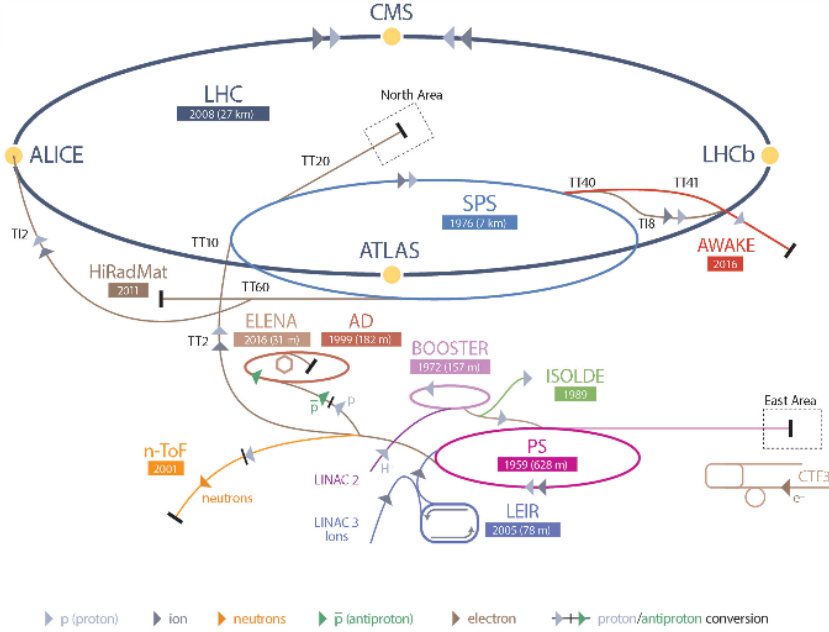


Figure 4.1: CERN complex, showing the LHC with its four main experiments, its injection chain, and other experiments

4.2 The Large Hadron Collider

The Large Hadron Collider (LHC), is the largest particle collider of the CERN complex, and in the world. It replaced a previous accelerator, named the Large Electron-Positron (LEP) collider. This lepton accelerator was active between 1989 and 2000 at a maximum energy of 209 GeV [94] and allowed the researcher to reach numerous important results, such as measuring for the first time the masses of the W and Z bosons [95]. The LHC reutilised the LEP tunnels, which spanned over a circumference 27 km long, but replacing the magnets and detectors to accommodate a proton-proton collider, designed to also be able to host also lead ions. Inside the tunnels there are 1232 Niobium-Titanium dipole magnets that generate a field of up to 8.3 T, with an operating temperature of 1.9 K.

In terms of its design, the LHC was designed to be the successor to the Tevatron accelerator complex. This hadron collider took its name from being able to achieve up to 1 TeV of energy at centre of mass. It was located at the Fermi National Acceleration Laboratory (Fermilab, or FNAL), in Illinois, USA, and allowed to obtain multiple advances in the field during its operation, from 1983 until 2011, when it was shutdown after a short overlap period with the LHC. Among the results obtained at the Tevatron, we cite the discovery of the top quark [96] and the establishment of stringent limits on the mass of the Higgs boson, helping to narrow down its search [97].

In its proton-proton configuration, the LHC accelerates two beams of approximately 10^{11} protons which are previously produced and boosted taking advantage of the CERN complex, utilising legacy detectors such as the Booster, Proton Synchrotron PS and Super Proton Synchrotron SPS. The accelerator chain is shown in Fig. 4.1. Once the proton bunches reach sufficient energy (typically around 450 GeV), they are injected in opposite directions into the LHC, where they are further boosted by 16 superconducting radiofrequency cavities to energies of several TeV. This adds up to 2808 proton bunches separated by 25 nm (equivalent to a collision rate of 40 MHz).

There are four interacting points, corresponding to the four main experiments in LHC: ATLAS, CMS, LHCb and ALICE. ATLAS (a large toroidal apparatus) and CMS (compact muon solenoid) are both general purpose detectors, aiming at precision measurements of observables in SM processes, as well as searching for rare unseen processes, such as supersymmetric particles or dark matter production [98]. They are designed to have a similar sensitivity, so that novel results can be checked independently. A more detailed description of the CMS detector will be presented in Section 4.3. As for the other two detectors, LHCb focuses on precision measurements of CP violation and rare decays of B hadrons [99], while ALICE (a large ion collider experiment) is dedicated to heavy ion physics [100].

4.2.1 LHC properties and parameters

Centre of mass energy

The centre of mass energy is the total energy of the colliding protons in their centre of mass frame of reference. For two protons of energy E , momentum \vec{p} and mass m , it amounts to:

$$\sqrt{s} = \sqrt{(m_1^2 + m_2^2 + 2(E_1 E_2 - 2|\vec{p}_1||\vec{p}_2|\cos(\theta)))} \quad (4.1)$$

The LHC has a design for up to $\sqrt{s} = 14$ TeV, albeit it has never operated at such a high energy. Instead, it operated at $\sqrt{s} = 7 - 8$ TeV between 2010 and 2013 [101], at $\sqrt{s} = 13$ TeV between 2015 and 2018 [102], and at $\sqrt{s} = 13.6$ TeV in the current data taking period, which started in 2022 and is expected to finish in 2026. These data taking periods are known in the LHC community as Run I, Run II and Run III respectively.

Luminosity

The instantaneous luminosity, labelled as \mathcal{L} , measures the frequency of proton-proton interactions per cross section unit. It is defined by the collider properties:

$$\mathcal{L} = \frac{\gamma f_{rev} k_B N_p^2}{4\pi \varepsilon_n \beta^* F} \quad (4.2)$$

Where:

- ◆ γ is the Lorentz factor
- ◆ f_{rev} the revolution frequency
- ◆ k_b the number of protons per beam
- ◆ N_p the number of protons per bunch
- ◆ ε_n the transverse normalised emittance
- ◆ β^* the betatron function at the interaction point
- ◆ F a reduction factor to account for the beam crossing angle at the interaction point

From Eq. 4.2, a value of $\mathcal{L} = 10^{34} \text{cm}^{-2} \text{s}^{-1}$ is retrieved, albeit the peak of experimentally measured instantaneous luminosity has reached the double of that value [102]. For a process with a cross section σ , the rate R of events produced per second will be given by:

$$R = \mathcal{L} \times \sigma \quad (4.3)$$

Conversely, if one desires to obtain the total number of events over a period of time, it would be given by:

$$N = L \times \sigma \quad (4.4)$$

Where L is the luminosity integrated over the collision period:

$$L = \int_0^L \mathcal{L}(t) dt \quad (4.5)$$

As for the case of the centre of mass energy, also the integrated luminosity has generally been increasing per each data taking period, as shown in the Fig. 4.2. The final data sets presented in this document include the data collected in the years 2016, 2017 and 2018 and correspond to an integrated luminosity of 36.3 fb^{-1} , 41.5 fb^{-1} and 59.8 fb^{-1} respectively, which add to a total of 138 fb^{-1} . This means that for a process with a production cross section of $\sigma = 1 \text{ fb}^{-1}$, 138 events should have been collected.

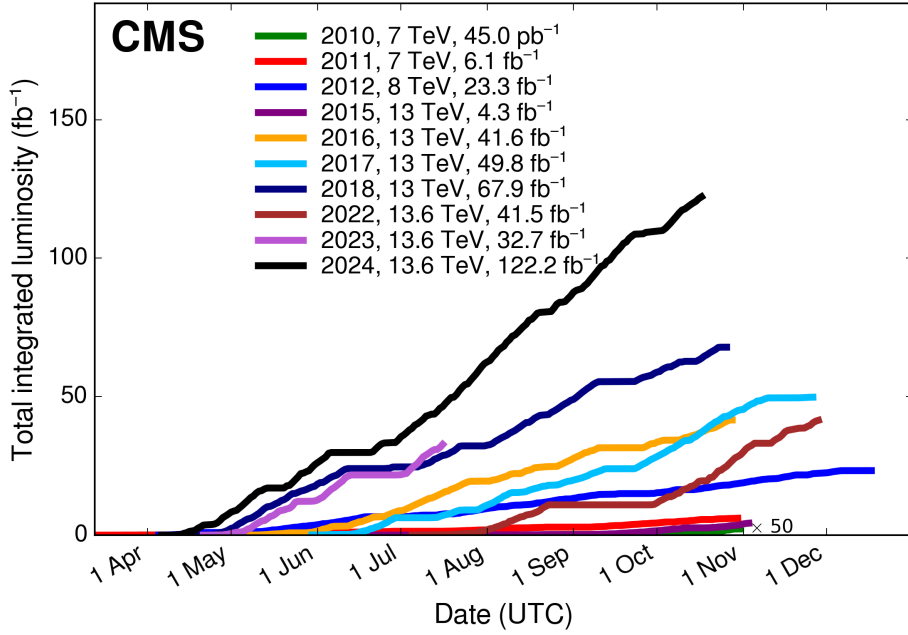


Figure 4.2: Summary of the integrated luminosity collected by the CMS collaboration, by year.

Number of simultaneous interactions: pile-up

One of the side effects of achieving such high luminosities is having multiple simultaneous interactions. Since typically only one collision generates a hard scattering, it is common to refer to the secondary collisions as *pile-up* (PU). The pile-up distributions for each of the data taking years of the Run II are shown in the Fig. 4.3, from where it can be extracted that the Run II data taking period averaged 34 interactions per bunch crossing.

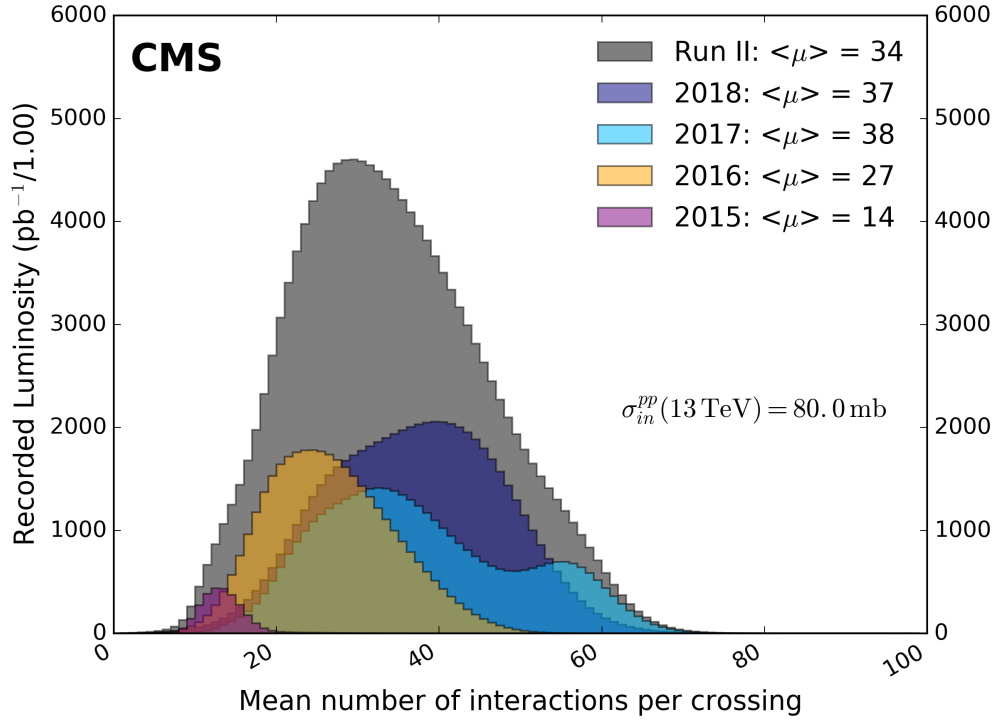


Figure 4.3: Distribution of pile-up during each of the Run II data taking period at the CMS collaboration.

4.2.2 Physics at the Large Hadron Collider

As was presented in the Section 2.1, protons are hadrons, non fundamental particles formed by quarks and gluons. In general, hadrons are characterised by the valence quarks that form their composite state, being the protons baryons formed by two quarks *up* and one quark *down* (by comparison neutrons are formed by one quark *up* and two *down*, for instance). These quarks are interacting with themselves by the exchange of gluons, which themselves can self-interact, thus producing additional quark-antiquark pairs, which form the so-called *sea* of quarks. The hadron's momentum is thus shared between the valence quarks, the sea quarks and the gluons, collectively referred to as partons. The fraction of the hadron's momentum carried by each parton is not fixed but instead described by the parton distribution functions (PDFs), which determine the probability of finding a parton of a given momentum $p_i = x_i P$, with x_i being the fraction of the total momentum P of the proton, as shown schematically in Fig. 4.4.

In general, at low energies, most of the momentum is carried by the valence quarks, but in collisions with a high energy transfer ($Q^2 \sim 1$ GeV), the *sea* quarks and gluons become accessible. The PDFs in general depend on the energy transfer Q^2 , as partons with a high fraction of the momentum x tend to radiate, producing other partons with lower x . PDFs are not calculated from first principles, due to the coupling constant of the partons being too large. Instead, PDFs are measured at a given Q^2 , and then extrapolated using QCD calculations. Example PDFs are shown in Fig. 4.5a and 4.5b for $Q^2 = 10$ GeV and $Q^2 = 10^4$ GeV, respectively. In proton-proton collisions, the primary hard interaction occurs between a single parton from each proton. However, it is also possible for additional interactions to take place among the remnants of the protons. These secondary interactions, referred to as the *underlying events*, are typically characterised by having lower energies compared to the main interaction, and thus do not generate easily distinguishable additional particles in the event. Nevertheless, these interactions can contribute to the overall amount of scattered energy.

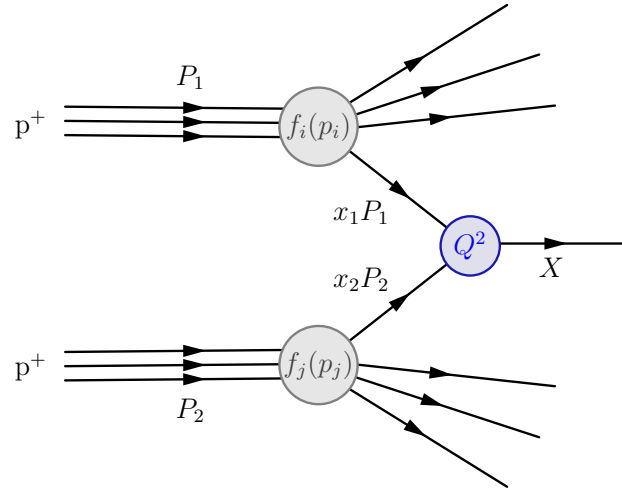


Figure 4.4: Schematic representation of the interaction between two partons in a proton-proton collision.

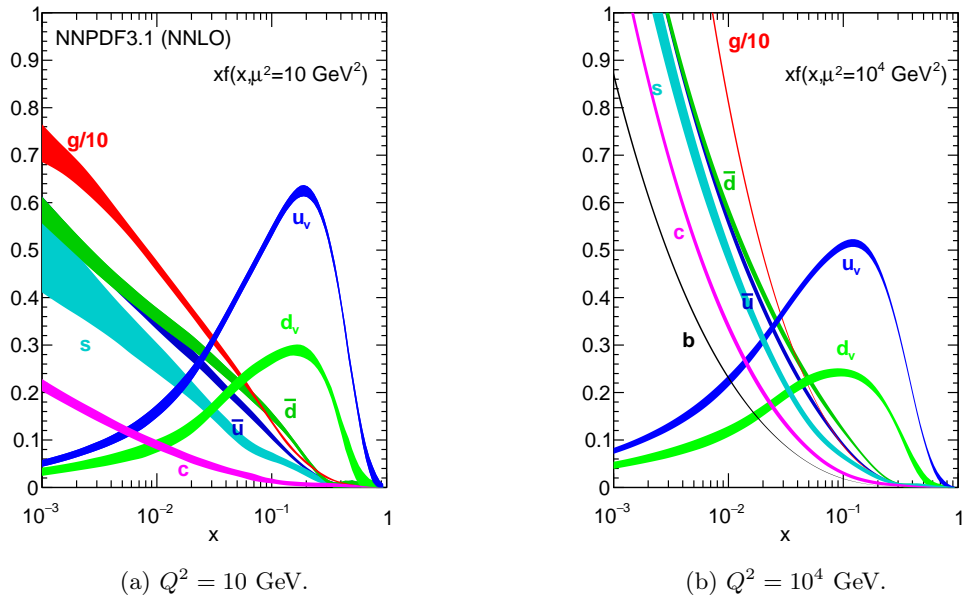


Figure 4.5: Parton distribution values at Next to Next to Leading Order (NNLO), calculated by the NNPDF collaboration [8]

4.3 The Compact Muon Solenoid

The compact muon solenoid (CMS) is, with ATLAS, one of the two general purpose detectors installed along the LHC tunnel, being located at the interaction point 5 of the tunnel, opposite to the main CERN complex at the base of the Jura mountains. More than 4000 people from more than 50 countries participate in this collaboration, whose main goals were to discover the Higgs boson, and to search for new BSM particles. While the former goal was achieved in 2012 [23, 24], no conclusive evidence of BSM physics has been observed to date. Nowadays, CMS is focused both on achieving ever more precise measurements of the SM parameters, and directly searching for new particles not expected by the SM either by probing new signal models or phase spaces that have recently become available.

The CMS detector has a cylindrical shape along the beam pipe, measuring around 15 metres in diameter and 28.7 meters in length and a weight of around 14000 tonnes. It is considered to be compact due to its high material density: in comparison, ATLAS is significantly larger (25 by 45 metres) while being lighter, weighting around 7000 tonnes. A schematic view of the detector and its parts is shown in Fig. 4.6.

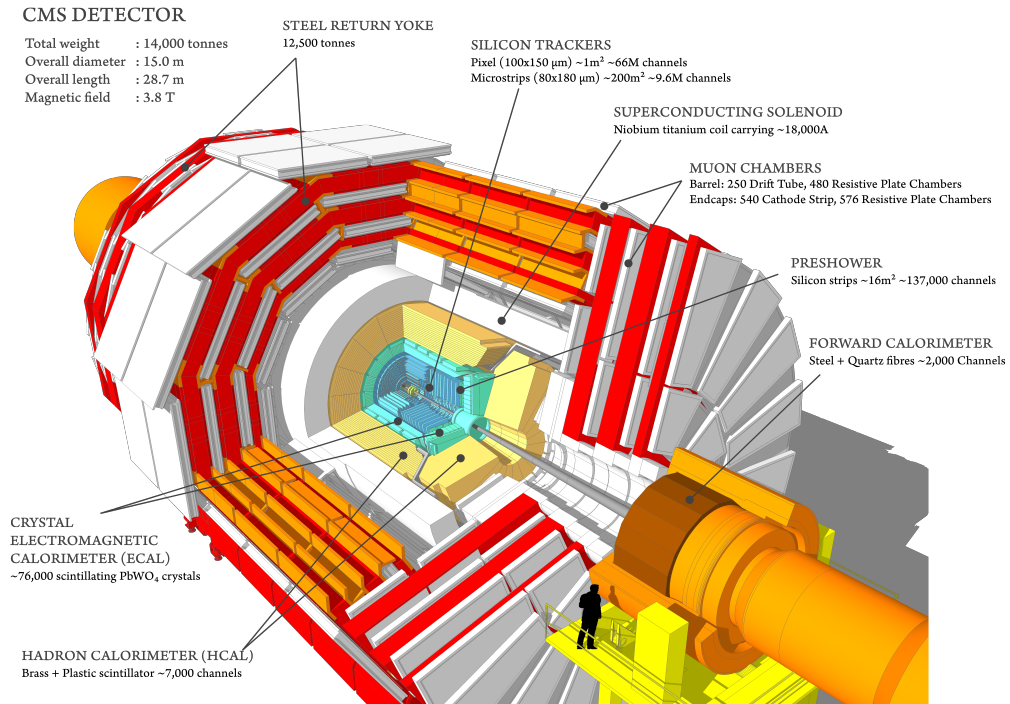


Figure 4.6: Schematic view of the CMS detector, with its main components and characteristics [9].

The CMS acronym arises partly from its central piece, a superconducting solenoid able to produce magnetic fields of up to 3.8 T. Inside of it, several subdetectors can be found, including a silicon tracker, an electromagnetic calorimeter (ECAL) and a hadronic calorimeter (HCAL). Outside of it two more components of the detector can be found: the muon chambers, and the steel return yoke that, besides structural stability, gives the detector its characteristic red colour. All aforementioned subdetectors and systems are covered in more detail in the following parts of the section.

Goals of the CMS detector

The CMS detector was defined as part of the LHC physics program, and was designed to achieve the following physics reconstruction goals:

- ◆ Obtain a good muon identification and momentum resolution: a 1% di-muon mass resolution uncertainty at 100 GeV, and the ability to determine unambiguously the charge of muons with a momentum up to 1 TeV.
- ◆ Have a good charge particle momentum resolution and reconstruction efficiency, both in terms of triggering, and offline tagging of τ leptons; and a high vertex reconstruction efficiency.
- ◆ Have a good electromagnetic energy resolution, di-photon and di-electron mass resolutions (approximately 1% at 100 GeV), with a wide geometric coverage, while also isolating photons and leptons efficiently at high luminosities.
- ◆ Reach a good resolution on the measurements of di-jet masses and missing transverse energy (p_T^{miss} , as described in detail in Section 5.6). Therefore, the hadron calorimeters are required to have a large hermetic coverage with a fine lateral segmentation.

CMS coordinate system

One important remark concerns the coordinate system adopted at CMS. As shown in Fig. 4.7, the x axis is defined radially towards the centre of the LHC ring, the y axis vertically, and the z axis is defined along the beam direction, whereas θ and ϕ are defined as the angles between the z and y axes; and the x and y axes respectively. Using these variables, it is common to work in

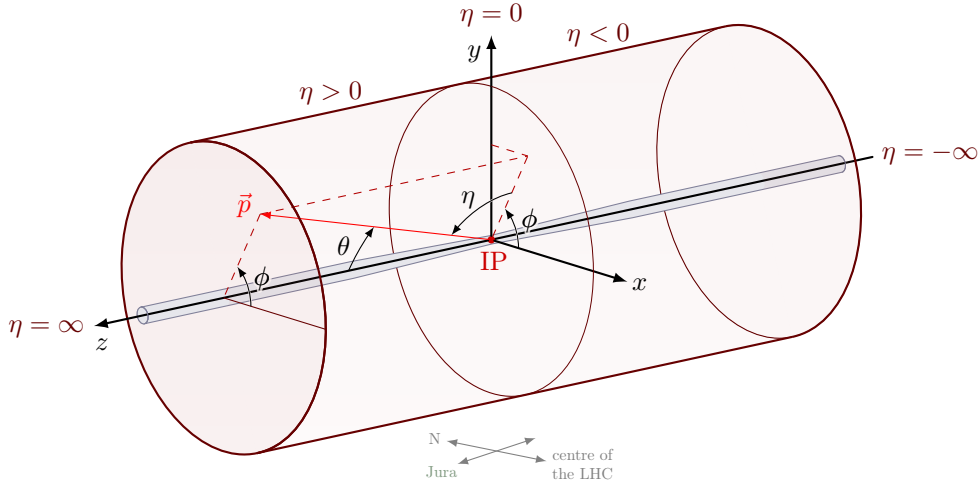


Figure 4.7: Schematic representation of the CMS coordinate system.

what's known as the transverse plane (XY plane), and use the transverse momentum p_T , since it is invariant under longitudinal boosts, defined as:

$$p_T = \sqrt{p_x^2 + p_y^2} \quad (4.6)$$

Another useful variable is the angle between the direction of a particle and the beam axis. This direction is commonly given through the rapidity, which is invariant under longitudinal transformations:

$$Y = \frac{1}{2} \ln \left[\frac{E + p_z}{E - p_z} \right] \quad (4.7)$$

In addition to that, it is found that when the particle is massless or with a momentum significantly larger than its mass (as it is often the case in the LHC physics), the rapidity is equivalent

to the pseudorapidity η , which is used in multiple analyses, including the one described in this document. It can be described simply in terms of the angle θ (as defined in Fig. 4.6) independently of the energy of the particle:

$$\eta = -\log \left(\tan \left(\frac{\theta}{2} \right) \right) \quad (4.8)$$

In the rest of the section, a more detailed description will be given for each CMS subdetector, as shown in Fig. 4.6, going from the ones closer to the collision to further out, thus covering the tracker, the electronic and hadronic calorimeters, the solenoid, and the muon system. The last part of the section will present the data acquisition process that is performed to record the data collected by the detector.

4.3.1 The inner tracker

The CMS subdetector closest to the interaction point is the tracking system. Its purpose is to reconstruct all primary and secondary interaction vertices, as well as the tracks of charged particles, whose momenta are also inferred thanks to the solenoid, which bends their trajectories. It has a diameter of 2.5 m and a length of 5.8 m, and it is composed of several silicon devices, covering an active area of around 200 m² [103]. It is designed to optimise the detector occupancy, that is, the fraction of active channels per LHC bunch crossing, while also having as small material budget as possible without affecting its performances. A schematic representation of its layout is shown in Fig. 4.8.

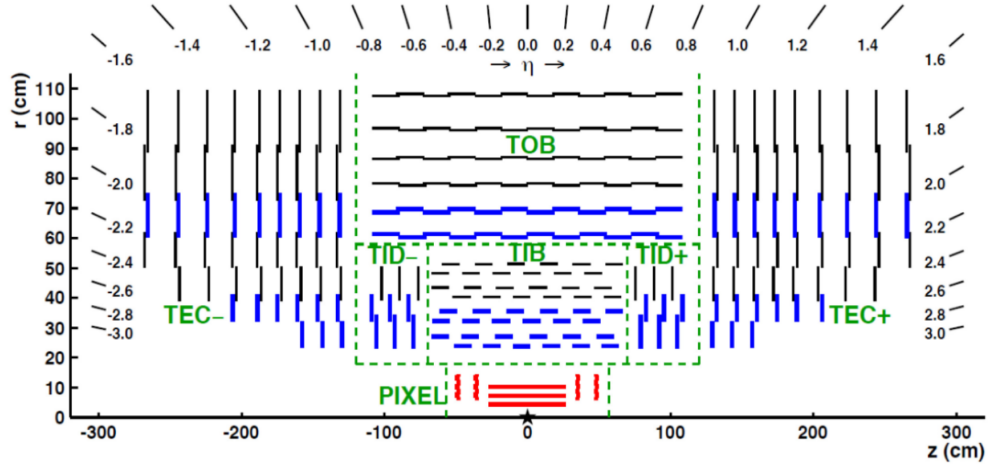


Figure 4.8: Schematic view of the CMS tracker in the r - z plane [10]. In the strip tracker, every line corresponds to a silicon strip detector. In the pixel detector, the lines represent the ladders and petals that hold the detectors in the barrel and endcaps, respectively.

The inner section of the tracking system is the pixel detector (SPD), used to reconstruct the secondary vertices of the interactions. It is shown in Fig. 4.8. Because of the ever-increasing luminosities, it was updated before the beginning of the 2017 data taking period, into what is known as Phase 1 pixel [104].

Prior to its upgrade, it was made by three layers of silicon pixel semiconductors, with approximate cylindrical shape and located at 4.4, 7.3 and 10.2 cm from the beam line in the barrel; as well as two endcap disks at each side, with a radius of 6 cm and 15 cm, and located at $|z| = 34.5$ cm and $|z| = 46.5$ cm, respectively. Each pixel forming the SPD has a surface of area of 100 by 150 μ m, and a thickness of 250 μ m, covering the region of $\eta < 2.6$, equivalent to approximately 1.1 m², totalling around 66 million pixels.

From 2017 onwards, there are four layers of silicon pixel semiconductors in the barrel, collectively labelled as the barrel pixel detector (BPIX), located at 2.9, 6.8, 10.9 and 16 cm from the beam line. Likewise, for the forward disks (FPIX), the two endcap disks were replaced by three, placed at 29.1, 39.6 and 51.6 cm from the centre of the detector, respectively. 672 modules were used for the BPIX and 672 for the FPIX, each sensor having a resolution of 160×416 . In total, the silicon area was increased to 1.9 m^2 . A comparison of the layout of the Phase-1 to the original detector is shown in Fig. 4.9 [104].

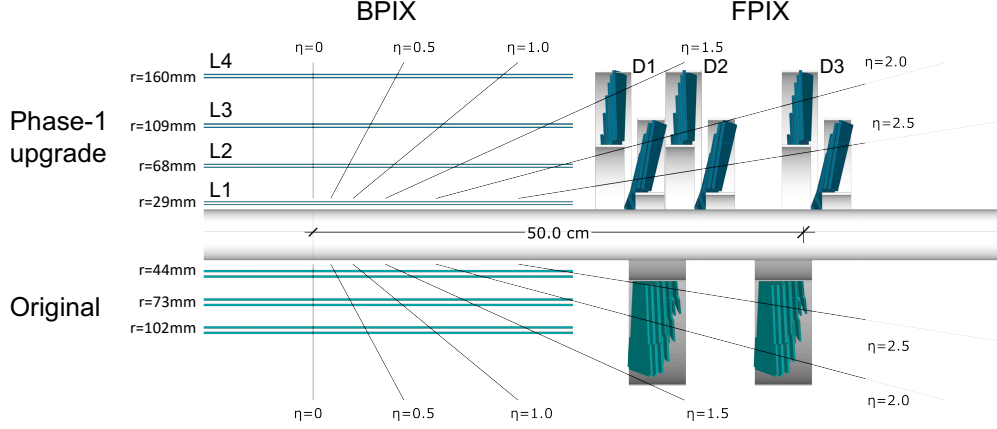


Figure 4.9: Layout of the CMS Phase-1 (top), compared to the original detector layout (bottom), in a longitudinal view.

The silicon strip detector (SSD) surrounds the SPD. This tracker subdetector is made of silicon strips, whose pitch vary between 80 and $180 \mu\text{m}$, and it's formed by 10 cylindrical layers in the barrel, as well as 9 disks in the endcap, covering in total the region of $|\eta| < 2.5$. The barrel section of the SSD is further subdivided in an inner (Tracker inner barrel, TIB), and an outer barrel ((Tracker outer barrel, TOB), whereas the section of the SSD is also further divided in two disk types, inner disk (TID) and an outer disk (TOD), located in the end caps(TEC). As it can be observed in Fig. 4.8, the TIB is slightly shorter than the TOD, due to the positioning of the TID, constructed in this way in order to avoid excessively shallow track crossing angles. All in all, the SSD has around 9.6 million silicon strips covering an area of approximately 200 m^2 .

The spatial resolution for both the SPD and SSD parts of the CMS tracker is shown in Table 4.1. From these values, the momentum resolution can be inferred, obtaining a resolution for tracks with $|\eta| < 1.6$ of:

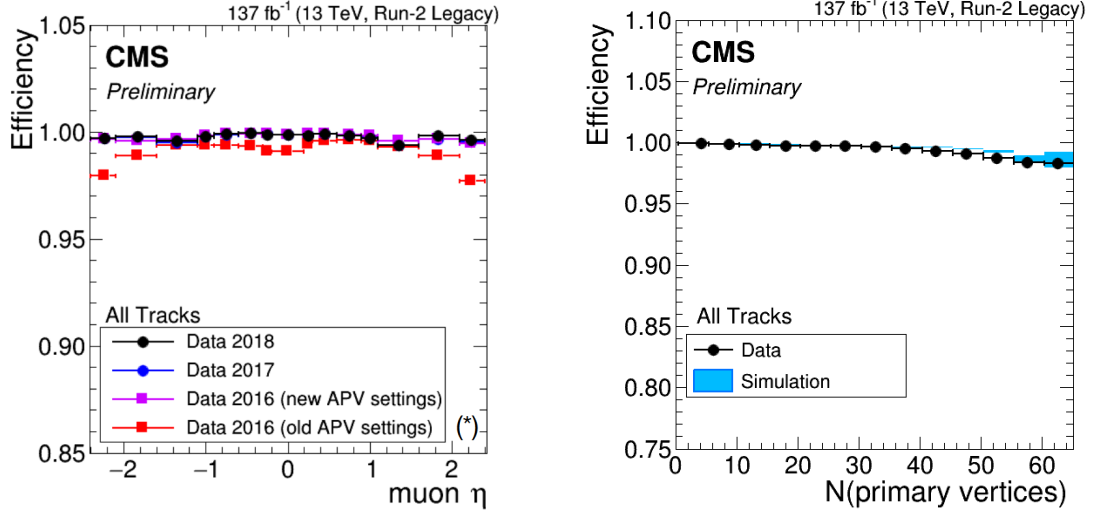
Detector		Resolution (r, ϕ)	Resolution (z)
SPD	barrel	$15 \mu\text{m}$	$11\text{-}17 \mu\text{m}$
	endcap	$15 \mu\text{m}$	$90 \mu\text{m}$
SSD		$15 \mu\text{m}$	1 mm

Table 4.1: Space resolution for each of the CMS tracker sub detectors, in terms of the (r, ϕ) plane and along the (z) axis, as defined in Fig. 4.7

$$\frac{\sigma(p_T)}{p_T} = \left(\frac{p_T}{\text{GeV}} \right) \cdot (0.015\% \oplus 0.5\%) \quad (4.9)$$

The resolution however lowers for higher values of η and the number of primary vertices, and thus may differ for each year. An example for these dependencies for Run II data is shown in Fig. 4.10.

Figure 4.10: Tracker reconstruction for muons measured during the Run II data taking and produced via $Z \rightarrow \mu\mu$ events, measured in terms of:



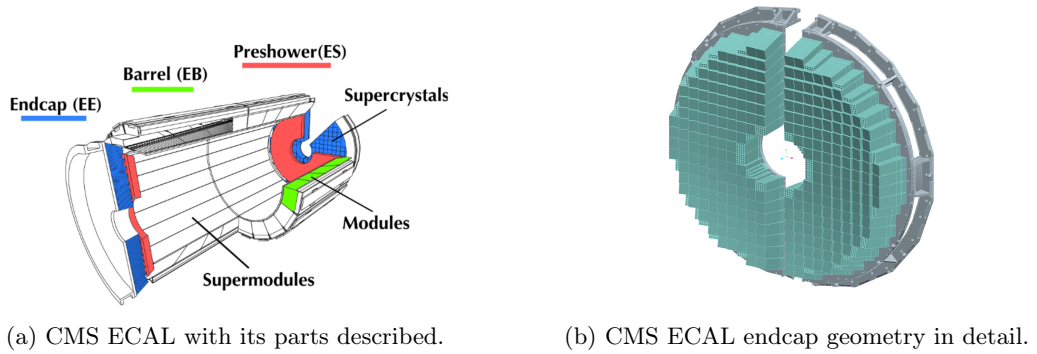
(a) Muon's η , for each of the data taking periods considered [105].

(b) Number of primary vertices [105].

4.3.2 The electromagnetic calorimeter

Immediately outwards than the tracker, the electromagnetic calorimeter (ECAL) is found. It is a hermetic detector, composed by scintillating crystals (PbWO_4) that serves to measure the energy of photons and electrons with precision, as well as to measure the fraction of electromagnetic showering existing in the energy of a jet. Similarly as for the tracker, it is formed by a barrel and two endcaps [106], with an additional subdetector, known as the preshower, located in front of the barrels. A schematic representation of the ECAL as well as each of its subdetectors is shown in Fig. 4.11a; while Fig. 4.11b shows a more in depth representation of one of the endcaps.

Figure 4.11: Schematic representation of the CMS ECAL [11]:



(a) CMS ECAL with its parts described.

(b) CMS ECAL endcap geometry in detail.

The barrel is formed by 61200 crystals, located at a radius of 1.29 m from the beam pipe, covering the area of $|\eta| < 1.479$, while the endcaps are located at 3.14 m from the interaction vertex along the z axis, and are formed by 7324 crystals, covering the region of $1.479 < |\eta| < 3$, as shown schematically in Fig. 4.12. The preshower detector is located in between the beam pipe and the endcaps, covering a region of $1.653 < |\eta| < 2.6$. Unlike in the tracker, ECAL crystals forming the barrel and endcap are very similar: the crystals in the barrel have a length of 230 mm and a cross section of $22 \times 22 \text{ mm}^2$, and the crystals in the endcap a length of 22 cm and a front face cross section of $28.6 \times 28.6 \text{ mm}^2$. In order to remove the possibility of a particle to pass

between two adjacent crystals, the crystals are mounted on a geometry that is slightly shifted with respect to the average position of the primary vertex. Lastly, the preshower detector is formed by two layers of lead absorbers followed by silicon strip sensors, such that both layers of strip sensors are placed orthogonally.

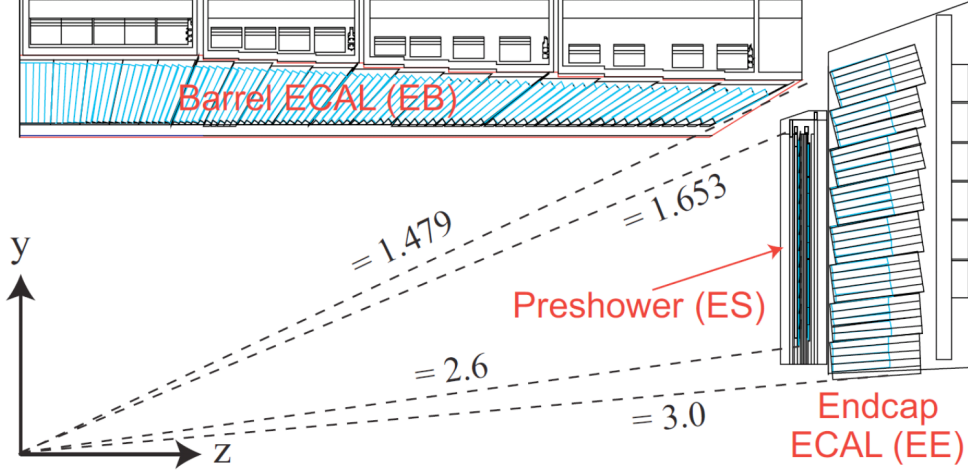


Figure 4.12: Geometric view of one quarter of the ECAL [12] in the rz -plane.

Extensive testing has been conducted on the calorimeter's performance using electron beams. In a test configuration where no magnetic field or inert material is present in front of the calorimeter, the resolution of the ECAL barrel energy (E) has been thoroughly measured, yielding the following results [12]:

$$\frac{\sigma_E}{E} = \frac{2.8\%}{\sqrt{E[\text{GeV}]}} \oplus \frac{12\%}{\sqrt{E[\text{GeV}]}} \oplus 0.3\% \quad (4.10)$$

The stochastic nature of the scintillation and showering processes is accounted for in the first term, while the second term represents electronic noise. The third term, on the other hand, captures the effects of detector non-uniformity and calibration uncertainty.

4.3.3 The hadronic calorimeter

Continuing going outwards from the beam, the next CMS subdetector, and the last found before the magnetic solenoid, is the hadronic calorimeter (HCAL) [107]. It shares similarities with the ECAL, but it is designed mainly to measure the energy and directions of the hadrons that form the jets, as well as to evaluate the missing transverse momentum (p_T^{miss}). Both quantities are of great importance when searching for new physics, especially the measurement of the missing transverse momentum, since BSM models typically involve new particles that are not measured directly by the detector. This is also the case of the searches presented on this document, as discussed in detail in Chapter 7.

The HCAL is designed to be the last measuring device for most particles, save for the neutrinos (or neutrino-like (BSM) particles), which do not interact directly with the CMS detector, and the muons, which can travel several metres through dense material. The HCAL is split in three regions. The central region ($|\eta| < 3$), further split in the typical barrel-endcap ((HB) and (HE), respectively) structure, is characterised by its excellent jet identification and moderate single particle and jet resolution. The other two regions are located in the edges, at 11 m with respect to the interaction vertex on the z axis, and are referred to as the forward (HF) calorimeters ($3 < |\eta| < 5$). They are characterised by a lower energy resolution but good jet identification capabilities. A schematic representation of the HCAL substructures is shown in Fig. 4.13.

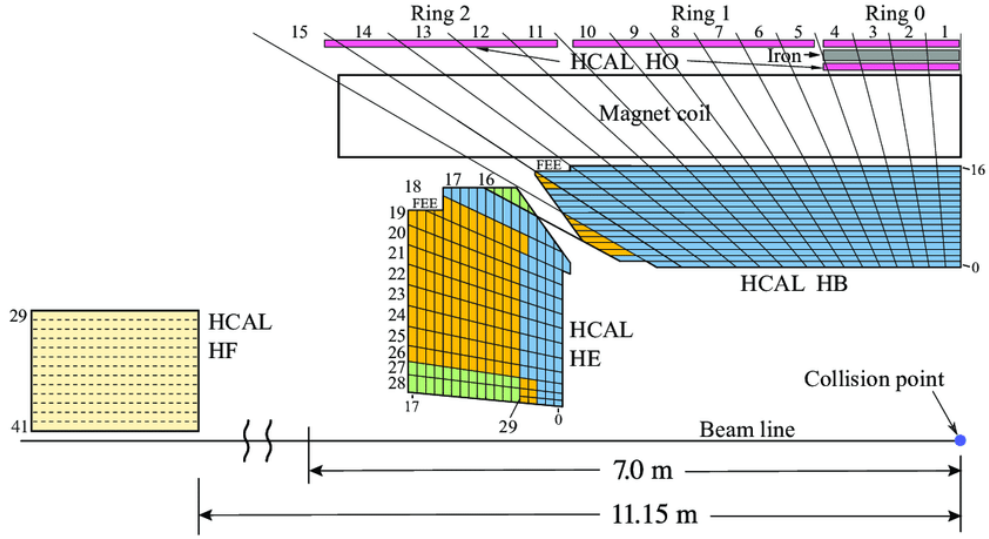


Figure 4.13: Geometric view of one quarter of the HCAL [12] in the $r-z$ plane, with each parts of the detector are shown: the hadron barrel HB, endcap HE, forward HF and outer HO [13].

The dimensions of the central HCAL were very constrained by design, as the detector had to fit between the outer section of the ECAL (at a radius of 1.77m), and the inner section of the magnetic solenoid, located at $r=2.95$ m. To enhance the sensitivity, an additional layer was placed directly outside the magnet, labelled as Hadron Outer (HO). The central part of the HCAL is formed by a combination of brass, which acts as absorbing material to facilitate the hadron showers, and a plastic scintillator, used to detect the particle. Likewise, in the HF, quartz fibers embedded in steel are used, to shield it from the much higher radiation under which the very forward regions are exposed. This configuration allows for achieving resolutions of:

$$\frac{\sigma_E}{E} = \frac{85\%}{\sqrt{E[\text{GeV}]}} \oplus 7.5\% \quad (4.11)$$

As for the case of the ECAL, the first term in the equation represents the stochastic contribution, whereas the second term corresponds to the effects arising from non-uniformity and calibration uncertainty. The HCAL is not as performing as the ECAL. This is understood given the limited amount of absorbing material, the intrinsically lower particle multiplicity of the hadronic showers with respect to the electromagnetic showers, as well as the HCAL being more of a sampling calorimeter, and the ECAL a homogeneous one.

4.3.4 The solenoid

The magnetic solenoid, located in between the central and the outer part of the calorimeter, is used as the main support structure for all the previously mentioned subdetectors [108]. It also plays a significant role, albeit indirect, in the particle detection, as it creates the magnetic field that bends the trajectories of the charged particles, allowing the charge sign and the transverse momentum (p_T) of those particles to be measured. The magnet located inside the CMS detector is one of the most powerful magnets ever built, as it can generate a magnetic field of up to 3.8 T at its interior, produced uniformly along the z -axis direction, being slightly lower than its originally designed value of 4 T [109]. It also produces a magnetic field of up to 2 T in the muon chambers situated immediately outward from the solenoid.

The magnet itself is generated by a cylindrical superconducting coil, as well as a vacuum tank, and a saturated iron yoke. The coil, located at a diameter greater than 5.9 m with a length of 12.9 m, is formed by high purity stabilised aluminium. The vacuum tank is made of stainless

steel, and is supported by the central ring of the barrel yoke, and itself supports the superconducting coil. The iron yoke, as was the case of the previously mentioned detectors, is split into a central barrel part, which is a dodecagonal prism, of a diameter up to 14m and a thickness of 1.5 metres, as well as two endcaps. It is intertwined with the muon chambers, providing them with additional structural stability, and it is what gives CMS its characteristic red colour.

4.3.5 The muon system

In addition to the previously mentioned HO, three different detectors are located outside the superconductive solenoid. They are collectively known as the muon system, as their purpose is to identify muons and measure their momenta [110]. Each of the three detectors is gas based, but designed with different technology, to account for the very different level of radiation to which they are exposed because of their location. In particular, drift tubes (DT) are found in the barrel, cathode strip chambers (CSC) in the endcaps, and resistive plate chambers (RPC) in both sections of the detector. A detailed scheme of each subdetector is shown in Fig. 4.14.

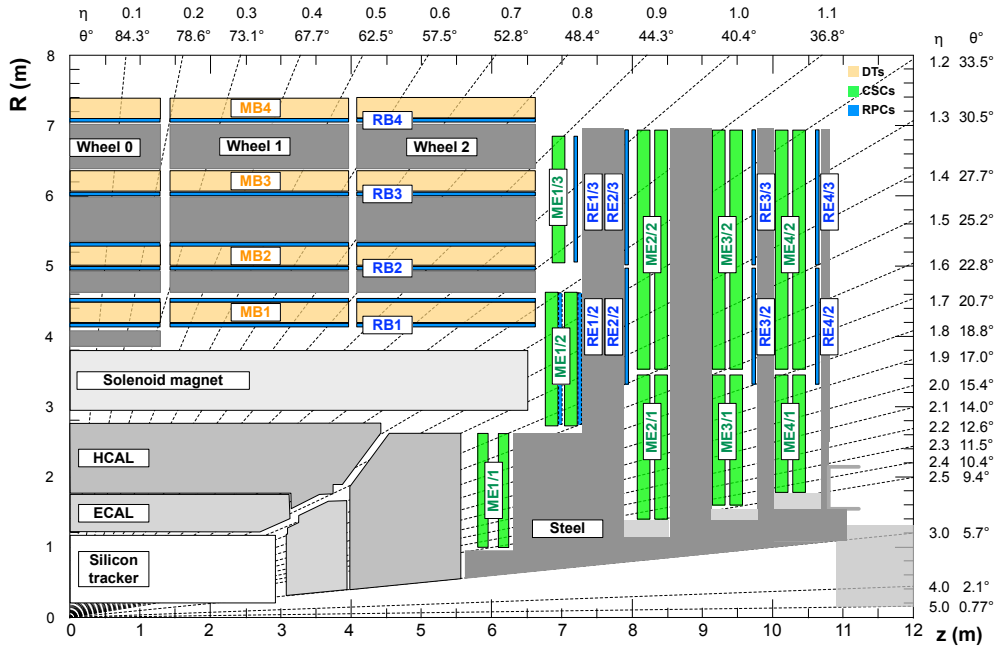


Figure 4.14: One quadrant of the CMS detector, with all subdetectors shown, as well as a bigger detail shown for each of the muon subdetectors, showing each of the DTs in orange, the CSC in green and the RPC in blue [14].

Collectively, the muon system covers the area of $|\eta| < 2.4$. The DTs cover the region of $|\eta| < 1.3$, characterised by having a small muon flux, and neutron induced background, with a low residual magnetic flux. The CSCs cover the area of $0.9 < |\eta| < 2.4$, where larger muon fluxes, neutron induced background, and a larger residual magnetic field are found. Lastly, the RPCs are designed with a good time resolution that allows them to identify the correct bunch crossing with higher precision than the DTs and CSCs, at the expense of having a lower position resolution. They are located in the region of $|\eta| < 2.1$. The location of the detectors is generally perpendicular to the incoming direction of the muon. The section of the muon system located in the barrel is arranged in four layers of detectors, intertwined with the iron yoke, where in each of them a layer of DTs can be found, surrounded by two RPCs in the two sections closer to the beam pipe, and only one layer in the two further sections. The endcap sections are similarly split in four different disks, perpendicular to the beam and all in concentric rings. In each ring, the CSC takes a central location, and is surrounded by a RPC layer.

In total, the muon system consists of nearly one million electronic channels, with a detection surface of around 2500 m^2 , which provides for a momentum resolution of 8-15% for a muon with a transverse momentum of 10 GeV, and between 20% and 40% for a 1 TeV muon. This

sensitivity can be further improved if combined with the muon information provided by the tracker, increasing the resolution to 1.0-1.5% for a 10 GeV muon, and 6-17% for a 1 TeV muon. Muons thus reconstructed are commonly referred to as *global muon*, to distinguish them from muons whose properties are derived using only information from the muon chambers (*standalone muon*) or from the tracking system (*tracker muon*). A more detailed explanation on how the muon reconstruction is performed is presented in Section 5.2.1.

4.3.6 The trigger system

As mentioned in Section 4.2, at the LHC, proton bunches collide every 25 ns, corresponding to a collision rate of 40 MHz. However, given the immense complexity of the CMS detector, the amount of data produced by the detector is of several terabits per second, which cannot be processed by computers, nor stored on tape. Therefore, a system, known as the trigger system, was put in place in order to select the most interesting events [111, 112, 113]. It is itself formed by two subsystems, or trigger levels.

Firstly, a hardware based trigger, known as the Level-1 trigger, is implemented. This trigger level retrieves information from each of the sub detectors, including the total missing momentum (p_T^{miss}), as well as the transverse momentum (p_T) of the particles. Subsequently, information from each subdetector is combined, applying thresholds on the previously mentioned variables, in order to select the most physically interesting events. This step is performed in real time, typically taking a few milliseconds, owing to the usage of custom-built hardware and fast electronics, and it provides with a reduction of the amount of data of several orders of magnitude, lowering the event rate from 40 MHz to around 100 kHz. A more comprehensive scheme of this procedure is depicted in Fig. 4.15.

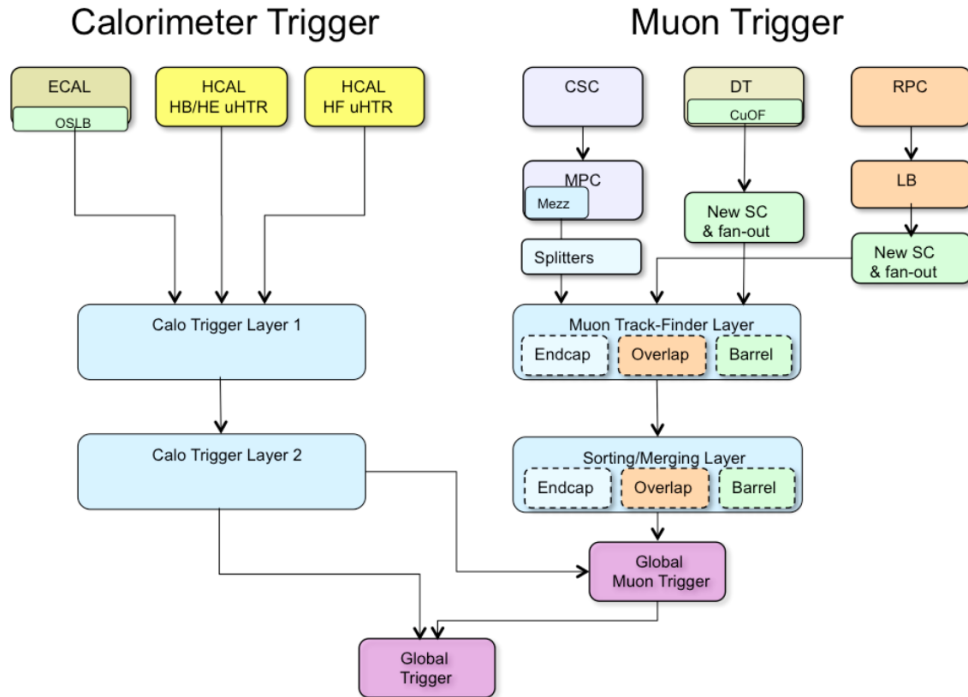


Figure 4.15: Scheme for CMS' Level-1 trigger system, with each sub detectors involved [15].

The second level of the trigger system, known as high-level trigger HLT, is then used to further reduce the rate by two more orders of magnitude, to around 1 kHz. This step is software based, running on commercial computers, and it is characterised by using more refined selections, including the incoming information of the Level-1 trigger but also information coming from the tracker, using a track reconstruction algorithm almost analogous to the offline track reconstruction algorithm, described in detail in Section 5. Because of this additional sophistication, the processing time is typically of the order of several tenths of a second, which, given the incoming

rate of 100 kHz, makes the usage of a computer farm indispensable.

The data processing of the HLT follows a structured approach known as *HLT path*, which comprises a series of algorithmic processing steps that progressively increase in complexity, focusing on physics reconstruction and selection. Each HLT path begins with the input of L1 objects, which have lower thresholds compared to higher level objects. Even after the HLT trigger selection, the data stream often remains sufficiently high to overwhelm the bandwidth for data collection. In such cases, in order to prevent saturation and to ensure an efficient data acquisition, the trigger algorithm is adjusted by prescaling or blocking it after a specific number of events within a defined data range have been recorded.

The data sets selected in real-time are determined based on physics priorities previously agreed by the CMS Collaboration. Typically, these data sets consist of events containing one lepton, events with multiple leptons, photons, leptons combined with jets, only jets, and/or events with a specific missing transverse momentum magnitude (p_T^{miss}). To facilitate their organisation, the data are naturally arranged into primary datasets (PDs) according to the trigger paths they correspond to.

4.4 Event data model and data tiers

A physics analysis using data from the CMS detector typically involves combining a diverse range of reconstructed information obtained from physics data recorded by the detector and Monte Carlo (MC) simulated data. This information can be classified into two categories: “event data” and “non-event data”. A detailed explanation of how Monte Carlo simulated data are generated and utilised at the CMS experiment is given in Chapter 6 of this document.

4.4.1 CMS event data model

The core of the CMS event data model revolves around the concept of an “event”, defined as a computational entity that encompasses all the physical information related to a triggered physics event, as well as information derived from the data acquisition process itself. Each event contains complete information of the collision, including raw digitised data, reconstructed products, simulation products, high-level analysis objects, as well as information pertaining to experimental or simulated proton-proton interactions.

Some additional information, crucial for a comprehensive understanding of the events, is provided in another category, labelled as “non-event data” category. Examples of non-event data include information of the status of each of the components of the CMS detector, such as their temperature, magnetic field, calibration or physical alignment, or information about the version of the software or algorithms used to reconstruct the event data.

Access to the content of an event is facilitated through a series of independent modules, each responsible for a specific event-processing task. Example modules include event data producers, which add new data products to the event, filters that operate during online triggering and offline selections, or event data analysers that examine event features, and input/output modules for both data acquisition and storage. Communication between these modules is facilitated through the event object, whereas the selection and sequence of modules to be utilised is determined by the user. This modular framework is helpful given the complexity of the experiment, as it ensures adaptability to new developments and conditions.

The event filtering, data flow and storage management is controlled by the CMS trigger and data acquisition (DAQ) system, which utilises real-time detector data from the front-end electronics to generate an initial set of reconstructed data that will be further utilised by physicists.

The process of data reconstruction encompasses all operations involved in constructing physics objects from detector readouts. Reconstruction is performed in multiple steps that progressively create higher-level reconstructed units suitable for high-level triggering or physics analysis. This process aims to reduce the event size while extracting ever more complex physics objects such as tracks, particles, vertices, and other entities arising from collisions.

To meet the flexibility and event size reduction requirements of CMS, multiple data formats with varying levels of detail and precision are generated. Data formats are organised into a hierarchy, with each subsequent format storing higher-level object information with a reduction of the event size. The main CMS analysis data format are:

- ◆ **DAQ-RAW**: This format serves as the primary record of a physics event. It includes detector data obtained from the front-end electronics, as well as the results from the Level-1 (L1) trigger. The DAQ-RAW data is used as input for the HLT processing.
- ◆ **RAW**: This format serves as the main event archive. It contains the detector data after undergoing online formatting, along with the L1 trigger results and the outcomes of the HLT selection. Additionally, it can include some of the higher-level quantities calculated during the HLT processing .
- ◆ **RECO**: The RECO (reconstructed) is a format that contains high-level selected objects and a comprehensive record of hits and clusters used in their production, while retaining sufficient information for subsequent reconstruction processes.
- ◆ **AOD**: The subset of the RECO format that is designated for analysis purposes is labelled as AOD (The analysis object data). In this format, the events exclusively consist of high-level physics objects, accompanied by additional information that facilitates kinematics refitting.

A schematic explanation of each data format and their relation is shown schematically in Fig 4.16:

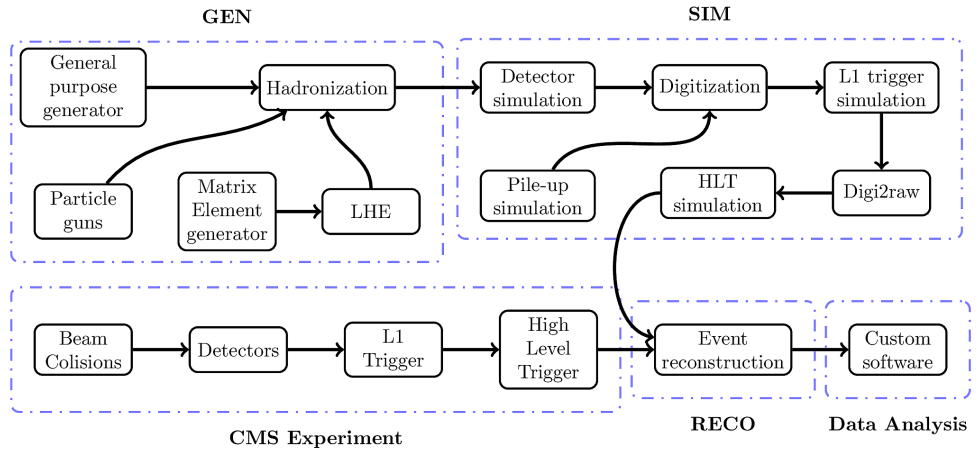


Figure 4.16: Main data formats and objects involved in them [16].

In addition to these data formats, it is common that analyses at the CMS Collaboration use other formats, namely miniAOD and nanoAOD, which are characterised by being compact versions of the AOD format, with possibly some additional higher level variables defined, which provide for quicker data processing, at the cost of simplifying some information. For each data format, there typically exist multiple versions, each version generally employing more refined calibrations to reconstruct the events in data from the detector or MC simulations. The analysis presented here utilises nanoAOD-v9 samples, which are known inside the CMS Collaboration as Ultra Legacy (UL) samples, while some comparisons are made with respect to the previous end-of-year (EOY)

samples, nanoAOD-v6.

4.4.2 CMS data tiers

Given the immense quantity of information (>10 PB per year just at the CMS Collaboration), and the speed at which it has to be processed (\mathcal{O} GBit/s), the processing of data is only possible if a grid of computers is set in place. Rather than concentrating all the data processing in a colossal facility located at CERN, the CMS computing infrastructure is designed as a distributed system, utilising various computing centres worldwide that collaborate through Grid services. This interconnected network of resources enables CMS to carry out essential tasks such as data processing, data archiving, Monte Carlo event generation, and other computing-related activities in an effective way, while taking advantage of the cooperative nature of the collaboration. The organisation of these centres, generally located at member states national laboratories or universities, follows a hierarchical structure based on data tiers:

- ◆ **Tier-0:** Located at CERN, this computer cluster receives data directly from the online system and performs prompt reconstruction of the raw data, from which the original RECO dataset is constructed. Additionally, a copy of the RAW and RECO data is exported to Tier-1 centres.
- ◆ **Tier-1:** Hosted by CMS collaborating national laboratories, these centres are responsible for long-term storage of RAW data and hold a portion of the CMS simulated and RECO data. They also reprocess the data from the Tier 0 cluster, using improved calibration and alignment constants. These centres also contain a complete copy of the AOD data format, and provide data storage and access for the smaller Tier-2 centres. There are currently 7 Tier-1 centres operational at the CMS Collaboration, five in Europe (in Italy, France, Germany, the UK, and Spain), one in the USA and one in Taiwan.
- ◆ **Tier-2:** These clusters, of smaller size, are hosted at several CMS institutes, including one at the Instituto de Física de Cantabria IFCA. They support local analysis and specialised activities, facilitate local data analysis for specific research purposes within the experiment, and handle the Monte Carlo production for the entire CMS Collaboration.

In summary, the CMS computing environment utilises a distributed system of interconnected computing centres, working together through Grid services. The hierarchy of data tiers ensures efficient data flow, storage, and processing across different centres, ultimately enabling comprehensive data analysis and simulation tasks for the CMS experiment. A schematic description of this process with its tiers 0, 1 and 2 is shown in Fig. 4.17.

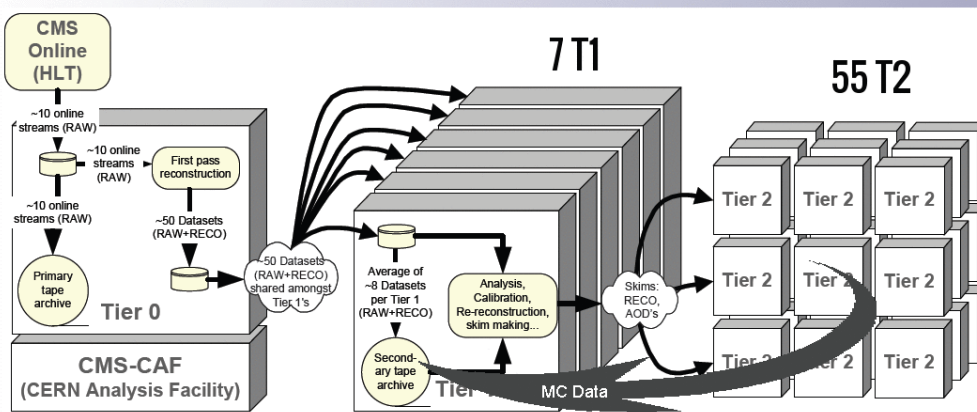


Figure 4.17: Detector data flow with each of the tiers and its function [17].

4.5 LHC plan and future

Operating an accelerator complex such as the LHC is by no means an easy task, having to account for the needs of each of the aforementioned detectors. For that reason, providing with a clear benchmark plan on how the machine will be operated in the upcoming years is a primordial task. Such a plan is outlined in Fig. 4.18, showing the expected luminosity, energy at centre of mass, and timeline for each of the past, present, and future data-taking periods, known as “Runs”.

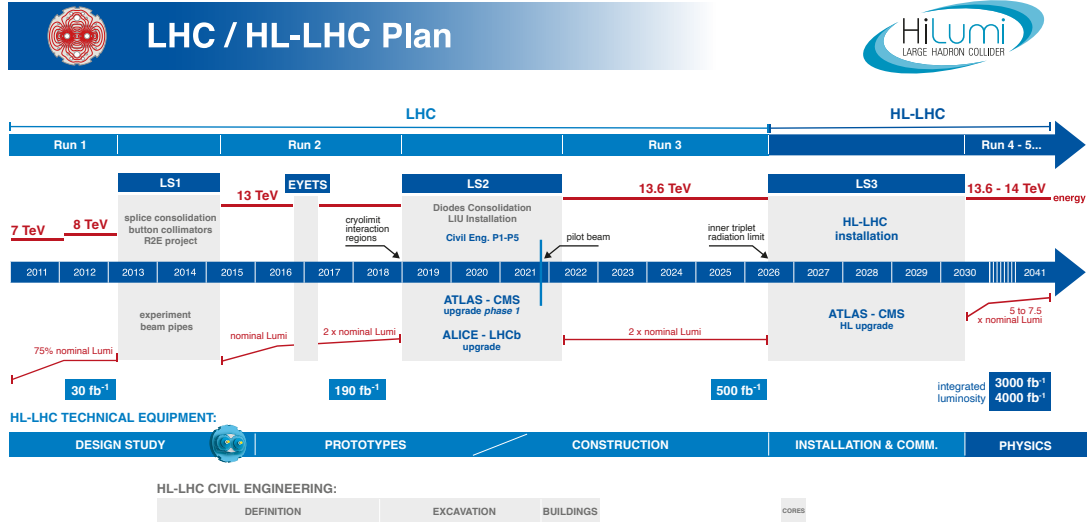


Figure 4.18: General LHC and high luminosity LHC(HL-LHC) plans, where for each Run, its working energy, year and designed luminosity are shown.

Each run is divided into several physics runs, which correspond to continuous data-taking cycles with coherent collision conditions and operating settings, each of them of the duration of a few hours at most and labelled by an increasing number.

The Runs are separated by programmed long inactive periods, known as long shutdowns (LSs), which are used to perform engineering work at the detectors and the collider.

Within the LHC program, the following Runs have been operated:

- ◆ The Run I, spanned between 2011 and 2012, was the first Run in the LHC operation, with an energy at centre of mass of 7 GeV in 2011 and of 8 GeV in 2012, and an integrated luminosity delivered by the LHC almost reaching the 30 fb^{-1} benchmark [114].
- ◆ The Run II comprises the 2015-2018 period (although often includes only the 2016-2018 period, given the relatively lower amount of data taken in 2015). Events taken in this period comes from collisions at an energy of 13 TeV and amounts to a delivered integrated luminosity of 165 fb^{-1} [114], close albeit slightly short of the expected integrated luminosity. The data collected during this Run are the ones used for the analysis presented in this document
- ◆ The Run III is the currently ongoing data-taking period. It started in 2022 and is expected to finish by 2026, with twice an expected integrated luminosity with respect to Run II. Currently, a total luminosity of 196 fb^{-1} has been delivered [114].

After Run III is finalised, an upgraded version of the LHC will be installed, the so called high-luminosity LHC(HL-LHC), which is expected to produce much more collimated beams, allowing the collection of data sets with significantly higher integrated luminosities (of around 3000 fb^{-1}) at an average of 200 PU interactions per bunch-crossing[114].

The high rate of collisions expected at the HL-LHC, besides the already significant challenges from the triggering and detection points of view, also comes with additional secondary challenges, such as the additional radiation damage in the detector caused by the extra particles. For this reason, it is of upmost importance to design detectors that are not only capable of detecting the crossing particles, but are also resistant to the radiation damage caused by them, and can be studied via simulations or by physically testing them. While several different algorithms exist to simulate the radiation to which the detectors are subjected, I utilised the *Fluka* software [115] to make such studies, as it provides the user with a 3D model of the CMS detector, from where 2D diagrams of the expected fluence for each part of the detector can be extracted, as shown in Fig. 4.19.

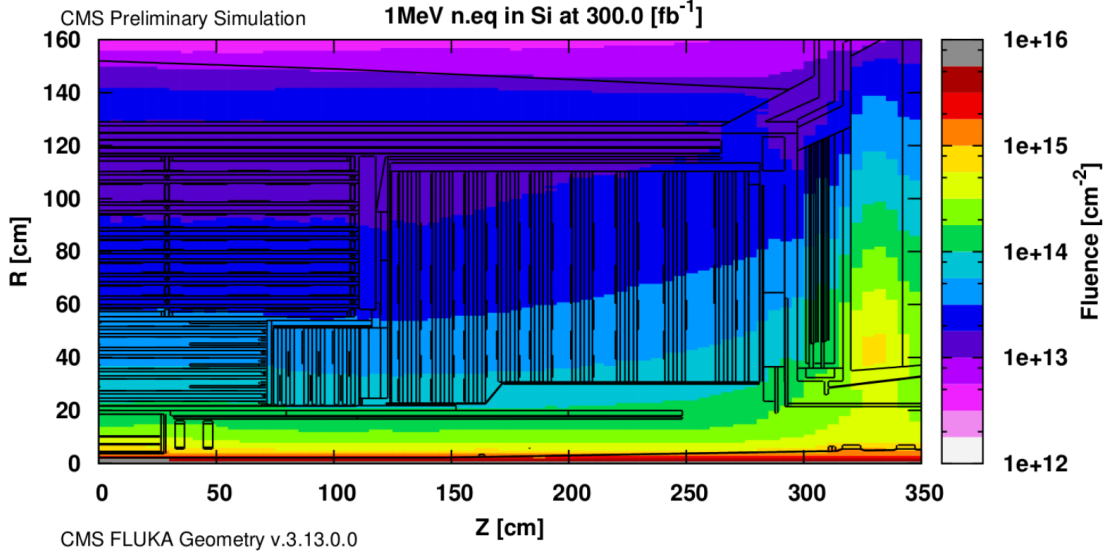


Figure 4.19: Expected fluence at the CMS detector for a luminosity of 300 fb^{-1} in the R-Z plane [18].

Similarly, the software allows for the separation of the contribution in terms of the particle type, as well as providing with a 1D projection, being able for instance to represent the equivalent fluence in terms of the radius of the detector, as shown in Fig. 4.20. My task in this point was to compare the results for the different versions and to compare Run II, Run III and HL-LHC results.

Once the amount of radiation sustained by the detectors is known, another important task is to ensure that the prototypes for the future versions of the CMS detector can sustain it. For that matter, one option is to irradiate a sensor and compare its measurement qualities before and after the irradiation. One example was the irradiation of silicon sensors by the RD50 collaboration [116], where the sensors were irradiated either with protons or neutrons [117, 118], a group with whom I worked at when I was a CERN Summer Student in 2017 [119].

A more comprehensive way of testing detectors is via what is known as *test beams*, where complete parts of the detectors are built, nearby a test facility, where a beam similar to what is expected by the HL-LHC is placed. In the CERN complex, this is done in either the North or East area depicted in Fig. 4.1, although it can be performed in other colliders, such as DESY in Germany [120]. In this case, I participated in the assembling and testing of the DT chambers, in the

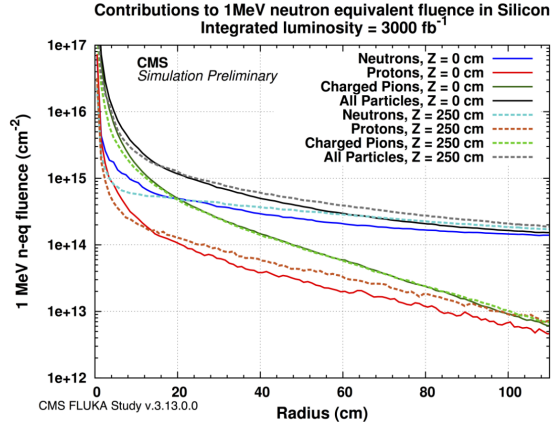


Figure 4.20: Expected contribution to the fluence at HL-LHC conditions for each of the particles with, in terms of the radius from the beam pipe. Results are presented at the collision point (solid line) and at a distance from the collision point of 250 cm (dashed line) [18].

Gamma Irradiation Facility (GIF++), located in the North area of the LHCcomplex depicted in Fig. 4.1.

Chapter 5

Physics objects reconstruction and identification

The CMS detector consists of various sub-detectors that generate electrical signals when particles pass through them, where these signals correspond to hits in the tracker and muon system, or energy deposits in the calorimeters. To reconstruct the particles and determine their properties (such as momentum, energy, and type), specialised algorithms are required. These algorithms utilise information from all CMS subsystems in a cohesive manner, employing the concept of *particle flow* (PF).

This chapter starts by providing a general overview of how the PF algorithm works in Section 5.1, followed by a detailed discussion of the reconstruction methods utilised to reconstruct different physics objects in the remaining sections of this chapter. An emphasis is placed on electrons (Section 5.2), muons (Section 5.3), jets (Section 5.5), and missing transverse momentum (Section 5.6), given that these are the physics objects on which the analysis presented in this document is based.

5.1 Particle flow reconstruction

The PF algorithm[121] serves as the fundamental approach for event reconstruction at the CMS experiment. It leverages information from all the sub-detectors that form the CMS detector, and uses them to reconstruct and classify all the particles in the final state of an event, as depicted in Figure 5.1. Examples of such particles include muons, electrons, photons, neutral hadrons, and charged hadrons. The algorithm also creates a collection of particle-based objects and observables, such as jets, missing transverse momentum, lepton isolation, or the tagging of jets coming from a b quark (commonly known as b-jet tagging).

The PF algorithm operates in two different stages. The reconstruction process begins with the identification of primitives, such as tracks and calorimeter clusters. The algorithm then links these primitives to specific particle candidates (like electrons, muons, photons, and hadrons). Particle candidates are reconstructed from the primitives in the following order:

- 1) The first reconstructed particle candidates are the muons. For this purpose, tracks reconstructed in the silicon tracker are selected if they match either a track or multiple hits reconstructed in the muon chambers. These tracks are also required to only exhibit small

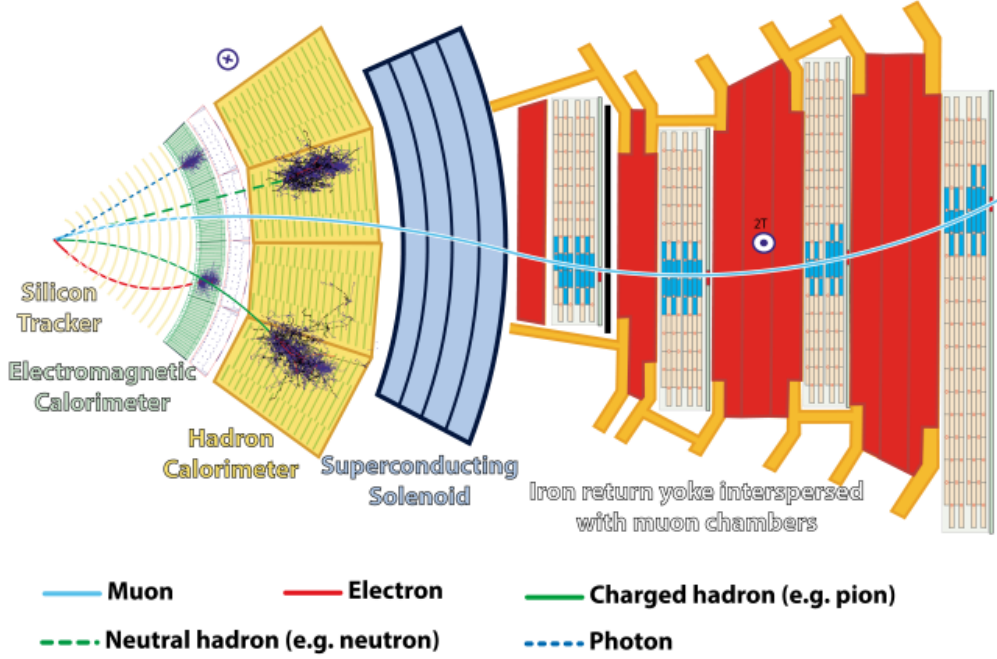


Figure 5.1: Section of CMS viewed from the transverse plane, with each of the subdetectors labelled and represented in a different colour. Also represented is how the various particles identified by the particle flow reconstruction are expected to interact with the detector [19].

energy deposits in the calorimeters. The hits in the tracker, muon chambers, and calorimeter deposits associated with these muons are then removed from the event. This exclusion ensures that they are not utilised in the subsequent reconstruction of electrons and jets.

- 2) Next, candidate electrons are reconstructed. These particles are identified as charged particle tracks associated with one or more energy deposits in the ECAL, where each of the energy deposits can be due to the electron itself or to a photon produced via (*bremstrahlung*) emission. After this step, the tracks and ECAL energy deposits used to reconstruct the candidate electrons are subsequently removed from the event.
- 3) Photons are reconstructed independently of electrons. Photons are identifiable thanks to them leaving energy deposits solely in the ECAL, without associated tracks in the tracker.
- 4) Neutral hadrons are reconstructed using energy deposits solely in the HCAL (hadronic calorimeter), without any corresponding tracks.
- 5) Finally, charged hadrons are identified using charged particle tracks associated with energy deposits in both the ECAL and HCAL.

By following this sequence, the particle flow algorithm can effectively reconstruct and characterise the different particles observed in an event, allowing for the construction of other objects commonly used in the analyses. These include the clustering of the jets, the computation of the missing transverse energy, the evaluation of the lepton isolation, and the tagging of the b-jets.

Generally, for each object, a compromise has to be made between the identification efficiency (i.e. percentage of the objects that are identified) and the misidentification rate (amount of other objects incorrectly identified). As each analysis may be more interested on purer objects or more amount of them, three operating points are typically defined, labelled as *loose*, *medium* and *tight* identification (ID) working points (WP), such that the *tight* WP will have a lower identification efficiency but also a lower misidentified objects than the *loose* WP.

5.2 Muon Reconstruction and identification

Muons are particles that possess a relatively short lifespan of approximately $2.2 \mu\text{s}$ at rest [48]. However, when produced at the LHC, they travel at nearly the speed of light, presenting decay lengths that are typically larger than the CMS detector. This results in them being effectively classified as stable particles by the reconstruction algorithms. However, since muons are charged particles, they engage with the tracker silicon detector as well as with the specially designed muon chambers. Conversely, muons generated by pp collisions at the LHC typically exhibit momenta ranging from hundreds of MeV to hundreds of GeV. Within this momentum range, and given their mass being around 200 times larger than the electrons' mass, muons in the CMS detector act as what is known as *minimum ionising particles*, meaning that they exhibit a close to minimal interaction with the calorimeters and thus deposit only small amounts of energy.

5.2.1 Muon Reconstruction

The presence of a muon in the CMS detector has to be identified by its track in the inner tracking system, matched with hits in at least some of the outer muon chambers, and accompanied by minor energy deposits in the calorimeters. The process of reconstructing a muon as a PF candidate relies on three different algorithms [122] based on whether the muon is reconstructed based on the information from the muon chambers (standalone muons), the tracker (tracker muons) or a combination of both (global muons), which are subsequently described in this section of the document.

Standalone Muons

The standalone algorithm of muon reconstruction relies on information gathered by the three muon systems. Its main objective is to reconstruct the trajectory of a muon by initially searching for hits in the DT, CSC, and RPC systems. For each chamber that registers a signal, a segment of the trajectory is formed by connecting the hits within the chamber's layers, utilising pattern recognition techniques. Each segment is associated with a vector containing the muon candidate position, momentum, and direction in that section.

To reconstruct the muon trajectory, a Kalman Filter technique [123] is employed, performing a fit to the vectors. The innermost vectors serve as seeds for the fit which are subsequently propagated to the next chamber, taking various factors into account, such as multiple scattering, energy losses in the muon chambers and return yoke. The fit thereupon searches for a compatible segment, and the trajectory is updated accordingly [124]. This process is repeated until the outer chamber is reached. For each added segment, a χ^2 selection is applied to assess the impact of incorporating a new chamber on the quality of the trajectory fit. This selection helps to identify and reject problematic hits originating from showering, delta rays, or pair production. The trajectory is built from the innermost to the outermost chambers using this method.

Once a complete trajectory, calculated from the inside to the outside, is retrieved, the same Kalman Filter technique is applied but in reverse, i.e. from the outer chambers to the inner chambers. Once the inner chamber is reached again, the trajectory is extrapolated to the point where it is closest to the beam axis. At this stage, the trajectory can be constrained by vertex requirements.

Some additional criteria need to be satisfied in order for the candidate to be classified as a standalone muon. For instance, the particle's trajectory must have a minimum of two compatible segments in the fit, with one of them originating from either the DT or CSC chambers. This criterion helps eliminate segments present in either DT or CSC that are actually the result of combinatorial effects.

Tracker Muons

Tracker muons, on the other hand, are defined by tracks reconstructed solely by the silicon tracker, which can themselves be associated with segments in the muon chambers or energy deposits in the calorimeters that align with the muon hypothesis. The reconstruction algorithm considers all tracker tracks with a transverse momentum (p_T) greater than 0.5 GeV and momentum (p) greater than 2.5 GeV. Tracks are categorised as tracker muons if they can be matched with at least one muon segment. Energy deposits compatible with a muon passing through the calorimeters are also used in the muon identification. This type of muon reconstruction is better performant than the standalone muons at low p_T , where the momentum resolution of muons measured in the muon chambers degrades, compared to the higher position precision and larger number of hits observed in the pixel chambers.

Global Muons

Global muons are identified by combining standalone muon tracks with independently reconstructed tracks from the inner tracking system. This matching process begins by extrapolating tracker tracks to the inner chamber of the muon system and searching for standalone muon tracks that are compatible in terms of their momentum, position, and direction. Once the two tracks are matched, a new global fit is performed using their hits. To ensure accurate matches between the inner and standalone tracks, quality criteria are applied. By incorporating information from both the tracker and the muon chambers, global muons provide an improved characterisation of muon properties with respect to the tracker or standalone algorithms previously mentioned. Generally, the tracker exhibits superior momentum resolution for momenta below 200 GeV. At very high momenta, the reduced bending provided by the magnetic field leads to a degradation in resolution, and the additional hits provided by the muon chambers at greater radii become critical to mitigate such resolution degradation of the silicon tracker. A comparison of the performance in the measurement of the muon momentum achieved by the global muon algorithm with respect to the tracker-only one is depicted in Figure 5.2.

In addition to these three algorithms, new algorithms have been developed during Run II, aimed at the reconstruction of muons that are produced displaced from the primary vertex (PV) of the interaction. These algorithms are known as displaced muon algorithms and are crucial for identifying muons originating from the decays of long-lived particles. In general, the behaviour of the displaced muon algorithms is more similar to the one of the tracker muon algorithm if the distanced travelled by the long-lived particle is small, and more relatable to the standalone algorithm if the distance is large. An example of the effectiveness of these algorithms for different values of the distance travelled by the long-lived particle is shown in Fig 5.3.

5.2.2 Muon identification

In the analysis presented in this document, the selection of muons follows the guidelines provided by the CMS Muon Physics Object Group (Muon POG). Five different WP were envisaged during the Run II data taking period at the CMS detector. Two of them are catered for either particularly low or high p_T muons, named the soft muon and high p_T identification (ID), while the other three are tailored for the intermediate p_T ranges that are used in the analysis hereby presented, and are named loose, medium and tight [20].

Loose ID

Loose muon identification is designed to select prompt muons that originate from the primary vertex and muons from light and heavy flavour decays, while maintaining a low rate of misidentifying charged hadrons as muons. A loose muon is defined as a muon selected by the PF algorithm that is reconstructed as either a tracker muon or a global muon.

Medium ID

Medium muon identification is optimised to select prompt muons and muons from heavy flavour decays. A medium muon is defined as a loose muon whose tracker track utilises hits from more

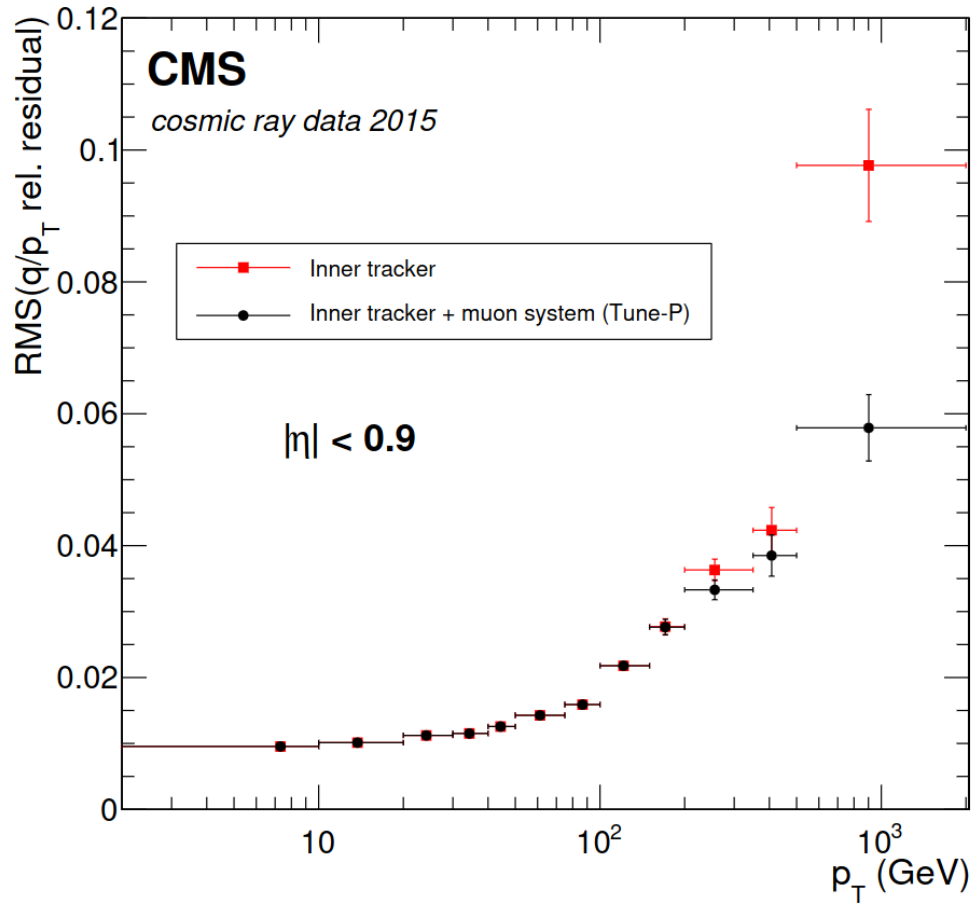


Figure 5.2: Root Mean Square (RMS) of two muon tracker (red) and global muon (red) algorithms in terms of the transverse momentum p_T for cosmic rays recorded in 2015 [20].

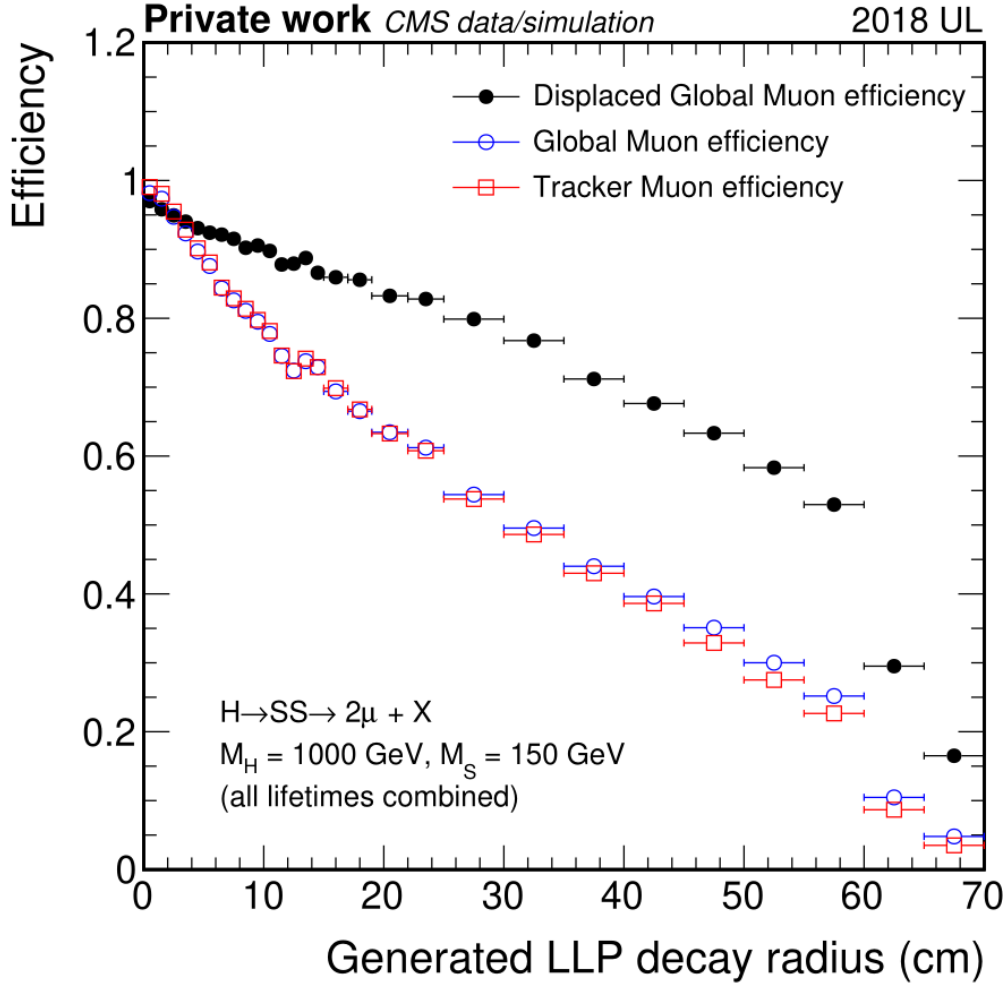


Figure 5.3: Reconstruction efficiency of the displaced global algorithm (black filled circles) compared to the global and tracker algorithms (blue empty circles and red empty squares, respectively). The efficiency was measured using simulated events where the Higgs boson decays to two long-lived S-bosons, where each of them decays into a pair of muons [21].

than 80% of the inner tracker layers it traverses. If the muon is reconstructed only as a tracker muon, the muon segment compatibility must exceed 0.451. For global muons, the segment compatibility requirement is relaxed to greater than 0.303. In this case, additional criteria are imposed:

- ◆ The global fit must have a goodness-of-fit per degree of freedom (χ^2/dof) less than 3.
- ◆ The position match between the tracker muon and the standalone muon must have $\chi^2 < 12$.
- ◆ The maximum χ^2 computed by the kink-finding algorithm must be less than 20.

The segment compatibility thresholds were fine-tuned after applying the other constraints to achieve an overall efficiency of 99.5% for muons from simulated W and Z boson events [20].

Tight ID

Tight muon identification is designed to suppress muons originating from decays in flight and from hadronic punch-through. A tight muon is defined as a loose muon whose tracker track includes hits from at least six layers of the inner tracker, including at least one pixel hit. Additionally, the muon must be reconstructed as both a tracker muon and a global muon, with at least one hit also in the muon chambers. In addition to that, some additional conditions are required in terms of track quality and impact parameters:

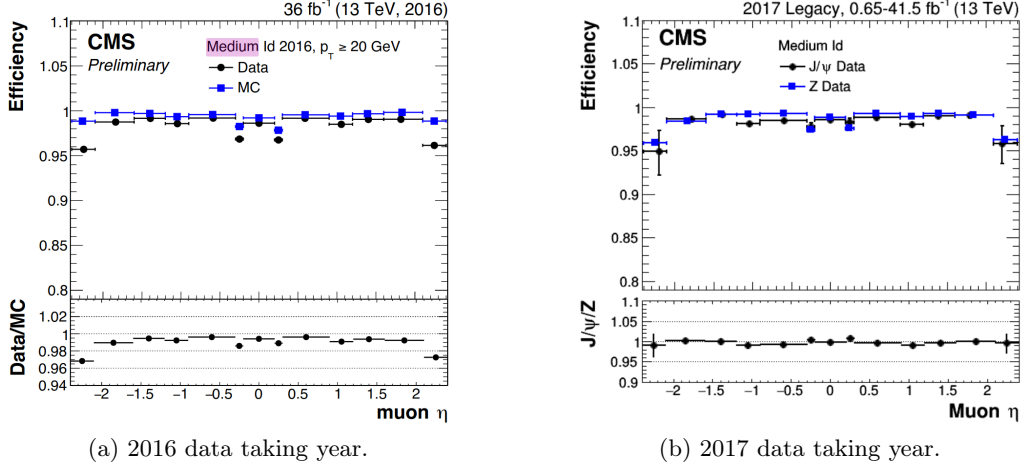
- ◆ **Track quality:** By selecting only tracks reconstructed with strict quality requirements, the amount of muons candidates from decay-in-flight and punch-through events (that is, particles such as mesons which reach the first of the muon chambers) is suppressed. This ensures a reliable estimation of the p_T and is performed involving the following requirements:
 - (χ^2/dof) of the global-muon track fit is required to be less than 10.
 - Muon segments must be present in at least two muon stations.
 - A minimum of five tracker layers with hits are required.
- ◆ **Impact parameter:** Requiring a small impact parameter for the muon tracker track with respect to the primary vertex helps suppress cosmic muons and decay-in-flight muons, which is done in terms of the transverse (d_0) and longitudinal (d_z) impact parameters. A similar procedure is generally used also in the case of the electrons, as described in Section 5.3. In the case of tight muons, it is required that $|d_0| < 0.2\text{cm}$ and $|d_z| < 0.5\text{cm}$ [20].

Example of muon identification efficiencies in terms of η are shown in Figs. 5.4a and 5.4b for 2016 and 2017, respectively, for the medium ID, which is the one used in the analysis presented in this document.

Isolation

In addition to the choosing of a WP, another important property of muon identification is the isolation, which is a measure of how much surrounding activity exists near a particle, such as a muon, within a specified cone in the detector. At the LHC, an isolated muon is one that is relatively free of nearby particles. Isolation is thus a useful tool to distinguish as a prompt muon (e.g. the decay of a W boson) from primary processes rather than from background sources like heavy-flavour decays or hadronic interactions, which are expected to have much more activity around them, due to the hadronisation process. Fig. 5.5 shows a schematic representation of an isolated and a non isolated muon, in Figs. 5.5a and 5.5b, respectively.

During the Run II data taking, five different definitions were used at the CMS detector [125], such as each search :

Figure 5.4: Muon identification efficiencies in terms of η for:

- 1) **Tracker isolation.** Under this definition, all the tracks within a cone of size $\Delta R < 0.3$ except the muons are added:

$$\text{ISO}_{\text{trk}} = \frac{\sum p_T^{\text{tracker tracks}}}{p_T^\mu} \quad (5.1)$$

This choice ensures that the offline isolation ID criteria are stricter than the selections employed at the trigger level.

- 2) **Calorimeter-based isolation:** All the energy deposits on the ECAL and HCAL within $\Delta R < 0.3$ are summed. This definition has the advantage of being sensitive to neutral hadrons or photons, but can be affected by Pileup, and underlying event activity.
- 3) **Combined Isolation:** It combines both tracker and calorimeter isolation into a single variable
- 4) **Particle-flow (PF) isolation.** This definition of isolation uses the PF algorithm to reconstruct and sum all the particles within a cone of size $\Delta R < 0.4$ around the muon. It is defined as:

$$\text{ISO} = \frac{\sum p_T^{\text{ch. had. (PV)}} + \max\left(0, \sum E_T^{\text{neut. had.}} + \sum E_T^{\text{ph.}} - 0.5 \times \sum p_T^{\text{ch. had. (PU)}}\right)}{p_T^\mu} \quad (5.2)$$

This is used by most Run II analyses, including the one depicted in this document, as it provides a high efficiency and background rejection, while mitigating pileup effects.

- 5) **Mini isolation:** It takes a similar definition of isolation as with the PF isolation, but using a cone whose size depends on the p_T of the muon:

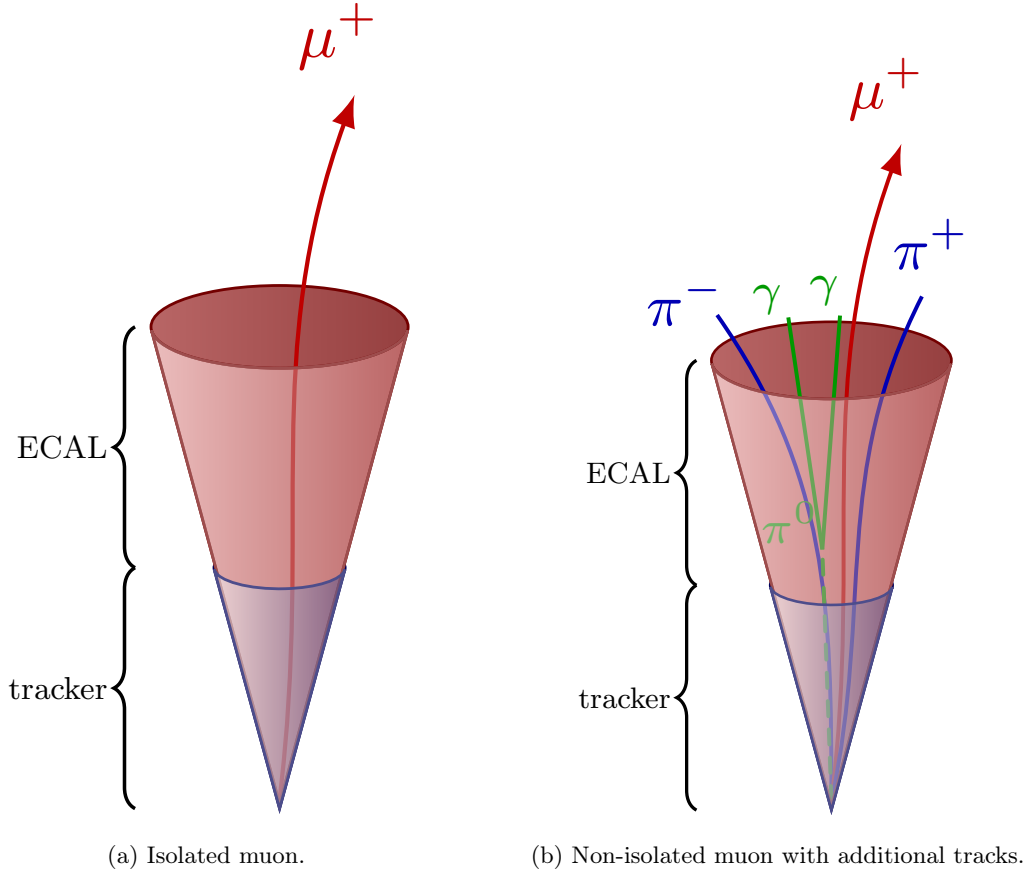
$$R_{\text{ISO}} = \frac{10 \text{ GeV}}{\min[\max(p_T^\mu, 50 \text{ GeV}), 200 \text{ GeV}]} \quad (5.3)$$

This definition is optimised for analyses that use high p_T muons, as by reducing the cone size at high p_T , the pileup contamination is reduced.

5.3 Electron reconstruction and identification

In the CMS experiment, electrons interact with the tracker system and the ECAL. The presence of an electron can thus be characterised by a single track pointing to an energy deposit (cluster) in the ECAL.

Figure 5.5: Schematic representation of how the cone used for lepton reconstruction in:



5.3.1 Electron Reconstruction

While passing through the tracker layers, the electron loses some energy through *bremsstrahlung*, emitting photons before reaching the calorimeter. As the electron's energy decreases, its path bends more within the magnetic field, causing the emitted photons to spread along the ϕ coordinate, whereas when an electron reaches the ECAL, it immediately produces an electromagnetic shower, where the most of its energy is collected by a small number of crystals surrounding the initial impact point. In order to accurately reconstruct the original electron energy, it is crucial to identify the photons associated with the *bremsstrahlung* as well as to account for their energy. This is achieved at the initial stage of the electron reconstruction algorithm, in a step known as *superclustering*, which enables the measurement of the electron's energy. Subsequently, the algorithm proceeds with the track-building stage and matches the information from the tracker and the ECAL.

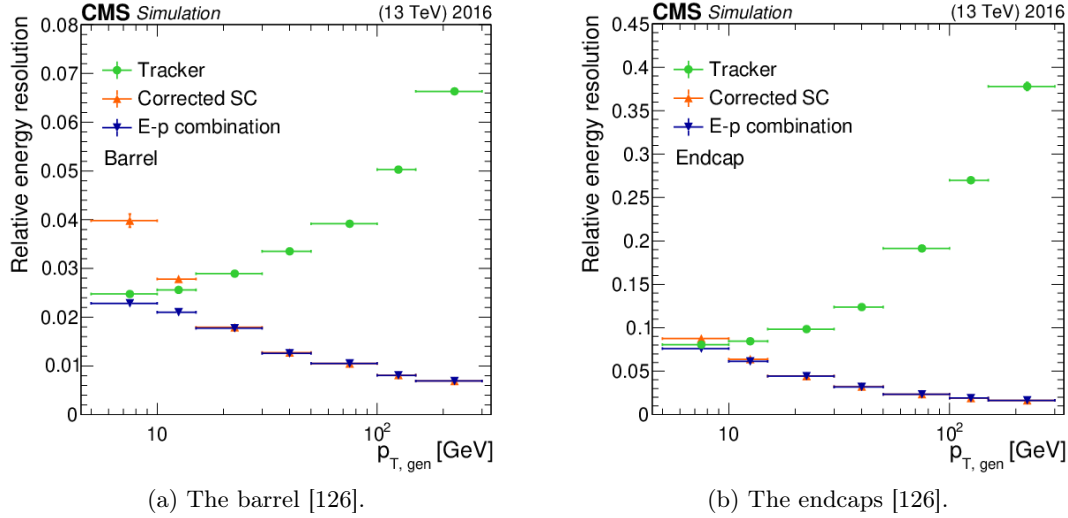
Superclusters (SCs) in the ECAL are formed by taking a seed crystal and grouping together all the crystals contiguous to it, provided their energy deposits exceed two standard deviations above the electronic noise [126]. The seed crystal is also required to have an energy above a specific threshold that varies in terms of the η coordinate. A minimum energy of 230 MeV is required in the barrel region, while in the endcaps, both the energy (E_{seed}) and the transverse energy (E_{seed}^T) are considered, such that for a crystal to be considered a seed, it must satisfy either $E_{seed}^T > 600$ MeV or $E_{seed}^T > 150$ MeV.

Once the supercluster has been identified, the next step of the electron reconstruction is the track-building stage. Given that the charge of the electron candidate is not known, both positive and

negative charge hypotheses have to be considered, tracing back the position of the supercluster to the nominal PV position by accounting for the magnetic field for both possible scenarios, using the Kalman Filter method. During this back-propagation, compatible hits in the pixel detector are sought, so that, if a pair or triplet of such hits is found, they serve as seeds to build the electron's track. The trajectory is reconstructed by fitting it using a Gaussian Sum Filter (GSF) [127], which approximates the probability density function of electron energy loss described by the Bethe-Heitler theory [128] using a sum of Gaussian functions. Energy losses in the material are also taken into account in this step.

In the final step, the supercluster and track information are merged, allowing for the integration of the energy measurement from the ECAL with the momentum measurement from the tracker. The resulting combination allows for an improvement on the electron energy resolution compared to the measurements from each subdetector separately. This improvement is primarily due to the contrasting behaviour of ECAL energy resolution and tracker momentum resolution, as while tracker resolution generally improves with increasing p_T , ECAL resolution plateaus. Generally, similarly to the results of muon reconstruction explained in Section 5.2.1, it is found that the impact of the tracker is more significant for the reconstruction of low energy electrons, while for more energetic electrons ($E > 15$ GeV) the reconstruction is driven by the ECAL performance. The relative uncertainty in the electron energy is shown in Fig. 5.6 for the two single reconstruction steps in the ECAL and the tracker, as well as for their combination, in the barrel (Fig. 5.6a and endcap (Fig. 4.11b).

Figure 5.6: Relative energy electron resolution versus electron p_T in 2016 simulations, as measured by the ECAL (“corrected SC”), by the tracker, and seen in the E-p combination, for:



Although not specifically used in the analysis presented in this document, we mention for completeness that photons are reconstructed with a similar procedure than the one just described for the electrons. Photon candidates are identified from an ECAL cluster not associated with a GSF track. The classification of electrons and photons in the particle flow global event representation can vary depending on specific analyses, employing different identification techniques.

5.3.2 Electron identification

The variables used to define the WPs for the identification of the electrons [129] can be grouped in several categories:

- ◆ **Calorimeter observables:** These observables take advantage of the distinctive characteristics of electromagnetic showers to differentiate between genuine electrons (either prompt electrons or electrons from photon conversion) and misidentified electrons (mainly hadronic jets with significant electromagnetic contributions). They leverage features such

as the narrower shape of electromagnetic showers compared to hadronic showers, or the transverse shape of showers in the ECAL. Additionally, the fraction of energy deposited in the HCAL and the preshower in the endcaps are considered. Discriminating variables of this type include:

- Hadron-to-electromagnetic energy ratio (H/E): The H/E ratio is characterised as the energy deposited in the HCAL within a cone of radius $\Delta R = 0.15$ around the direction of the superclusters, divided by the energy deposited in the ECAL by the candidate photon or electron.
- The squared variance of the logarithmically weighted distribution of crystal energies along the η direction ($\sigma_{i\eta i\eta}$), which is computed within a 5 by 5 matrix centred on the highest energy crystal within the supercluster, and adjusted to crystal size units. It is defined by:

$$\sigma_{i\eta i\eta} = \sqrt{\frac{\sum_i^{5 \times 5} \omega_i (\eta_i - \bar{\eta}_{5 \times 5})^2}{\sum_i^{5 \times 5} \omega_i}} \quad (5.4)$$

Where η_i and ω_i are the pseudorapidity and a weight factor of the i th crystal; and $\bar{\eta}_{5 \times 5}$ the pseudorapidity mean position.

- ◆ **Tracking observables:** Tracking observables primarily aim to improve the separation between electrons and charged hadrons. They make use of information from the GSF-fitted track associated with the electron candidate. Example tracking observables are:
 - $\Delta\eta$: absolute difference in pseudorapidity between the track and the cluster seed.
 - $\Delta\phi$: absolute azimuthal angular difference between the track’s position and the superclusters’.
- ◆ **Comparison observables:** These observables compare the measurements from the ECAL and the tracker, examining the information obtained from the track-cluster matching, from where a comparison is made between the characteristics of the energy deposits in the ECAL and the properties of the associated track.
- ◆ **Isolation variables:** A significant portion of the background contamination to isolated prompt electrons arises from either misidentified jets or genuine electrons originating from semileptonic decays of a b or c quark inside a jet. In both cases, the electron candidates exhibit a noticeable energy flow in close proximity of their trajectories. In order to define isolation requirements, suitable variables, similar to the ones introduced for the muons, are used to quantify the amount of nearby energy due to charged/neutral hadrons, or photons.
- ◆ **Conversion rejection variables:** These variables are employed to discriminate against secondary electrons originating when a pair of photons produce a e^+e^- pair crossing the tracker material. This type of background is rejected by exploiting the characteristic pattern of hits in tracks from electrons stemming from photon conversions, where the first hit often does not reside in the innermost layer of the tracker, resulting in missing hits in that particular region. On the other hand, prompt electrons originating from the primary interaction, are not expected to have missing hits in the inner layers. In addition, constraints on the transverse (d_0) and longitudinal (d_z) impact parameters are set to ensure that the electron originates from the PV of the interaction.

Two approaches are considered by CMS for the electron identification. The first approach is known as “cut-based” selection, in which several sequential requirements are applied on various variables. The second approach involves a multivariate analysis (MVA), where different variables are combined using techniques such as boosted decision trees (BDT) to achieve improved discrimination between prompt and non-prompt electrons [130]. The MVA-based electron identification is primarily utilised in analyses that require high efficiency even for electrons with low p_T , while maintaining good rejection against non-prompt electrons. One example of such

analyses is the search for Higgs bosons in leptonic final states [131]. In the MVA approach, only two WPs are defined, corresponding to signal efficiencies of 80% and 90% [129]

However, In the analysis presented in this document, electrons are selected using the cut-based identification algorithms, following the recommendations from the CMS EGamma (EGM) POG. This choice is made since the electron's p_T is relatively high, and to prioritise a higher selection efficiency over the purity of the selected electrons, as the latter can be relaxed.

The cut-based approach consists of four basic working points (WP)s, which are defined based on the average identification efficiency and non-prompt rejection. The tight WP, with an average efficiency of approximately 70% and the lowest misidentification rate, is typically used in analyses where background suppression is of special importance. The medium and loose WPs, with median efficiencies of about 80% and 90% respectively, are generally used in scenarios with lower background rates. In addition to these, a fourth working point, the very loose or veto WP, with an average efficiency of 95%, is typically reserved for the third lepton veto requirement. As an example of the requirements used by the cut-based identification WPs, the selection cuts for the tight WP are shown in Table 5.1. The electron identification efficiency as a function of the electron transverse energy for the veto working point is shown in Fig 5.7 [129].

Table 5.1: Electron identification requirements for the cut-based tight working point in the barrel and in the endcaps. Other cut-based working points apply a looser selection on the same variables.

Variable	Barrel (tight WP)	Endcaps (tight WP)
$\sigma_{\eta\eta}$	< 0.010	< 0.035
$ \Delta\eta_{\text{in}}^{\text{seed}} $	< 0.0025	< 0.005
$ \Delta\phi_{\text{in}} $	$< 0.022 \text{ rad}$	$< 0.024 \text{ rad}$
H/E	$< 0.026 + 1.15 \text{ GeV} / E_{\text{SC}}$	$< 0.019 + 2.06 \text{ GeV} / E_{\text{SC}}$
	$+0.032\rho / E_{\text{SC}}$	$+0.183\rho / E_{\text{SC}}$
I_{combined}/E_T	$< 0.029 + 0.51 \text{ GeV} / E_T$	$< 0.0445 + 0.963 \text{ GeV} / E_T$
$ 1/E - 1/p $	$< 0.16 \text{ GeV}^{-1}$	$< 0.0197 \text{ GeV}^{-1}$
Number of missing hits	$= < 1$	$= < 1$
Pass conversion veto	Yes	Yes

5.4 Hadron reconstruction

Once electrons, muons, and isolated photons are identified, the remaining particle candidates in the event are classified as hadrons. Hadrons can be either neutral (e.g. neutrons or π^0), or charged (e.g. K^\pm , π^\pm , or protons). At this stage, non isolated photons need also to be reconstructed, as they typically arise from neutral hadron decays, such as π^0 .

As presented in Fig. 5.1, neutral hadrons and photons are expected to only leave a deposit in the calorimeters. Therefore, their reconstruction starts with energy clusters in the ECAL and HCAL that do not correspond to any track in the tracker system. Typically, HCAL clusters are associated with neutral hadrons, whereas ECAL clusters are associated with photons, since it is found that within the tracker acceptance ($\eta < 2.5$), approximately 25% of the energy of hadronic jets is deposited in the ECAL by photons, compared to the 3% of the energy that is deposited by neutral hadrons. On the other hand, outside the tracker acceptance, charged and neutral particles become harder to distinguish, because of the absence of tracks. In such cases, ECAL clusters linked to a specific HCAL cluster are assumed to originate from the same hadron shower, and the particle is reconstructed as a charged or neutral hadron. If no such link exists, the ECAL cluster is classified as a photon.

In order to identify energy deposits from neutral hadrons when they overlap with charged hadron deposits, particle identification relies on an accurate calibration of the calorimeter system. If the

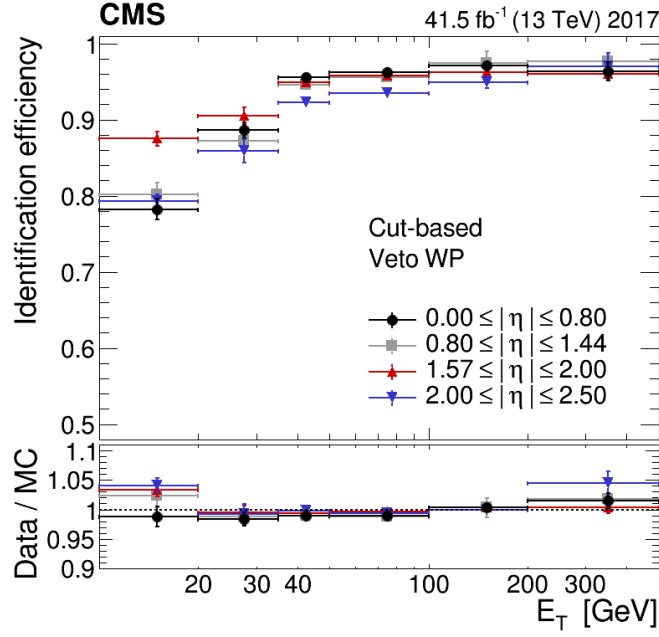


Figure 5.7: Electron identification efficiency measured in data (top panel) and efficiency ratios between data and simulation (bottom panel), as a function of the electron transverse energy E_T , for the cut-based identification veto working point. The vertical bars on the markers represent combined statistical and systematic uncertainties.

calibrated calorimetric energy exceeds the sum of all associated charged particle track momenta by an amount greater than the expected calorimeter energy resolution for hadrons, the excess of energy is attributed to a neutral hadron or a photon. Conversely, if the calorimetric energy is compatible with the sum of all charged particle track momenta, it is assumed that no neutral particles have been produced. Finally, it is possible that the calibrated calorimetric energy is smaller than the sum of all track momenta. If this difference is small (a few standard deviations), it may indicate the presence of muons that were not previously identified. This redundancy of measurements in the tracker and calorimeters allows for the discovery of additional muons previously not identified, while not significantly increasing the misidentified muon rate. If instead this difference is significantly larger, it suggests the presence of tracks with poorly reconstructed p_T . This scenario is addressed by storing the tracks in decreasing order of p_T uncertainty and sequentially removing them from the total sum of track momenta until the compatibility of the total calibrated energy is restored, or a calorimeter energy excess is observed, thereby falling back to one of the two situations described earlier.

5.5 Jet reconstruction

One common feature of high energy collisions in hadron colliders is the production of hadronic jets. The arising of these objects is a direct consequence of the colour confinement already discussed in Section 2.1.2. For a very high energetic parton produced in proton-proton collisions, colour confinement leads to the production of a shower of particles, which are collimated, i.e. travelling in approximately the same direction of the original parton.

The correct reconstruction of the jets is a complex process, as it needs to be infrared and collinear safe, such that low energetic or collinear partons do not affect the stability of the reconstruction. The jet reconstruction algorithm currently used at CMS, which satisfies both conditions, is known as the anti-kt algorithm [132], and works by taking all the reconstructed PF particles' four momentum and computing the distance parameter between a particle i and another particle j (d_{ij}), as well as the distance parameter d_{iB} between the particle i and the beam B :

$$d_{ij} = \min \left(\frac{1}{p_{T_i}^2}, \frac{1}{p_{T_j}^2} \right) \frac{\Delta R_{ij}^2}{R^2}, \quad d_{iB} = \frac{1}{p_{T_i}^2} \quad (5.5)$$

Where R_{ij}^2 is the distance between the two PF particles in the $\eta\phi$ plane, and R the radius parameter, defined in this plane, which is typically chosen to be $R = 0.4$ at CMS for a standard jet, while other jets can require higher values (for instance, the jets with a wider radius parameter $R = 0.8$, known as *fat* jets, are utilised in the study of event final states with boosted topologies [133]).

Particularly, the algorithm works by merging all PF particles with $d_{ij} < d_{iB}$ to a jet, and removing from them the list of PF particles, repeating this process until only jets are present in the event, subsequently calculating the jet momentum as the sum of the momenta of all particles associated to it. This strategy helps to reduce the impacts of misreconstruction, detector response variations, and pileup effects, the jet energy response.

In addition to that, in order to account for inaccuracies in the way the raw jet energy measured in the detector represents the initial energy carried by the hadronising parton, a set of corrections, known as jet energy correction (JEC), have been developed by the CMS Collaboration. This approach follows a factorised procedure, consisting of three main levels of corrections, each applied sequentially in a fixed order, targeting specific effects associated with the jet's four momentum components. Each level of correction addresses distinct sources of energy mis-measurement:

- ◆ **Level 1 correction:** Also known as the offset correction, it subtracts the energy that is not associated with the high- p_T scattering, including contributions from pileup interactions (secondary proton-proton collisions in the same bunch crossing) as well as electronic noise.
- ◆ **Level 2 correction:** It aims to correct for the dependence of the jet response on p_T and η , taking as reference the centre of the barrel. This step attempts to correct for effects produced by non linearities in the calorimeter response, p_T thresholds, or geometric effects of the detector. They are generally referred to relative or MC corrections, given that these type of corrections are performed using simulations.
- ◆ **Level 3 correction:** Known as the residual or absolute correction, it accounts for the remaining differences, or residuals, between the average response of the jet energy scale (JES) in MC events and the JES measured in data. This correction is exclusively applied to data, ensuring the calibration is accurately tailored to the experimental conditions.

Once the JES are applied, the MC simulations undergo jet energy resolutions (JER) adjustments to match actual data. For simulations, the JER is estimated by fitting particle-level response with a Gaussian across varying PU scenarios. For Run II, typical scale factors range between 10-15%, and are higher in transition regions [134].

For the analysis presented in this document, only the corrected jets are utilised. Simulation studies indicate that, on average, the reconstructed jet momentum is within 5 to 10% of the true momentum across the entire p_T range and detector acceptance.

5.5.1 Heavy flavour jet identification

In addition to the general information about the jet, such as the total p_T of the particles, it is often important in LHC analyses to know the flavour of the original quark that produced the jet. Heavy-flavour jets (coming from the b and c quarks) are of particular importance when performing a search for new physics, as BSM models generally predict that new physics will be paired with heavy quarks. This identification is possible for all quarks but the top quark, as

it has a very short lifetime, and hence decays prior to any significant hadronisation. However, since the top quark decays mostly to a b quark and a W boson, b-tagging is a fundamental part of analyses that study events with top quarks, as is the case of the analysis presented here, as already presented in the Section 7.1.

To identify the original parton flavour of the jets, dedicated identification algorithms take advantage of the distinct properties of the heavy hadrons compared to lighter ones. For instance, hadrons containing a b quark have lifetimes on the order of $\tau \sim 1.5$ ps, while hadrons containing a c quark have a lifetime of approximately $\tau \leq 1$ ps. Due to their long lifetimes, heavy-flavour hadrons in b or c jets undergo displaced decays, resulting in the presence of displaced tracks with large impact parameters originating from secondary vertices (SV). Fig. 5.8

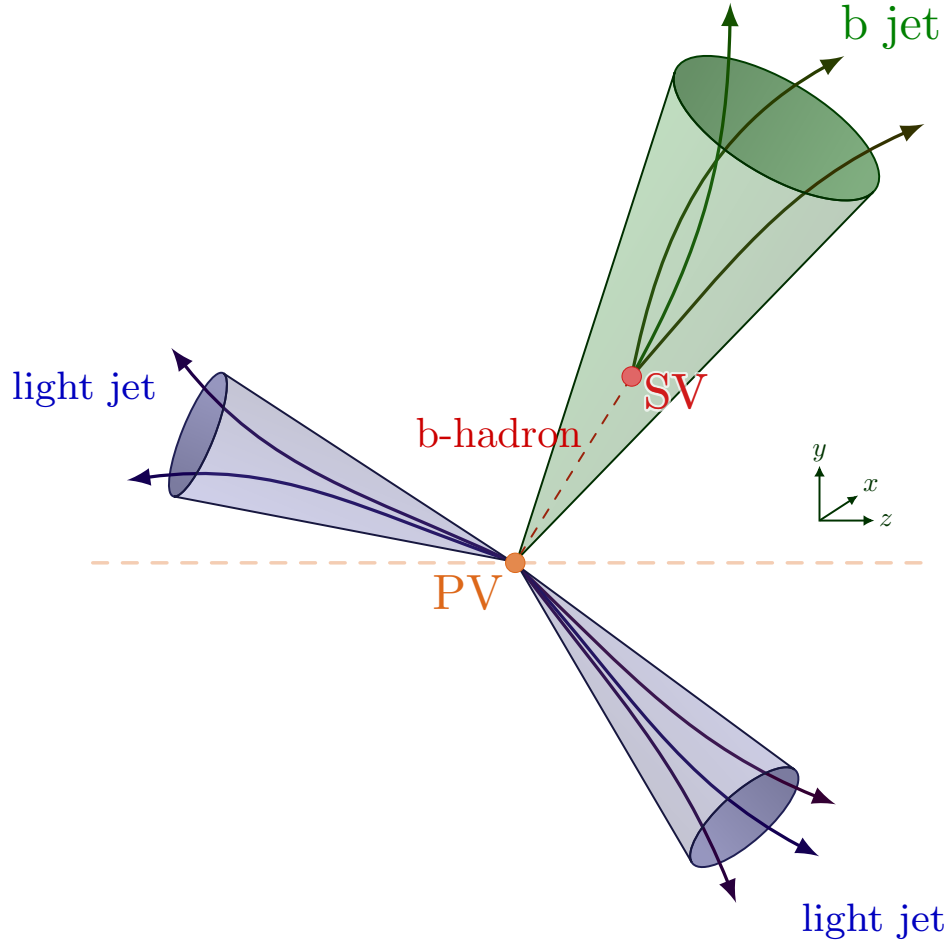


Figure 5.8: Schematic representation of the differences between b-jets compared to lighter jets.

Furthermore, heavy-flavour quarks have larger masses and harder fragmentation compared to light quarks and massless gluons. As a result, the decay products of heavy-flavour hadrons tend to have, on average, high p_T relative to the jet axis compared to other constituents of the jet. Another important characteristic is the presence of soft electrons or muons, as they can be produced via semi-leptonic decays of heavy-flavour hadrons. Approximately a muon or an electron is detected in the decay of a b (c) hadron in 20% (10%) of the cases.

Therefore, the properties of secondary vertices, the large impact parameter of displaced tracks, the presence of charged leptons inside the jet, and the p_T of the jet constituents relative to the

jet axis are useful features to discriminate between jet flavour. In order to exploit this information, various variables are constructed, using objects such as tracks, primary and secondary vertices, or isolated leptons. These variables form the basis for the discriminating observables that reflect the properties of heavy-flavour jets, and therefore an important component of the identification algorithms that calculate a single discriminator value for each tagged jet. Depending on the chosen threshold for this value, different operating points can be defined with specific misidentification probabilities for light jets.

Several algorithms to combine the information from the discriminating observables into a single discriminator value are currently used by the CMS Collaboration, continuously enhancing the identification efficiency for b and c jets [135]. Some of the most effective b taggers used in LHC Run I and Run II are described below:

- ◆ Jet probability (JP): Employed in both Run I and some early Run II analyses, this algorithm calculates its discriminator value by assuming that all tracks associated with the jet originate from the primary vertex, using a track probability measured in inclusive jets as a function of the track impact parameter significance.
- ◆ Combined secondary vertex (CSV): Utilised solely in Run1, this tagger is built by combining properties of secondary vertices, such as flight distance significance and vertex mass, with track-based lifetime information. Two likelihood ratios are derived from these variables, one to discriminate against c and another to discriminate against light-flavour jets.
- ◆ Combined secondary vertex version 2 (CSVv2): This algorithm, used in the early stages of Run II was built upon the CSV algorithm from Run1, incorporating a larger number of variables by utilising the secondary vertex and track-based lifetime information within a neural network (NN).
- ◆ Combined multivariate algorithm version 2 (cMVAv2): This algorithm, developed for Run II, taking the Run I cMVA algorithm as a base, combines information from six distinct b jet identification discriminators, including JP, CSVv2, and other simpler taggers, using a BDT.
- ◆ DeepCSV: Defined as a further extension of the CSVv2 algorithm, inherits its fundamental features, while utilising a deep neural network (DNN) instead of a simpler NN to combine all variables, including the information on up to six charged particle tracks. This algorithm has been extensively used by multiple analyses targeting the full Run II dataset, including the one hereby presented.

With respect to the newly developed jet identification algorithms, a special mention needs to be given to the DeepJet tagger, whose main difference with respect to the DeepCSV algorithm is the inclusion in the training of a much larger number of variables, subsequently improving the performance of the algorithm [136]. This tagger is therefore expected to be favoured by new analyses based on data collected during the Run III along with two other algorithms, named ParticleNet and PartT, respectively [137, 138]. Specifically, ParticleNet employs graph neural networks while PartT uses transformer models, which enables them to process low-level particle information directly and therefore enhance jet tagging performance over the traditional deep learning approaches used in Run II.

In order to assess the behaviour of a heavy-flavour tagger, simulated event samples from QCD processes and $t\bar{t}$ production are used. Two numbers are typically used for that purpose: the efficiency and the misidentification probability. The efficiency is measured as the ratio of the number of correctly identified jets with a specific flavour to the total number of jets with that flavour. Similarly, the misidentification probability refers to the likelihood of jets from any flavour other than the one of interest being incorrectly identified as jets of that particular flavour. For instance, the misidentification probabilities for c or light flavour jets compared to the b

jet identification efficiencies at 13 TeV, using the running conditions of 2016 for several jet identification taggers is shown in Fig. 5.9.

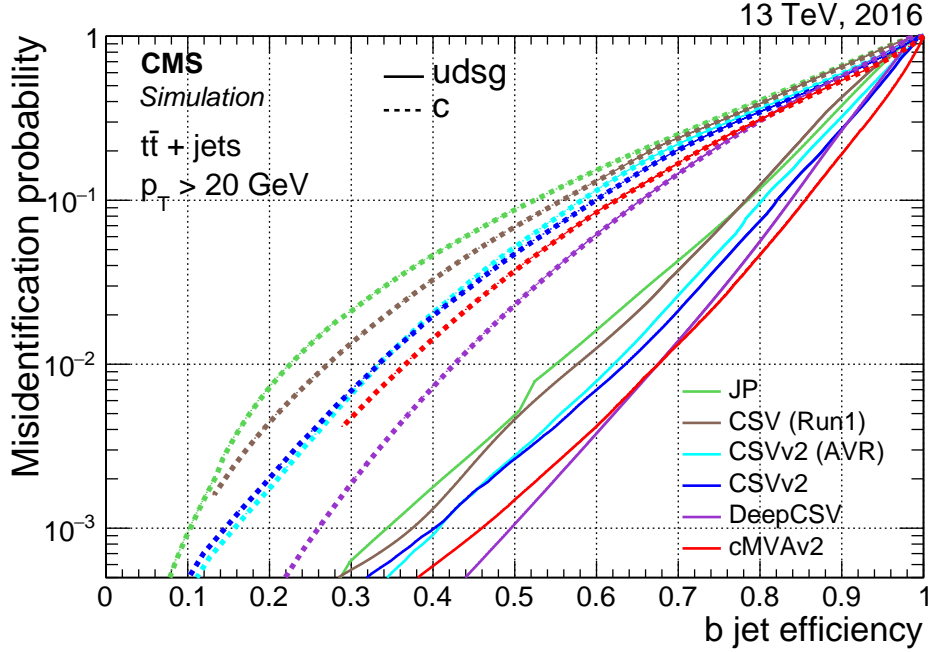


Figure 5.9: Misidentification probabilities for c and light jets versus b jet efficiency for several jet taggers. The performance curve for c jets is shown in dashed, while the one for light jets is shown in solid lines.

Jets selected to assess the performance of heavy-flavour identification algorithms are required to have $p_T \geq 20$ GeV and $|\eta| < 2.4$. The DeepCSV algorithm exhibits superior discrimination against c and light-flavour jets for b-tagging efficiencies below 70%, while the cMVA v2 tagger performs better against light jets for efficiencies above 70%. Both algorithms improve the performance of CSVv2 by approximately 3% for a 1% misidentification rate of light jets, reaching b-tagging efficiencies of up to 67%.

For each b-tagging algorithm, three standard operating points (loose, medium, and tight) are defined, based on simulated multijet samples. For a jet with a p_T of 75 GeV, these working points correspond to different misidentification probabilities for light jets (approximately 10%, 1%, and 0.1% for loose, medium, and tight, respectively). In the analysis hereby presented, the identification of jets originating from bottom quark hadronisation is done using the DeepCSV algorithm at the medium operating point, resulting in a b jet identification efficiency ranging from 50% to 70% for jets with p_T between 20 and 100 GeV. The misidentification rate for light quark and gluon jets falls to around 1% within the same p_T range.

5.5.2 Tau lepton reconstruction

Finally, the only lepton whose reconstruction has not previously been described is the τ lepton. As discussed in Section 2.1, the τ lepton cannot be observed directly at CMS, given its short lifetime. Although τ leptons can decay leptonically into charged leptons (electrons or muons) and their associated neutrinos (with a branching fraction of approximately 35% [48]), their relatively large mass causes most of the decays to be hadronic, primarily to pions. These particles, if sufficiently energetic, can undergo hadronisation and form a jet. In such cases, the discrimination of τ -jets is performed based on criteria such as multiplicity, collimation, and isolation of the decay products [139].

5.6 Missing transverse momentum

Recalling the fundamental particles that form the SM, presented in the Chapter 2 and illustrated in Fig. 2.1, the only fundamental particle whose reconstruction has not been discussed in this chapter is the neutrino. This is not casual, but instead originates from the fact that the neutrino interact weakly with matter, and hence does not leave any hits in the tracker nor energy deposits in the calorimeter. The presence of neutrinos (or any other weakly interacting particles, such as the neutralinos discussed in Chapter 3) in an event can be detected taking advantage of the fact that the sum of all particles' transverse momentum (p_T) should be zero. One can then define a variable, the transverse momentum imbalance (p_T^{miss}), as the vectorial sum of all the N reconstructed particles in the event:

$$p_T^{\text{miss}} = - \sum_i^N p_T^i \quad (5.6)$$

which is interpreted as a measure of the sum of the momenta of all the weakly interacting particles in the event. A schematic representation of a typical CMS event with two jets and p_T^{miss} is shown in Fig. 5.10.

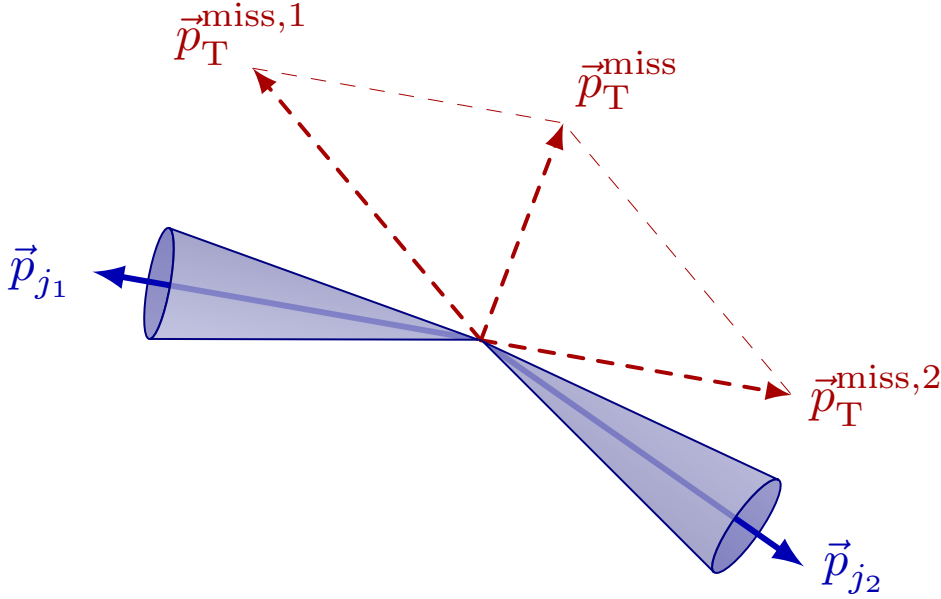


Figure 5.10: Example of the calculation of the missing transverse momentum in an event with two jets.

Several techniques to estimate the p_T^{miss} for each event have been developed over the years [140, 141]. In the analysis hereby presented, the approach employed utilises the PF reconstruction algorithm to calculate p_T^{miss} , which propagates all the JEC previously discussed in Section 5.5 into the p_T^{miss} . Therefore, obtaining an accurate estimation of p_T^{miss} relies on precisely identifying these physics objects, and the uncertainty of the estimation heavily depends on the event's topology.

Chapter 6

Monte Carlo simulated samples

As it has just been discussed in the previous chapter, the reconstruction of particles is a very intricate task, and even with the extremely refined algorithms currently in place, particle identification is not perfect. What is more, even if they were, as discussed in Section 5.6, particles like the neutrino effectively do not interact with the CMS detector, rendering them inseparable from one another. In addition to that, from a more theoretical perspective, one of the fundamental features of quantum physics in general, and QFT in particular, is the statistical nature of the observations. This redounds in the impossibility of knowing with certainty the original particle produced given the information reconstructed in the detector.

Therefore, in order to test a hypothesis such as the search of supersymmetric particles presented in this document, data needs to be compared with a statistically calculated theoretical prediction. In the high energy physics field, this simulation is typically performed using what are known as Monte Carlo (MC) methods. These methods, as a sharp reader may have guessed, share its name from the principality of Monaco, since these kinds of simulations share many of the random elements that characterise the events happening in a casino. MC simulations trace their roots to the 1940s, with the first model being published in 1949 [142]. Nowadays, MC methods have outgrown its initial physical niche, being commonly used in fields from engineering to finance [143].

Monte Carlo simulations are particularly useful when studying the LHC physics, given the intricate nature of proton-proton collisions discussed in Chapter 2 of this document. In this way, the usage of MC simulations enables analysts to properly characterise and constrain the backgrounds, and provides with an idea of how the expected signal would look like, all while aiding to estimate possible uncertainties in the model.

This chapter is divided in two sections. Section 6.1 portrays the way the Monte Carlo event generator works at the CMS Collaboration, explaining each of the steps required for the generation of a simulated sample, as well as the storage structure employed by the CMS Collaboration, while Section 6.2 presents a brief discussion of the corrections used to match the simulation to data.

6.1 The Monte Carlo event Generator

The Monte Carlo method [142] is based on the generation of (pseudo)random number that reproduce the probability density functions for various observable quantities, defined by the equations

describing the specific processes. This allows the generation of a large number of events. To perform this task, software tools, known as *event generators*, are used. These programs go through several steps to provide an accurate description of the simulated events:

- 1) The first step involves simulating the hard scattering between partons for the selected process, including the decay of unstable particles within the detector volume.
 - 2) Next, the underlying events are simulated. These events arise from secondary interactions between the remnants of the incoming protons.
 - 3) Once the underlying event is generated, the parton showering is simulated, which involves the emission of coloured particles.
 - 4) Finally, the hadronisation process converts the parton showers into outgoing hadrons.
- ⊕ Once the generation of the physics event is complete, it is crucial to simulate the passage through the detector of all final-state particles. This step accounts for the simulation of the observed hits in the tracking system and energy deposits in the calorimeter, creating an event format that allows for comparison with real data. The interaction of particles with the detector material, including multiple scattering and energy losses, is considered in this simulation step. Two commonly used packages for simulating particle interactions with the detector are GEANT4 [144], which provides a detailed description of particle-material interactions, and DELPHES [145], which offers a parameterised simulation for faster processing.

A schematic representation of each of the steps is presented in Fig 6.1. In the rest of this section,

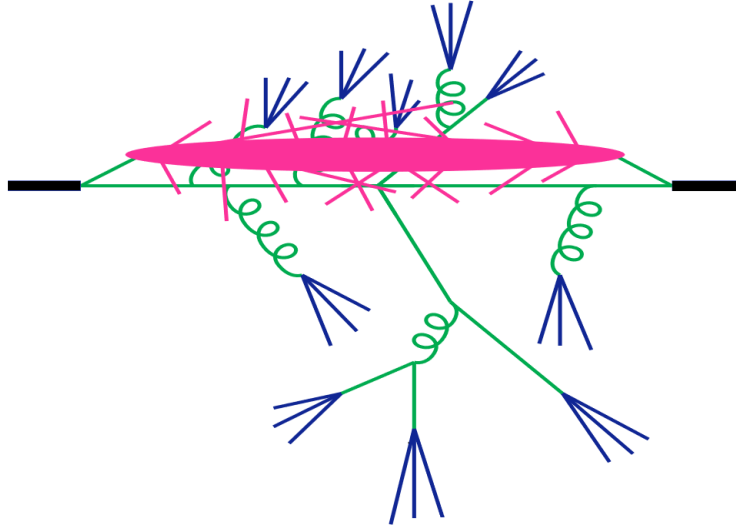


Figure 6.1: Diagram showing the structure of a proton-proton collision, with each of the colours representing a different stage of the Monte Carlo event generator [22]. The hard process is represented in black, with the pink blob representing the underlying events. The parton shower is shown in green, while the hadronisation is shown in blue.

a more extensive overview of these steps is presented.

6.1.1 Hard Scattering

As it was previously mentioned, the MC simulation first step is to simulate the hard scattering. This process leads to the production of events of interest, where both heavy mediator particles, and energetic particles in the final state are present. and is opposed to the underlying event, generally labelled as soft scattering. This process thus occurs when two partons a and b within

the protons collide, and can be described by the parton-level cross section $\sigma_{ab \rightarrow X}$, which can be connected to the hadronic cross section $\sigma_{h_1, h_2 \rightarrow X}$, with h_1 and h_2 corresponding to the incoming protons. The relationship between these two cross sections is determined by the parton distribution functions (PDFs) and can be expressed by the following equation:

$$\sigma_{pp \rightarrow X} = \sum_{a,b} \int_0^1 dx_a dx_b \int f_a^{h_1}(x_a, \mu_F) f_b^{h_2}(x_b, \mu_F) d\hat{\sigma}_{ab \rightarrow X}(\mu_F, \mu_R) \quad (6.1)$$

Where all the possible partons are being summed, given their longitudinal momentum fractions x_a and x_b , and the protons PDFs $f_a^{h_1}(x_a, \mu_F)$ and $f_b^{h_2}(x_b, \mu_F)$. Similarly, the production cross section can be expressed in terms of the perturbative QCD theory, that is, in terms of the renormalised couplings $\alpha_s(\mu_R^2)$, being μ_R^2 a given renormalisation scale, such that the normalisation Eq. 6.1 can be rewritten as:

$$\begin{aligned} \sigma_{p_1 p_2 \rightarrow X} = \sum_{H=0}^{\infty} \alpha_s^n(\mu_R^2) \sum_{ab \in \{q,g\}} \int dx_a dx_b f_{a,p_1}(x_a, \mu_F^2) f_{b,p_2}(x_b, \mu_F^2) \\ \times \sigma_{ab \rightarrow X}^n(x_a x_b s, \mu_R^2, \mu_F^2) + \mathcal{O}\left(\frac{\Lambda^2}{M_X^4}\right) \end{aligned} \quad (6.2)$$

Where $\mathcal{O}\left(\frac{\Lambda^2}{M_X^4}\right)$ accounts for other non perturbative contributions. It must be mentioned that while, traditionally, cross-sections were calculated at leading order (LO), newer MC generators are also capable of including higher order interactions, including loops. These calculation levels are known as next-to-leading order (NLO), or even next-to-next leading order (NNLO). Other corrections may include correcting for soft gluon terms, which are typically handled in next-to-next-to-leading logarithm order (NNLL). Examples of generators that can handle higher order calculations include MADGRAPH [146], POWHEG [147], aMCNNLO [148] Sherpa [149] .

6.1.2 Underlying events

As already discussed in the Section 4.2.2, besides the hard scattering process, other secondary interactions between the proton remnants may exist, known as the *underlying* interactions or events (UE). These events include contributions from multiple parton interactions (MPI), where additional parton pairs from the colliding protons undergo soft or semi-hard scatterings. Other contributions to the underlying events include beam-beam remnants (the remnants of the protons after the collision), as they typically emit gluons and quarks before and after the hard interaction. Properly accounting for the underlying event is essential as it affects observable quantities such as particle multiplicities, energy deposits in calorimeters, and the reconstruction of jets and missing transverse energy.

Monte Carlo event generators such as PYTHIA [150] and Herwig [151] are employed to simulate the UE at the CMS Collaboration. These generators utilise sophisticated models to represent MPI, as well as the initial and final-state radiation (ISR and FSR, respectively). The parameters governing these models are not precisely predicted by theory and therefore require tuning to experimental data. CMS performs dedicated UE measurements in various kinematic regimes to obtain distributions of UE-sensitive observables, such as the p_T or the angular distributions of charged particles. This way, distributions between data and simulation are compared, and thus the parameters within the event generators are adjusted, ensuring that the simulated UE closely matches the observed characteristics in the experimental data, thereby improving the reliability of the Monte Carlo simulations for both SM measurements and searches for new physics phenomena.

6.1.3 Parton Showering

As outlined when presenting the fundamental elements of the SM in Section 2.1, coloured particles cannot exist in isolation. Instead, since collisions at the LHC are produced at very large energies ($\sqrt{s} = 13$ TeV during the Run II data taking period), resulting particles are very energetic, and thus, a portion of their energy is converted into cascades of additional coloured particles (either gluons or quark-antiquark pairs). This process continues until the energy becomes too low to produce more particles, at which point the newly produced particles combine with each other to form colourless hadrons, in a process known as hadronisation, also discussed in Section 5.5.

Accurately modelling the parton showering at the CMS detector is essential for simulating realistic collision events, as it directly influences the reconstruction of jet properties and the discrimination between signal and background processes. For such tasks, advanced Monte Carlo generators are used, including PYTHIA [150] and Herwig [151], which incorporate sophisticated algorithms to simulate these showers, ensuring that the theoretical predictions align closely with the complex phenomena observed experimentally.

6.1.4 Hadronisation

As mentioned in the previous step, the partons produced via the parton showers cannot exist freely, due to the phenomenon of colour confinement in QCD (see a more detail discussion of this topic in Section 2.1.2 of this document). Instead, they transform into colour-neutral hadrons, in a process known as called hadronisation. As for the previous steps, the MC generators used to study hadronisations are mainly PYTHIA [150] and Herwig [151]. The former simulates the hadronisation process using the Lund string model [152], in which quarks are bound together by a gluon string; whereas the latter models the resulting hadrons are grouped in clusters, in a process known as clustering [153].

6.1.5 Pile-Up Generation

To fully simulate an event, the occurrence of secondary interactions (pile-up) overlapping to the primary one has to be taken into account. This is done by generating a set of minimum-bias interactions according to the pp inelastic cross section, and superimposing a certain number of them to each event, in such a way as to reproduce the expected distribution of pile-up interactions in data. Fig. 4.3 shows these distributions for the Run II data taking. In order to improve the accuracy with which the pile-up distribution in the simulation models the one in data, weights are applied to the simulated events to match the pile-up distribution actually observed in data.

6.1.6 Monte Carlo simulation structure at the CMS experiment

In addition to simulating the primary proton-proton (pp) interaction, simulated data samples need to also incorporate the conditions of the detection apparatus, to ensure an accurate modelling of real data samples. This entails not only a comprehensive simulation of the pp hard scattering process but also of the response of the detector. For this purpose, two different types of simulation can be distinguished:

- ◆ **Full simulation (FullSim):** The full simulation is based on the GEANT4-based detector simulation [144], encompassing the modelling of the CMS detector's geometry and behaviour, including the generation of hits in the sensitive devices, configuration, calibration, and replication of the detector electronics response. It also incorporates the magnetic field map from the 3.8 T solenoid, so that the magnetic field effects are accurately replicated. This approach is followed to generate the samples that simulate the SM processes that constitute the main backgrounds in the analysis presented in this document.
- ◆ **Fast simulation (FastSim):** FastSim adopts a parametric approach to simulate and reconstruct events within the CMS detector, aiming to reduce the CPU time required for simulation while still maintaining an accurate representation of the detector effects.

It achieves this by employing simplified models and approximations, allowing for faster event processing without compromising the overall simulation quality. This type of sample simulation is typically used for processes from new physics models where one or more theoretical parameters are unknown, and the generation of a large number of subsamples is therefore needed to scan an appropriate range of physically sensitive parameter values. In the analysis presented in this thesis, (FastSim) is used to simulate signal events from multiple (SUSY) models, exploring a large range of mass hypotheses for the supersymmetric particles involved.

The information on the simulated physics event thus produced is stored in a data format organised on several levels:

- 1) **GEN**: Represents the information on the physical properties of the generated particles
- 2) **SIM**: At this level, GEN particles are propagated through a detailed simulation of the CMS detector, modelling the interactions of particles with the detector materials, creating a collection of simulated hits, or energy deposits for each part of the detector.
- 3) **DIGI**: Involves the conversion of SIM hits into the detector's response.

At this point, the simulated data structure is essentially equivalent to the RAW output recorded by the detector in real proton-proton collisions, and the same event reconstruction outlined for collision data in Section 4.4.1 can be applied.

6.2 Monte Carlo Corrections

The reconstruction of physics objects at the CMS Collaboration can be affected by various factors. The sub-detectors may have blind spots, dead zones, or cracks, while the triggering algorithms might utilise only a partial amount of the available information due to time and/or storage limitations. These factors can result in inefficiencies in trigger selections and in the reconstruction and identification of physics objects. The CMS Collaboration has appointed several physics object groups (POGs) to measure the performances of the object reconstruction in data and to provide scale factors to adjust the performance in MC simulations correspondingly. However, some corrections depend strongly on the event selection, and need to be derived on an analysis-by-analysis basis. For the search object of this thesis, I derived dedicated trigger efficiencies and lepton identification scale factors, presented in the Appendices B.2 and C, respectively. Another set of corrections I developed for the analysis is used to adjust the reconstruction efficiencies in FastSim samples to the one observed in FullSim samples, as discussed in Appendix D.

In addition to the performance measurement, another important task of the POGs is to validate the reconstruction of all the fundamental observables both in data and MC samples. This process is called commissioning and during my PhD I have contributed to its implementation within the group charged of the development of the algorithms for the identification of heavy-flavour jets. This work was based on data collected during the Run III data-taking period, and the first results have already been made public in [154]. In the following, I will present the results to which I contributed directly, namely the study of the Drell–Yan (DY) production in association with jets.

6.2.1 Commissioning of b-tagging variables in Drell–Yan+Jets events

As already mentioned, jets originating from heavy-flavour hadrons are identified using information from charged particle track reconstruction and secondary vertices within these jets. It's vital to test how well simulations reproduce data for kinematic variables that influence the behaviour

of heavy-flavour tagging algorithms. As LHC Run III began, the CMS experiment implemented new track reconstruction techniques and adjusted data collection conditions. In this section, a comparison of early Run III data with simulations for various kinematic variables in four samples enriched in b-quark, c-quark, and light (udsg jets) jets is presented. In particular, 7.65 fb^{-1} of early 2022 data have been used.

In this document, a dataset dominated by Drell–Yan +jets events is presented. These events are characterised for being rich in light jets, thus allowing for a test of misidentified jet modelling [155, 156]. A di-muon trigger path to select $Z \rightarrow \mu\mu$ events is used to collect the data. The primary muon has $p_T > 15 \text{ GeV}$, while the secondary one requires $p_T > 12 \text{ GeV}$. Both muons must meet the condition $|\eta| < 2.4$ and satisfy the strict identification and isolation requirements [157]. The di-muon system is required to have an invariant mass within 10 GeV from the Z boson mass, and $p_T > 15 \text{ GeV}$. There must be at least one jet with $p_T > 20 \text{ GeV}$ and $|\eta| < 2.5$, meeting stringent identification criteria, and sufficiently separated from the selected muons, with a separation of $\Delta R(\text{jet}, \mu) > 0.4$. A comparison of observed and simulated distributions is shown in Fig. 6.2 for some jet kinematic variable and b-tagging discriminator and in 6.3 for few track and vertex observables.

Figure 6.2: Observed and simulated distributions in Drell–Yan +jets events. Left: Jet p_T (top), and η (bottom). Centre: Reconstructed Z bosons’ p_T (top) and η (bottom). Right: DeepJet discriminant of the first jet against b-jets (top) and c-jets (bottom):

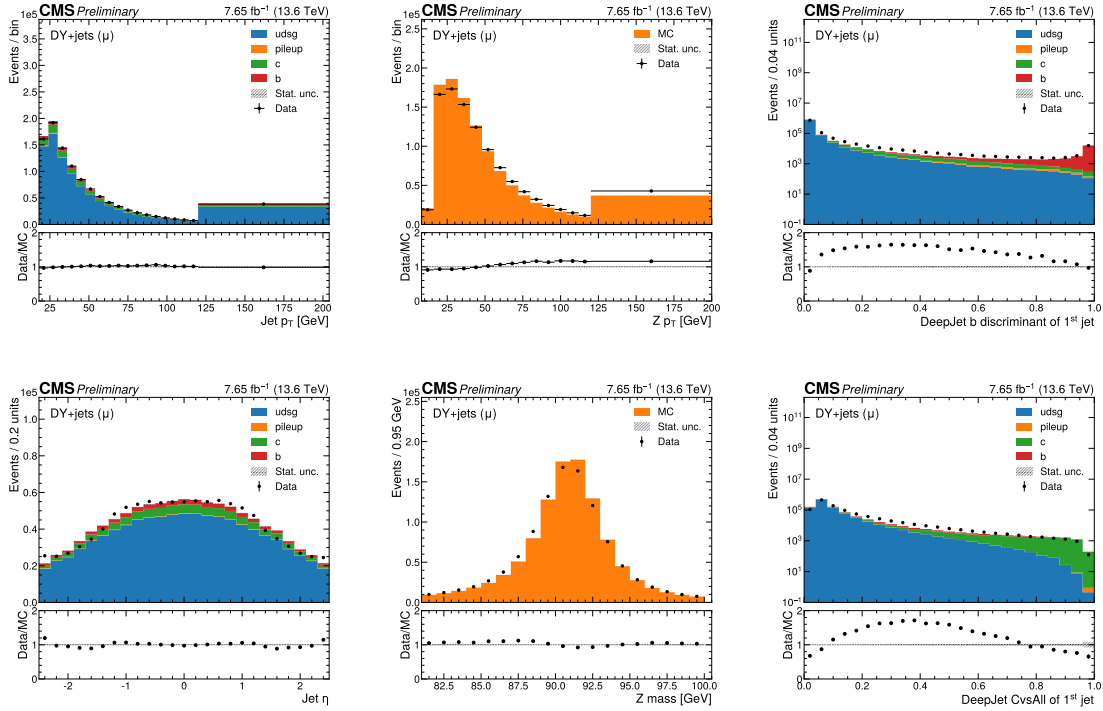
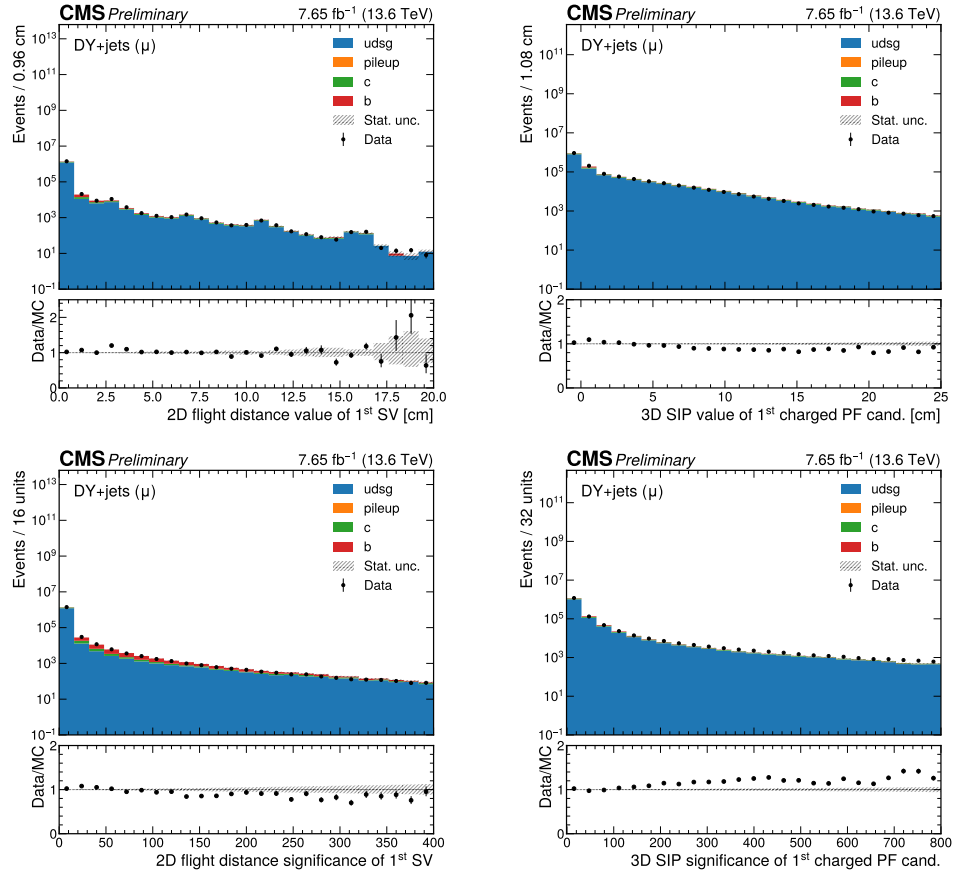


Figure 6.3: Observed and simulated distributions in Drell-Yan +jets events. Left: Measured distance a particle travels in the transverse plane (2D flight distance) for the most energetic secondary vertex SV (top) and its significance (bottom). Right: Measured distance a particle travels in the 3-D space (3D impact parameter) for the most energetic charged PF particle (top) and its significance (bottom):



Chapter 7

Supersymmetric models and main backgrounds

In the previous chapters, a general introduction to the theoretical framework and the experimental setup of the search object of this thesis has been presented. In this chapter, a closer look is given to the main components of the analysis, namely the signal models considered and their main backgrounds. This chapter is divided in three sections. Section 7.1 gives a more detailed description of the SUSY signal models considered in this search. Section 7.2 discusses the main background processes contributing to the SRs, from a theoretical perspective, while Section 7.3 provides the reader with a description of the samples used in the analysis presented in this document. A description of how the event selection is optimised to maximise the sensitivity to the signal production and how the modelling of the backgrounds is validated is instead presented in Chapter 8

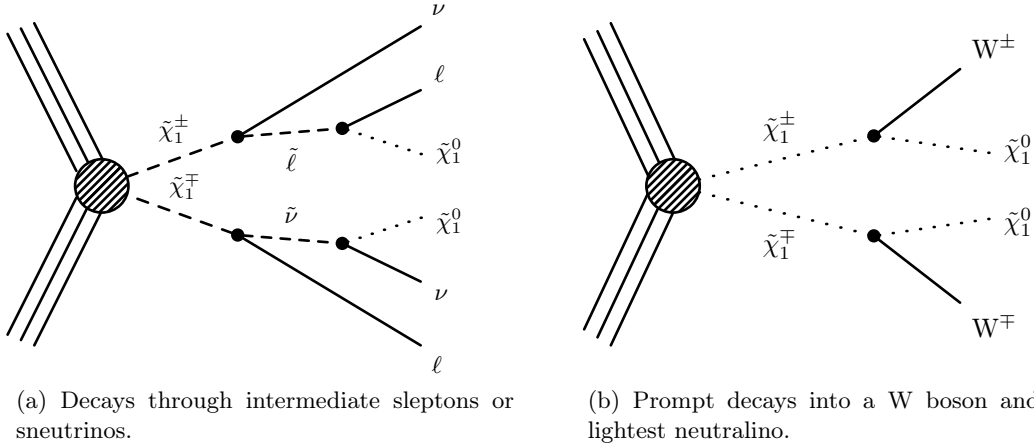
7.1 Direct search for supersymmetric particles in this document

This section presents a search for the production of pairs of supersymmetric particles in final states with two oppositely charged (OC) leptons (ℓ), considering electrons (e) and muons (μ). These models, assume R-Parity to be conserved, causing the LSP, in this case the lightest neutralino ($\tilde{\chi}_1^0$), to be stable, and whose p_T adds to the p_T^{miss} produced by the SM neutrinos. Therefore, the production of supersymmetric particles in all these models should result in events with a large amount of missing transverse momentum (p_T^{miss}). The production of three types of SUSY particles are considered: The lightest chargino ($\tilde{\chi}_1^\pm$), top squark (\tilde{t}_1) and slepton ($\tilde{\ell}$), all produced in pairs. In such models, given that both the mass of the pair produced supersymmetric particle and the LSP mass are unknown, several mass hypotheses are considered for each particle. This way, each mass hypothesis is known as a mass-point.

Two different decay scenarios are considered for the chargino pair production: as a reference, a model where the charginos decay into a lepton, a neutrino (ν), and the lightest neutralino ($\tilde{\chi}_1^0$) via an intermediate charged slepton ($\tilde{\chi}_1^\pm \rightarrow \nu \tilde{\ell} \rightarrow \nu \ell \tilde{\chi}_1^0$) or sneutrino ($\tilde{\chi}_1^\pm \rightarrow \ell \tilde{\nu} \rightarrow \ell \nu \tilde{\chi}_1^0$) is considered. In this model, shown in the Fig. 7.1a), the three generations of sleptons are assumed to be degenerate, with a mass equal to the average of the chargino and neutralino masses. The branching fractions (\mathcal{B} 's) of the chargino decays into charged sleptons or sneutrinos are assumed to be equal. In addition to that, results are also interpreted in terms of a second model (Fig. 7.1b), where each chargino decays into the lightest neutralino and a W boson.

Searches for chargino pair production have been previously published by the CMS Collaboration in the context of the first scenario using $\sqrt{s} = 8$ TeV collision data [158] as well as using $\sqrt{s} = 13$ TeV collision data. In this energy regime, two analyses were published, the first of them used 2016 data with 36.3 fb^{-1} [44], and is the precursor of the analysis presented in this document, while the second targeted events with no leptons using the full Run II data set 138 fb^{-1} [159], being thus complementary to the analysis here presented. The ATLAS Collaboration probed for the production of a pair of charginos in the context of both considered scenarios using 8 TeV [160, 161, 162] and 13 TeV using 2016 collision data [163, 164, 165] as well as the full 2016–2018 collision data [166, 167, 168, 169, 170], also performing a combination of several analyses probing the model where the chargino decays via W bosons [171], also summarised in a physics report reuniting the main SUSY performed using the full 2016–2018 data [172].

Figure 7.1: Simplified-model diagrams of chargino pair production with two benchmark decay modes:



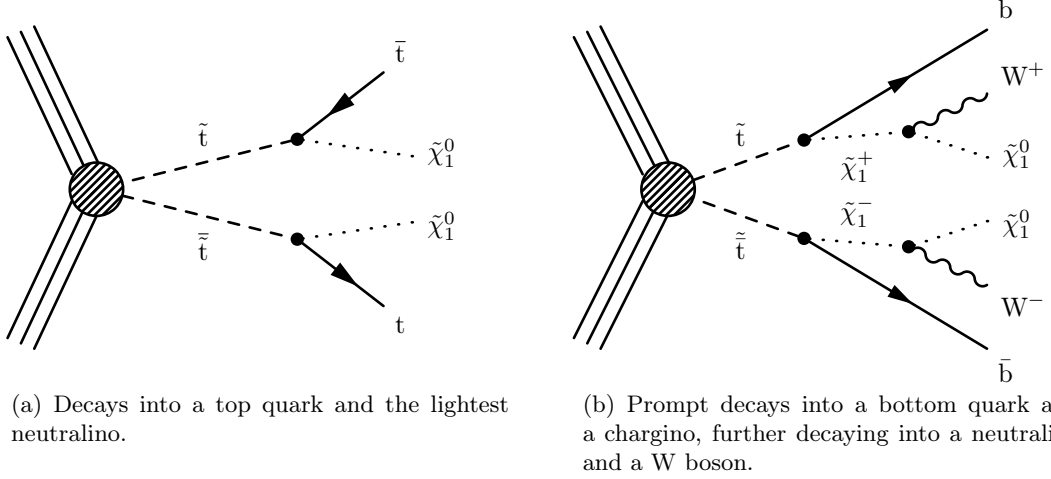
The search for top squark pair production focuses on a SMS in which the top squark decays into a top quark and the lightest neutralino, as shown in Fig. 7.2a. The analysis strategy is optimised for a compressed spectrum scenario where the mass difference (Δm) between the top squark and the lightest neutralino lies between the top quark and W boson masses $m_W < \Delta m \lesssim m_t$. In this regime, the top quarks are produced off-shell, resulting in final states with low-momentum bottom quarks that often fail to be identified.

Further interpretations of the results are given by considering an additional model, shown in Fig. 7.2b where each of the pair-produced top squarks decays into a bottom quark and a chargino, which subsequently decays into a W boson and the lightest neutralino. In this model, the mass of the chargino is assumed to be equal to the mean between of the masses of the neutralino and the top squark. A complementary analysis to the one presented in this document was published by the CMS Collaboration, targeting scenarios with $\Delta m > m_t$ in OC dilepton final states, which result in signatures with on-shell top quarks with higher momentum decay products. Similar analyses were performed using 138 fb^{-1} [173]. With respect to that analysis, this search gains sensitivity in the compressed mass region by loosening the requirements on the jets from bottom quark hadronisation and optimising the signal event selection for the lower momentum carried by the neutralino LSPs.

The CMS Collaboration has also published other searches targeting the same signal models in the final states with different number of leptons. Results with exactly one lepton were explored using 138 fb^{-1} [174], and with no leptons [175] using 2016 data and also covering the four-body-decay of the top squark in the region $\Delta m < 80 \text{ GeV}$. Results were also obtained for an equivalent analysis, probing the same final state but using the full 138 fb^{-1} [176]. An equivalent analysis probing four-body-decays in final states with one lepton was also performed [177]. Similarly, production of pairs top squark in the region of $\Delta m < 80 \text{ GeV}$ was also probed with high p_T^{miss} using various lepton and jet multiplicities [178]. Lastly, pair production of top squarks in di-tau final states was also considered [179].

The ATLAS Collaboration also published several searches addressing these signal models using all three final states, both with 2016 data [180, 181, 182] and 2016–2018 data [183, 184, 185, 186]. Other signatures were also considered, such as the production of the top squark in final states with 0,1 or two leptons in the presence of multiple jets by the CMS collaboration [187], or the top squark decaying via charm quarks by the ATLAS collaboration [188]. All such analyses are combined in the summary article [172].

Figure 7.2: Simplified-model diagrams of top squark pair production with two benchmark decay modes of the top squark:



Finally, a model with pair production of charged sleptons is considered, with each slepton subsequently decaying into charged leptons and neutralinos, as shown in Fig. 7.3. The CMS Collaboration has published a search targeting this model with 13 TeV collision data collected during the 2016 year [189], as well as two analyses using the full 138 fb^{-1} [190, 191], which were subsequently combined [192]. Slepton pair production was also probed in compressed scenarios by the CMS collaboration, using the full 138 fb^{-1} [178]. The analysis here presented is expected to be more sensitive to intermediate mass splitting. The ATLAS Collaboration published a similar search using data collected during the 2016, 2017, and 2018 years [193, 166, 167], as well as in the summary [172].

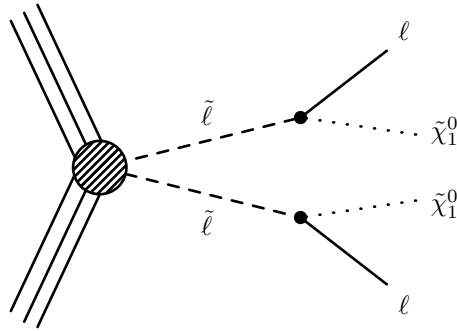


Figure 7.3: Simplified-model diagram of charged slepton pair production. The analysis is focused on a scenario where each slepton decays into a charged lepton and a neutralino.

7.2 Main backgrounds in the dilepton channel

There are several SM production processes with final states similar to those arising from top squark and chargino pair production. Such processes act as irreducible background to the signal events, and thus their contributions to the selected data sample need to be studied and modelled in detail. In this section, each of the main SM backgrounds is presented and classified: backgrounds containing top quarks are discussed in Section 7.2.1, Section 7.2.2 discusses background

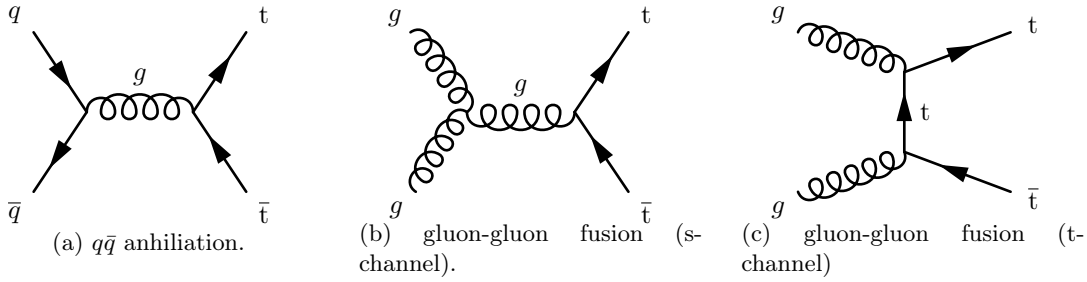
processes with Z boson production, followed by a description of the main diboson and triboson production backgrounds in Sections 7.2.3 and 7.2.4, respectively, and of the main background processes with Higgs boson production in Section 7.2.5.

7.2.1 Top Backgrounds

The principal SM processes containing top quarks relevant to the analysis presented in this document are:

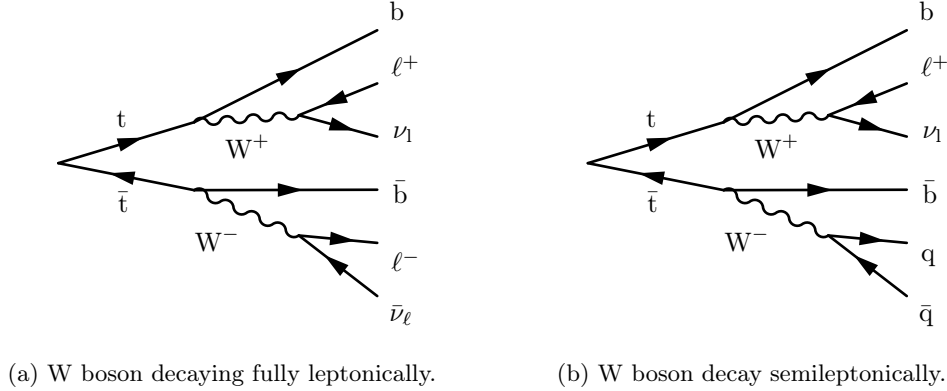
- ◆ **Top-antitop quarks pair production ($t\bar{t}$):** This process can occur in pp collisions at the LHC via mechanisms like gluon-gluon (gg) fusion or quark antiquark ($q\bar{q}$) annihilation, as depicted in Figure 7.4.

Figure 7.4: Feynman diagrams portraying the leading $t\bar{t}$ production Feynman diagrams via:



Due to its large mass and low decay lifetime, the top quark decays prior to the hadronisation. In the vast majority of cases (over 99% of the cases [48]) each top quark decays to a b quark and a W boson, where the W^\pm boson can subsequently decay either leptonically or hadronically. The entire decay sequence can be seen in Fig. 7.5.

Figure 7.5: Top quark pair decay chain into a b quark pair and W boson pair



If both the W bosons in a $t\bar{t}$ event decay leptonically, the final state will be formed by a pair of oppositely charged leptons and two neutrinos (plus the bottom quarks previously produced), therefore having the same observable content as the ones produced in the considered signal models (shown in Figs. 7.1a to 7.3), as the only difference in latter is the presence of neutralinos, which are not directly detectable but only give an additional contribution to the missing transverse energy in the event. This results in the $t\bar{t}$ production being one of the main backgrounds for all considered models.

- ◆ **Single top quark production in association with a W boson (tW):** Even though top quarks at the LHC are primarily produced in pairs via the strong interaction, the production of an individual top quark is possible through a charged-current electroweak

interaction. At leading order interactions, single top production can occur through three distinct sub-processes, as illustrated in Figs. 7.6 and 7.7. Specifically, the single top quark production in association with a W boson is a significant background in this search, especially when the W boson decays leptonically.

Figure 7.6: Leading-order Feynman diagram for single top quark production in:

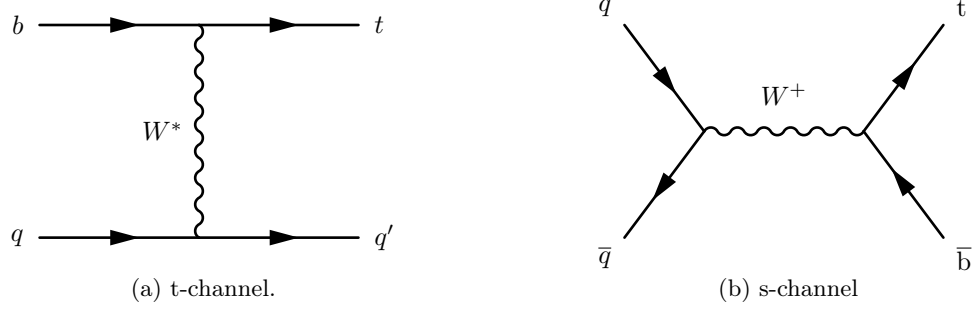
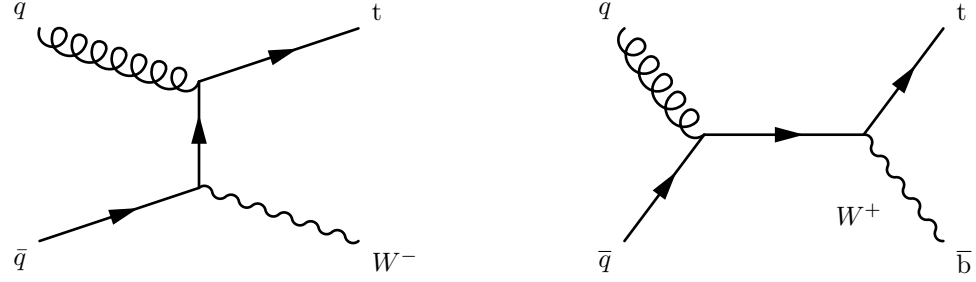
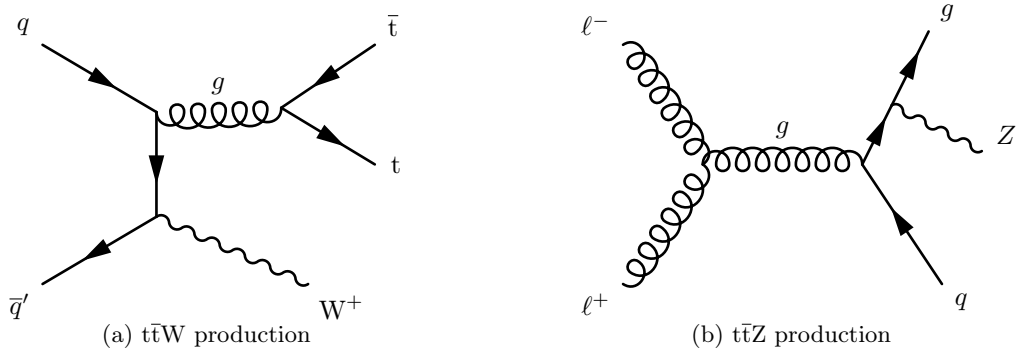


Figure 7.7: Leading order diagrams for the production of a single top quark in association with a W boson



- ◆ **Top-antitop pair production in association with a weak boson ($t\bar{t}W$, $t\bar{t}Z$):** In addition to the two processes just mentioned, production of two top quarks in conjunction with either a W^\pm or a Z boson can contribute to the background processes when at least two of the three bosons present in the event after the decays of the top quarks decay leptonically. The leading production diagrams for $t\bar{t}W$ and $t\bar{t}Z$ in pp collisions at the LHC are shown in Fig 7.8

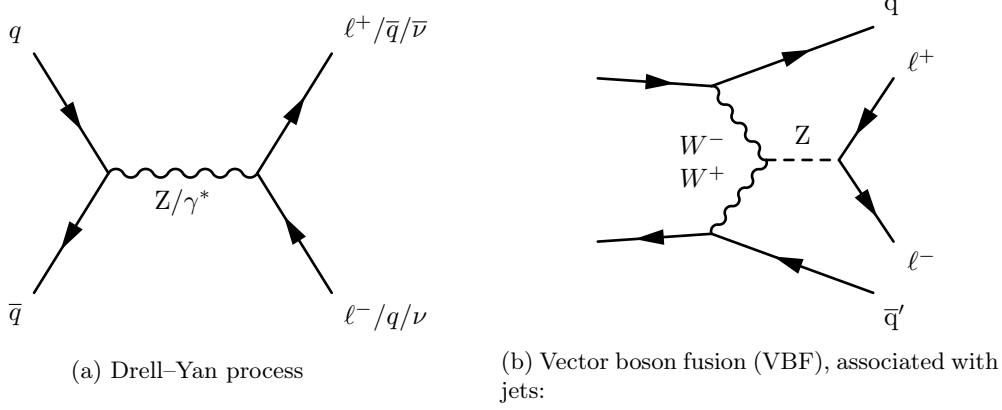
Figure 7.8: Primary Feynman diagrams for:



7.2.2 Z boson backgrounds

In proton-proton (pp) collisions at the LHC, the primary mechanism for Z boson production is the *Drell–Yan* process, produced through quark-antiquark annihilation, as depicted in Figure 7.9a, possibly involving jets (Z +jets), as shown in Fig. 7.10. There are secondary processes that can also lead to Z boson production, such as vector boson fusion, shown in Fig. 7.9b.

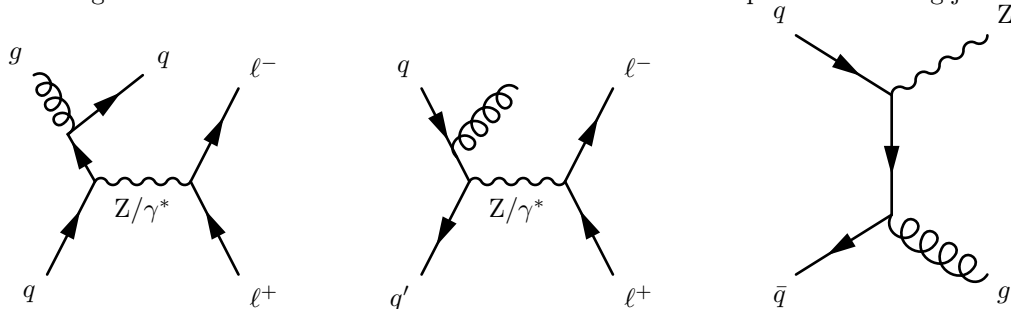
Figure 7.9: Production of the Z boson via:



These kinds of events do not possess a genuine source of p_T^{miss} , as no neutrino is produced, but, because of their large production cross section, they can become a non-negligible background once mismeasurements or detector resolution effects are taken into account.

- ◆ **Drell–Yan:** This process involves the annihilation of a quark from one hadron with an antiquark from a different hadron. The annihilation results in the formation of either a virtual photon (γ^*) or a Z boson, which subsequently produce a pair of leptons of the same flavour but opposite charge. This process can also produce final states with two leptons of difference flavour, through decays into a pair of τ leptons, subsequently decaying leptonically ($Z \rightarrow \tau\tau \rightarrow \mu\nu_\mu\nu_\tau + e\nu_e\nu_\tau$). A notable characteristic of the Drell–Yan process is the existence of an interference between Z boson and γ^* production. Disentangling the contributions of each particle is challenging, and it is often done taking advantage of the fact that when the Z boson is involved, the invariant mass of the resultant lepton pair falls predominantly around the Z boson’s mass (91.2 GeV) with a width of around 2.5 GeV [48], while decays from γ^* typically results in low-mass resonances, usually below 50 GeV.
- ◆ **Z +jets production:** This process refers to scenarios where jets are produced alongside the Z boson. An example of the Z boson in events involving jets via vector boson fusion (VBF) is shown in Fig. 7.9b, while different process of production of Z bosons in presence of jets are shown in Fig. 7.10

Figure 7.10: Production of the Z boson via the Drell–Yan process involving jets

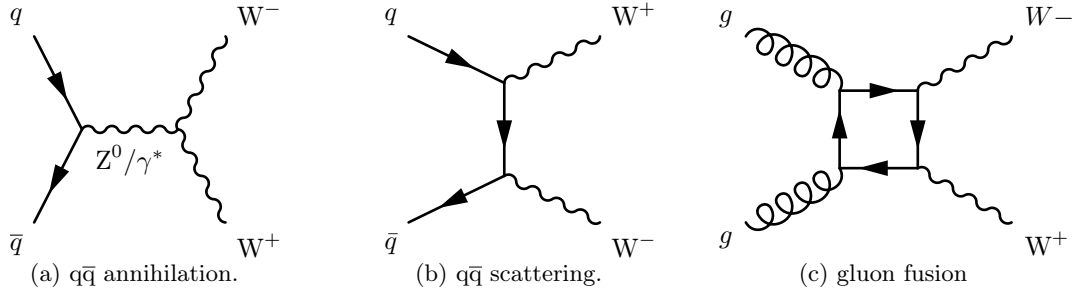


7.2.3 Diboson backgrounds

The production of a pair of weak bosons (diboson production) is a non-negligible background, since the production of these particles can result in events that match the final stated considered in this analysis. These processes include:

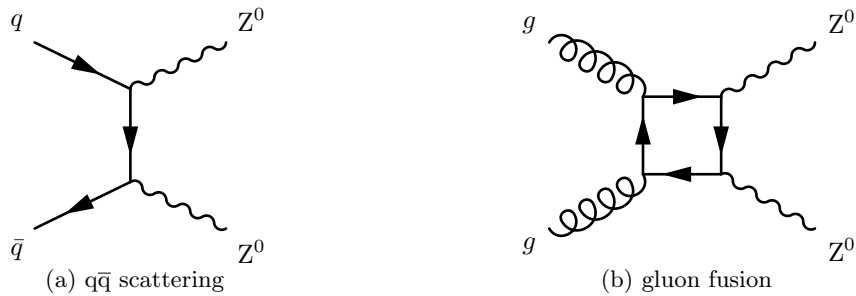
- ◆ **Production of a pair of W bosons (WW):** The leading order production of WW production at the LHC is dominated by quark-antiquark annihilation through the triple gauge coupling in the s-channel or the quark-antiquark scattering in the t-channel, as shown in Figs. 7.11a and 7.11b, respectively. Another possible production channel is via the gluon fusion, possible via a quark loop similar to that illustrated in Fig. 7.11. This process is one of the most significant backgrounds when both W bosons decay leptonically, since the final states with two leptons and two neutrinos that contribute to the p_T^{miss} is very similar to the final state produced by the signal models discussed in Section 7.1.

Figure 7.11: Representative Feynman diagram for the production of a pair of W bosons at the LHC.



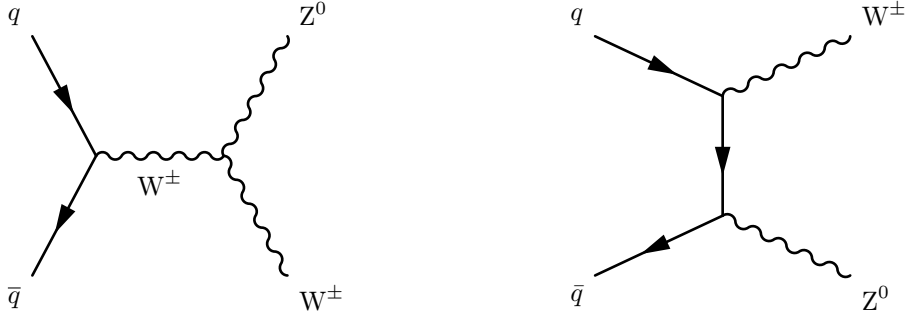
- ◆ **Z boson pair production (ZZ):** Similarly to the case of the WW production, this process is also predominantly produced through quark-antiquark interaction followed by gluon fusion diagrams similar to those for the WW process. Two examples of important mechanisms for the production of ZZ bosons are shown in Fig. 7.12. This process contributes to the background when one of the Z bosons decays into two OC leptons, and the other into neutrinos, resulting in events with high p_T^{miss} .

Figure 7.12: Representative Feynman diagram for the production of a pair of Z bosons at the LHC.



- ◆ **production of a W boson in association with a Z boson (WZ):** In the LHC, the WZ diboson production at leading order arises predominantly from quark-antiquark annihilation or scattering, similarly to the WW production. Examples of WZ production diagrams are shown in Fig. 7.13. Events from WZ production mainly contribute to the background when both bosons decay leptonically and one of the three resulting leptons is not reconstructed.

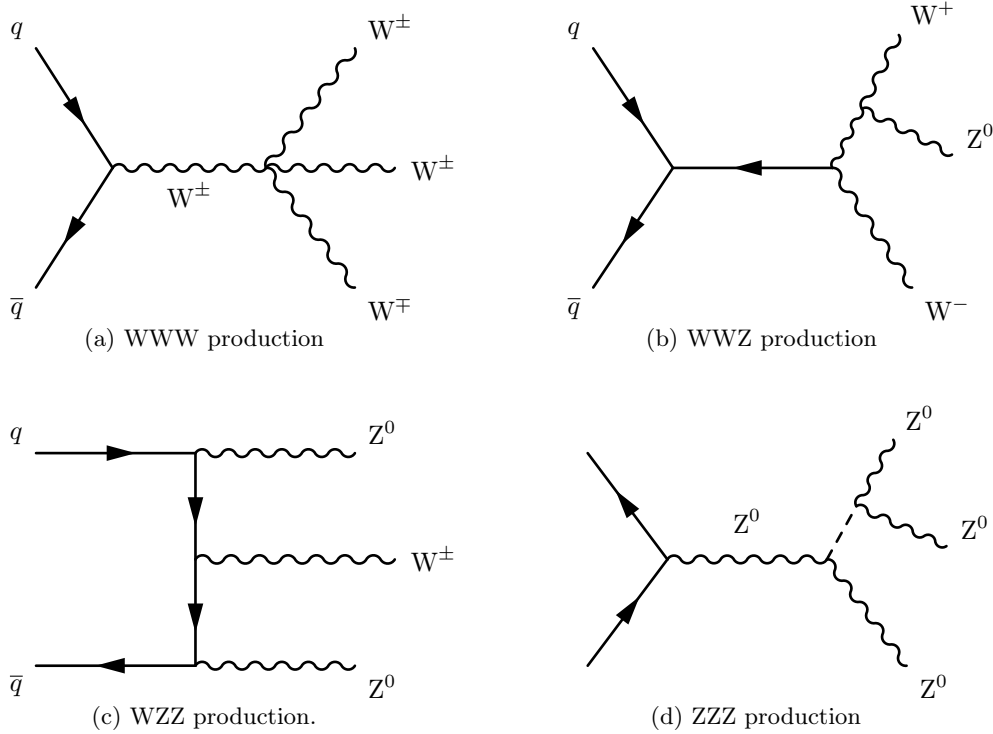
Figure 7.13: Production of pair of W and Z bosons via:



7.2.4 Triboson backgrounds

The triboson processes typically involve interactions with both triple and quartic vertices between charged bosons or combinations of charged and neutral bosons, such as $W^+W^-W^+$, $W^-W^+W^-$, W^+W^-Z or $W^+W^-\gamma$. In the context of the analysis presented in this document, the following processes are taken into account: WWW , WWZ , WZZ and ZZZ . The primary Feynman diagrams contributing to the cross sections of these processes at the LHC are depicted in Figure 7.14. In these scenarios, the $qq \rightarrow VVV$ is found to be the dominant production mechanism.

Figure 7.14: Representative Feynman diagrams for the production of three SM bosons at the LHC



These specific processes contribute to the background when at least two bosons decay leptonically.

7.2.5 Higgs backgrounds

In pp collisions, the Higgs boson can be produced through various mechanisms. The principal channel of Higgs production at leading order at the LHC is via gluon fusion. This process is illustrated in Figure 7.15, with the lower order diagram depicted in Fig 7.15a, and example diagrams for the associated production with a jet from radiation presented in Fig 7.15b.

Figure 7.15: Higgs boson production via gluon fusion

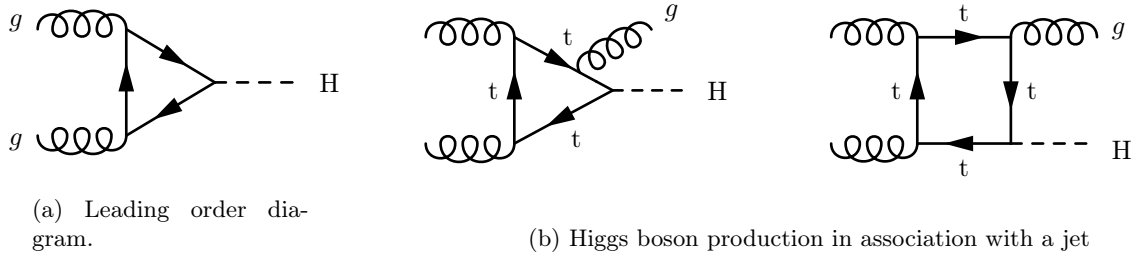
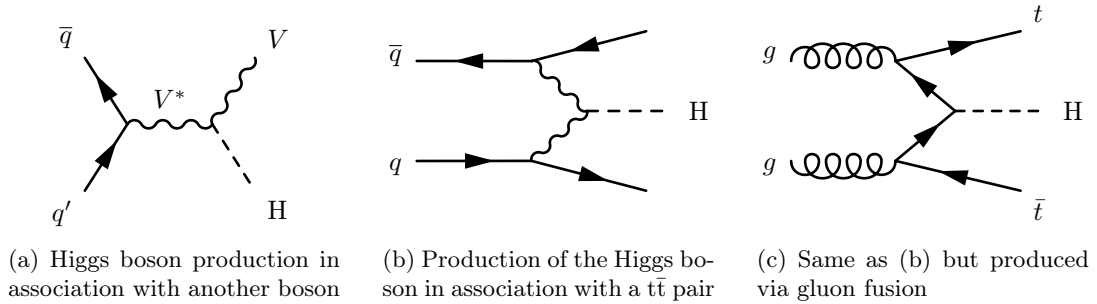


Fig. 7.16 shows other possible Higgs boson production mechanisms, in association with other particles. For the purposes of this analysis, only two decay channels of the Higgs boson are taken into account: The Higgs boson decaying into a pair of W bosons (WW), and into a pair of τ bosons.

Figure 7.16: Representative Feynman diagram for the production of a Higgs boson in association with other bosons at the LHC



7.3 Monte Carlo simulated samples used in this analysis

MC simulated event samples are utilised to study the SM processes' contribution to the selected data set and estimate the acceptance of the signal for the considered SUSY models.

Events from top quark-antiquark pair ($t\bar{t}$) production are generated using POWHEG-v2 [194, 195, 196] and normalised to the cross section computed at NNLO in perturbative QCD, including NNLL soft gluon term resummation [197]. Single top quark events produced in association with a W boson (tW) are generated via POWHEG-v1 [198] and normalised to an approximate NNLO cross section [199]. WW and ZZ productions are simulated using POWHEG-v2 at NNLO [200, 201]. The WW event yields are scaled to the NNLO cross section [202], while events from $q\bar{q} \rightarrow ZZ$ production are reweighed through NNLO/NNLO K factors [203]. Diboson production via gluon fusion is simulated using MCFM v7 [204], with NNLO cross sections corrected using NNLO/NNLO K factors [205, 203]. Drell-Yan events are produced using MADGRAPH5_AMCNLO v2.2.2 at NNLO and normalised to the NNLO cross section [206]. Events from WZ, $t\bar{t}Z$, $t\bar{t}W$, and triboson production are generated at NNLO with the MADGRAPH5_AMCNLO generator [207, 208]. Higgs boson production through gluon fusion and vector-boson fusion is simulated using POWHEG-v2 at NNLO [209, 210].

All the processes that are simulated for the search presented in this document are generated using the NNPDF3.1 [211] parton distribution function (PDFs) sets. The parton showering, hadronisation, and the underlying event are modelled using PYTHIA 8.2 [212] with the CP5 [213] underlying event tune for all the processes, except that in the generation of $t\bar{t}$ events the first emission is done at the matrix element level with POWHEG v2. Weights for the estimation of theoretical systematic uncertainties, including those related to the choice of PDFs, and renormalisation and factorisation scales, are included in simulated events.

As for the simulated signal events, the chargino, top squark, and slepton pair production models are generated using MADGRAPH5_AMCNLO at LO with up to two extra partons in the matrix element calculations, and are normalised to the respective cross sections computed assuming all the other sparticles to be heavy and decoupled. Cross sections for chargino pair production and slepton pair production are computed at NLO plus next-to-leading logarithmic (NLL) precision [214, 215, 216, 217]. In the case of chargino pair production, calculations are performed in a limit where the wino $\tilde{\chi}_2^0$ and $\tilde{\chi}_1^\pm$ is assumed to be mass-degenerate, with a light bino $\tilde{\chi}_1^0$. For the slepton pair production, cross sections are computed for any single generation of left- or right-handed sleptons. The top squark pair production cross sections are determined at the approximate next-to-next-to-leading order (NNLO_{approx}) plus NNLL precision [218, 219, 220, 221, 222, 223, 224, 225, 226, 227, 228, 229, 230].

The detector response to the generated events is simulated using a realistic model of the CMS detector based on GEANT4 [231] for SM processes, known as (FullSim), while signal events are simulated using a fast simulation of the detector based on a parametrisation of the average response to particles is used, known as (FastSim) [232]. Simulated events are subsequently reconstructed using the same algorithms as applied to data.

In order to model the effect of multiple interactions per bunch crossing (PU), simulated events are mixed with minimum-bias events simulated with PYTHIA, and are reweighed in order to match the observed rate of multiple interactions in data.

Chapter 8

Event selection and background estimation

After presenting the signal models and the main SM backgrounds, the next step consists in explaining how the analysis probes for the aforementioned signal models, and how the background processes are modelled. This chapter therefore revolves around such a task, and is split as follows: Section 8.1 defines the common search strategy for all the models. Section 8.2 portrays how the issues on the CMS detector during the data taking are addressed. A precise definition of the search regions (SR) defined for the chargino and top squark signal hypotheses is given in Section 8.3. Subsequently, Section 8.4 presents how each of the backgrounds are treated. Lastly, a summary of all the systematic uncertainties considered in this work is shown in Section 8.5.

8.1 Baseline selection

As mentioned in Section 7.1, two main signal models are considered, the chargino pair production and the top squark pair production. Both models share a final state that contains two opposite charged (OC) leptons as well as two neutrinos and two of the lightest neutralinos leading to significant p_T^{miss} . Consequently, the baseline selection for this analysis begins by requiring the events to have two oppositely charged leptons, either electrons or muons, passing stringent identification and isolation criteria. τ leptons are not explicitly considered because of the very different reconstruction techniques needed by its relative shorter lifetime, albeit electrons and muons which form part of the decay products of a τ lepton decaying leptonically are taken into account in the selection.

Electrons are selected using the cut based medium ID [233] requirements, while muons are required to satisfy the medium ID and the very tight isolation criteria [20]. In order to reduce the amount of other objects misidentified as electrons or muons, some additional requirements are set in place:

- ◆ Requirements on the transverse (d_0) and longitudinal (d_z) impact parameters: $d_0 < 0.05$ cm and $d_z < 0.1$ cm
- ◆ Requirements on the significance of the 3D impact parameter $S_{3D}^d < 4$. For electrons, an additional requirement is set to reject photon conversions:
- ◆ The electron track must not have missing hits in the innermost layers.

Both selected leptons are required to have an absolute pseudorapidity of $|\eta| < 2.4$ and a minimum transverse momentum of at least $p_T \geq 25$ GeV for the more energetic (leading) lepton, with a 20 GeV requirement for the second more energetic (trailing) one. A looser lepton selection is also defined to veto events with a third lepton. For electrons, the cut-based veto ID criteria are used, and the requirement of not having missing hits is removed. For muons, candidates are selected that satisfy the loose ID and very loose isolation criteria. All other requirements are kept unchanged, thus vetoing events with a third lepton with $p_T \geq 10$ GeV and $|\eta| < 2.4$.

In order to reject contributions from low mass resonances, as well as non-prompt leptons produced as part of the decay chain of hadronic jets, a minimum threshold on the dilepton invariant mass m_T is set at 20 GeV. In addition to that, if both leptons are of the same flavour (SF), an additional requirement is set on the dilepton mass, requiring it to be at least 15 GeV higher or lower than the Z mass. Lastly, in order to take into account the presence of neutrinos and neutralinos in the signal final states, a requirement of high $p_T^{\text{miss}} > 160$ GeV is set. A summary of the baseline selection is presented in Table 8.1.

Table 8.1: Baseline selection used for both the chargino and top squark pair production searches. A selection optimised for the full Run II data set is presented in Section 8.3.1.

Variable	Selection
Lepton flavour	e^+e^- , $\mu^+\mu^-$, $e^\pm\mu^\mp$
Leading lepton	$p_T \geq 25$ GeV, $ \eta < 2.4$
Trailing lepton	$p_T \geq 20$ GeV, $ \eta < 2.4$
Third lepton veto	$p_T \geq 10$ GeV, $ \eta < 2.4$
m_T	≥ 20 GeV
$ m_{\ell\ell} - m_Z $	> 15 GeV only for ee and $\mu\mu$ events
p_T^{miss}	≥ 140 GeV

Once the baseline selection of the events to be analysed is established, we need to choose a suitable set of trigger paths to pre-select them during the data taking out of the 40 MHz of collisions provided by the LHC. To this purpose, triggers which require the presence of two leptons (ee , $\mu\mu$, $e\mu$) are used. The threshold on the transverse momentum of the leading lepton is 23 GeV for the ee and $e\mu$ triggers, and 17 GeV for the $\mu\mu$ triggers. The threshold for the trailing lepton is 8 (12) GeV for muons (electrons). During the 2017 and 2018 data-taking periods, the p_T threshold for the trailing muon in the $e\mu$ triggers has been raised to 12 GeV. To increase the efficiency of the trigger selection, events are also accepted by triggers requiring at least one electron or muon passing tighter p_T requirements and identification criteria than the ones applied in the double-lepton triggers. Details on the trigger paths used for each data-taking period are given in Tables B.1 to B.4, in Appendix B. The trigger performances are measured in events from cross triggers, as described in Appendix B.2. The combined efficiency of the dilepton and single-lepton triggers for signal events is found to range between 75 and 99%, depending on the p_T of the leptons, as illustrated in Figs. B.1 and B.2.

Events passing the baseline selection are analysed and compared to SM predictions to search for signal of supersymmetric particle production. As already stated, MC simulation of signal and background processes play a crucial role at this purpose. Several corrections and weights are applied to simulated events, to adjust for possible differences between the reconstruction performance in data and simulations, as discussed in 6. These include pileup reweighing 6.1.5 and scale factors to adjust the performance of the object reconstruction in simulation to the one observed in data 6.2. While most of these corrections are centrally provided by the POGs, for this thesis I computed specific scale factors to correct for possible discrepancies between data and simulation for the additional lepton selection requirements on the impact parameters, S_{3D}^d , and missing hits, as explained in detailed in Appendix C, as well as dedicated FULLSIM/FASTSIM correction factors to account for possible differences in the MC events simulated through the FASTSIM and FULLSIM simulations, as detailed in Appendix D. Finally, corrections to improve

the resolution of the measured muon p_T , known as Rochester corrections, are also applied.

8.2 Data taking issues and their treatment

During the Run-II data taking period, a few detector issues occurred at the CMS detector that need to be taken into account, including high occupancy in the tracker strip modules in 2016 data taking year, prefiring of ECAL trigger primitives in the 2016 and 2017 data taking years, large level of noise detected in the ECAL endcaps in 2017, and two inoperative sectors in the HCAL in 2018. An explanation on how these issues are addressed is presented in Sections 8.2.1, Section 8.2.3 and Section 8.2.4, respectively.

8.2.1 2016 Tracker strip occupancy issue

In the initial phase of 2016 data collection, the CMS tracker experienced significant inefficiencies in its strip modules, due to the increased luminosity causing the read-out chips to have deadtime following events with a high charge deposition from highly ionising particles. Consequently, these chips became inefficient for several bunch crossings, leading to lost hits and shorter reconstructed tracks. This issue was eventually addressed by adjusting the preamplifier voltage feedback bias (VFP) parameter. Given the distinct reconstruction conditions before and after this adjustment, the 2016 dataset was categorised into pre- and post-VFP, sometimes referred to as HIPM/noHIPM or 2016APV/2016. Simulations that account for this effect have been developed, and both preVFP and postVFP simulations have been updated with the relevant efficiencies for muon identification, tracking, trigger, and impact parameter, described in Section 5.2.1.

8.2.2 2016 and 2017 ECAL trigger primitive prefiring

In the final part of 2016 and throughout all 2017 data-taking periods, the gradual timing shift of ECAL was not properly propagated to L1 trigger primitives (TP), resulting in a significant fraction of high- η TP being mistakenly associated to the previous bunch crossing. Correction factors on an event by event basis are obtained using the prefiring maps associated to each physics object.

8.2.3 2017 ECAL endcaps noise

In the 2017 data, significant noise was detected in the endcap ECAL (EE) at high pseudorapidity, as presented in the left graph of Fig. 8.1, where the observed and expected distributions for the uncorrected transverse momentum (p_T^{raw}) of the jets in the pseudorapidity zone impacted by the EE noise ($2.650 < |\eta| < 3.139$) are shown using the previous end-of-year (EOY) reconstruction of Run II data. To counteract the EE noise's influence on the tails of the p_T^{miss} distributions, a correction proposed by the JetMET (JME) POG [234] was applied to the events in the EOY samples. This involved excluding jets with $p_T^{\text{raw}} < 50$ GeV and $2.650 < |\eta| < 3.139$ from the p_T^{miss} computation. A more refined solution was integrated in the UL data production, leading to a significant improvement in the agreement of the observed and expected jet p_T^{raw} distributions, as shown in the right graph of Fig. 8.1.

Fig. 8.2 compares the azimuthal difference between the p_T^{miss} and high- p_T (> 50 GeV) jets with $p_T^{\text{raw}} > 50$ GeV in the noise region. In the EOY production (Fig. 8.2a), noise-induced jets are evident as an excess of jets back-to-back to the p_T^{miss} in data, an excess which is absent in the UL production (Fig. 8.2b).

Lastly, Fig. 8.3 displays the sum of all jet's p_T (H_T) for all jets within $2.650 < |\eta| < 3.139$ and $p_T^{\text{raw}} < 50$ GeV for both EOY (Fig. 8.3a) and UL (Fig. 8.3b) productions. While the UL production shows a better match between observed and expected distributions, a slight excess at high values of H_T remains visible in the data. Consequently, in this study, we exclude events with $H_T < 60$ GeV for both 2017 data and simulated samples.

Figure 8.1: Observed and expected distributions of the p_T^{raw} for jets in the pseudorapidity region affected by the EE noise ($2.650 < |\eta| < 3.139$)

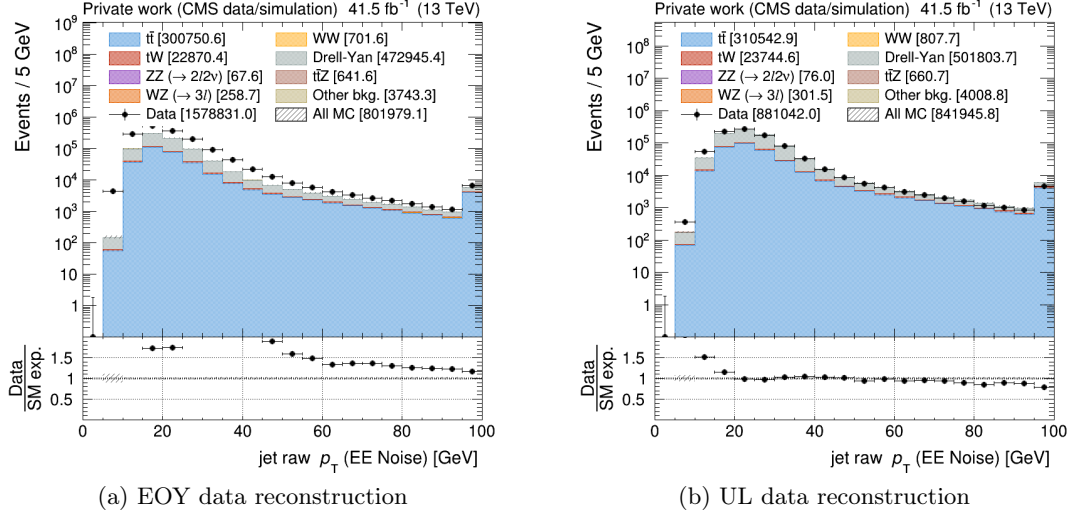


Figure 8.2: Azimuthal separation between the p_T^{miss} and the high- p_T (> 50 GeV) jets with $p_T^{\text{raw}} > 50$ GeV

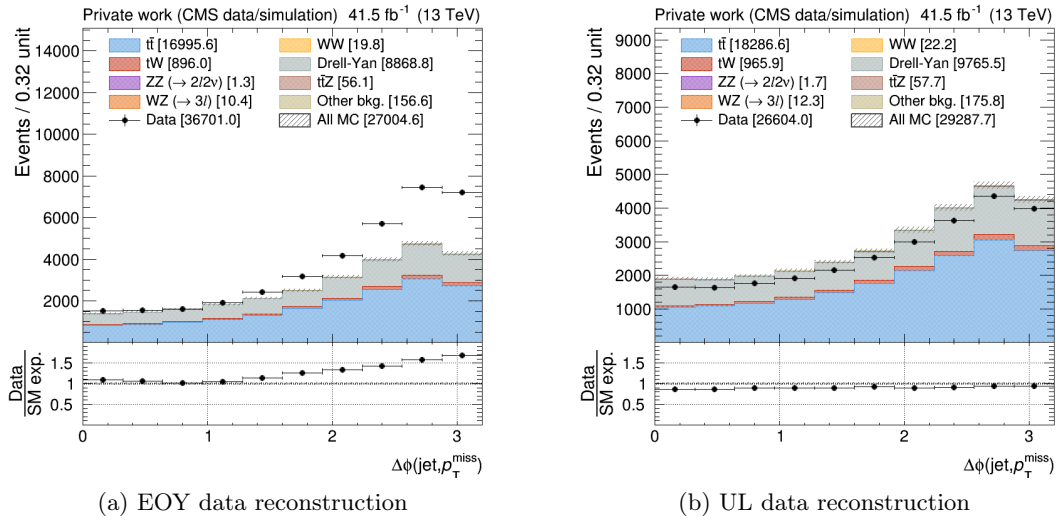
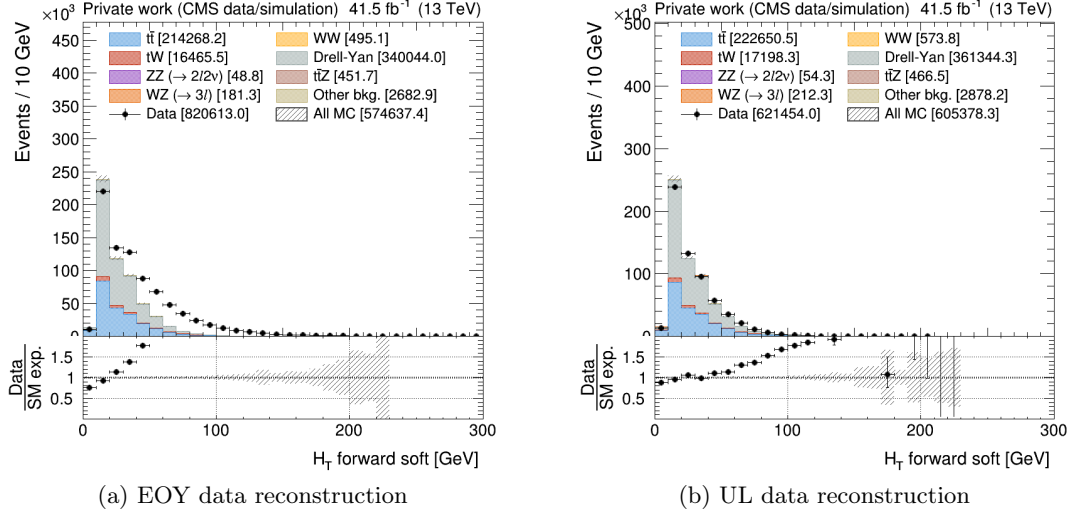
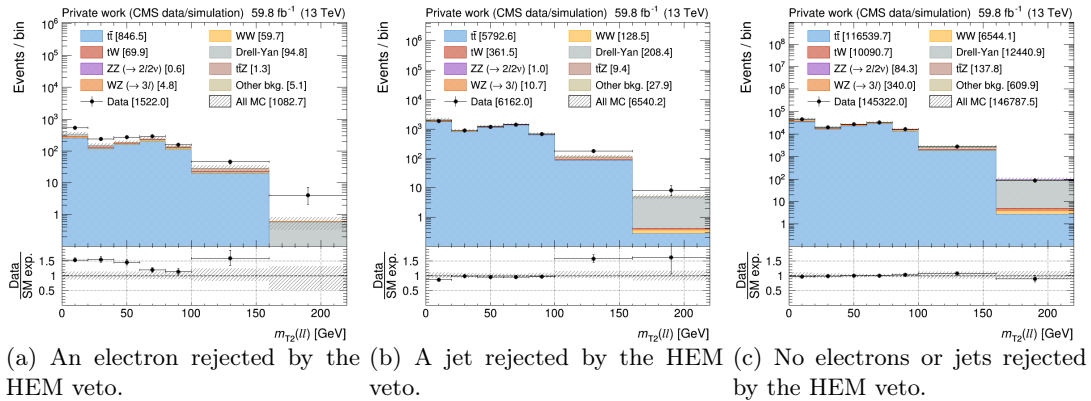


Figure 8.3: Sum of the jet's p_T for all jets with $2.650 < |\eta| < 3.139$ and $p_T^{\text{raw}} < 50$ GeV.

8.2.4 2018 inoperative HCAL sectors

Following the power interruptions generated by false fire alarms which occurred towards the end of June 2018, negative endcap HCAL sectors HEM15 and HEM16 (corresponding to a 40 degree HCAL section at $-3.0 < \eta < 1.3$ and $-1.57 < \phi < -0.87$) could no longer be operated until the end of the 2018 run of data taking. To mitigate the effect on the agreement between data and simulated samples, we veto events with any electron with $p_T > 30$ GeV, $-3.0 < \eta < -1.4$, and $-1.57 < \phi < -0.87$ or any jet with $p_T > 30$ GeV, $-3.2 < \eta < -1.2$, and $-1.77 < \phi < -0.67$. This veto is applied to data taken starting from physics run 319077. In simulations, events passing the veto are weighted by the fraction of integrated luminosity of data taken before physics run 319077. In the baseline search region, the veto is found to reject about 10% of $t\bar{t}$ and top squark pair production events, and about 5% of chargino pair production events for the year 2018. We test the effectiveness of the veto in events in a sideband region to our search region with $100 \leq p_T^{\text{miss}} < 140$ GeV. Figure 8.4 compares the observed and expected distributions of $m_{T2}(\ell\ell)$ in the 2018 data sets for events rejected by the veto (events with rejected electrons on the left plot, and events with rejected jets on the middle one) as well as for events that pass the veto (right plot).

Figure 8.4: Observed and expected $m_{T2}(\ell\ell)$ distributions for events in the 2018 dataset with $100 \leq p_T^{\text{miss}} < 140$ GeV, on events with:

8.3 Search strategy

Out of the SM processes discussed in Section 7.2, the main contributing background processes following the baseline selection are found to be $t\bar{t}$, tW , and WW production. For all these backgrounds, both the lepton pair and \vec{p}_T^{miss} originate from a W boson pair. Hence, a useful variable for the study of these backgrounds is the transverse mass (m_T) of the lepton-neutrino system from the W boson decay, defined in Eq. 8.1:

$$m_T = \sqrt{2E_T^\ell p_T^{\text{miss}} \cdot (1 - \cos(\Delta\phi))} \quad (8.1)$$

where the p_T^{miss} is taken as a proxy for the transverse momentum of the neutrino, and $\Delta\phi$ is the angular separation between the lepton and the p_T^{miss} . In the considered case of a lepton and a neutrino coming from a W boson, it can be seen that $m_T \leq m_W$. Similarly, the $m_{T2}(\ell\ell)$ [235] variable is introduced to extend the transverse mass (m_T) for a system with two invisible particles, utilising the two leptons as visible systems, as depicted in Eq 8.2:

$$m_{T2}(\ell\ell) = \min_{\vec{p}_T^{\text{miss}1} + \vec{p}_T^{\text{miss}2} = \vec{p}_T^{\text{miss}}} \left(\max \left[m_T \left(\vec{p}_T^{\text{lep}1}, \vec{p}_T^{\text{miss}1} \right), m_T \left(\vec{p}_T^{\text{lep}2}, \vec{p}_T^{\text{miss}2} \right) \right] \right) \quad (8.2)$$

This observable approaches a kinematic endpoint at the m_W for the main backgrounds of this search. In contrast, signal events display $m_{T2}(\ell\ell)$ spectra without this endpoint, due to the additional contribution to the \vec{p}_T^{miss} coming from the neutralinos. The analysis sensitivity is further increased by dividing the baseline SR in several p_T^{miss} bins. This allows the analysis not only to exploit the larger tails in the p_T^{miss} distribution of the signal events, but also to optimise the sensitivity to signals with different mass separation between the produced supersymmetric particle and the LSP. Each p_T^{miss} bin is in turn divided into events with SF and different flavour (DF) leptons to exploit the smaller contamination from WZ , ZZ , and Drell–Yan production of the latter. The procedure followed for the binning optimisation in p_T^{miss} and $m_{T2}(\ell\ell)$ is described in Section 8.3.1.

The SRs are further subdivided based on the specific characteristics of each signal model. A veto on b-tagged jets is applied to reject $t\bar{t}$, tW , $t\bar{t}Z$, and $t\bar{t}W$ events in the chargino search. Selected events in the lowest p_T^{miss} bins are then split in two different subregions, depending on the presence of a jet with $p_T > 20 \text{ GeV}$ and $|\eta| < 2.5$. This allows for a better discrimination between signal events and top quark background ($t\bar{t}$ and tW), which still contaminates the SRs after applying the b-tagged jet veto. Events with b-tagged jets serve as a CR for the background normalisation from top quark production, as discussed in Section 8.4.

Final states in top squark pair production event are characterised by the presence of two bottom quarks. When the mass difference between the top squark and the neutralino approaches the compressed region boundary, $\Delta m \gtrsim m_W$, the bottom quarks produced in this model are soft, leading to jets with relatively low momentum and a lower probability to be tagged as b-tagged jets. Under these circumstances, the top squark final states are similar to those from chargino pair production. Thus, requiring a veto on b-tagged jets is again an effective strategy to define SRs where the contamination from $t\bar{t}$, tW , $t\bar{t}Z$, and $t\bar{t}W$ backgrounds is reduced. On the other hand, for signal scenarios with larger Δm , the b jets have higher momentum and the final states are more similar to the events that include $t\bar{t}$ production. Consequently, under this scenario, the sensitivity to top squark production is enhanced by requiring a b-tagged jet, which is used to reduce the background from diboson and Drell–Yan events.

Another tool to discriminate top squark production with respect to the SM processes discussed in Section 7.2 of this document is the presence of high- p_T ISR jets in the events. As previously

discussed, both neutrinos and neutralinos are effectively invisible to the CMS detector. These particles, if produced in the decay chain of the top squark in the compressed scenario, are expected to be soft (i.e. of a relatively low energy). However, events with harder, more energetic, neutralinos can arise when the top squark pair system recoils against a high- p_T ISR jet. In this hard ISR regime, background is still constrained by the kinematic m_W endpoint in $m_{T2}(\ell\ell)$, and therefore can be effectively separated from the signal. Events that include a very energetic ISR jet are selected by requiring that the leading jet satisfies the requirement $p_T > 150$ GeV and is not b tagged. In order to favour the topology in which the jet recoils against the rest of the system, the angular difference between the jet and the $\vec{p}_T^{\text{miss}}(\Delta\phi)$ is required to be larger than 2.5 rad. This requirement is found to be effective in discriminating top squark production from background events in the highest p_T^{miss} bins.

8.3.1 Search region optimisation

Building upon the 2016 version of this analysis [109], an optimisation of the p_T^{miss} and $m_{T2}(\ell\ell)$ binning in the SRs is performed, in order to improve the sensitivity of the search. Such study was mainly optimised for two models:

- ◆ The chargino model where the charginos decay into a lepton, a neutrino (ν), and the lightest neutralino ($\tilde{\chi}_1^0$) via an intermediate charged slepton ($\tilde{\chi}_1^\pm \rightarrow \nu\tilde{\ell} \rightarrow \nu\ell\tilde{\chi}_1^0$) or sneutrino ($\tilde{\chi}_1^\pm \rightarrow \ell\tilde{\nu} \rightarrow \ell\nu\tilde{\chi}_1^0$), shown in Fig. 7.1a.
- ◆ The top squark model where the top squark decays into a top quark and the lightest neutralino, and optimised for a compressed spectrum, depicted in Fig. 7.2a.

In order to perform the optimisation of the p_T^{miss} and $m_{T2}(\ell\ell)$ binning, a signal significance is maximised, defined as in Eq. 8.3:

$$\text{Significance}(\{N_{p_T^{\text{miss}}}\}, \{N_{m_{T2}(\ell\ell)}\}) = \sqrt{\sum_{i_{p_T^{\text{miss}}}}^{N_{p_T^{\text{miss}}}} \sum_{j_{m_{T2}(\ell\ell)}}^{N_{m_{T2}(\ell\ell)}} \left(\frac{N_{i,j}^{\text{sig}}}{\sqrt{N_{i,j}^{\text{sig}} + N_{i,j}^{\text{bkg}}}} \right)^2}, \quad (8.3)$$

Where $\{N_{p_T^{\text{miss}}}\}$ and $\{N_{m_{T2}(\ell\ell)}\}$ indicate a choice of binning for p_T^{miss} and $m_{T2}(\ell\ell)$, with some constraints on the total number of bins. The expected yields for the signal production N^{sig} are computed as the average yields over the signal mass points in a region of the $(m_{\tilde{\chi}_1^\pm/\tilde{t}_1}, m_{\tilde{\chi}_1^0})$ plane around the expected exclusion boundary, assuming the same cross section for each mass point.

Given the slightly varying kinematics of the studied signal models, the defined signal significance is maximised independently for pair produced charginos decaying through intermediate sleptons or sneutrinos and for pair produced top squark decaying into a top and the lightest neutralino, the latter in the compressed $80 < \Delta m < 175$ GeV region. A common p_T^{miss} binning with edges at 160, 220, 280, and 380 GeV is derived for both the signal models.

As for the $m_{T2}(\ell\ell)$ variable, two regions are defined, dividing them in $m_{T2}(\ell\ell)$ masses either greater or smaller than 100 GeV. For the former, the range 0–100 GeV is divided in five bins of 20 GeV each. This $m_{T2}(\ell\ell)$ region has a relatively low signal contribution, and is hence utilised to more accurately constrain the contributions of the dominant backgrounds in the SRs with one b-tagged jet (dominated by $t\bar{t}$ and tW production) and without b-tagged jets (where WW production becomes relevant).

However, for the region where $m_{T2}(\ell\ell) \geq 100$ GeV, different optimised binnings were obtained

depending on the signal production model. This different binning arises from the different kinematics for each signal model, since most of the significance is expected to be found at higher values of $m_{T2}(\ell\ell)$ for chargino production events with respect to the top squark signal, as for the latter we focus our search on the compressed $80 < \Delta m < 175$ GeV region, where $m_{T2}(\ell\ell)$ values would not be expected to be as high.

For the chargino search, the optimal binning is thus found to be 100–160 GeV, 160–240 GeV, 240–370 GeV, and $m_{T2}(\ell\ell) \geq 370$ GeV, whereas for the top squark signal two bins with $100 < m_{T2}(\ell\ell) < 160$ GeV and $m_{T2}(\ell\ell) \geq 160$ GeV are used. The rest of the signal models defined in Section 7.1 utilise the same signal regions as just defined. The chargino pair production in decays involving W bosons and the slepton pair production are studied using the signal regions optimised for the reference chargino model, while the top squark decaying via chargino uses the reference top squark search regions.

A summary of the resulting SRs for the chargino and top squark searches is given in Tables 8.2, indicating the p_T^{miss} range, the selection on the multiplicity of jets (N_{jets}) and b jets ($N_{\text{b jets}}$) in the event, and the ISR jet requirement. The $m_{T2}(\ell\ell)$ binning used in each SR is also shown, while the SRs and $m_{T2}(\ell\ell)$ binnings used in the chargino and top squark searches performed in the 2016 version of this analysis [109] are shown in Tables 8.3 and 8.4 for comparison.

Table 8.2: Definition of the SRs for the chargino, slepton and top squark searches as a function of the p_T^{miss} value, the b-jet multiplicity and jet multiplicity, and the lepton pair channels, as well as the ISR requirement used for the top squark production. Also shown are the CRs with b-tagged jets used for the normalization of the $t\bar{t}$ and tW backgrounds for the chargino and slepton searches. The last row for each search type shows the $m_{T2}(\ell\ell)$ binning used in the ML fit performed to extract the signal.

	SR1			SR2			SR3		SR4	
$p_{\text{T}}^{\text{miss}}$ [GeV]	160–220			220–280			280–380		≥ 380	
Channels	SF,DF			SF,DF			SF,DF		SF,DF	
	Chargino and slepton searches									
	$\text{SR1}_{0\text{tag}}^{\text{0jet}}$	$\text{SR1}_{0\text{tag}}^{\text{jets}}$	CR1_{tags}	$\text{SR2}_{0\text{tag}}^{\text{0jet}}$	$\text{SR2}_{0\text{tag}}^{\text{jets}}$	CR2_{tags}	$\text{SR3}_{0\text{tag}}$	CR3_{tags}	$\text{SR4}_{0\text{tag}}$	CR4_{tags}
$N_{\text{b jets}}$	0	0	≥ 1	0	0	≥ 1	0	≥ 1	0	≥ 1
N_{jets}	0	≥ 1	≥ 1	0	≥ 1	≥ 1	≥ 0	≥ 1	≥ 0	≥ 1
$m_{\text{T}2}(\ell\ell)$	0–20, 20–40, 40–60, 60–80, 80–100, 100–160, 160–240, 240–370, ≥ 370 GeV									
	Top squark search									
	$\text{SR1}_{0\text{tag}}$	SR1_{tags}		$\text{SR2}_{0\text{tag}}$	SR2_{tags}		$\text{SR3}_{0\text{tag}}^{\text{ISR}}$	$\text{SR3}_{\text{tags}}^{\text{ISR}}$	$\text{SR4}_{0\text{tag}}^{\text{ISR}}$	$\text{SR4}_{\text{tags}}^{\text{ISR}}$
$N_{\text{b jets}}$	0	≥ 1		0	≥ 1		0	≥ 1	0	≥ 1
N_{jets}	≥ 0	≥ 1		≥ 0	≥ 1		≥ 1	≥ 2	≥ 1	≥ 2
ISR jets	≥ 0	≥ 0		≥ 0	≥ 0		≥ 1	≥ 1	≥ 1	≥ 1
$m_{\text{T}2}(\ell\ell)$	0–20, 20–40, 40–60, 60–80, 80–100, 100–160, ≥ 160 GeV									

Table 8.3: Definition of the SRs for the 2016 chargino search as a function of the p_T^{miss} value, the b-jet multiplicity and jet multiplicity. Also shown are the CRs with b-tagged jets used for the normalisation of the $t\bar{t}$ and tW backgrounds. Each of the regions is further divided in seven $m_{T2}(\ell\ell)$ bins, as described in the last row.

	$\text{SR1}_{0\text{tag}}^{0\text{jet}}$	$\text{SR1}_{0\text{tag}}^{\text{jets}}$	CR1_{tags}	$\text{SR2}_{0\text{tag}}^{0\text{jet}}$	$\text{SR2}_{0\text{tag}}^{\text{jets}}$	CR2_{tags}	$\text{SR3}_{0\text{tag}}$	CR3_{tags}
p_T^{miss} [GeV]	140–200	140–200	140–200	200–300	200–300	200–300	≥ 300	≥ 300
$N_{\text{b jets}}$	0	0	≥ 1	0	0	≥ 1	0	≥ 1
N_{jets}	0	≥ 1	≥ 1	0	≥ 1	≥ 1	≥ 0	≥ 1
Channels	SF, DF	SF, DF	SF, DF	SF, DF	SF, DF	SF, DF	SF, DF	SF, DF
$m_{T2}(\ell\ell)$	0–20, 20–40, 40–60, 60–80, 80–100, 100–120, ≥ 120 GeV							

A simultaneous binned maximum likelihood (ML) fit to the $m_{T2}(\ell\ell)$ distribution in all the SRs is performed to extract the signal. Details of the fit and of the subsequent procedure to derive exclusion regions in the $(m_{\tilde{\chi}_1^\pm/\tilde{t}_1}, m_{\tilde{\chi}_1^0})$ plane are given in Sections 9.3 and 9.4.

Table 8.4: Definition of the SRs for the 2016 top squark production search as a function of the p_T^{miss} value, the b-jet multiplicity and the ISR jet requirement. Each of the regions is further divided in seven $m_{T2}(\ell\ell)$ bins, as described in the last row.

	SR1 _{0tag}	SR1 _{tag}	SR2 _{0tag}	SR2 _{tag}	SR3 _{0tag} ^{ISR}	SR3 _{tag} ^{ISR}
p_T^{miss} [GeV]	140–200	140–200	200–300	200–300	≥ 300	≥ 300
$N_{\text{b jets}}$	0	≥ 1	0	≥ 1	0	≥ 1
N_{jets}	≥ 0	≥ 1	≥ 0	≥ 1	≥ 1	≥ 2
ISR jets	≥ 0	≥ 0	≥ 0	≥ 0	≥ 1	≥ 1
Channels	SF, DF	SF, DF	SF, DF	SF, DF	SF, DF	SF, DF
$m_{T2}(\ell\ell)$	0–20, 20–40, 40–60, 60–80, 80–100, 100–120, ≥ 120 GeV					

8.4 Background estimation

From the background (SM) processes, illustrated in Section 7.2, the primary contributions to the SRs arise primarily from the $t\bar{t}$, tW , and WW productions. These background are normalised through the low $m_{T2}(\ell\ell)$ bins in the ML fit, as mentioned in Section 8.3. These backgrounds are characterised by having a $m_{T2}(\ell\ell)$ shape with an endpoint at the m_W . Therefore, events from these backgrounds enter the significant region for signal extraction ($m_{T2}(\ell\ell) > 80$ GeV) because of detector resolution effects, which are challenging to model accurately. For this reason, the $m_{T2}(\ell\ell)$ distributions of these processes are assessed in specific CRs using data, as outlined in Section 8.4.1.

Likewise, the modelling of other secondary backgrounds like WZ , ZZ , $t\bar{t}Z$, and Drell–Yan is validated in CRs, which are also incorporated into the ML fit in order to constrain their normalisations, as explained in Section 8.4.2. A summary of the additional CRs included in the fit for these subleading backgrounds is portrayed in Table 8.5. Other minor backgrounds, including $t\bar{t}W$, $H \rightarrow WW$, $H \rightarrow \tau\tau$, and triboson production, have minimal impact in the SRs, and therefore their contributions are estimated directly from simulations.

Table 8.5: Preview of the additional CRs included in the ML fit, split according to the same p_T^{miss} and jet multiplicity bins as for the SRs discussed in Table 8.2. Details on the constructions of these CRs are given in Sections 8.4.2 to 8.4.2

	Process	Selection criteria
Subleading Z+X backgrounds	WZ	Three leptons and p_T^{miss} in SR threshold
	ZZ	Reconstructed $ZZ \rightarrow 4\ell$ events, one Z's p_T added to p_T^{miss}
	$t\bar{t}Z$	From $t\bar{t}Z \rightarrow \geq 3\ell$ events: Z's p_T added to p_T^{miss}

8.4.1 Modelling of $m_{T2}(\ell\ell)$ in $t\bar{t}$, and WW events

In this section, we study how the simulation of $t\bar{t}$, tW , and WW backgrounds reproduces the observed $m_{T2}(\ell\ell)$ distributions above the kinematic endpoint $m_{T2}(\ell\ell) > m_W$.

We start by looking at data in a sideband CR with $100 < p_T^{\text{miss}} < 140$ GeV. The $p_T^{\text{miss}} > 100$ GeV requirement is chosen in order to reject most of the Drell–Yan events, whereas the requirement on events to have $p_T^{\text{miss}} < 140$ GeV is necessary as to minimise the signal contamination. Additionally, in order to further reject the possible presence of Drell–Yan events, only DF events are considered. Resultant $m_{T2}(\ell\ell)$ distributions, separated by year for events with at least one b-tagged jet are shown in Fig. 8.5, with equivalent distributions for DF events with no b-tagged jets but at least on jet and in DF events with no jets shown in Figs. 8.6 and 8.7, respectively.

It can be observed that events with b-tagged jets (Fig. 8.5) are largely dominated by events including top production, mainly $t\bar{t}$ and tW , while a larger proportion of events from other SM processes populate the distributions where no b-tagged jets are required, and particularly if no

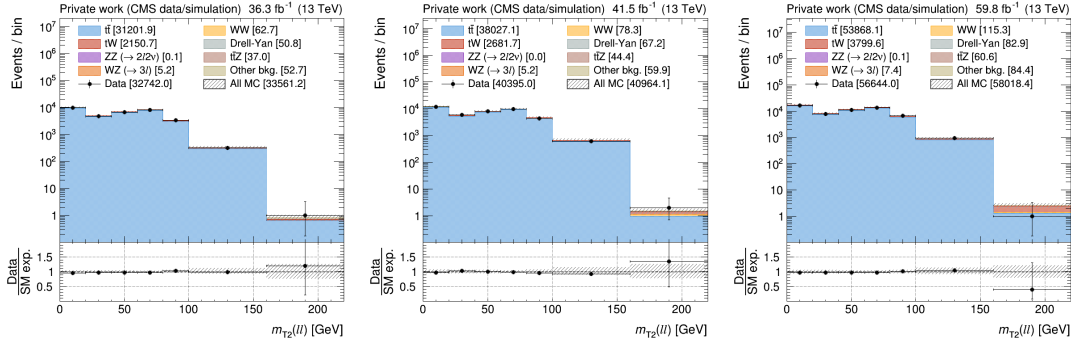


Figure 8.5: Distributions of $m_{T2}(\ell\ell)$ in DF events with $100 < p_T^{\text{miss}} < 140$ GeV and at least one b-tagged jet for 2016 (left plot), 2017 (middle), and 2018 (right) data. The last bin includes the overflow entries. In the bottom panel, the ratio of data and SM expectations is shown. The hatched band represents the total uncertainty, including the sources discussed in Section 8.5.

jets are required (Fig. 8.7), where the number of WW events is roughly of the same size as the number of top events. Overall, data is found to be in good agreement with the expectations from the simulations. For events with no jets, an excess of data is observed, which might be related to a similar excess found in the study of WW boson pair production [236, 237, 238]. In order to mitigate this issue, in the ML fit used to extract the signal, the normalisation of the WW background is constrained to the observed data in the low $m_{T2}(\ell\ell)$ region of the SRs, as described in Section 9.3. In addition to that, the compatibility of the observed data to the expected SM contributions in these CRs is studied by performing a ML fit, similar to the one used to extract the signal in the SRs. Detailed results of this test are discussed in detail in Appendix E. We observe good post-fit agreement between observed events and SM expectations, with the most pulled nuisances being the one describing the uncertainties on the jet energy scale and resolution, and the rate parameter associated with the normalisation of the WW production process.

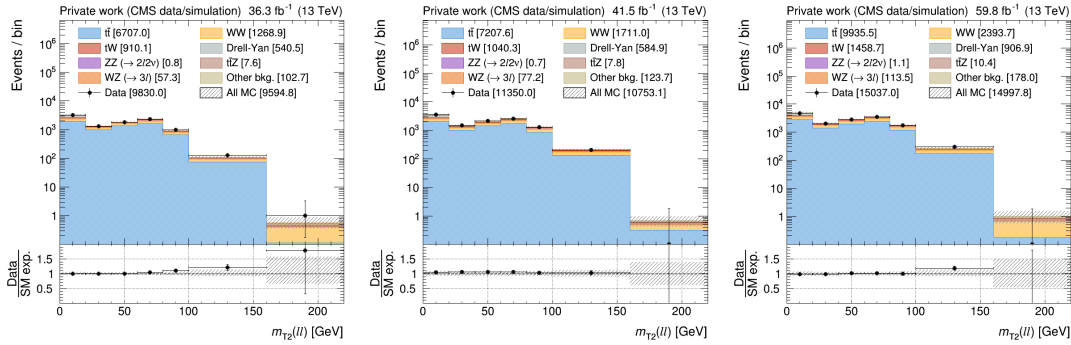


Figure 8.6: The same distributions of $m_{T2}(\ell\ell)$ as Fig. 8.5, but in events with at least one jet but no b-tagged jets.

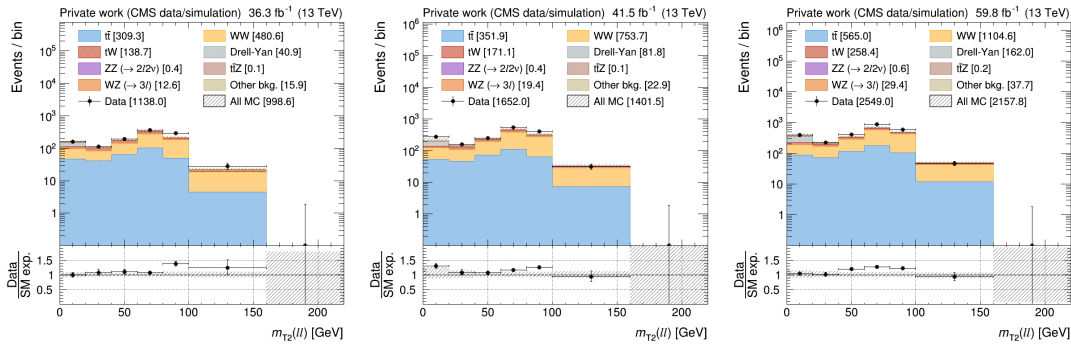


Figure 8.7: The same distributions of $m_{T2}(\ell\ell)$ as Fig. 8.5, but in events with no jets.

Modelling of $m_{T2}(\ell\ell)$ in events with high p_T^{miss}

A second CR is constructed to validate the modelling of the $m_{T2}(\ell\ell)$ distributions in events with $p_T^{\text{miss}} > 160$ GeV, so in a p_T^{miss} range more representative of the SRs. For such purpose, we select events from $WZ \rightarrow 3\ell 1\nu$ production and emulate the $m_{T2}(\ell\ell)$ shape of WW and top quark events. We take the lepton from the decay of the Z boson with the same charge as the lepton from the W boson, and we add its \vec{p}_T vectorially to \vec{p}_T^{miss} , effectively treating it like a neutrino. Subsequently, the $m_{T2}(\ell\ell)$ is computed from the other two leptons and the newly obtained p_T^{miss} .

The events are selected by requiring three leptons and vetoing the presence of a fourth lepton passing the veto lepton requirements. A veto is applied to events with b-tagged jets to remove residual $t\bar{t}$ events. Among the three selected leptons, we require a pair of OC SF leptons with an invariant mass within 15 GeV of the Z boson mass to identify the Z boson. The simulation is found to slightly underestimate the data in the tail of the $m_{T2}(\ell\ell)$ distribution, as shown in the left plot of Fig. 8.8.

We further study this disagreement by loosening the cut on the p_T^{miss} at 100 GeV to gain statistics, as shown in the middle plot of Fig. 8.8. Overall, the ratio of observed vs expected events exhibits a certain trend across the tail of the $m_{T2}(\ell\ell)$ distribution. We quantify this behaviour by fitting the ratio of the (background-subtracted) observed events to the expected WZ events to a linear function. The result of the fit in the region $p_T^{\text{miss}} > 100$ GeV is taken as a correction to the modelling of the $m_{T2}(\ell\ell)$ tails in background events with two W bosons in the final states. Similarly, we take the uncertainty in the slope parameter of the linear fit (fitted slope = $0.00188 \pm 0.00153 \text{ GeV}^{-1}$) as the uncertainty in the correction. Such uncertainty is treated as correlated across data-taking years and uncorrelated across p_T^{miss} bins. The right plot of Fig. 8.8 summarises the $m_{T2}(\ell\ell)$ tail correction together with its uncertainty. Lastly, figure 8.9 shows the impact on the expected (blinded) exclusion regions for the chargino and top squark signal models when applying the $m_{T2}(\ell\ell)$ tail correction.

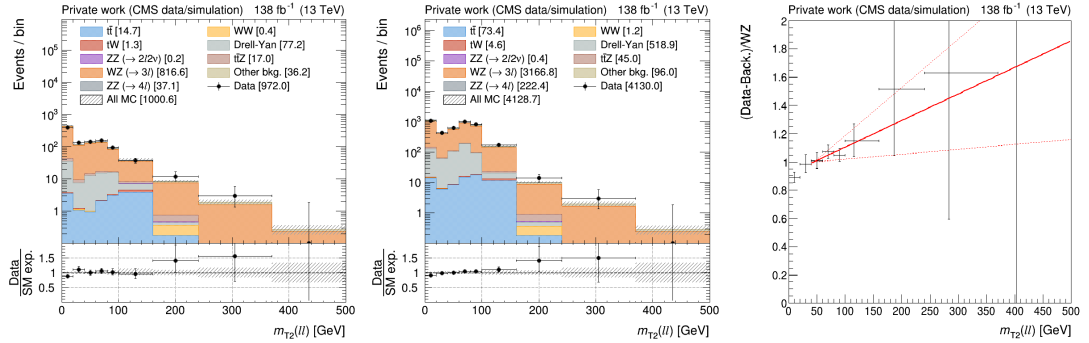
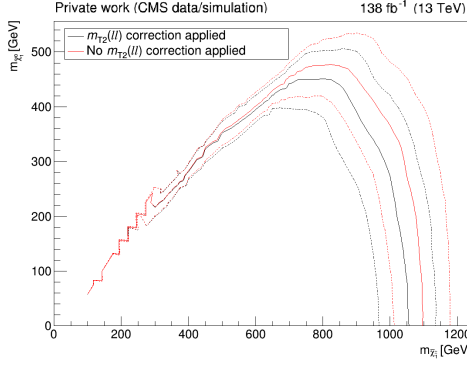


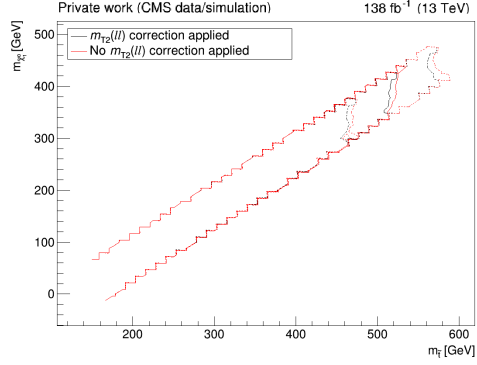
Figure 8.8: Left: distributions of $m_{T2}(\ell\ell)$ in $WZ \rightarrow 3\ell 1\nu$ events with $p_T^{\text{miss}} > 160$ GeV after the WW emulation. Data from all the data-taking years have been merged to increase statistics. The last bin includes the overflow entries. In the bottom panel, the ratio of data and SM expectations is shown. The hatched band represents the total uncertainty, including the sources discussed in Section 8.5. Middle: same as the left plot for events with $p_T^{\text{miss}} > 100$ GeV. Right: linear fit of the ratio of the (background-subtracted) observed events to the expected WZ events with $p_T^{\text{miss}} > 100$ GeV.

Lastly, The effect of the $m_{T2}(\ell\ell)$ correction on the expected (blinded) exclusion regions is studied, both for the chargino and top squark signal models, as displayed on Figs. 8.9a and 8.9b. Further studies have been performed in this CR to test the modelling of the observable quantities entering the computation of the $m_{T2}(\ell\ell)$ in events with high p_T^{miss} . An imperfect agreement is observed in the bulk of the distribution of the minimum azimuthal distance between the p_T^{miss} and any lepton in the event ($\Delta\phi^{\text{min}}(\ell, p_T^{\text{miss}})$) for $p_T^{\text{miss}} \geq 380$ GeV, as observed in Figure 8.10 (left). We fit the background subtracted data/WZ ratio by an appropriate function (chosen as the ratio of two exponentials: $(A + B * \exp(C * x)) / (D + E * \exp(F * x))$) to derive an uncertainty for the background processes in events in this p_T^{miss} range (Fig. 8.10, right). The effect of this additional

Figure 8.9: Impact of the $m_{T2}(\ell\ell)$ tail correction on the expected (blinded) exclusion regions for:



(a) Chargino pair production, with the chargino decaying into a charged lepton, a neutrino, and a neutralino via an intermediate slepton



(b) Top squark pair production, with the top squark subsequently decaying into a top quark and a neutralino.

uncertainty on the expected (blinded) exclusion regions is found to be very small, as shown in Figure 8.11.

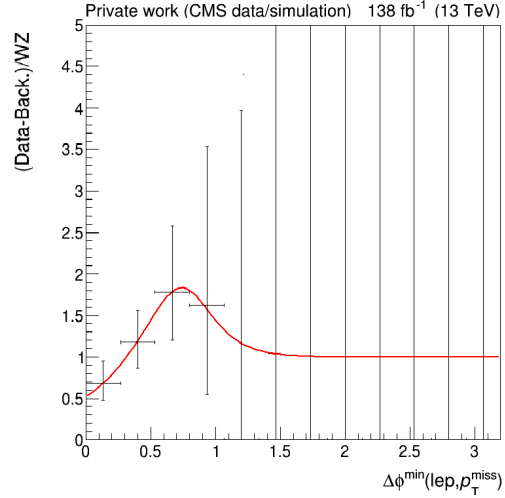
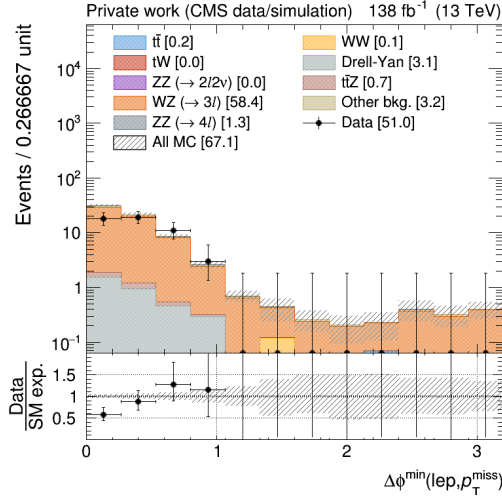
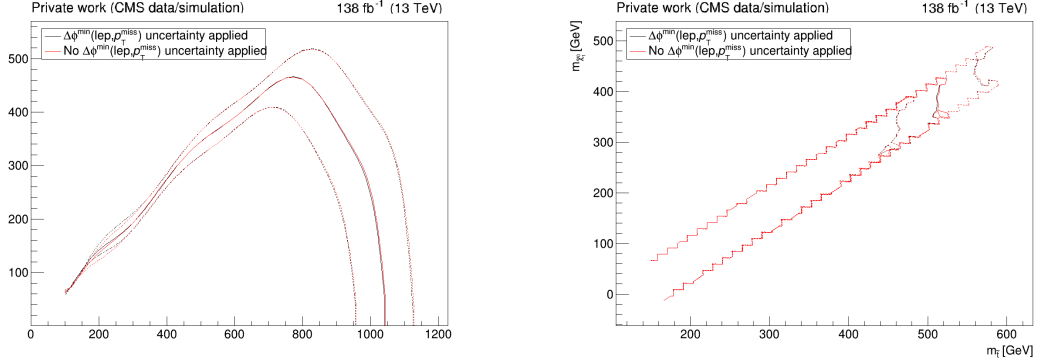


Figure 8.10: Left: observed and expected distributions of the minimum azimuthal distance between the p_T^{miss} and any lepton in the event in $WZ \rightarrow 3\ell 1\nu$ events with $p_T^{\text{miss}} > 380$ GeV after the WW emulation. In the bottom panel, the ratio of data and SM expectations is shown. The hatched band represents the total uncertainty, including the sources discussed in Section 8.5. Right: fit of the ratio of the (background-subtracted) observed events to the expected WZ events with $p_T^{\text{miss}} > 380$ GeV.

Figure 8.11: Impact of the additional $\Delta\phi^{\min}(\ell, p_T^{\text{miss}})$ uncertainty on the expected (blinded) exclusion regions for:



(a) Chargino pair production, with the chargino decaying into a charged lepton, a neutrino, and a neutralino via an intermediate slepton

(b) Top squark pair production, with the top squark subsequently decaying into a top quark and a neutralino.

Nonprompt leptons

Another potential source of mismodelling in the $m_{T2}(\ell\ell)$ distribution tails is the existence of events with nonprompt leptons, which might come from either semileptonic decays of B hadrons in b jets or from hadronic jets accidentally meeting the lepton criteria. The value of $m_{T2}(\ell\ell)$ in $t\bar{t}$, tW , and WW events with one nonprompt lepton replacing a prompt one failing the selection requirements will not be bound by the m_W endpoint. These events are significant since, even though they contribute less than 1% of the expected background in the various SRs, they can still account for up to 20% of the $t\bar{t}$ background at high $m_{T2}(\ell\ell)$ and p_T^{miss} values.

We study the modelling of the nonprompt lepton rate in simulated events by selecting events with two leptons with the same charge. Events with $p_T^{\text{miss}} > 160$ GeV are selected, and data from each of the three data-taking years are considered separately. As presented in Section 8.2.1, 2016 data are split in two different eras, pre-VFP and post-VFP, which are analysed separately. Example distributions for several variables used in the SR definition are presented in Fig. 8.12. Across all data-taking years, data shows a mild excess with respect to the SM predictions. In order to cover from that effect, a scale factor K_{norm} is derived from this observed surplus, thus adjusting the nonprompt lepton rate expected by the simulation for each era. It is defined as:

$$K_{\text{norm}} = \frac{N_{\text{Data}} - \sum_{\text{bkg} \neq \text{non-prompt}} N_{\text{bkg}}}{N_{\text{non-prompt}}} \quad (8.4)$$

Where N_{data} , $N_{\text{non-prompt}}$ and N_{bkg} represent the number of observed events, the number of simulated events with at least one nonprompt lepton, and the number of simulated events without nonprompt leptons, respectively. Similarly, the uncertainty of this scale factor is determined by fitting its dependence on several observables (p_T^{miss} , jet and b -tagged jet multiplicity, leading jet and lepton p_T , $m_{T2}(\ell\ell)$, depicted in Fig. 8.12) to a linear function and taking the maximum deviation from the central estimate. The results are summarised in Table 8.6. These scale factors are used as an extra weight for events with a nonprompt lepton in all simulated datasets.

We also study how the simulation models the shape of the $m_{T2}(\ell\ell)$ distributions in events with nonprompt leptons by analysing events where a third lepton meets the veto lepton conditions but fails to meet the criteria for analysis lepton selection. To emulate events with nonprompt leptons in the SRs, we randomly elevate the third lepton to the level of one of the two primary leptons and recalculate the $m_{T2}(\ell\ell)$ with the newly formed lepton pair. During this process, the p_T of the excluded lepton is not incorporated into the event \vec{p}_T^{miss} , as a lepton that does not

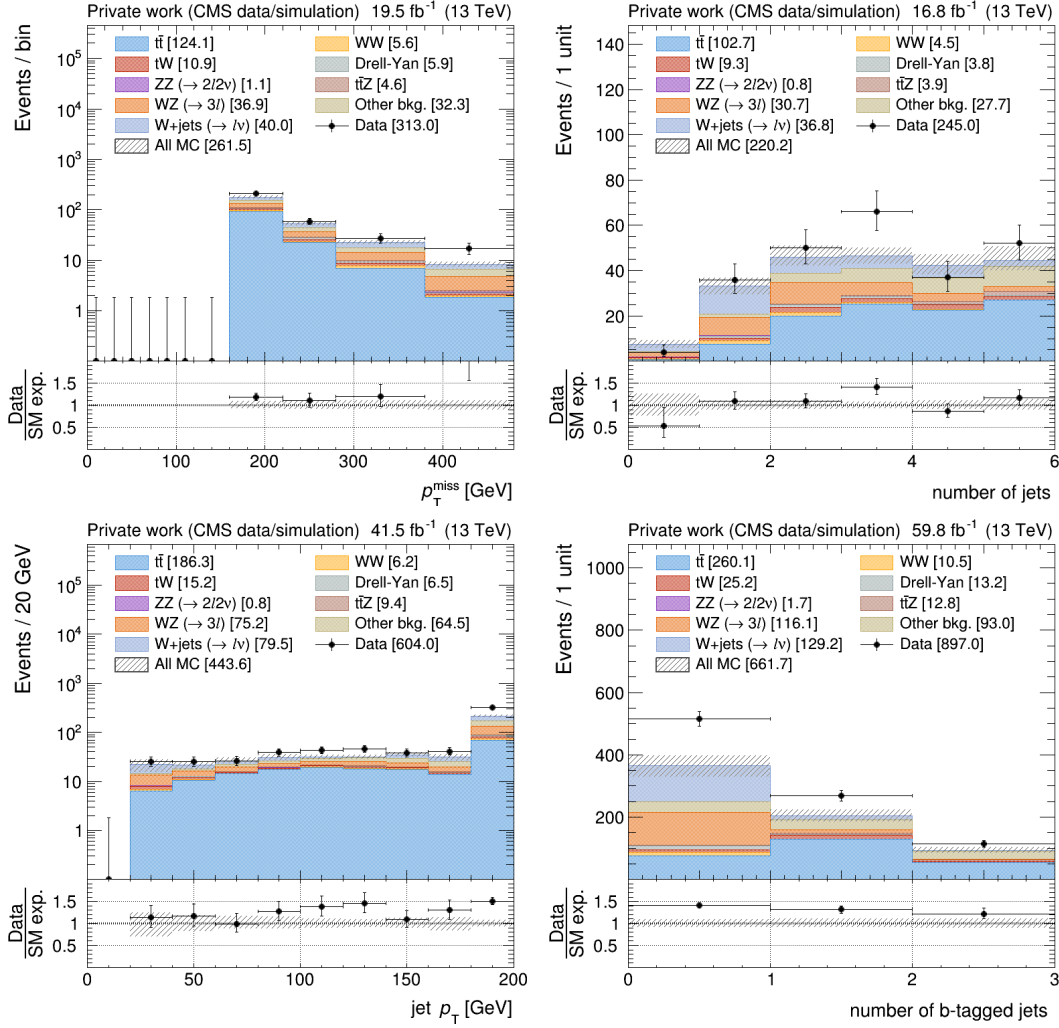


Figure 8.12: Examples of the observed distributions for different selection variables in the same-charge CR with $p_T^{\text{miss}} > 160$ GeV: p_T^{miss} in 2016 pre-VFP events (top left plot), jet multiplicity in 2016 post-VFP events (top right), leading jet p_T in 2017 events (bottom left), and b-tagged jet multiplicity in 2018 events (bottom right) data. The last bin includes the overflow entries. In the bottom panel, the ratio of data and SM expectations is shown. The hatched band represents the total uncertainty, including the sources discussed in Section 8.5.

Table 8.6: Normalisation scale factors for the nonprompt lepton rate for each of the four data-taking periods.

year	value
2016preVFP	1.18 ± 0.30
2016postVFP	1.10 ± 0.40
2017	1.38 ± 0.29
2018	1.36 ± 0.25

satisfy the analysis identification and isolation requirements is still likely to have created a track or made an energy deposit in the calorimeter. A b-tagged jet is also required in order to suppress diboson production events, which may produce events with three leptons. The resulting $m_{T2}(\ell\ell)$ distributions, presented for the combination of the three years of data acquisition, are shown in Fig. 8.13, where a good agreement is observed between the recomputed $m_{T2}(\ell\ell)$ shape in the data and the simulations.

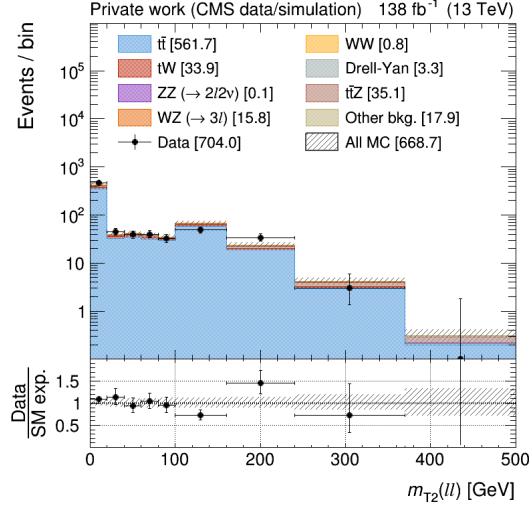


Figure 8.13: Distributions of $m_{T2}(\ell\ell)$ computed after swapping one of the leptons by a third one, passing the veto lepton requirements but failing the analysis lepton selection. Events from the three data-taking years have been merged. The last bin includes the overflow entries. In the bottom panel, the ratio of data and SM expectations is shown. The hatched band represents the total uncertainty, including the sources discussed in Section 8.5.

8.4.2 Normalization and modelling of subleading background processes

WZ production

Events stemming from WZ production enter the signal event selection when both bosons undergo a leptonic decay, and one of the three decay leptons does not meet the veto lepton criteria. The modelling of this background is evaluated using a CR that consists of exactly three leptons and no b-tagged jets. The normalisation of WZ events is studied as a function of the main variables that define the SRs (p_T^{miss} and the jet multiplicity). This way, figure 8.14 displays the observed versus expected p_T^{miss} distributions for each year of data-taking. Similarly, Figure 8.15 presents the jet multiplicity in events with $p_T^{\text{miss}} > 160$ GeV. On the whole, data are found to describe well the SM predictions. In order to constrain the normalisation of the WZ background in the SRs, the CRs are incorporated into the ML fit that extracts the signal, based on the event selection outlined in this section and using the same p_T^{miss} and jet multiplicity bins as in the SR definition described in Section 8.3.1.

Figure 8.14: Distributions of p_T^{miss} in events with exactly three leptons and no b-tagged jets. The same binning used to define the SRs is shown. The last bin includes the overflow entries. In the bottom panel, the ratio of data and SM expectations is shown. The hatched band represents the total uncertainty, including the sources discussed in Section 8.5. Results are shown for:

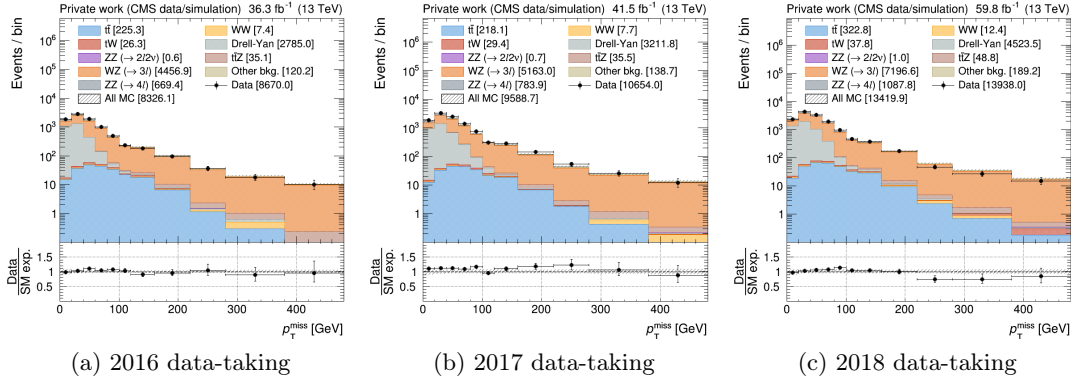
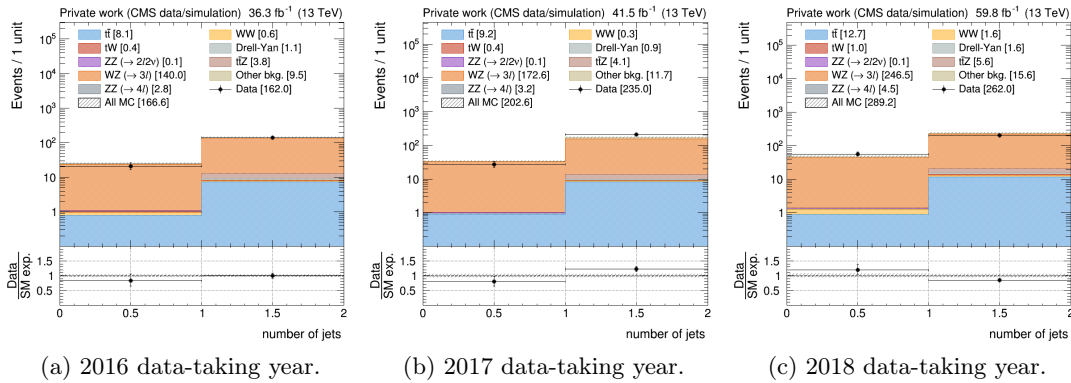


Figure 8.15: Same as for Fig. 8.14 but for jet multiplicity. Results are shown for:



The modelling of the $m_{T2}(\ell\ell)$ distributions in WZ events is also assessed using the same events. From the three prompt leptons resulting from the vector boson decays, there are two potential combinations to create an OC lepton pair: one involves the lepton from the W boson decay paired with the OC lepton from the Z boson decay (referred to as mixed pair), while the other uses the lepton pairs from the Z boson decay (Z pair). The expected contributions of these two WZ background components to the search region are compared in Fig. 8.16. At lower $m_{T2}(\ell\ell)$ values, mixed pairs are the primary contributors. However, they reach a kinematic endpoint

around the W and Z boson mass values. In contrast, Z pairs, which do not have this endpoint, become the leading contributors at higher $m_{T2}(\ell\ell)$ values.

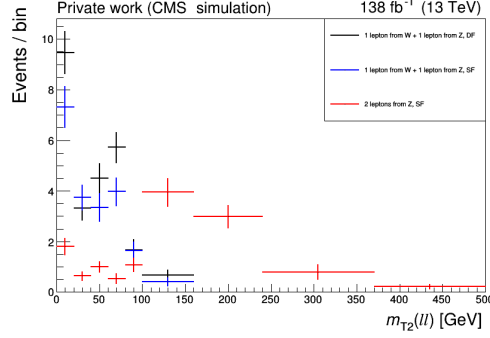


Figure 8.16: Expected contributions of the WZ background to the search region, divided by leptons' flavour and origin.

The observed versus expected $m_{T2}(\ell\ell)$ distributions for Z pairs and mixed pairs in the WZ CR are illustrated in Fig. 8.17. In order to avoid possible normalisation biases, the WZ distributions are normalised to data using the same WZ CR bins previously mentioned for the ML fit. It is worth noting again the different shape of the $m_{T2}(\ell\ell)$ distributions for the two lepton pair choices: when the W boson lepton is selected, the $m_{T2}(\ell\ell)$ has a natural endpoint at the m_W , while when the lepton pair from the Z boson decay is used the $m_{T2}(\ell\ell)$ distribution exhibits a larger tail. The expected distribution for Z-boson lepton pairs seems to underpredict the data at large $m_{T2}(\ell\ell)$. We cover possible mismodellings by setting an uncertainty of the size of the observed discrepancy for WZ events with $m_{T2}(\ell\ell) \geq 370$ GeV.

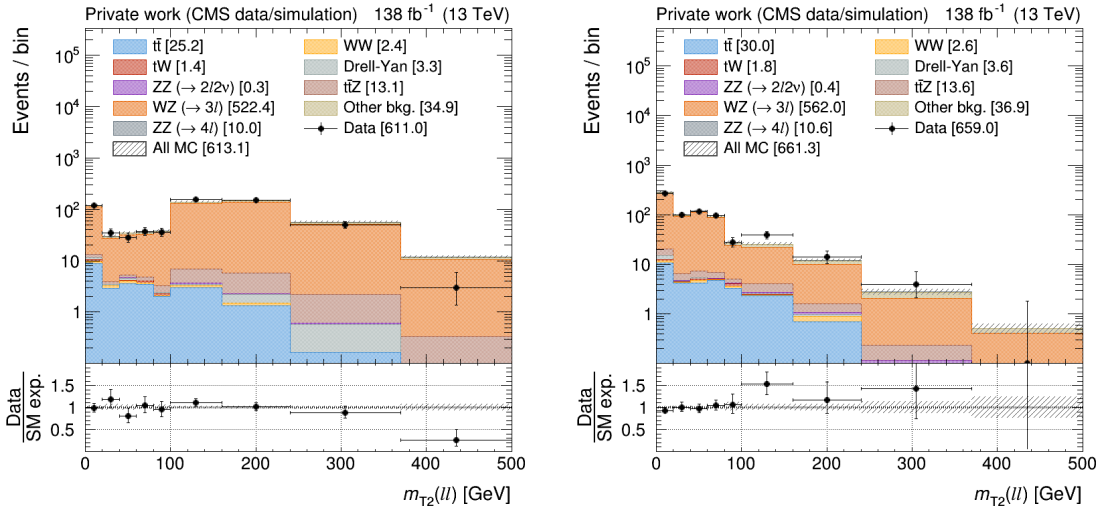


Figure 8.17: Left: Distributions of $m_{T2}(\ell\ell)$ in events with exactly three leptons, no b-tagged jets, and $p_T^{\text{miss}} > 160$ GeV. The $m_{T2}(\ell\ell)$ observable is computed using OC lepton pairs where both leptons come from the candidate Z boson. Data from all the data-taking years have been merged to increase statistics. WZ expectations are normalized to data for each data-taking year in the same CR bins described in the text for the ML fit. The last bin includes the overflow entries. In the bottom panel, the ratio of data and SM expectations is shown. The hatched band represents the total uncertainty, including the sources discussed in Section 8.5. Right: same as in the left plot, when the $m_{T2}(\ell\ell)$ observable is computed using OC lepton pairs where just one lepton comes from the candidate Z boson, and the other comes from the candidate W boson.

ZZ events

The ZZ background consists primarily of events where one boson decays into charged leptons and the other into neutrinos. In order to examine this contribution, the $ZZ \rightarrow 2\ell 2\nu$ production is simulated using $ZZ \rightarrow 4\ell$ events. In this process, the \vec{p}_T^{miss} of one of the reconstructed Z bosons (randomly selected from those meeting the $|m_{\ell\ell} - m_Z| < 15 \text{ GeV}$ criteria) is added to the \vec{p}_T^{miss} . Events are selected by requiring four leptons, where one lepton is allowed to meet the looser veto lepton criteria, thus enhancing the acceptance for ZZ production. Events are required to have four leptons that can be grouped into two OC SF pairs, each having an invariant mass exceeding 30 GeV, with at least one pair with invariant mass within 15 GeV of the Z boson mass.

We then use the events thus reconstructed to perform normalisation studies along the lines followed for the WZ background, detailed in Section 8.4.2. Figures 8.18 and 8.19 display the observed and expected distributions of p_T^{miss} and jet multiplicity in ZZ events for each year of data taking. Just as for the WZ production, CRs are incorporated into the ML fit to constrain the normalisation of the ZZ background, using the same p_T^{miss} and jet multiplicity bins defined in the SR.

Figure 8.18: Distributions of p_T^{miss} in $ZZ \rightarrow 4\ell$ events after the $ZZ \rightarrow 2\ell 2\nu$ emulation. The same binning used to define the SRs is shown. The last bin includes the overflow entries. In the bottom panel, the ratio of data and SM expectations is shown. The hatched band represents the total uncertainty, including the sources discussed in Section 8.5. Results are shown for:

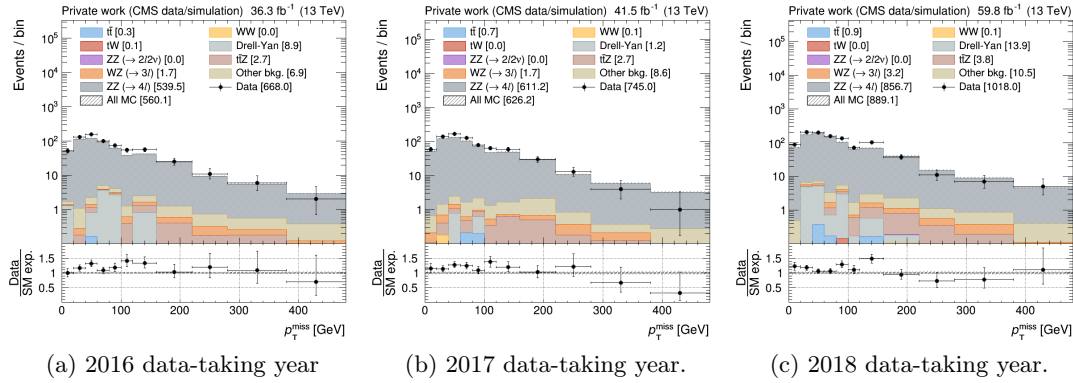
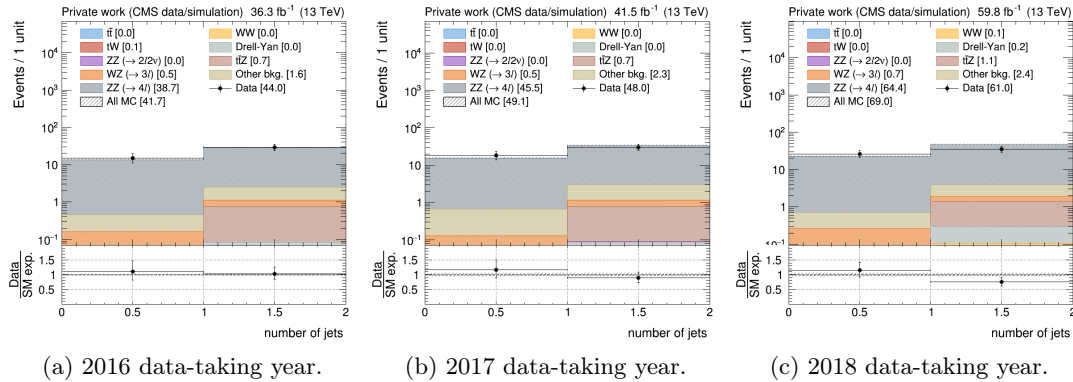


Figure 8.19: Same as for Fig. 8.18 but for jet multiplicity. Results are shown for:



A comparison between the observed and expected $m_{T2}(\ell\ell)$ distributions in $ZZ \rightarrow 2\ell 2\nu$ emulated events with $p_T^{\text{miss}} > 160 \text{ GeV}$ is given in Fig. 8.20. As done for the WZ background study, ZZ expectations are scaled to match data events in each ZZ CR bin described above. The agreement is reasonable within the limited statistics available.

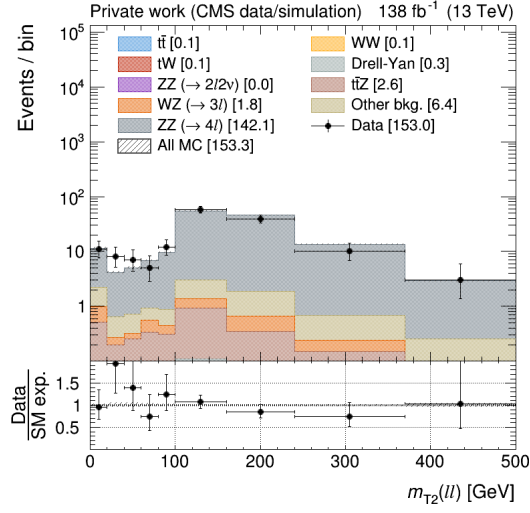


Figure 8.20: Distributions of $m_{T2}(\ell\ell)$ in $ZZ \rightarrow 4\ell$ events with $p_T^{\text{miss}} > 160$ GeV after the $ZZ \rightarrow 2\ell 2\nu$ emulation. Data from all the data-taking years have been merged to increase statistics. ZZ expectations are normalized to data for each data-taking year in the same CR bins described in the text. The last bin includes the overflow entries. In the bottom panel, the ratio of data and SM expectations is shown. The hatched band represents the total uncertainty, including the sources discussed in Section 8.5.

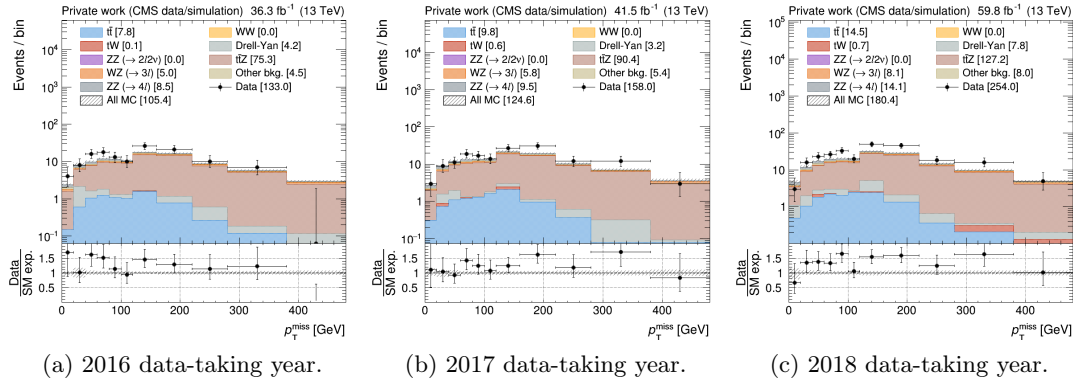
$t\bar{t}Z$ background

The production of $t\bar{t}Z$ events, where both W bosons from the decays of the top quarks undergo leptonic decay and the Z boson decays into neutrinos, results in final states that are experimentally similar to the signal events. The reconstructed $m_{T2}(\ell\ell)$ distribution lacks a natural endpoint due to the additional contribution of the neutrinos from the Z boson decay to the \vec{p}_T^{miss} .

To evaluate the normalisation and the modelling of the $t\bar{t}Z$ production, two CRs are defined. The common CR selection aims at reconstructing $t\bar{t}Z$ events where the Z boson decays into charged leptons by requiring at least three leptons and two jets with $p_T > 20$ GeV, of which at least one is tagged as b-jet. At least one pair of OC SF leptons with an invariant mass not further than 15 GeV from the Z boson mass is also required, and the \vec{p}_T of the reconstructed Z boson is added to the \vec{p}_T^{miss} .

The CR for testing the normalisation of the $t\bar{t}Z$ background is obtained by further requiring two b-tagged jets if exactly three leptons are present in the event. Figure 8.21 shows the observed and expected distributions of p_T^{miss} for each data-taking year. An excess of events is found in data, which we describe in the ML fit by letting the $t\bar{t}Z$ production be normalized in dedicated CRs, based on the $t\bar{t}Z$ emulation presented in this section and divided in the same p_T^{miss} bins used in the SR definition.

Figure 8.21: Distributions of p_T^{miss} in $t\bar{t}Z \rightarrow 4\ell$ events after the $t\bar{t}Z \rightarrow 2\ell$ emulation. The same binning used to define the SRs is shown. The last bin includes the overflow entries. In the bottom panel, the ratio of data and SM expectations is shown. The hatched band represents the total uncertainty, including the sources discussed in Section 8.5. Results are shown for:



Similarly, We study the modelling of the $m_{T2}(\ell\ell)$ distribution for the $t\bar{t}Z$ background by selecting events with a fourth lepton passing the veto lepton requirements. Fig 8.22 shows the observed and expected distributions of the $m_{T2}(\ell\ell)$ reconstructed out of the two leptons not associated to the reconstructed Z boson, where albeit the statistical power of this test is limited, it still allows large $m_{T2}(\ell\ell)$ mismodelling to be ruled out.

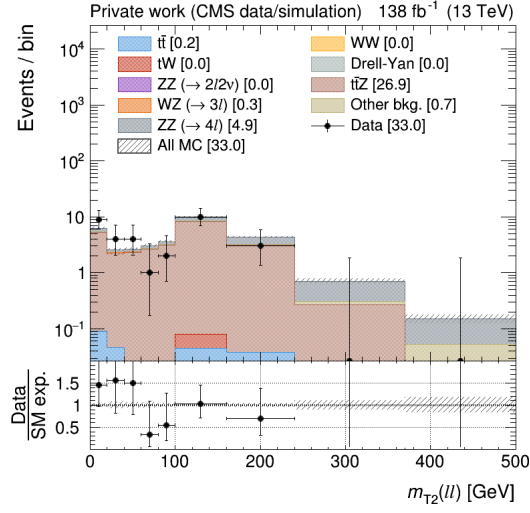


Figure 8.22: Distributions of $m_{T2}(\ell\ell)$ in $t\bar{t}Z \rightarrow 4\ell$ events with $p_T^{\text{miss}} > 160$ GeV after the $t\bar{t}Z \rightarrow 2\ell$ emulation. Data from all the data-taking years have been merged to increase statistics. $t\bar{t}Z$ expectations are normalized for each data-taking year in the same CR bins described in the text. The last bin includes the overflow entries. In the bottom panel, the ratio of data and SM expectations is shown. The hatched band represents the total uncertainty, including the sources discussed in Section 8.5.

Drell–Yan production

While most of the DY events fail the p_T^{miss} requirement of the baseline selection, a fraction of them still enters in the SRs because of inaccuracies in the p_T^{miss} measurement. Given the large cross section of the DY process, this becomes a non-negligible background. We study the modelling of the DY production in events with exactly two OC SF leptons with $|m_{\ell\ell} - m_Z| < 15 \text{ GeV}$ and no b-tagged jets. The $m_{T2}(\ell\ell)$ distributions for events with $p_T^{\text{miss}} > 160 \text{ GeV}$ across the three data-taking years are depicted in Fig. 8.23. In the $m_{T2}(\ell\ell)$ tails, the DY contribution is found to be relatively smaller than that from diboson production.

In the 2017 data for the EOY production, a significant mismodelling was observed at lower $m_{T2}(\ell\ell)$ values. Fig. 8.24 compares the $m_{T2}(\ell\ell)$ distributions for 2017 events in EOY (on the left) and UL (on the right) datasets. A significant improvement in the modelling of the DY events is observable, driven by the treatment of the EE noise issue integrated in the UL production.

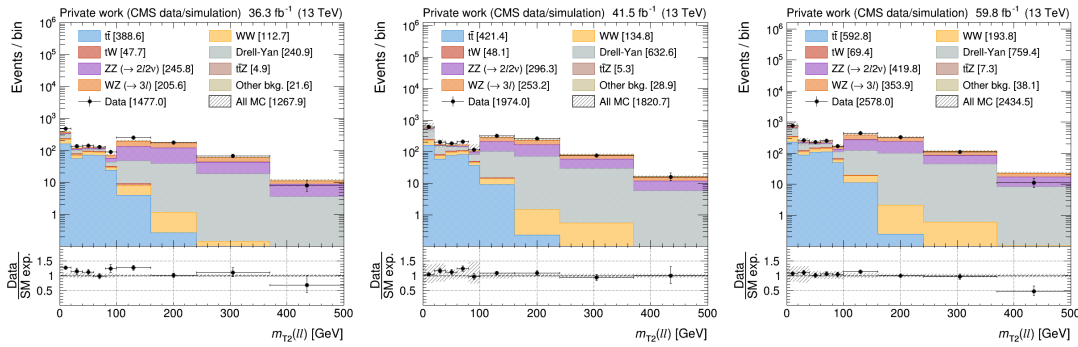


Figure 8.23: Distributions of $m_{T2}(\ell\ell)$ in SF events with $|m_{\ell\ell} - m_Z| < 15 \text{ GeV}$, $p_T^{\text{miss}} > 160 \text{ GeV}$, and no b-tagged jets for 2016 (left plot), 2017 (middle), and 2018 (right) data. The last bin includes the overflow entries. In the bottom panel, the ratio of data and SM expectations is shown. The hatched band represents the total uncertainty, including the sources discussed in Section 8.5.

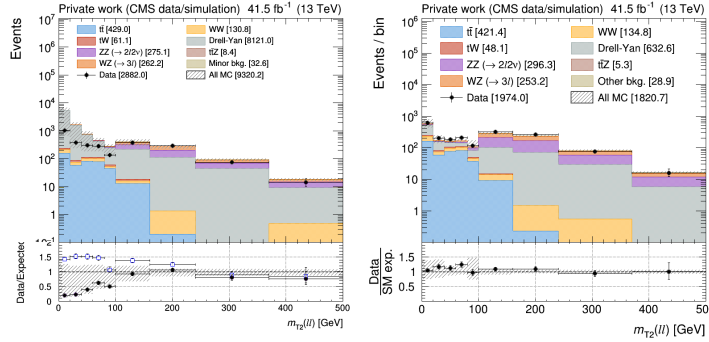


Figure 8.24: Distributions of $m_{T2}(\ell\ell)$ in SF events with $|m_{\ell\ell} - m_Z| < 15 \text{ GeV}$, $p_T^{\text{miss}} > 160 \text{ GeV}$, and no b-tagged jets for 2017 data with the EOY (left) and UL (right) productions. The last bin includes the overflow entries. The open blue squares in the EOY plot show the SM predictions with no jet energy resolution (JER) smearing of jet p_T applied. In the bottom panel, the ratio of data and SM expectations is shown. The hatched band represents the total uncertainty, including the sources discussed in Section 8.5.

8.5 Uncertainties

In science in general, the uncertainty in a measurement is intrinsically tied to both the nature of the system being measured, and the instruments used for the measurement. This section attempts to describe such measurement uncertainties.

8.5.1 Statistical uncertainties

Statistical uncertainty arises from the inherent fluctuations when sampling a random variable with a limited number of events. In these cases, the uncertainty diminishes as the sample size grows. Common causes of statistical uncertainty include random variations from detector noise, stringent selection criteria, or a limited number of generated events.

In this document, the statistical uncertainties of both data and simulation are considered. As for the former, the event count in every SR and within each bin of the $m_{T2}(\ell\ell)$ distributions is employed to determine the signal strength via the ML fit, whereas for the latter, the impact of the size of the simulated samples on the modelling of the $m_{T2}(\ell\ell)$ distributions is considered.

8.5.2 Systematic uncertainties

Systematic uncertainties pertain to errors introduced by the measurement methodologies themselves, and their thorough study is of paramount importance in high energy physics. While other definitions exist, a systematic uncertainty is commonly described simply as an uncertainty in a measurement that is not due to statistical fluctuations in data (also including simulated data). Examples of systematic uncertainties typically considered include the uncertainties on the detector resolution or calibration, on the reconstruction and identification of physics objects (e.g. electrons, jets...), on the modelling of signal and background processes. In this analysis, the following sources of systematic uncertainties have been considered:

Uncertainties on the normalisation and $m_{T2}(\ell\ell)$ shape of background and signal events

- ◆ **Luminosity:** The overall uncertainty in the integrated luminosity is estimated to be between 1.2 and 2.5% [239, 240, 241]. The correlations of these uncertainties between the data-taking years are taken into account.
- ◆ **Trigger efficiency:** The uncertainty in the measured trigger efficiency is 2%.
- ◆ **Pile-up:** The recommended pp inelastic cross section is varied by $\pm 4.6\%$ [242], and new pileup weights are computed and propagated through the analysis.
- ◆ **JER and JES:** The jet energy resolution (JER) and jet energy scale (JES) are varied by their uncertainty [243], and the changes are propagated to all the related observables in the event.
- ◆ **Jet unclustered energy:** The energy scale of the low- p_T particles that are not clustered in jets is varied by its uncertainty, and the changes are propagated to the \vec{p}_T^{miss} .
- ◆ **Prefiring uncertainties:** The uncertainties in the prefiring correction factors are propagated in 2016 and 2017 samples.
- ◆ **Lepton identification and isolation:** Lepton identification and isolation efficiencies are corrected by data-to-simulation scale factors measured in $Z \rightarrow \ell\ell$ events. The corresponding uncertainties are typically smaller than 2% per lepton.
- ◆ **Uncertainties on the additional cuts:** The uncertainties in the efficiencies of the additional cuts applied in the lepton selection, as measured in Appendix C, vary between

1% and 5%, depending on the p_T , η and flavour of the lepton.

- ◆ **Lepton p_T scale:** The uncertainties in the lepton p_T 's scales are neglected, as their effect on the $m_{T2}(\ell\ell)$ is much smaller than the one due to the uncertainties in the p_T^{miss} (from JES, JER, unclustered energy, and pileup).
- ◆ **B-jet identification:** The efficiencies and misidentification rates of the b-jet identification algorithms are also corrected by data-to-simulation scale factors measured in inclusive jet and $t\bar{t}$ events [244]. The respective uncertainties range between 1 and 6%, depending on the p_T and η of the jets.
- ◆ **Renormalisation and factorisation:** Uncertainties in the renormalisation and factorisation scales, and PDFs are propagated by taking the largest changes in the acceptance when independently doubling and halving the renormalisation and factorisation scales, and by using the NNPDF3.1 replicas of the PDFs according to PDF4LHC recommendations [245]. The PDFs uncertainties are not considered for signal models as they are found to be redundant, once the uncertainty in the ISR modelling is included.

Specific uncertainties in the modelling of the SM processes

- ◆ **Background normalisation:** The uncertainty of the background normalisation is applied separately for each background. The normalisations of the main backgrounds, namely top ($t\bar{t}$ and tW), WW , WZ , ZZ , and $t\bar{t}Z$ production, are determined by the ML fit, as depicted in Section 9. In order to account for the tW 's relative normalisation with the $t\bar{t}$ production and potential interference effects between them, an additional 10% uncertainty is assigned to the tW process. Other minor backgrounds whose normalization is not constrained in the fit are assigned a conservative uncertainty of 50%.
- ◆ **Modelling of events with no jets:** The modelling of the yields of events with no jets has been explicitly studied for WZ and ZZ production, as described in Section 8.4.2. For these backgrounds, separate free parameters are used in the ML fit to constrain their rates in the chargino search regions with and without jets to the rates observed in the respective CRs. For the top and WW processes, we introduce a related uncertainty by adding free parameters in the ML fit, scaling their respective rate of events with no jets. The total number of expected events without b-tagged jets is then constrained to remain invariant, so that only a migration of top and WW events between the SRs with and without jets is allowed.
- ◆ **Modelling of $m_{T2}(\ell\ell)$ tails:** Uncertainties in the modelling of the $m_{T2}(\ell\ell)$ tails are set based on the studies presented in Section 8.4.1. For the backgrounds with a kinematic endpoint at the W boson mass, a correction to the $m_{T2}(\ell\ell)$ tails is derived, together with its uncertainty. For the WZ production, an uncertainty of 75% is set above 370 GeV. These systematic uncertainties are taken as uncorrelated through the p_T^{miss} bins.
- ◆ **Modelling of $\Delta\phi^{\text{min}}(\ell, p_T^{\text{miss}})$:** An uncertainty to account for the observed mismodelling in $\Delta\phi^{\text{min}}(\ell, p_T^{\text{miss}})$ for events with $p_T^{\text{miss}} \geq 380$ GeV is also set, as discussed in Section 8.4.1.
- ◆ **nonprompt weights:** The weight of events with nonprompt leptons in simulated samples is varied by the uncertainty in the correction factors derived in events with two same-charge leptons, as described in Section 8.4.1.
- ◆ **Top quark spectrum:** The top quark p_T spectrum measured in $t\bar{t}$ events is found to be softer in data than in simulated events [246, 247, 248]. In order to cover this difference, an additional systematic uncertainty is included, derived from the observed variations when reweighting the $t\bar{t}$ events to the p_T distribution observed in data.

Additional uncertainties in the signal modelling

- ◆ **FastSim lepton identification efficiency:** The uncertainty in the lepton identification efficiency in events simulated with FastSim, relative to the full detector simulation, is estimated to be 2% per lepton.
- ◆ **FastSim b-jet identification efficiency:** The b-tagging efficiency in FastSim samples, relative to the FULLSIM uncertainty, is found to range between 0.2–0.5%.
- ◆ **FastSim \vec{p}_T^{miss} modelling:** The modelling of \vec{p}_T^{miss} in FastSim events is computed by comparing the acceptances determined using the \vec{p}_T^{miss} at the generator level to those after event reconstruction. The central value for the acceptance is derived from the average of these two values, while the uncertainty is set as half the difference between them and is fully correlated across bins.
- ◆ **ISR reweighting:** Simulated signal events are reweighted to improve the modelling of the jets from ISR, as described in Section 7.3. Uncertainties on the reweighting procedure are derived from closure tests.

A procedure has been developed for smoothing the variations in the $m_{T2}(\ell\ell)$ distributions due to the uncertainties in JES, JER, and unclustered energy in bins with low statistics, as described in Appendix F.

Correlations in the ML fit

In the ML fit, the correlations of each source of systematic uncertainty across the search regions and data-taking years are taken into account as follows: uncertainties of a theoretical nature (pp inelastic cross section, renormalisation and factorisation scales, PDFs) are treated as correlated across all data-taking years and search regions; uncertainties related to the detector performance (trigger efficiencies, object reconstruction efficiencies, jet energy scale and resolutions, etc.) are treated as uncorrelated across data-taking years (but for specific POG recommendations such as luminosity and b-tagging efficiencies where the uncertainties are broken down into correlated and uncorrelated contributions); uncertainties in the modelling of the $m_{T2}(\ell\ell)$ observable at high p_T^{miss} (from the studies presented in Section 8.4) are treated as correlated across data-taking years and uncorrelated across p_T^{miss} bins.

Table 8.7 provides a summary of the sources of uncertainty, the corresponding nuisance parameters in the ML fit, and the correlation of each of them across data-taking years and p_T^{miss} bins.

8.5.3 Uncertainties in the SR yields

In this section, the effect of each of the previously mentioned uncertainties is quantified for the predicted yields in the SRs of the chargino and top squark searches (as described in Section 8.3.1), for both the SM processes (Tables 8.8 and 8.9) and two representative signal mass hypotheses, one of the chargino pair production (Table 8.10) and another for the top squark pair production (Table 8.11).

Table 8.7: A summary of the sources of uncertainty, the corresponding nuisances in the ML fit data cards, and their correlation across data-taking years and p_T^{miss} bins.

Source Uncertainty	Nuisance	Correlated	
		By year	By p_T^{miss}
Integrated luminosity	<i>lumi</i>	partially	✓
Trigger efficiency	<i>trigger</i>	✗	✓
Pileup	<i>CMS_pileup</i>	✓	✓
Jet energy scale	<i>CMS_jesTotal</i>	✗	✓
Jet energy resolution	<i>CMS_jer</i>	✗	✓
Unclustered energy	<i>CMS_unclustEn</i>	✗	✓
Prefiring	<i>CMS_prefiring</i>	✗	✓
Lepton Reconstruction	<i>CMS_lepReco</i>	✗	✓
Lepton ident./isolation	<i>CMS_lepIdIso</i>	✗	✓
b tagging	<i>CMS_btag</i>	partially	✓
b tagging (misidentification)	<i>CMS_mistag</i>	partially	✓
b tagging (light jets)	<i>CMS_ctag</i>	✗	✓
Simulated samples statistics	<i>prop_bin</i>	✗	✗
Renorm./fact. scales	<i>CMS_qcdScale</i>	✓	✓
PDFs	<i>CMS_pdf</i>	✓	✓
Drell-Yan normalization	<i>normDYall</i>	✗	✓
tW normalization	<i>normSTtWall</i>	✗	✓
Minor bkg. normalization	<i>normminorall</i>	✗	✓
$m_{T2}(\ell\ell)$ tails (m_W endpoint)	<i>WWtails</i>	✓	✗
$m_{T2}(\ell\ell)$ tails (WZ)	<i>CMS_WZbin</i>	✗	✗
Nonprompt leptons	<i>CMS_nonpromptLep</i>	✗	✓
$t\bar{t}$ p_T reweighting	<i>CMS_toppt</i>	✓	✓
Lepton ident./isolation (FASTSIM)	<i>CMS_lepIdIsoFS</i>	✗	✓
b tagging (FASTSIM)	<i>CMS_btagFS</i>	✗	✓
b tagging (misidentification, FASTSIM)	<i>CMS_mistag</i>	✗	✓
b tagging (light jets, FASTSIM)	<i>CMS_ctagFS</i>	✗	✓
ISR reweighting	<i>CMS_isrFS</i>	✓	✓
p_T^{miss} (FASTSIM)	<i>CMS_ptmissfastsim</i>	✓	✓
Top normalization	<i>topnorm</i>	✗	✗
WW normalization	<i>WWnorm</i>	✗	✗
WZ normalization	<i>[CR name]_WZ</i>	✗	✗
ZZ normalization	<i>[CR name]_ZZ</i>	✗	✗
$t\bar{t}Z$ normalization	<i>[CR name]_ttZ</i>	✗	✗

Table 8.8: Size of the systematic uncertainties in the predicted yields of SM processes for the chargino search SRs (Top part of Table 8.2). The yields columns show the range of the uncertainties in the global background normalisation across the different data-taking years and SRs, for each p_T^{miss} bin separately. The $m_{T2}(\ell\ell)$ shape columns quantify the effect on the $m_{T2}(\ell\ell)$ shape. This is computed by taking the maximum variation across the $m_{T2}(\ell\ell)$ bins (after renormalising for the global change of all the distribution) in each SR. The range of this variation across the data-taking years and SRs is given for each p_T^{miss} bin separately.

Source of uncertainty	SR1 $160 \leq p_T^{\text{miss}} < 220 \text{ GeV}$		SR2 $220 \leq p_T^{\text{miss}} < 280 \text{ GeV}$		SR3 $280 \leq p_T^{\text{miss}} < 380 \text{ GeV}$		SR4 $p_T^{\text{miss}} \geq 380 \text{ GeV}$	
	Yields	$m_{T2}(\ell\ell)$ shape	Yields	$m_{T2}(\ell\ell)$ shape	Yields	$m_{T2}(\ell\ell)$ shape	Yields	$m_{T2}(\ell\ell)$ shape
Integrated luminosity	1-3%	—	1-3%	—	1-3%	—	1-3%	—
Trigger efficiency	2%	< 1%	2%	≤ 1%	2%	< 1%	2%	≤ 2%
Pileup	≤ 4%	3-9%	≤ 3%	3-19%	≤ 1%	2-13%	< 1%	5-13%
Jet energy scale	1-6%	3-10%	≤ 6%	2-10%	3-5%	2-8%	3-4%	2-9%
Jet energy resolution	1-5%	2-6%	1-3%	2-7%	1-2%	1-5%	1-2%	2-8%
Unclustered energy	1-5%	5-8%	2-5%	3-7%	1%	2-4%	1-2%	4-6%
Prefiring	1%	< 1%	1-2%	≤ 3%	1%	< 1%	≤ 1%	1-2%
Lepton reconstruction	< 1%	< 1%	< 1%	< 1%	< 1%	< 1%	< 1%	< 1%
Lepton ident./isolation	2-5%	≤ 5%	2-4%	1-5%	2-3%	1-5%	2-4%	1-11%
Lepton additional cuts	1-2%	< 1%	1-2%	≤ 1%	1%	≤ 2%	1%	≤ 2%
b tagging	3-5%	2-4%	3-5%	2-5%	2-4%	2-4%	2-3%	2-3%
b tagging (light jets)	< 1%	< 1%	< 1%	≤ 6%	< 1%	< 1%	< 1%	≤ 2%
Simulated samples statistics	≤ 6%	4-22%	1-10%	11-58%	1-2%	11-27%	2-3%	15-46%
Renorm./fact. scales	2-4%	1-4%	4-6%	3-12%	9%	5-6%	12-13%	8-10%
PDFs	≤ 1%	1-2%	1-2%	1-5%	1%	1-3%	2%	2-4%
Drell-Yan normalisation	1-7%	3-22%	≤ 6%	2-23%	4-7%	4-11%	4-7%	4-8%
tW normalisation	1%	≤ 2%	1-2%	1-2%	1%	1%	1%	1-2%
Minor bkg. normalisation	1-2%	1-3%	1-3%	1-9%	2%	1-3%	2-3%	1-6%
$m_{T2}(\ell\ell)$ tails (m_W endpoint)	1-3%	4-14%	1-5%	5-21%	1%	8-22%	1-2%	11-35%
$m_{T2}(\ell\ell)$ tails (WZ)	—	< 1%	< 1%	≤ 1%	< 1%	≤ 2%	< 1%	≤ 16%
Nonprompt leptons	< 1%	≤ 2%	< 1%	≤ 3%	< 1%	≤ 6%	< 1%	≤ 2%
tt p_T reweighting	1%	1-3%	1-2%	2-4%	2%	4%	2%	4-5%

Table 8.9: Same as in Table 8.8 for the top squark SRs (Bottom part of Table 8.2).

Source of uncertainty	SR1 $160 \leq p_T^{\text{miss}} < 220 \text{ GeV}$		SR2 $220 \leq p_T^{\text{miss}} < 280 \text{ GeV}$		SR3 $280 \leq p_T^{\text{miss}} < 380 \text{ GeV}$		SR4 $p_T^{\text{miss}} \geq 380 \text{ GeV}$	
	Yields	$m_{T2}(\ell\ell)$ shape	Yields	$m_{T2}(\ell\ell)$ shape	Yields	$m_{T2}(\ell\ell)$ shape	Yields	$m_{T2}(\ell\ell)$ shape
Integrated luminosity	1-3%	—	1-3%	—	1-3%	—	1-3%	—
Trigger efficiency	2%	< 1%	2%	< 1%	2%	< 1%	2%	< 1%
Pileup	≤ 2%	3-9%	≤ 1%	2-12%	≤ 1%	2-20%	< 1%	3-18%
Jet energy scale	3-8%	3-10%	3-7%	2-8%	3-6%	2-5%	3-6%	3-7%
Jet energy resolution	1-2%	2-8%	1-2%	2-8%	1-2%	2-5%	1-2%	2-8%
Unclustered energy	1-2%	5-10%	1-2%	3-7%	1-2%	2-11%	1-2%	3-13%
Prefiring	< 1%	≤ 1%	1%	< 1%	< 1%	< 1%	< 1%	≤ 1%
Lepton reconstruction	< 1%	< 1%	< 1%	< 1%	< 1%	< 1%	< 1%	< 1%
Lepton ident./isolation	2-4%	≤ 2%	2-3%	≤ 3%	1-3%	1-5%	2-4%	1-15%
Lepton additional cuts	1%	≤ 1%	1%	< 1%	1%	< 1%	1%	≤ 1%
b tagging	1-4%	≤ 4%	1-5%	≤ 4%	≤ 5%	≤ 2%	≤ 3%	≤ 6%
b tagging (light jets)	< 1%	≤ 2%	< 1%	≤ 3%	< 1%	≤ 1%	< 1%	≤ 2%
Simulated samples statistics	< 1%	4-18%	≤ 2%	5-21%	1-2%	12-29%	1-3%	18-37%
Renorm./fact. scales	2-3%	1-15%	5-6%	2-7%	10-16%	2-5%	13-23%	2-13%
PDFs	< 1%	≤ 1%	< 1%	≤ 2%	< 1%	≤ 2%	≤ 2%	≤ 9%
Drell-Yan normalisation	≤ 5%	≤ 26%	≤ 6%	≤ 16%	≤ 7%	≤ 8%	≤ 7%	≤ 7%
tW normalisation	< 1%	≤ 2%	1%	≤ 1%	1%	≤ 1%	1-2%	1-3%
Minor bkg. normalisation	< 1%	1-5%	≤ 1%	1-8%	≤ 2%	1-3%	1-3%	1-5%
$m_{T2}(\ell\ell)$ tails (m_W endpoint)	1-2%	5-14%	1%	6-16%	< 1%	5-14%	< 1%	5-20%
$m_{T2}(\ell\ell)$ tails (WZ)	—	< 1%	< 1%	< 1%	—	—	< 1%	≤ 7%
Nonprompt leptons	< 1%	≤ 8%	< 1%	≤ 7%	< 1%	≤ 2%	< 1%	≤ 3%
tt p_T reweighting	1-2%	2-3%	2-4%	2-6%	2-4%	1-3%	2-6%	1-4%

Table 8.10: Same as in Table 8.8 for a representative mass hypothesis of the chargino pair production model ($\tilde{\chi}_1^\pm \rightarrow \tilde{\ell}\nu(\ell\bar{\nu}) \rightarrow \ell\nu\tilde{\chi}_1^0$, with $m_{\tilde{\chi}_1^\pm} = 800$ GeV and $m_{\tilde{\chi}_1^0} = 200$ GeV).

Source of uncertainty	SR1 $160 \leq p_T^{\text{miss}} < 220$ GeV		SR2 $220 \leq p_T^{\text{miss}} < 280$ GeV		SR3 $280 \leq p_T^{\text{miss}} < 380$ GeV		SR4 $p_T^{\text{miss}} \geq 380$ GeV	
	Yields	$m_{T2}(\ell\ell)$ shape	Yields	$m_{T2}(\ell\ell)$ shape	Yields	$m_{T2}(\ell\ell)$ shape	Yields	$m_{T2}(\ell\ell)$ shape
Integrated luminosity	1-3%	—	1-3%	—	1-3%	—	1-3%	—
Trigger efficiency	2%	< 1%	2%	< 1%	2%	< 1%	2%	< 1%
Pileup	1-4%	1-4%	$\leq 3\%$	1-4%	$\leq 2\%$	$\leq 2\%$	$\leq 3\%$	1-3%
Jet energy scale	1-5%	1-10%	1-5%	1-9%	$\leq 2\%$	1-6%	$\leq 3\%$	$\leq 6\%$
Jet energy resolution	$\leq 3\%$	1-10%	$\leq 2\%$	1-12%	< 1%	1-14%	< 1%	$\leq 5\%$
Unclustered energy	$\leq 2\%$	2-10%	$\leq 3\%$	2-8%	< 1%	1-8%	< 1%	$\leq 3\%$
Prefiring	< 1%	< 1%	< 1%	< 1%	< 1%	< 1%	< 1%	< 1%
Lepton reconstruction	< 1%	< 1%	< 1%	< 1%	< 1%	< 1%	< 1%	< 1%
Lepton ident./isolation	2-6%	1-2%	2-6%	$\leq 3\%$	3-6%	$\leq 1\%$	3-7%	$\leq 3\%$
b tagging	< 1%	< 1%	< 1%	< 1%	< 1%	< 1%	< 1%	< 1%
b tagging (light jets)	< 1%	< 1%	< 1%	< 1%	< 1%	< 1%	< 1%	< 1%
Simulated samples statistics	6-14%	9-21%	5-15%	9-22%	3-7%	8-16%	3-6%	6-21%
Renorm./fact. scales	< 1%	< 1%	$\leq 1\%$	< 1%	< 1%	< 1%	< 1%	< 1%
Nonprompt leptons	< 1%	< 1%	< 1%	< 1%	< 1%	< 1%	< 1%	< 1%
ISR reweighting	1-2%	$\leq 2\%$	1-2%	$\leq 5\%$	$\leq 2\%$	1-4%	$\leq 2\%$	1-5%
Lepton ident./isolation (FastSim)	4.0%	—	4.0%	—	4.0%	—	4.0%	—
b tagging (FastSim)	< 1%	< 1%	< 1%	< 1%	< 1%	< 1%	< 1%	< 1%
p_T^{miss} (FastSim)	$\leq 11\%$	2-24%	$\leq 7\%$	$\leq 13\%$	1-2%	$\leq 9\%$	$\leq 2\%$	1-8%

Table 8.11: Same as in Table 8.9 for a representative mass hypothesis of the top squark pair production model ($\tilde{t}_1 \rightarrow t\tilde{\chi}_1^0$, with $m_{\tilde{t}_1} = 400$ GeV and $m_{\tilde{\chi}_1^0} = 275$ GeV).

Source of uncertainty	SR1 $160 \leq p_T^{\text{miss}} < 220$ GeV		SR2 $220 \leq p_T^{\text{miss}} < 280$ GeV		SR3 $280 \leq p_T^{\text{miss}} < 380$ GeV		SR4 $p_T^{\text{miss}} \geq 380$ GeV	
	Yields	$m_{T2}(\ell\ell)$ shape	Yields	$m_{T2}(\ell\ell)$ shape	Yields	$m_{T2}(\ell\ell)$ shape	Yields	$m_{T2}(\ell\ell)$ shape
Integrated luminosity	1-3%	—	1-3%	—	1-3%	—	1-3%	—
Trigger efficiency	2%	< 1%	2%	< 1%	2%	< 1%	2%	< 1%
Pileup	$\leq 1\%$	1-3%	$\leq 2\%$	1-7%	$\leq 2\%$	1-7%	$\leq 2\%$	$\leq 7\%$
Jet energy scale	$\leq 4\%$	1-4%	$\leq 5\%$	2-6%	$\leq 4\%$	2-6%	$\leq 4\%$	2-7%
Jet energy resolution	< 1%	1-4%	< 1%	1-4%	$\leq 1\%$	1-3%	< 1%	1-5%
Unclustered energy	< 1%	1-4%	< 1%	1-7%	$\leq 1\%$	2-6%	< 1%	1-7%
Prefiring	< 1%	< 1%	1%	< 1%	< 1%	< 1%	< 1%	$\leq 1\%$
Lepton reconstruction	< 1%	< 1%	< 1%	< 1%	< 1%	< 1%	< 1%	< 1%
Lepton ident./isolation	1-3%	$\leq 2\%$	1-3%	$\leq 3\%$	1-4%	$\leq 2\%$	1-3%	1-6%
Lepton additional cuts	1%	< 1%	1%	< 1%	1%	< 1%	1%	< 1%
b tagging	1%	< 1%	1%	< 1%	1%	< 1%	$\leq 1\%$	< 1%
b tagging (light jets)	< 1%	< 1%	< 1%	< 1%	< 1%	< 1%	< 1%	< 1%
Simulated samples statistics	1-3%	4-7%	2-4%	6-13%	3-5%	8-16%	3-5%	10-16%
Renorm./fact. scales	< 1%	< 1%	1%	< 1%	1-2%	< 1%	2%	$\leq 1\%$
Nonprompt leptons	< 1%	< 1%	< 1%	< 1%	< 1%	< 1%	< 1%	< 1%
ISR reweighting	2-3%	2-3%	4-5%	1-3%	5-6%	$\leq 2\%$	6-8%	$\leq 4\%$
Lepton ident./isolation (FastSim)	4.0%	—	4.0%	—	4.0%	—	4.0%	—
b tagging (FastSim)	< 1%	< 1%	< 1%	< 1%	< 1%	< 1%	< 1%	< 1%
p_T^{miss} (FastSim)	$\leq 5\%$	2-8%	$\leq 6\%$	$\leq 14\%$	$\leq 5\%$	3-18%	4-8%	4-15%

Chapter 9

Results and interpretation

Once each of the background processes have been modelled and the possible uncertainties assessed, the next step in a physics analysis is to present the results and interpret them. Such task is performed in the present chapter, which is divided into four sections. Section 9.1 explains the general procedure of the ML fit applied to data. Section 9.2 show the observed and expected event yields for the $m_{T2}(\ell\ell)$ distributions for each of the previously described SRs. Subsequently, Section 9.3 shows the equivalent distributions but after applying the ML fit. Finally, the results are presented in terms of the considered theoretical models in Section 9.4.

In these studies, three different types of distributions are studied, named “prefit”, “postfitS” and “postfitB”. The former correspond to the distributions as observed before any ML fit, while the two latter refer to the distributions after applying the ML fits to the data, specifically targeting the separation and analysis of signal (S) and background (B) contributions within a particle physics experiment. They are defined as:

- ◆ **Prefit**: This type of representation refers to the distributions before applying any fits to the data. It sets the baseline for the observed distributions against which the post-fit results are compared, including the initial estimates of signal and background contributions based on theoretical models, simulations, or control samples, without adjusting these estimates to better match the observed data. The prefit distributions are crucial for understanding the possible existing discrepancies between the model predictions and the data, independent of the fit.
- ◆ **PostfitS** (post-fit signal): This representation refers to those distributions or parameters obtained after fitting the data under the hypothesis that both signal and background contributions are present. The fit adjusts the model parameters to best match the observed distributions, taking into account the expected signal based on theoretical models or previous measurements. The “postfitS” results are crucial for understanding whether any statistically significant data-to-simulation discrepancies observed in data correspond to any signal hypothesis or not.
- ◆ **PostfitB** (post-fit background): In contrast, “postfitB” refers to the fit results obtained under a background-only hypothesis, where the observed data are assumed to be due to known SM processes without any new physics signal. This fit is typically compared to the postfitS model to check whether the background+signal hypothesis or the background-only one is the more probable.

The distinction between “postfitS” and “postfitB” is fundamental in particle physics analyses,

as it helps researchers to separate new physics signals from known background processes, thus enabling the discovery of new particles or the setting of limits on their production. In the analysis presented in the document, no statistically significant deviations compatible to any signal hypothesis were observed, so the distributions presented are either “prefit” or “postfitB”.

9.1 Signal extraction

In order to extract the signal from the supersymmetric models probed in this document, a simultaneous binned ML fit to the $m_{T2}(\ell\ell)$ distribution across all SRs is used. If we assume that for each bin, the events form a Poisson distribution, then the overall likelihood function, denoted as $L(data|\mu, \theta)$, can be calculated as a multiplication of Poisson probabilities covering every bin, channel, and SR. For a signal s and a background b , the likelihood function can be defined as follows:

$$L(data|\mu, \theta) = \prod \text{Poisson}(data|\mu \cdot s(\theta) + b(\theta)) \cdot p(\theta|\tilde{\theta}) \quad (9.1)$$

Where the parameter μ is referred to as the signal strength modifier, which is interpreted as a scale factor for the signal cross section compared to the observed data and can be described as the ratio of the count of signal events that best adjusts to the data to the count predicted by the model, represented as (σ/σ_{nom}) . Likewise, θ represents a set of nuisance parameters describing the unknowns of the fit, as described more in detail later. Lastly, the Poisson $(data|\mu \cdot s(\theta) + b(\theta))$ term can be mathematically expressed as:

$$\text{Poisson}(data|\mu \cdot s(\theta) + b(\theta)) = \prod_i^n \frac{(\mu s_i + b_i)^{n_i}}{n_i!} e^{-(\mu s_i + b_i)} \quad (9.2)$$

That is, the product over all N bins of the Poisson probabilities of observing n_i events in the i th bin, given that the average expected number for each bin is $\nu = \mu s_i + b_i$.

Before fitting the data, the estimations for both the signal yields (s) and the background yields (b) are affected by several sources of uncertainty, which are modelled introducing the nuisance parameters θ , causing the signal and background predictions to become functions of these parameters, represented as $s(\theta)$ and $b(\theta)$.

The difference in the shapes of the $m_{T2}(\ell\ell)$ distributions as predicted for the SM background and the SUSY signal are used to extract the signal contribution to the observed data and eventually establish an upper limit on the production cross section for the considered signal model.

Some of the parameters considered in the fit, such as the cross section of the signal process, are included unconstrained into the ML fit, while others are constrained by suitable probability distributions $p(\theta)$ around their default value $\tilde{\theta}$.

As discussed in Section 8.5 of this document, some of the uncertainties considered in the analysis hereby presented are included as nuisance parameters with log-normal prior distributions. Example of such parameters include uncertainties arising from signal and background normalisation, or the luminosity. Uncertainties on the shape of the $m_{T2}(\ell\ell)$ distributions are included using a template morphing technique with Gaussian constrained morphing parameters [249].

The normalisation of the main background processes from top quark ($t\bar{t}$, tW) and WW production are left to be determined in the fit through the constraint provided by the low $m_{T2}(\ell\ell)$

region in the events with a b-tagged jet or with no b-tagged jets, respectively. The predicted rate for these backgrounds gets a multiplicative factor, treated as a free parameter in the simultaneous ML fit. The relative normalisation of top quark pair production and single top quark production is further constrained to be within 10% from the SM expectation, to take into account theoretical uncertainties on its value. Since the chargino search regions with no b-tagged jets are split in two subregions according to whether any jet with $p_T \geq 20$ GeV is found in the event or not, additional free parameters are added in the fit, normalizing the rate of events with no jets for the WW and top quark backgrounds, respectively. The total number of yields expected for each process in the two regions with and without jets is constrained to remain invariant, so that only a migration of events from the two search regions is allowed. The normalization of the subleading WZ, ZZ, and $t\bar{t}Z$ backgrounds is determined by introducing in the fit the CRs described in Section 8.4.2.

It should be noted that the ML fit to the chargino SRs benefits of more CRs than the one of the top squark SRs, namely the regions with b-tagged jets that from the point of view of the top squark search are signal regions. This does not entail a different treatment of the two fits. Instead, as mentioned above, the separation of events with and without b-tagged jets allows for a constraint of the normalisation of the top quark and WW background processes, which are dominating in the low $m_{T2}(\ell\ell)$ bins. The chargino pair production is expected to have a negligible contribution in the SRs with b-tagged jets, but these regions are kept in the fit to retain the capability to constrain the normalization of $t\bar{t}$ events. Conversely, top squark pair production is expected to significantly contribute to the SRs with b-tagged jets, but the difference in the $m_{T2}(\ell\ell)$ shape still allows the $t\bar{t}$ events to be constrained in the low $m_{T2}(\ell\ell)$ bins.

9.2 Observed and expected yields

Having defined how the signal is extracted, the subsequent step required for this analysis is to proceed to compare the number of expected events, both for signal and background, with the observed events. As explained at the beginning of this chapter, firstly, the studied distributions are presented prior to performing the fit, in what is known as prefit distributions. In particular, for the analysis described in this document, $m_{T2}(\ell\ell)$ distributions are presented for each of the signal regions defined in Section 8.3. For each distribution, the contributions from the SM processes are shown, as well as the observed yields and the expected contribution for a few representative signal mass points. The uncertainty bands on the expected yields from SM processes account for both MC statistical uncertainties and all the systematic uncertainties described in detail in Section 8.5.

The rest of this section is dedicated to show the prefit distributions just described, both for the chargino SRs, in Section 9.2.1. and the top squark SRs, in Section 9.2.2. Likewise, A summary of the observed and expected yields for both SM processes and representative signal mass points in each chargino SR are presented in Tables 9.1 and 9.2 for (SF) and (DF) events, respectively. Similarly, the observed and expected yields in the top squark SRs are summarised in Table 9.3 for the SF channel and Table 9.4 for the DF channel.

9.2.1 Chargino search regions

The $m_{T2}(\ell\ell)$ distributions for the chargino pair production SRs, are presented in Figs. 9.1 to 9.3, using the full Run II dataset. Different signal mass points for the chargino model are shown for SR1 and SR2 (Figs. 9.1 and 9.2) than for SR3 and SR4 (Fig. 9.3), in order to show signal distributions for mass hypotheses that are more sensitive for each SR.

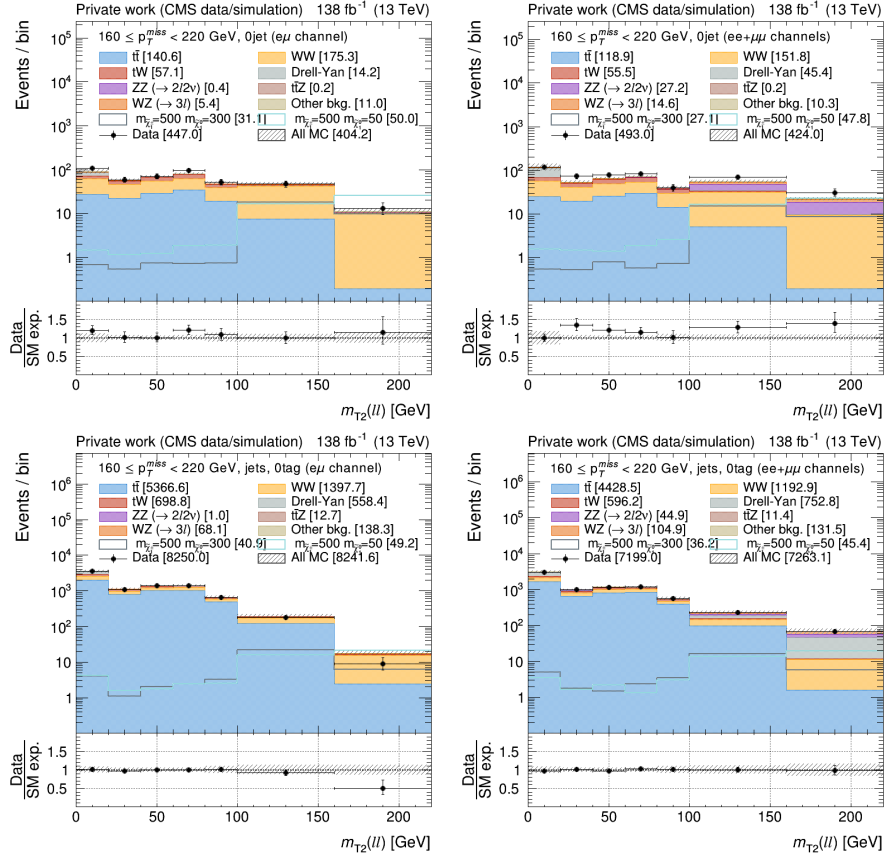


Figure 9.1: Observed and expected $m_{T2}(\ell\ell)$ distributions for SM processes and the signal production for a chargino mass of 500 GeV with a neutralino mass of 300 GeV (grey) and 50 GeV (cyan) in the SR1. Distributions corresponding to different flavour events are shown on the left, while same flavour events are presented on the right. The distributions for events with no jets are depicted in the top plots, while the ones for events with jets but no b-tagged jets are shown in the bottom ones. In the bottom panel, the ratio of data and SM expectations is shown. The hatched band represents the total uncertainty, including the sources discussed in Section 8.5.

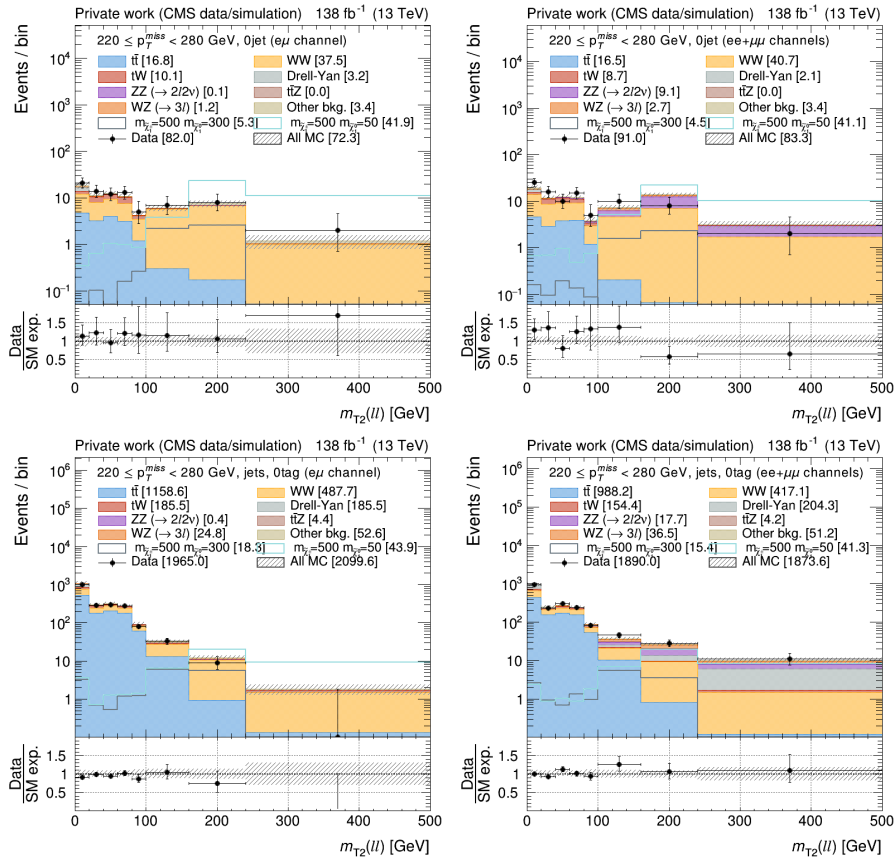


Figure 9.2: Equivalent distributions as presented in Fig. 9.1 but for the SR2.

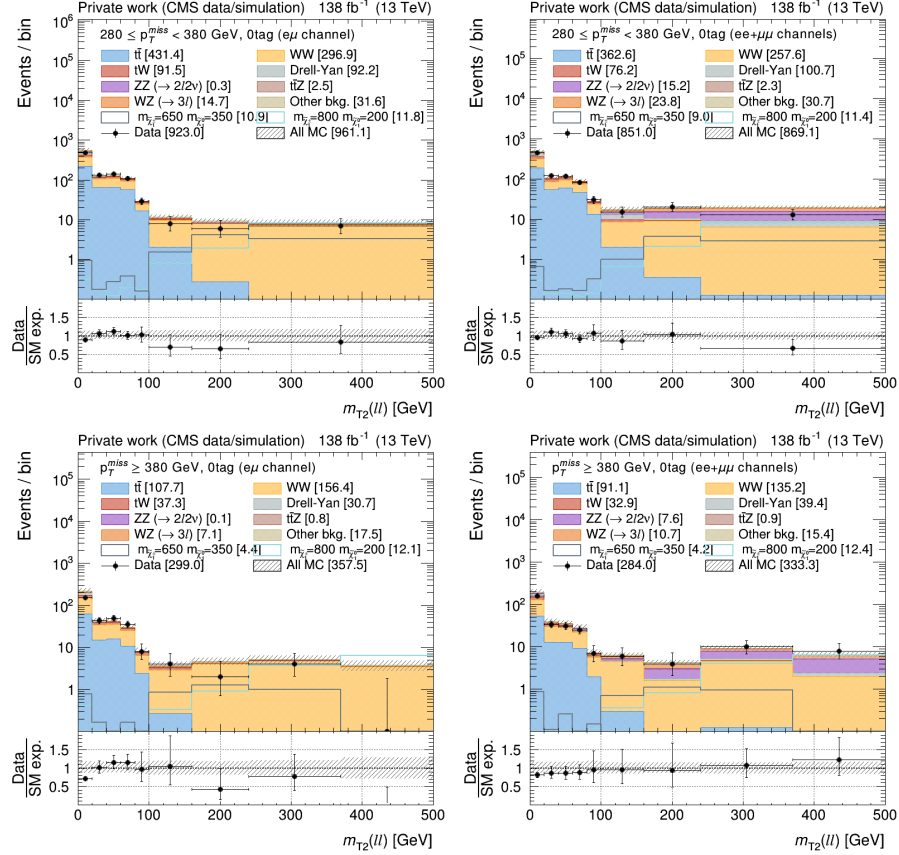


Figure 9.3: Observed and expected $m_{T2}(\ell\ell)$ distributions for SM processes and the signal production for a chargino mass of 650 GeV with a neutralino mass of 350 GeV (grey) and for a chargino mass of 800 GeV with a neutralino mass of 200 GeV (cyan) for the SR3 and SR4 for events with no b-tagged jets. Distributions corresponding to different flavour events are shown on the left, while same flavour events are presented on the right. The distributions for the SR3 are depicted in the top plots, while the distributions for the SR4 are shown in the bottom ones. In the bottom panel, the ratio of data and SM expectations is shown. The hatched band represents the total uncertainty, including the sources discussed in Section 8.5.

9.2.2 Top squark search regions

The $m_{T2}(\ell\ell)$ distributions for top squark pair production SRs, as defined in the bottom part of Table 8.2, are depicted in Figs. 9.4 and 9.7 similarly to the distributions for the chargino pair production SRs previously shown.

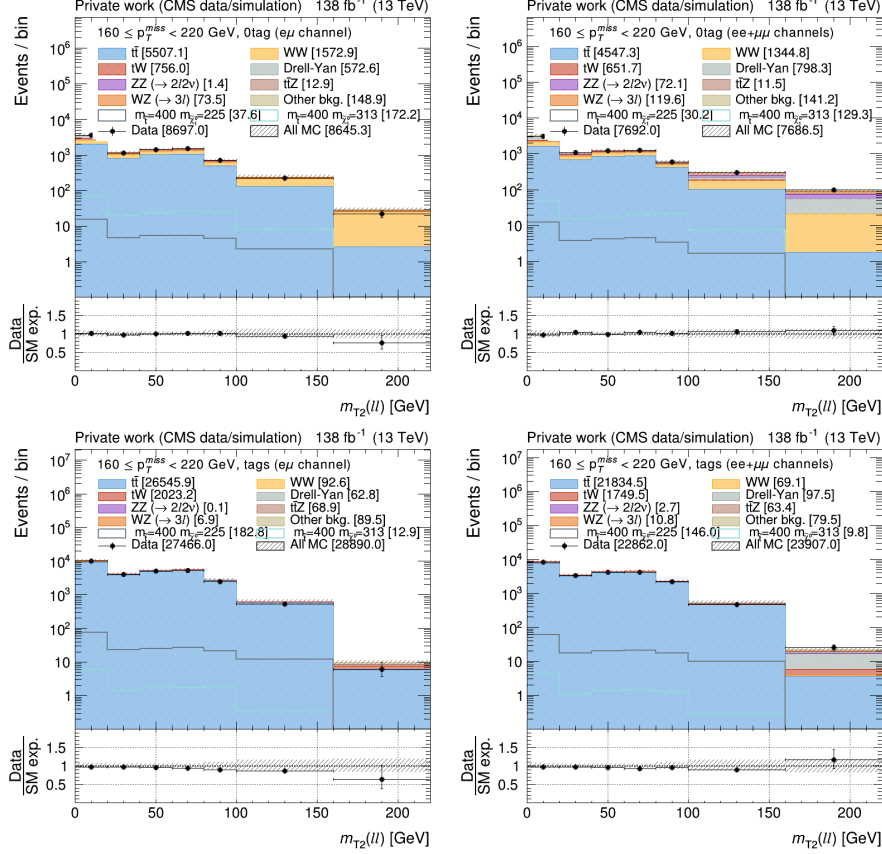


Figure 9.4: Observed and expected $m_{T2}(\ell\ell)$ distributions for SM processes and the expected signals produced for a top squark mass of 400 GeV with a neutralino mass of 225 GeV (grey) and for a top squark mass of 400 GeV with a neutralino mass of 313 GeV (cyan) for the SR1. Distributions corresponding to different flavour events are shown on the left, while same flavour events are presented on the right. Top plots represent events with no b-tagged jets, whereas events with at least one b-tagged jet are depicted in the bottom plots. For each distribution, the ratio of data and SM expectations is shown in the bottom panel. The hatched band represents the total uncertainty, including the sources discussed in Section 8.5.

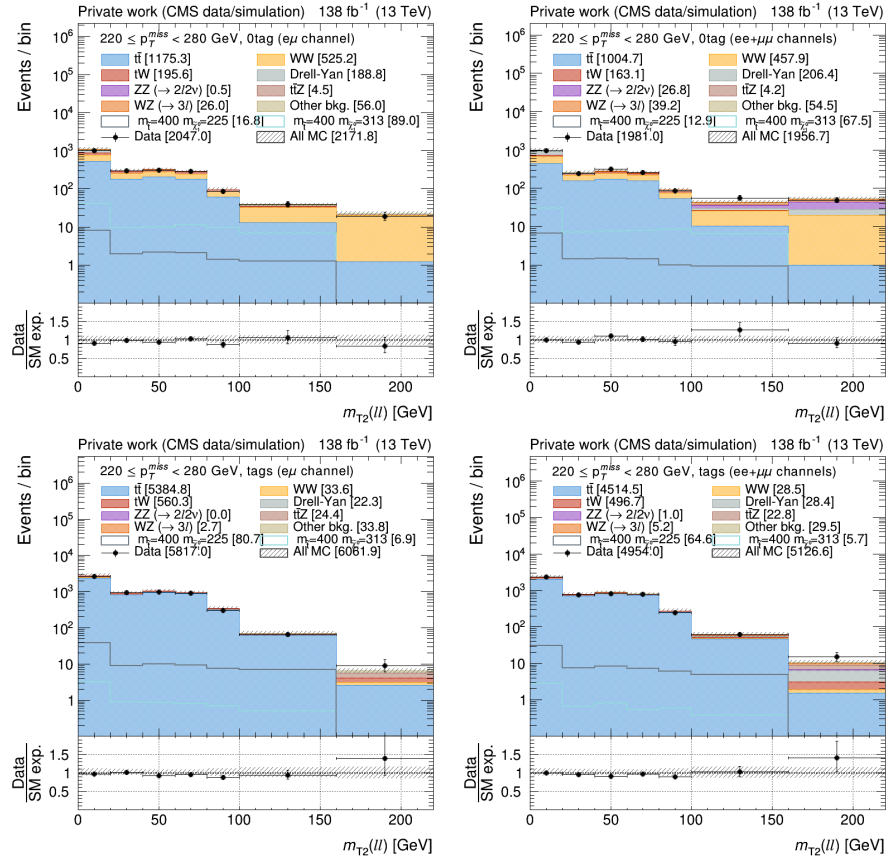


Figure 9.5: Equivalent distributions as presented in Fig. 9.4 for the SR2.

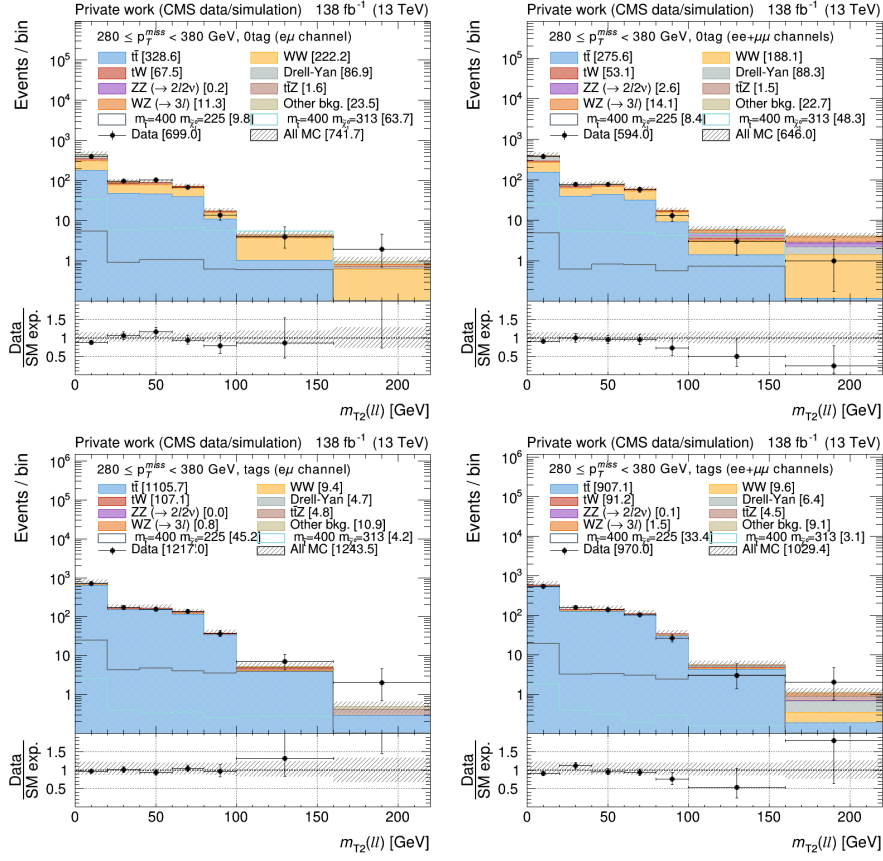


Figure 9.6: Equivalent distributions as presented in Fig. 9.4 for the SR3.

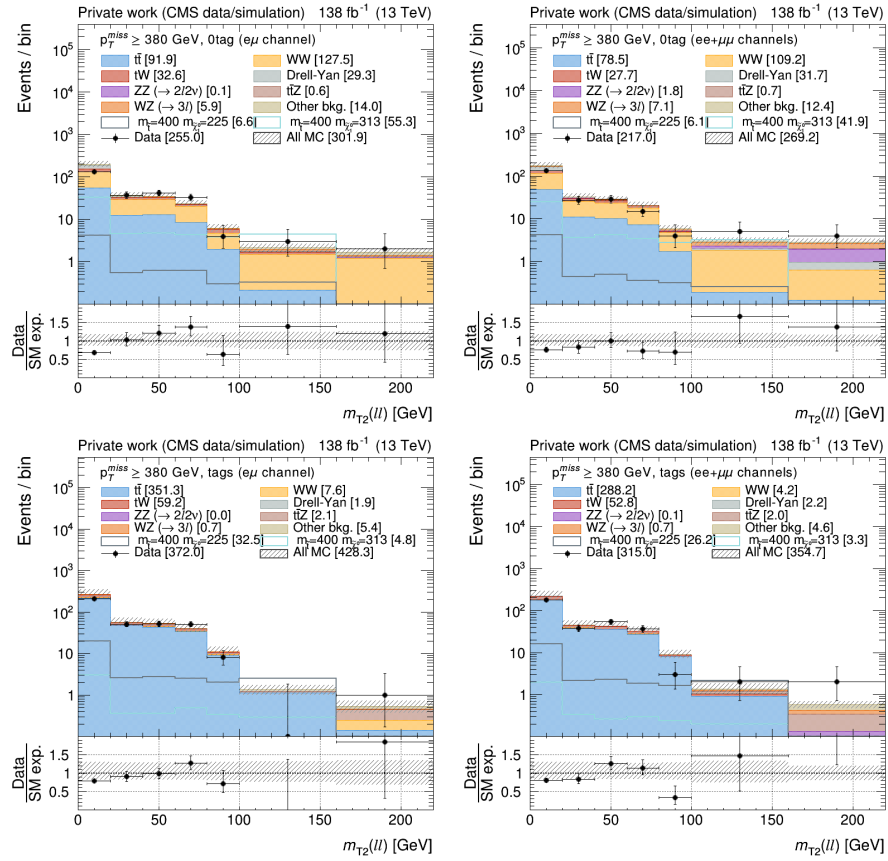


Figure 9.7: Equivalent distributions as presented in Fig. 9.4 for the SR4.

Table 9.1: Observed and expected yields as a function of $m_{T2}(\ell\ell)$ for SM processes and two representative signal mass points. Rows correspond to the chargino SRs for the SF channel.

$m_{T2}(\ell\ell)$ [GeV]		0-20	20-40	40-60	60-80	80-100	100-160	160-240	240-370	≥ 370
SF events										
SR1 _{0jet} _{0tag}	SM Processes	117 \pm 20	53.9 \pm 3.6	65.2 \pm 4.1	71.5 \pm 4.8	39.4 \pm 4.4	54.5 \pm 5.2	22.1 \pm 2.1		
	Data	118	73	79	82	40	70	31		
	$m_{\tilde{\chi}_1^\pm} = 500, m_{\tilde{\chi}_1^0} = 50$	1.6 \pm 0.2	1.5 \pm 0.2	1.4 \pm 0.1	1.9 \pm 0.2	2.6 \pm 0.6	16.5 \pm 0.9	22.5 \pm 1.3		
	$m_{\tilde{\chi}_1^\pm} = 500, m_{\tilde{\chi}_1^0} = 300$	0.55 \pm 0.05	0.52 \pm 0.10	0.79 \pm 0.06	0.57 \pm 0.10	0.74 \pm 0.06	15.2 \pm 1.1	8.7 \pm 0.5		
	SM Processes	3093 \pm 251	981 \pm 58	1174 \pm 67	1160 \pm 77	557 \pm 59	229 \pm 29	69.2 \pm 10.6		
SR1 _{1jets} _{0tag}	Data	2992	1002	1142	1202	562	231	68		
	$m_{\tilde{\chi}_1^\pm} = 500, m_{\tilde{\chi}_1^0} = 50$	3.5 \pm 0.3	1.7 \pm 0.3	2.2 \pm 0.2	1.4 \pm 0.3	3.0 \pm 0.7	13.9 \pm 0.9	19.8 \pm 1.0		
	$m_{\tilde{\chi}_1^\pm} = 500, m_{\tilde{\chi}_1^0} = 300$	5.0 \pm 0.4	1.8 \pm 0.2	1.5 \pm 0.4	2.4 \pm 0.3	3.4 \pm 0.3	16.4 \pm 0.9	5.7 \pm 0.5		
	SM Processes	19.3 \pm 2.1	11.7 \pm 1.3	12.4 \pm 1.2	11.9 \pm 1.2	3.8 \pm 0.6	7.3 \pm 1.0	13.8 \pm 1.6	3.1 \pm 0.5	
	Data	25	16	10	15	5	10	8	2	
SR2 _{0jet} _{0tag}	$m_{\tilde{\chi}_1^\pm} = 500, m_{\tilde{\chi}_1^0} = 50$	0.67 \pm 0.12	0.69 \pm 0.19	0.95 \pm 0.24	0.47 \pm 0.12	0.74 \pm 0.26	5.2 \pm 0.5	22.2 \pm 1.5	10.2 \pm 1.3	
	$m_{\tilde{\chi}_1^\pm} = 500, m_{\tilde{\chi}_1^0} = 300$	0.16 \pm 0.12	0.09 \pm 0.05	0.19 \pm 0.06	0.13 \pm 0.08	0.09 \pm 0.02	1.5 \pm 0.2	2.3 \pm 0.5	0.00 \pm 0.00	
	SM Processes	952 \pm 93	250 \pm 20	270 \pm 20	241 \pm 20	87.9 \pm 10.2	36.7 \pm 4.1	26.5 \pm 2.8	10.1 \pm 1.6	
	Data	947	230	303	243	82	46	28	11	
	$m_{\tilde{\chi}_1^\pm} = 500, m_{\tilde{\chi}_1^0} = 50$	2.4 \pm 0.2	0.87 \pm 0.30	1.0 \pm 0.1	0.87 \pm 0.09	1.8 \pm 0.2	6.9 \pm 0.4	19.3 \pm 1.1	8.1 \pm 0.8	
SR2 _{1jets} _{0tag}	$m_{\tilde{\chi}_1^\pm} = 500, m_{\tilde{\chi}_1^0} = 300$	2.6 \pm 0.3	0.91 \pm 0.08	0.68 \pm 0.12	1.3 \pm 0.2	0.95 \pm 0.08	5.4 \pm 0.4	3.6 \pm 0.2	0.00 \pm 0.00	
	SM Processes	477 \pm 57	108 \pm 11	111 \pm 11	88.7 \pm 8.8	28.1 \pm 3.5	17.4 \pm 2.7	19.0 \pm 2.3	19.4 \pm 2.3	
	Data	454	119	118	82	30	15	20	13	
	$m_{\tilde{\chi}_1^\pm} = 650, m_{\tilde{\chi}_1^0} = 350$	0.65 \pm 0.06	0.16 \pm 0.03	0.18 \pm 0.05	0.16 \pm 0.04	0.32 \pm 0.03	0.99 \pm 0.06	3.7 \pm 0.2	2.8 \pm 0.2	
	$m_{\tilde{\chi}_1^\pm} = 800, m_{\tilde{\chi}_1^0} = 200$	0.29 \pm 0.07	0.13 \pm 0.01	0.14 \pm 0.02	0.12 \pm 0.01	0.14 \pm 0.01	0.65 \pm 0.03	2.0 \pm 0.1	7.9 \pm 0.3	
SR3 _{0tag}	SM Processes	196 \pm 30	39.1 \pm 5.9	36.2 \pm 5.2	28.5 \pm 5.2	7.3 \pm 1.6	6.3 \pm 1.2	4.3 \pm 0.6	9.3 \pm 1.7	6.5 \pm 1.2
	Data	159	34	31	25	7	6	4	10	8
	$m_{\tilde{\chi}_1^\pm} = 650, m_{\tilde{\chi}_1^0} = 350$	0.88 \pm 0.12	0.11 \pm 0.06	0.26 \pm 0.06	0.05 \pm 0.02	0.15 \pm 0.02	0.70 \pm 0.06	1.1 \pm 0.1	0.96 \pm 0.14	0.00 \pm 0.00
	$m_{\tilde{\chi}_1^\pm} = 800, m_{\tilde{\chi}_1^0} = 200$	0.37 \pm 0.02	0.11 \pm 0.02	0.08 \pm 0.01	0.08 \pm 0.00	0.12 \pm 0.02	0.37 \pm 0.02	0.81 \pm 0.07	4.1 \pm 0.2	6.3 \pm 0.3
	SM Processes	196 \pm 30	39.1 \pm 5.9	36.2 \pm 5.2	28.5 \pm 5.2	7.3 \pm 1.6	6.3 \pm 1.2	4.3 \pm 0.6	9.3 \pm 1.7	6.5 \pm 1.2
SR4 _{0tag}	Data	159	34	31	25	7	6	4	10	8
	$m_{\tilde{\chi}_1^\pm} = 650, m_{\tilde{\chi}_1^0} = 350$	0.88 \pm 0.12	0.11 \pm 0.06	0.26 \pm 0.06	0.05 \pm 0.02	0.15 \pm 0.02	0.70 \pm 0.06	1.1 \pm 0.1	0.96 \pm 0.14	0.00 \pm 0.00
	$m_{\tilde{\chi}_1^\pm} = 800, m_{\tilde{\chi}_1^0} = 200$	0.37 \pm 0.02	0.11 \pm 0.02	0.08 \pm 0.01	0.08 \pm 0.00	0.12 \pm 0.02	0.37 \pm 0.02	0.81 \pm 0.07	4.1 \pm 0.2	6.3 \pm 0.3
	SM Processes	196 \pm 30	39.1 \pm 5.9	36.2 \pm 5.2	28.5 \pm 5.2	7.3 \pm 1.6	6.3 \pm 1.2	4.3 \pm 0.6	9.3 \pm 1.7	6.5 \pm 1.2
	Data	159	34	31	25	7	6	4	10	8

Table 9.2: Same as for Table 9.1 but for the DF channel.

$m_{T2}(\ell\ell)$ [GeV]		0-20	20-40	40-60	60-80	80-100	100-160	160-240	240-370	≥ 370
DF events										
SR ^{1_{0jet}} _{0tag}	SM Processes	90.6 \pm 10.0	57.9 \pm 3.8	69.5 \pm 4.3	80.3 \pm 5.9	47.6 \pm 6.1	47.1 \pm 6.2	11.2 \pm 1.9		
	Data	109	59	70	97	52	47	13		
	$m_{\tilde{\chi}_1^\pm} = 500, m_{\tilde{\chi}_1^0} = 50$	1.4 \pm 0.1	1.1 \pm 0.1	1.2 \pm 0.3	1.9 \pm 0.3	1.9 \pm 0.2	16.6 \pm 1.0	25.9 \pm 1.4		
	$m_{\tilde{\chi}_1^\pm} = 500, m_{\tilde{\chi}_1^0} = 300$	0.68 \pm 0.08	0.53 \pm 0.12	0.74 \pm 0.25	0.72 \pm 0.13	0.74 \pm 0.12	17.9 \pm 1.4	9.8 \pm 0.6		
SR ^{1_{jets}} _{0tag}	SM Processes	3487 \pm 264	1129 \pm 66	1376 \pm 77	1392 \pm 94	646 \pm 70	194 \pm 29	18.0 \pm 3.1		
	Data	3545	1099	1368	1397	653	179	9		
	$m_{\tilde{\chi}_1^\pm} = 500, m_{\tilde{\chi}_1^0} = 50$	4.1 \pm 0.3	1.6 \pm 0.3	1.8 \pm 0.3	2.5 \pm 0.2	2.5 \pm 0.2	15.7 \pm 0.8	21.0 \pm 1.2		
	$m_{\tilde{\chi}_1^\pm} = 500, m_{\tilde{\chi}_1^0} = 300$	4.1 \pm 0.2	1.1 \pm 0.2	2.0 \pm 0.2	2.5 \pm 0.4	3.3 \pm 0.4	21.8 \pm 0.9	6.2 \pm 0.4		
SR ^{2_{0jet}} _{0tag}	SM Processes	18.5 \pm 2.8	11.4 \pm 1.2	12.5 \pm 1.2	10.8 \pm 1.2	4.3 \pm 0.7	6.0 \pm 1.0	7.5 \pm 1.4	1.2 \pm 0.3	
	Data	21	14	12	13	5	7	8	2	
	$m_{\tilde{\chi}_1^\pm} = 500, m_{\tilde{\chi}_1^0} = 50$	0.35 \pm 0.06	0.63 \pm 0.07	1.1 \pm 0.1	0.98 \pm 0.21	0.85 \pm 0.38	3.8 \pm 0.3	23.2 \pm 1.2	11.0 \pm 0.9	
	$m_{\tilde{\chi}_1^\pm} = 500, m_{\tilde{\chi}_1^0} = 300$	0.03 \pm 0.04	0.10 \pm 0.02	0.05 \pm 0.02	0.16 \pm 0.05	0.26 \pm 0.03	2.2 \pm 0.5	2.6 \pm 0.6	0.00 \pm 0.00	
SR ^{2_{jets}} _{0tag}	SM Processes	1081 \pm 105	292 \pm 23	317 \pm 24	272 \pm 22	91.9 \pm 10.9	31.7 \pm 4.5	12.2 \pm 2.2	1.8 \pm 0.5	
	Data	982	286	297	278	80	33	9	0	
	$m_{\tilde{\chi}_1^\pm} = 500, m_{\tilde{\chi}_1^0} = 50$	3.6 \pm 0.5	0.71 \pm 0.10	1.3 \pm 0.3	1.3 \pm 0.1	1.4 \pm 0.3	6.4 \pm 0.6	20.0 \pm 1.1	9.2 \pm 0.7	
	$m_{\tilde{\chi}_1^\pm} = 500, m_{\tilde{\chi}_1^0} = 300$	3.2 \pm 0.3	0.68 \pm 0.18	0.52 \pm 0.10	1.2 \pm 0.1	1.2 \pm 0.3	6.0 \pm 0.5	5.5 \pm 0.5	0.00 \pm 0.00	
SR ^{3_{0tag}}	SM Processes	545 \pm 66	125 \pm 13	126 \pm 13	108 \pm 11	28.3 \pm 3.6	11.6 \pm 1.9	9.3 \pm 1.8	8.4 \pm 2.2	
	Data	488	134	142	109	29	8	6	7	
	$m_{\tilde{\chi}_1^\pm} = 650, m_{\tilde{\chi}_1^0} = 350$	0.94 \pm 0.09	0.17 \pm 0.03	0.27 \pm 0.07	0.38 \pm 0.03	0.16 \pm 0.03	1.5 \pm 0.1	4.1 \pm 0.3	3.3 \pm 0.5	
	$m_{\tilde{\chi}_1^\pm} = 800, m_{\tilde{\chi}_1^0} = 200$	0.32 \pm 0.04	0.17 \pm 0.01	0.12 \pm 0.01	0.20 \pm 0.02	0.17 \pm 0.04	0.79 \pm 0.06	1.9 \pm 0.1	8.1 \pm 0.3	
SR ^{4_{0tag}}	SM Processes	217 \pm 34	42.4 \pm 6.7	42.5 \pm 6.3	30.2 \pm 5.3	8.3 \pm 1.9	3.8 \pm 0.8	4.7 \pm 1.1	5.2 \pm 1.5	3.8 \pm 1.4
	Data	154	43	49	35	8	4	2	4	0
	$m_{\tilde{\chi}_1^\pm} = 650, m_{\tilde{\chi}_1^0} = 350$	0.79 \pm 0.07	0.17 \pm 0.02	0.05 \pm 0.01	0.17 \pm 0.03	0.06 \pm 0.03	0.86 \pm 0.07	1.3 \pm 0.1	0.99 \pm 0.09	0.00 \pm 0.00
	$m_{\tilde{\chi}_1^\pm} = 800, m_{\tilde{\chi}_1^0} = 200$	0.40 \pm 0.03	0.08 \pm 0.01	0.08 \pm 0.02	0.08 \pm 0.01	0.07 \pm 0.01	0.33 \pm 0.02	0.91 \pm 0.04	3.7 \pm 0.2	6.4 \pm 0.3

Table 9.3: Observed and expected yields as a function of $m_{T2}(\ell\ell)$ for SM processes and two representative signal mass points. Rows correspond to the top squark SRs for the SF channel as defined in the bottom part of Table 8.2.

$m_{T2}(\ell\ell)$ [GeV]		0-20	20-40	40-60	60-80	80-100	100-160	≥ 160
SF events								
SR1 _{tags}	SM Processes	8673 \pm 577	3458 \pm 182	4380 \pm 223	4573 \pm 292	2280 \pm 234	521 \pm 83	21.5 \pm 3.6
	Data	8405	3351	4211	4232	2173	465	25
	$m_{\tilde{t}_1^\pm} = 400, m_{\tilde{\chi}_1^0} = 313$	4.3 \pm 0.3	1.1 \pm 0.1	1.4 \pm 0.1	1.5 \pm 0.1	1.3 \pm 0.1	0.28 \pm 0.04	0.00 \pm 0.00
	$m_{\tilde{t}_1^\pm} = 400, m_{\tilde{\chi}_1^0} = 225$	59.9 \pm 2.8	17.2 \pm 0.7	20.3 \pm 1.2	21.2 \pm 1.4	17.7 \pm 1.4	9.8 \pm 1.7	0.02 \pm 0.01
SR1 _{0tag}	SM Processes	3211 \pm 263	1034 \pm 60	1239 \pm 68	1231 \pm 80	596 \pm 62	284 \pm 34	91.3 \pm 11.4
	Data	3110	1075	1221	1284	602	301	99
	$m_{\tilde{t}_1^\pm} = 400, m_{\tilde{\chi}_1^0} = 313$	47.9 \pm 2.7	15.1 \pm 1.2	17.3 \pm 0.9	20.0 \pm 1.0	21.5 \pm 1.1	7.5 \pm 0.8	0.00 \pm 0.00
	$m_{\tilde{t}_1^\pm} = 400, m_{\tilde{\chi}_1^0} = 225$	12.6 \pm 0.7	3.7 \pm 0.2	4.3 \pm 0.3	4.6 \pm 0.3	3.4 \pm 0.2	1.7 \pm 0.4	0.00 \pm 0.01
SR2 _{tags}	SM Processes	2319 \pm 234	779 \pm 59	885 \pm 63	797 \pm 60	275 \pm 30	60.2 \pm 9.7	10.7 \pm 1.5
	Data	2308	742	811	770	246	62	15
	$m_{\tilde{t}_1^\pm} = 400, m_{\tilde{\chi}_1^0} = 313$	2.8 \pm 0.3	0.66 \pm 0.08	0.82 \pm 0.09	0.53 \pm 0.07	0.60 \pm 0.06	0.37 \pm 0.05	0.00 \pm 0.00
	$m_{\tilde{t}_1^\pm} = 400, m_{\tilde{\chi}_1^0} = 225$	30.6 \pm 1.9	7.6 \pm 0.4	8.2 \pm 0.5	7.3 \pm 0.7	6.0 \pm 0.6	4.9 \pm 0.6	0.00 \pm 0.01
SR2 _{0tag}	SM Processes	971 \pm 94	262 \pm 20	282 \pm 21	252 \pm 20	91.6 \pm 10.4	43.9 \pm 4.8	53.5 \pm 5.6
	Data	972	246	313	258	87	56	49
	$m_{\tilde{t}_1^\pm} = 400, m_{\tilde{\chi}_1^0} = 313$	29.8 \pm 2.1	7.2 \pm 0.5	7.6 \pm 0.5	7.9 \pm 0.5	8.4 \pm 0.5	6.5 \pm 0.7	0.00 \pm 0.00
	$m_{\tilde{t}_1^\pm} = 400, m_{\tilde{\chi}_1^0} = 225$	6.7 \pm 0.4	1.4 \pm 0.1	1.5 \pm 0.1	1.4 \pm 0.1	1.00 \pm 0.07	0.93 \pm 0.11	0.00 \pm 0.00
SR3 _{tags} ^{ISR}	SM Processes	595 \pm 106	142 \pm 24	142 \pm 23	110 \pm 18	34.4 \pm 5.9	5.7 \pm 1.0	1.1 \pm 0.2
	Data	542	158	136	103	26	3	2
	$m_{\tilde{t}_1^\pm} = 400, m_{\tilde{\chi}_1^0} = 313$	1.8 \pm 0.2	0.39 \pm 0.05	0.31 \pm 0.06	0.19 \pm 0.03	0.29 \pm 0.03	0.15 \pm 0.03	0.00 \pm 0.00
	$m_{\tilde{t}_1^\pm} = 400, m_{\tilde{\chi}_1^0} = 225$	18.6 \pm 1.4	3.2 \pm 0.4	3.3 \pm 0.2	3.0 \pm 0.3	2.3 \pm 0.2	3.0 \pm 0.3	0.03 \pm 0.03
SR3 _{0tag} ^{ISR}	SM Processes	402 \pm 50	75.9 \pm 9.3	79.9 \pm 9.6	60.1 \pm 7.1	17.8 \pm 2.4	6.1 \pm 1.0	4.2 \pm 0.6
	Data	368	76	76	57	13	3	1
	$m_{\tilde{t}_1^\pm} = 400, m_{\tilde{\chi}_1^0} = 313$	24.3 \pm 1.7	5.2 \pm 0.4	5.2 \pm 0.4	4.9 \pm 0.3	4.2 \pm 0.3	4.6 \pm 0.4	0.00 \pm 0.00
	$m_{\tilde{t}_1^\pm} = 400, m_{\tilde{\chi}_1^0} = 225$	4.9 \pm 0.3	0.61 \pm 0.07	0.82 \pm 0.09	0.79 \pm 0.08	0.57 \pm 0.07	0.72 \pm 0.13	0.00 \pm 0.00
SR4 _{tags} ^{ISR}	SM Processes	223 \pm 54	45.2 \pm 10.6	42.7 \pm 9.2	32.4 \pm 6.9	9.0 \pm 2.1	1.4 \pm 0.4	0.57 \pm 0.09
	Data	179	38	54	37	3	2	2
	$m_{\tilde{t}_1^\pm} = 400, m_{\tilde{\chi}_1^0} = 313$	1.9 \pm 0.3	0.33 \pm 0.05	0.26 \pm 0.03	0.30 \pm 0.05	0.24 \pm 0.03	0.20 \pm 0.04	0.00 \pm 0.00
	$m_{\tilde{t}_1^\pm} = 400, m_{\tilde{\chi}_1^0} = 225$	16.2 \pm 1.8	2.1 \pm 0.2	2.3 \pm 0.3	1.8 \pm 0.2	1.6 \pm 0.2	2.1 \pm 0.5	0.04 \pm 0.01
SR4 _{0tag} ^{ISR}	SM Processes	175 \pm 27	32.7 \pm 5.2	28.8 \pm 4.2	20.8 \pm 3.6	5.8 \pm 1.1	3.0 \pm 0.6	2.9 \pm 0.5
	Data	133	27	29	15	4	5	4
	$m_{\tilde{t}_1^\pm} = 400, m_{\tilde{\chi}_1^0} = 313$	24.6 \pm 2.7	3.7 \pm 0.6	4.3 \pm 0.4	3.4 \pm 0.4	2.7 \pm 0.3	3.2 \pm 0.6	0.00 \pm 0.00
	$m_{\tilde{t}_1^\pm} = 400, m_{\tilde{\chi}_1^0} = 225$	4.2 \pm 0.5	0.45 \pm 0.04	0.50 \pm 0.04	0.36 \pm 0.09	0.32 \pm 0.04	0.26 \pm 0.07	0.02 \pm 0.01

Table 9.4: Same as for Table 9.3 but for the DF channel.

$m_{T2}(\ell\ell)$ [GeV]		0-20	20-40	40-60	60-80	80-100	100-160	≥ 160
SF events								
SR1 _{tags}	SM Processes	8673 \pm 577	3458 \pm 182	4380 \pm 223	4573 \pm 292	2280 \pm 234	521 \pm 83	21.5 \pm 3.6
	Data	8405	3351	4211	4232	2173	465	25
	$m_{t\bar{t}} = 400, m_{\tilde{\chi}_1^0} = 313$	4.3 \pm 0.3	1.1 \pm 0.1	1.4 \pm 0.1	1.5 \pm 0.1	1.3 \pm 0.1	0.28 \pm 0.04	0.00 \pm 0.00
	$m_{t\bar{t}} = 400, m_{\tilde{\chi}_1^0} = 225$	59.9 \pm 2.8	17.2 \pm 0.7	20.3 \pm 1.2	21.2 \pm 1.4	17.7 \pm 1.4	9.8 \pm 1.7	0.02 \pm 0.01
SR1 _{0tag}	SM Processes	3211 \pm 263	1034 \pm 60	1239 \pm 68	1231 \pm 80	596 \pm 62	284 \pm 34	91.3 \pm 11.4
	Data	3110	1075	1221	1284	602	301	99
	$m_{t\bar{t}} = 400, m_{\tilde{\chi}_1^0} = 313$	47.9 \pm 2.7	15.1 \pm 1.2	17.3 \pm 0.9	20.0 \pm 1.0	21.5 \pm 1.1	7.5 \pm 0.8	0.00 \pm 0.00
	$m_{t\bar{t}} = 400, m_{\tilde{\chi}_1^0} = 225$	12.6 \pm 0.7	3.7 \pm 0.2	4.3 \pm 0.3	4.6 \pm 0.3	3.4 \pm 0.2	1.7 \pm 0.4	0.00 \pm 0.01
SR2 _{tags}	SM Processes	2319 \pm 234	779 \pm 59	885 \pm 63	797 \pm 60	275 \pm 30	60.2 \pm 9.7	10.7 \pm 1.5
	Data	2308	742	811	770	246	62	15
	$m_{t\bar{t}} = 400, m_{\tilde{\chi}_1^0} = 313$	2.8 \pm 0.3	0.66 \pm 0.08	0.82 \pm 0.09	0.53 \pm 0.07	0.60 \pm 0.06	0.37 \pm 0.05	0.00 \pm 0.00
	$m_{t\bar{t}} = 400, m_{\tilde{\chi}_1^0} = 225$	30.6 \pm 1.9	7.6 \pm 0.4	8.2 \pm 0.5	7.3 \pm 0.7	6.0 \pm 0.6	4.9 \pm 0.6	0.00 \pm 0.01
SR2 _{0tag}	SM Processes	971 \pm 94	262 \pm 20	282 \pm 21	252 \pm 20	91.6 \pm 10.4	43.9 \pm 4.8	53.5 \pm 5.6
	Data	972	246	313	258	87	56	49
	$m_{t\bar{t}} = 400, m_{\tilde{\chi}_1^0} = 313$	29.8 \pm 2.1	7.2 \pm 0.5	7.6 \pm 0.5	7.9 \pm 0.5	8.4 \pm 0.5	6.5 \pm 0.7	0.00 \pm 0.00
	$m_{t\bar{t}} = 400, m_{\tilde{\chi}_1^0} = 225$	6.7 \pm 0.4	1.4 \pm 0.1	1.5 \pm 0.1	1.4 \pm 0.1	1.00 \pm 0.07	0.93 \pm 0.11	0.00 \pm 0.00
SR3 _{tags}	SM Processes	595 \pm 106	142 \pm 24	142 \pm 23	110 \pm 18	34.4 \pm 5.9	5.7 \pm 1.0	1.1 \pm 0.2
	Data	542	158	136	103	26	3	2
	$m_{t\bar{t}} = 400, m_{\tilde{\chi}_1^0} = 313$	1.8 \pm 0.2	0.39 \pm 0.05	0.31 \pm 0.06	0.19 \pm 0.03	0.29 \pm 0.03	0.15 \pm 0.03	0.00 \pm 0.00
	$m_{t\bar{t}} = 400, m_{\tilde{\chi}_1^0} = 225$	18.6 \pm 1.4	3.2 \pm 0.4	3.3 \pm 0.2	3.0 \pm 0.3	2.3 \pm 0.2	3.0 \pm 0.3	0.03 \pm 0.03
SR3 _{0tag}	SM Processes	402 \pm 50	75.9 \pm 9.3	79.9 \pm 9.6	60.1 \pm 7.1	17.8 \pm 2.4	6.1 \pm 1.0	4.2 \pm 0.6
	Data	368	76	76	57	13	3	1
	$m_{t\bar{t}} = 400, m_{\tilde{\chi}_1^0} = 313$	24.3 \pm 1.7	5.2 \pm 0.4	5.2 \pm 0.4	4.9 \pm 0.3	4.2 \pm 0.3	4.6 \pm 0.4	0.00 \pm 0.00
	$m_{t\bar{t}} = 400, m_{\tilde{\chi}_1^0} = 225$	4.9 \pm 0.3	0.61 \pm 0.07	0.82 \pm 0.09	0.79 \pm 0.08	0.57 \pm 0.07	0.72 \pm 0.13	0.00 \pm 0.00
SR4 _{tags}	SM Processes	223 \pm 54	45.2 \pm 10.6	42.7 \pm 9.2	32.4 \pm 6.9	9.0 \pm 2.1	1.4 \pm 0.4	0.57 \pm 0.09
	Data	179	38	54	37	3	2	2
	$m_{t\bar{t}} = 400, m_{\tilde{\chi}_1^0} = 313$	1.9 \pm 0.3	0.33 \pm 0.05	0.26 \pm 0.03	0.30 \pm 0.05	0.24 \pm 0.03	0.20 \pm 0.04	0.00 \pm 0.00
	$m_{t\bar{t}} = 400, m_{\tilde{\chi}_1^0} = 225$	16.2 \pm 1.8	2.1 \pm 0.2	2.3 \pm 0.3	1.8 \pm 0.2	1.6 \pm 0.2	2.1 \pm 0.5	0.04 \pm 0.01
SR4 _{0tag}	SM Processes	175 \pm 27	32.7 \pm 5.2	28.8 \pm 4.2	20.8 \pm 3.6	5.8 \pm 1.1	3.0 \pm 0.6	2.9 \pm 0.5
	Data	133	27	29	15	4	5	4
	$m_{t\bar{t}} = 400, m_{\tilde{\chi}_1^0} = 313$	24.6 \pm 2.7	3.7 \pm 0.6	4.3 \pm 0.4	3.4 \pm 0.4	2.7 \pm 0.3	3.2 \pm 0.6	0.00 \pm 0.00
	$m_{t\bar{t}} = 400, m_{\tilde{\chi}_1^0} = 225$	4.2 \pm 0.5	0.45 \pm 0.04	0.50 \pm 0.04	0.36 \pm 0.09	0.32 \pm 0.04	0.26 \pm 0.07	0.02 \pm 0.01

9.3 Post-fit Results

In the analysis presented in this document, the simultaneous binned ML fit is performed using the Higgs Combine tool [250]. $m_{T2}(\ell\ell)$ distributions are fitted across all the different SRs and CRs. Systematic uncertainties are integrated into the fit via nuisance parameters, as described in Section 9.1.

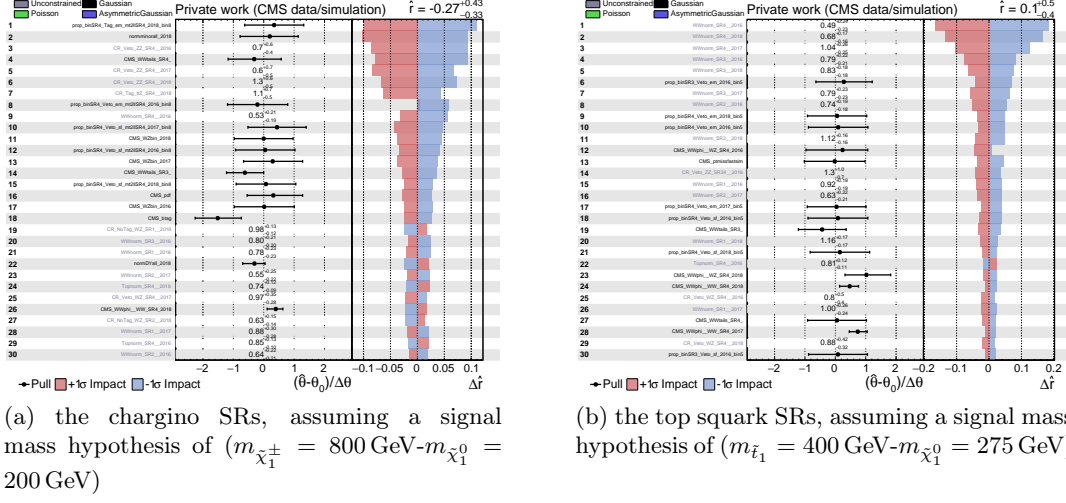
Detailed information on the observed and expected yields after the background-only fit are given in Tables 9.7–9.8 for all dilepton final states and all SRs. No excess over SM prediction is observed in data. The asymptotic approximation of the confidence level CLs criterion [251, 252, 253] is used to set upper limits at 95% CL on the production cross sections for the different signal models considered.

In the remaining of this section, we study how the expected $m_{T2}(\ell\ell)$ post-fit distributions describe the observed data in all the SRs. These results are used in Section 9.4 to set upper limits on the signal production cross sections for the considered signal model.

The first step taken in this analysis is to calculate a goodness-of-fit test, aimed at determining how closely the observed data resembles our theoretical physics model. We evaluate the two main signal hypotheses, obtaining a p-value of approximately 79% for the chargino search regions and 5% for the top squark search regions. These values show that the SM background modelling is compatible with the observed data within the experimental uncertainties. The pulls and impacts for each of the nuisance parameters are shown in Figures 9.8a and 9.8b for a fit to the data in the chargino SRs and in the top squark SRs, respectively.

The remaining of the Section is split in three parts. Firstly, Section 9.3.1 summarises the values

Figure 9.8: Pulls and impacts of the nuisance parameters for the fit to data in the SRs (only the thirty nuisance parameters with the highest impacts are shown). The results are presented for:



of the rate parameters used for the background normalisation obtained by applying the fit, both for the chargino/slepton and the top squark searches. The remaining two parts of the Section are focused on showing a comparison of the observed $m_{T2}(\ell\ell)$ distributions with respect to the expected distributions after performing a background-only fit to the data. Results for the chargino SRs are presented in Section 9.3.2 (Figures 9.10 to 9.12), while the equivalent distributions for the top squark SRs are presented in Section 9.3.3 (Figures 9.13 to 9.16).

9.3.1 Fitted values of the rate parameters for the backgrounds' normalisation

Tables 9.5 to 9.6 summarise the fitted values of the rate parameters for the chargino/slepton search and the top squark search. Figure 9.9 shows the distributions of the significance of the difference in the fitted values of the rate parameters for each pair of data taking year for the chargino/slepton (left) and top squark (right) searches.

Table 9.5: Fitted values of the rate parameters for the normalization of the backgrounds in the chargino/slepton SRs.

t \bar{t}	SR1 no-jet rate	SR1	SR2 no-jet rate	SR2	SR3	SR4
2016	$1.33^{+0.3}_{-0.31}$	$0.95^{+0.06}_{-0.05}$	$1.71^{+0.64}_{-0.64}$	$0.91^{+0.08}_{-0.06}$	$0.86^{+0.09}_{-0.08}$	$0.85^{+0.13}_{-0.1}$
2017	$1.37^{+0.3}_{-0.31}$	$1.0^{+0.07}_{-0.06}$	$1.48^{+0.78}_{-0.8}$	$1.0^{+0.09}_{-0.07}$	$0.94^{+0.1}_{-0.08}$	$0.85^{+0.13}_{-0.1}$
2018	$0.89^{+0.29}_{-0.29}$	$0.95^{+0.08}_{-0.07}$	$1.0^{+0.65}_{-0.7}$	$0.94^{+0.09}_{-0.08}$	$0.9^{+0.1}_{-0.09}$	$0.74^{+0.12}_{-0.09}$
WW	SR1 no-jet rate	SR1	SR2 no-jet rate	SR2	SR3	SR4
2016	$1.21^{+0.7}_{-0.46}$	$0.78^{+0.23}_{-0.23}$	$1.03^{+0.98}_{-0.59}$	$0.64^{+0.22}_{-0.21}$	$0.8^{+0.21}_{-0.2}$	$0.53^{+0.21}_{-0.19}$
2017	$1.15^{+0.69}_{-0.43}$	$0.88^{+0.3}_{-0.28}$	$0.98^{+1.42}_{-0.89}$	$0.55^{+0.25}_{-0.22}$	$0.84^{+0.23}_{-0.21}$	$0.99^{+0.24}_{-0.22}$
2018	$1.56^{+0.52}_{-0.39}$	$0.99^{+0.2}_{-0.19}$	$1.65^{+0.65}_{-0.49}$	$0.99^{+0.18}_{-0.17}$	$0.99^{+0.17}_{-0.16}$	$0.7^{+0.15}_{-0.15}$
WZ	CR1_NoJet	CR1_NoTag	CR2_NoJet	CR2_NoTag	CR3_Veto	CR4_Veto
2016	$0.9^{+0.28}_{-0.24}$	$0.98^{+0.15}_{-0.14}$	$0.6^{+0.48}_{-0.32}$	$1.18^{+0.26}_{-0.23}$	$0.89^{+0.27}_{-0.23}$	$0.93^{+0.38}_{-0.3}$
2017	$1.0^{+0.26}_{-0.22}$	$1.28^{+0.17}_{-0.15}$	$0.25^{+0.28}_{-0.17}$	$1.5^{+0.27}_{-0.24}$	$1.07^{+0.27}_{-0.23}$	$0.97^{+0.35}_{-0.28}$
2018	$1.21^{+0.25}_{-0.22}$	$0.98^{+0.13}_{-0.12}$	$1.26^{+0.48}_{-0.38}$	$0.63^{+0.15}_{-0.14}$	$0.7^{+0.18}_{-0.16}$	$0.89^{+0.31}_{-0.25}$
ZZ	CR1_NoJet	CR1_NoTag	CR2_NoJet	CR2_NoTag	CR3_Veto	CR4_Veto
2016	$1.52^{+0.43}_{-0.37}$	$0.96^{+0.3}_{-0.25}$	$0.27^{+0.39}_{-0.22}$	$1.72^{+0.57}_{-0.48}$	$1.41^{+0.57}_{-0.47}$	$0.67^{+0.59}_{-0.42}$
2017	$1.29^{+0.39}_{-0.33}$	$0.92^{+0.26}_{-0.22}$	$1.77^{+0.81}_{-0.65}$	$1.22^{+0.48}_{-0.39}$	$0.56^{+0.35}_{-0.26}$	$0.63^{+0.71}_{-0.48}$
2018	$1.44^{+0.34}_{-0.3}$	$0.75^{+0.2}_{-0.18}$	$0.65^{+0.4}_{-0.29}$	$0.8^{+0.35}_{-0.28}$	$0.7^{+0.32}_{-0.26}$	$1.33^{+0.6}_{-0.49}$
t \bar{t} Z	CR1_Tag		CR2_Tag		CR3_Tag	CR4_Tag
2016	$1.43^{+0.39}_{-0.34}$		$1.49^{+0.56}_{-0.47}$		$0.85^{+0.42}_{-0.34}$	
2017	$1.9^{+0.41}_{-0.36}$		$1.24^{+0.46}_{-0.38}$		$2.34^{+0.72}_{-0.61}$	$1.78^{+0.95}_{-0.74}$
2018	$1.77^{+0.33}_{-0.3}$		$1.53^{+0.43}_{-0.37}$		$1.89^{+0.53}_{-0.46}$	$1.07^{+0.68}_{-0.52}$

Table 9.6: Fitted values of the rate parameters for the normalization of the backgrounds in the top squark SRs.

$t\bar{t}$	SR1	SR2	SR3	SR4
2016	$0.94^{+0.05}_{-0.05}$	$0.9^{+0.06}_{-0.06}$	$0.82^{+0.08}_{-0.08}$	$0.81^{+0.12}_{-0.11}$
2017	$1.01^{+0.07}_{-0.07}$	$1.0^{+0.08}_{-0.08}$	$0.9^{+0.09}_{-0.09}$	$0.91^{+0.13}_{-0.12}$
2018	$0.98^{+0.07}_{-0.07}$	$0.97^{+0.08}_{-0.08}$	$0.94^{+0.09}_{-0.09}$	$0.73^{+0.1}_{-0.09}$
WW	SR1	SR2	SR3	SR4
2016	$0.92^{+0.19}_{-0.19}$	$0.74^{+0.19}_{-0.18}$	$0.79^{+0.22}_{-0.21}$	$0.49^{+0.24}_{-0.23}$
2017	$1.0^{+0.26}_{-0.24}$	$0.63^{+0.22}_{-0.21}$	$0.79^{+0.23}_{-0.23}$	$1.04^{+0.26}_{-0.25}$
2018	$1.16^{+0.17}_{-0.17}$	$1.12^{+0.16}_{-0.16}$	$0.83^{+0.18}_{-0.18}$	$0.68^{+0.17}_{-0.16}$
WZ	CR1_Veto	CR2_Veto	CR3_Veto	CR4_Veto
2016	$0.97^{+0.13}_{-0.12}$	$1.08^{+0.22}_{-0.2}$	$0.88^{+0.37}_{-0.3}$	$0.84^{+0.52}_{-0.37}$
2017	$1.23^{+0.15}_{-0.14}$	$1.29^{+0.23}_{-0.2}$	$0.94^{+0.34}_{-0.28}$	$0.99^{+0.45}_{-0.35}$
2018	$1.07^{+0.12}_{-0.11}$	$0.74^{+0.15}_{-0.13}$	$0.53^{+0.24}_{-0.19}$	$0.88^{+0.42}_{-0.32}$
ZZ	CR1_Veto	CR2_Veto	CR3_Veto	CR4_Veto
2016	$1.2^{+0.25}_{-0.22}$	$1.17^{+0.38}_{-0.32}$	$1.33^{+1.01}_{-0.71}$	
2017	$1.04^{+0.22}_{-0.19}$	$1.37^{+0.4}_{-0.34}$	$1.21^{+1.18}_{-0.74}$	$0.98^{+1.43}_{-0.81}$
2018	$1.03^{+0.18}_{-0.17}$	$0.78^{+0.27}_{-0.22}$	$1.24^{+0.79}_{-0.6}$	
$t\bar{t}Z$	CR1_Tag	CR2_Tag	CR3_Tag	CR4_Tag
2016	$1.4^{+0.39}_{-0.34}$	$1.4^{+0.54}_{-0.45}$	$0.32^{+0.8}_{-0.45}$	
2017	$1.91^{+0.41}_{-0.36}$	$1.25^{+0.47}_{-0.38}$	$4.7^{+2.04}_{-1.62}$	$1.28^{+1.54}_{-1.0}$
2018	$1.79^{+0.33}_{-0.3}$	$1.53^{+0.43}_{-0.37}$	$2.52^{+1.42}_{-1.07}$	$1.13^{+1.17}_{-0.74}$

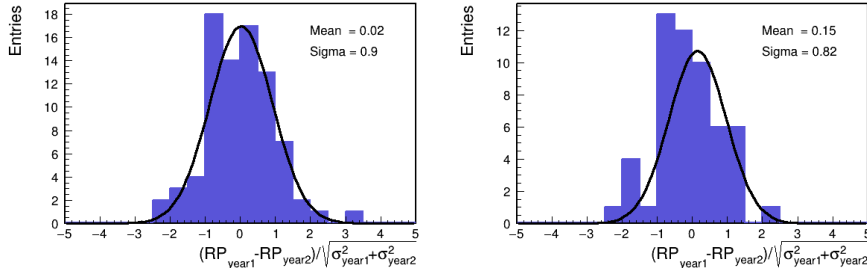


Figure 9.9: Distributions of the significance of the difference in the fitted values of the rate parameters for each of the data taking years for the chargino/slepton (left) and top squark (right) searches.

9.3.2 Chargino search regions

The $m_{T2}(\ell\ell)$ distributions after a background-only fit to the data in the chargino pair production SRs, as defined in the top part of Table 8.2, are presented in Figs. 9.10 to 9.12, using the full Run II dataset. The expected $m_{T2}(\ell\ell)$ distributions for a signal hypothesis with a chargino mass of 800 GeV and a neutralino mass of 200 GeV are also shown as a reference.

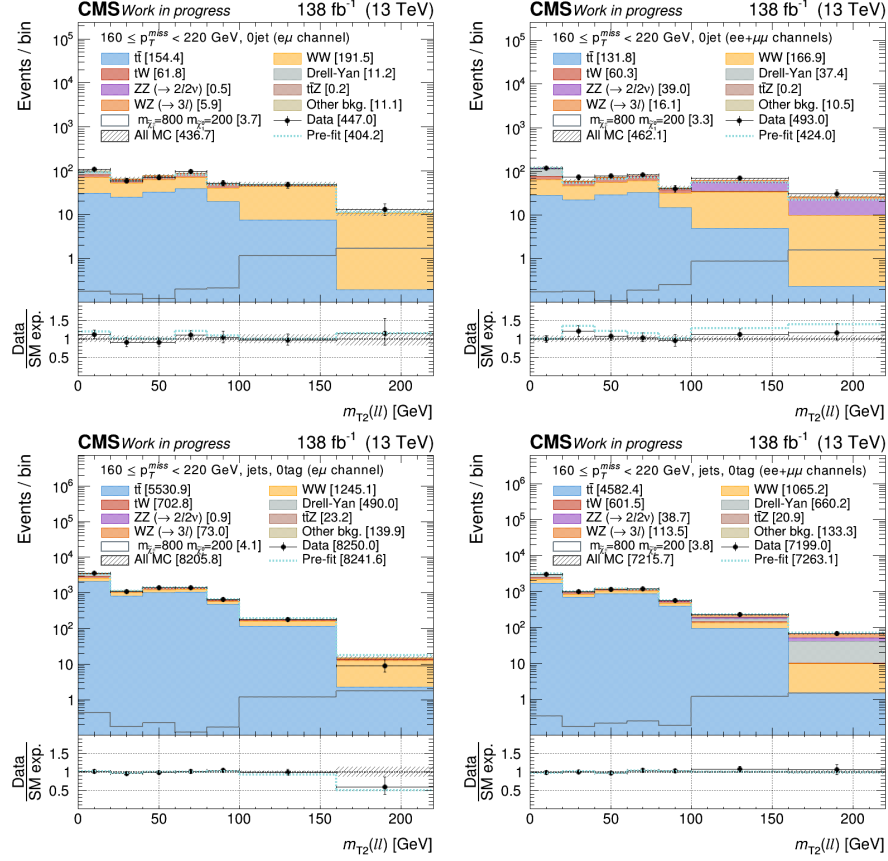


Figure 9.10: Observed and expected $m_{T2}(\ell\ell)$ distributions for SM processes in the SR1 after a background-only fit to the data in the chargino SRs. The $m_{T2}(\ell\ell)$ distributions for a signal hypothesis with a chargino mass of 800 GeV and a neutralino mass of 200 GeV are also shown. The distributions in the SR1 with no jets are shown at the top, and the ones in the SR1 with jets but no b-tagged jets are shown at the bottom, with the plots on the left corresponding to different flavour events and the ones on the right to same flavour events, respectively. In the bottom panel, the ratio of data and SM expectations is shown. The hatched band represents the total uncertainty, including the sources discussed in Section 8.5.

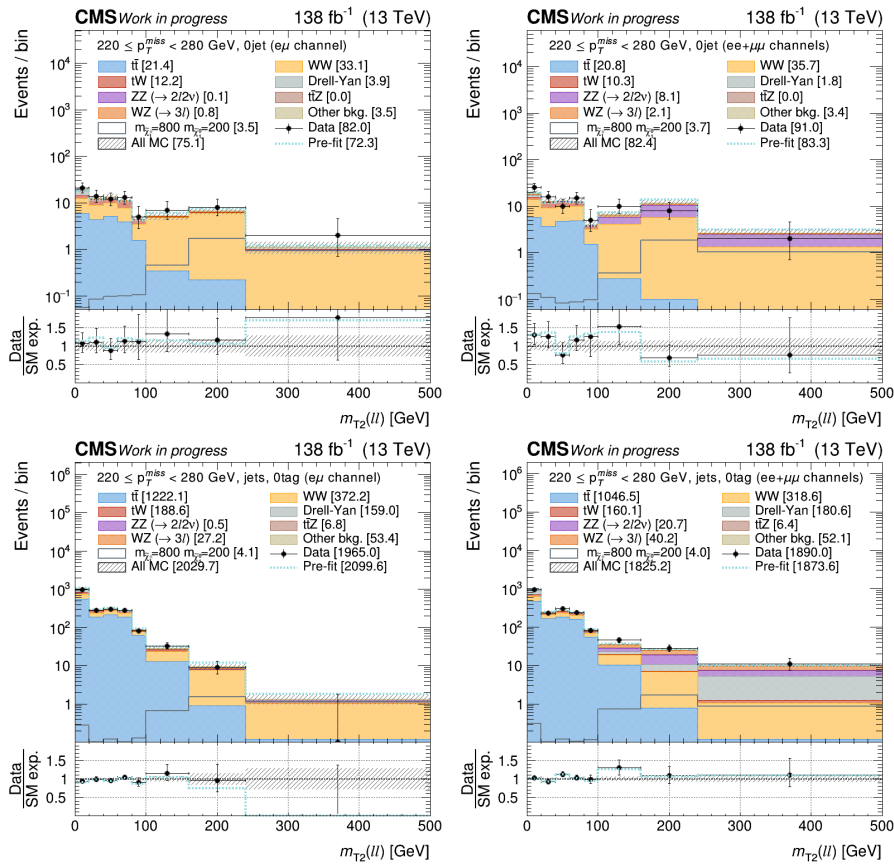


Figure 9.11: Same as for Fig. 9.10 but for the SR2.

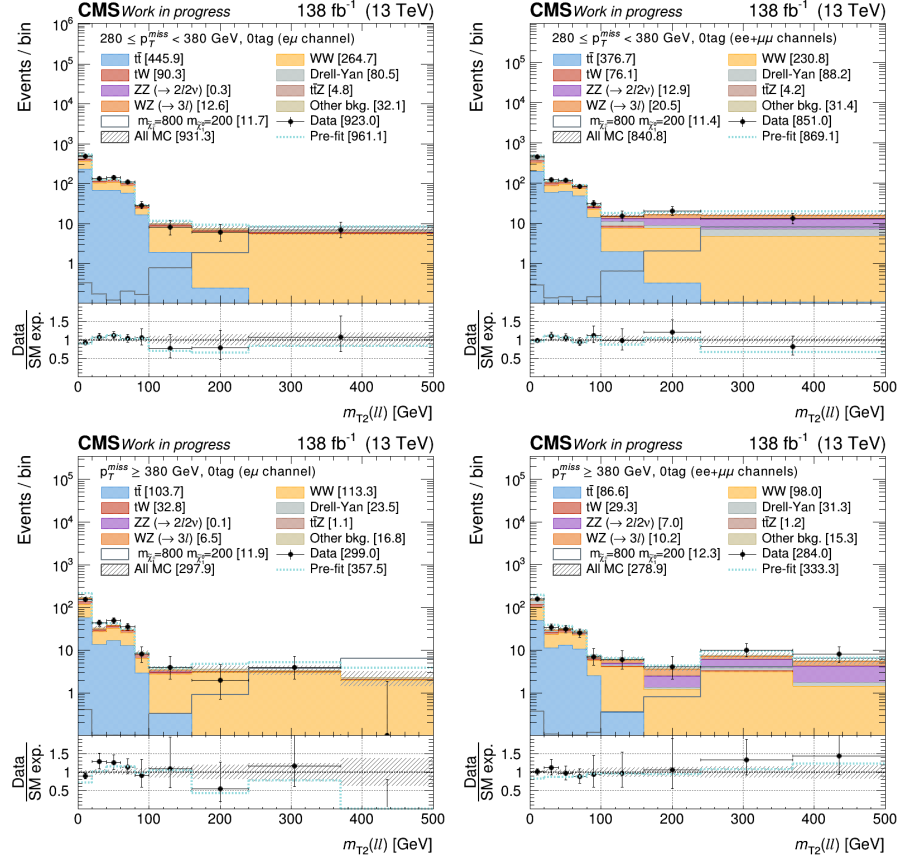


Figure 9.12: Observed and expected $m_{T2}(\ell\ell)$ distributions for SM processes in the SR3 and SR4 after a background-only fit to the data in the chargino SRs. The $m_{T2}(\ell\ell)$ distributions for a signal hypothesis with a chargino mass of 800 GeV and a neutralino mass of 200 GeV are also shown. The distributions in the SR3 are shown at the top, and the ones in the SR4 are shown at the bottom, with the plots on the left corresponding to different flavour events and the ones on the right to same flavour events, respectively. In the bottom panel, the ratio of data and SM expectations is shown. The hatched band represents the total uncertainty, including the sources discussed in Section 8.5.

9.3.3 Top squark search regions

The $m_{T2}(\ell\ell)$ distributions after a background-only fit to the data in the top squark pair production SRs, defined in the bottom part of Table 8.2, are depicted in Figs. 9.13 and 9.16, similarly to chargino signal regions previously shown.

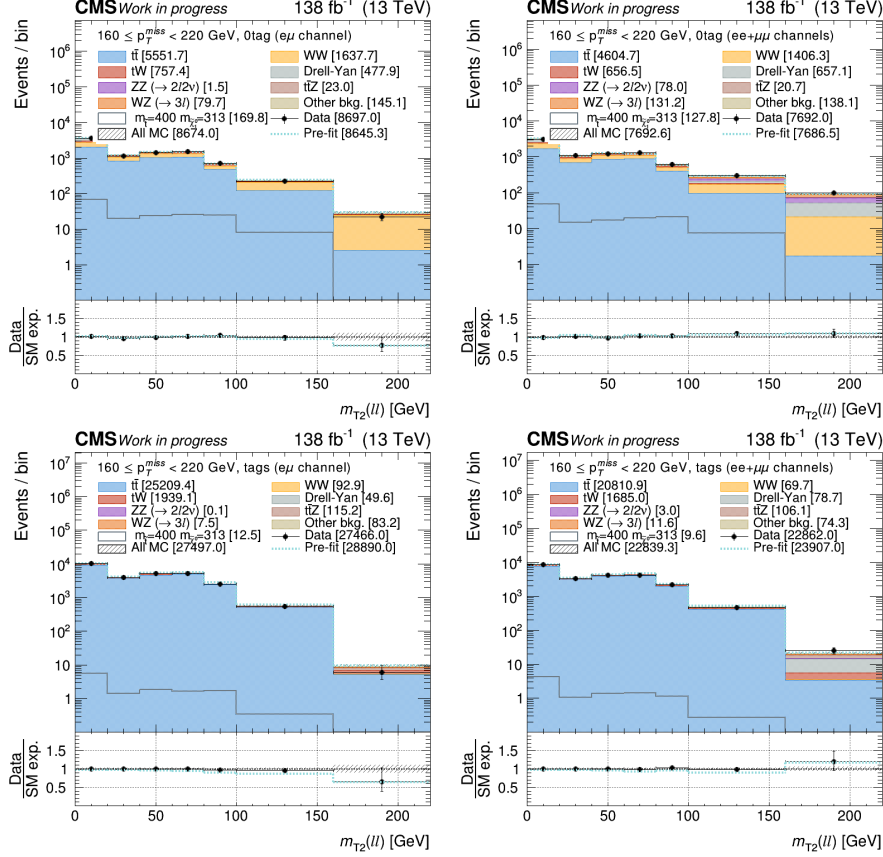


Figure 9.13: Observed and expected $m_{T2}(\ell\ell)$ distributions for SM processes in the SR1 after a background-only fit to the data in the top squark SRs. The $m_{T2}(\ell\ell)$ distributions for a signal hypothesis with a top squark mass of 400 GeV and a neutralino mass of 313 GeV are also shown. Top plots are for DF (left) and SF (right) events with no b-tagged jets. Bottom plots are for DF (left) and SF (right) events with at least one b-tagged jets. In the bottom panel, the ratio of data and SM expectations is shown. The hatched band represents the total uncertainty, including the sources discussed in Section 8.5.

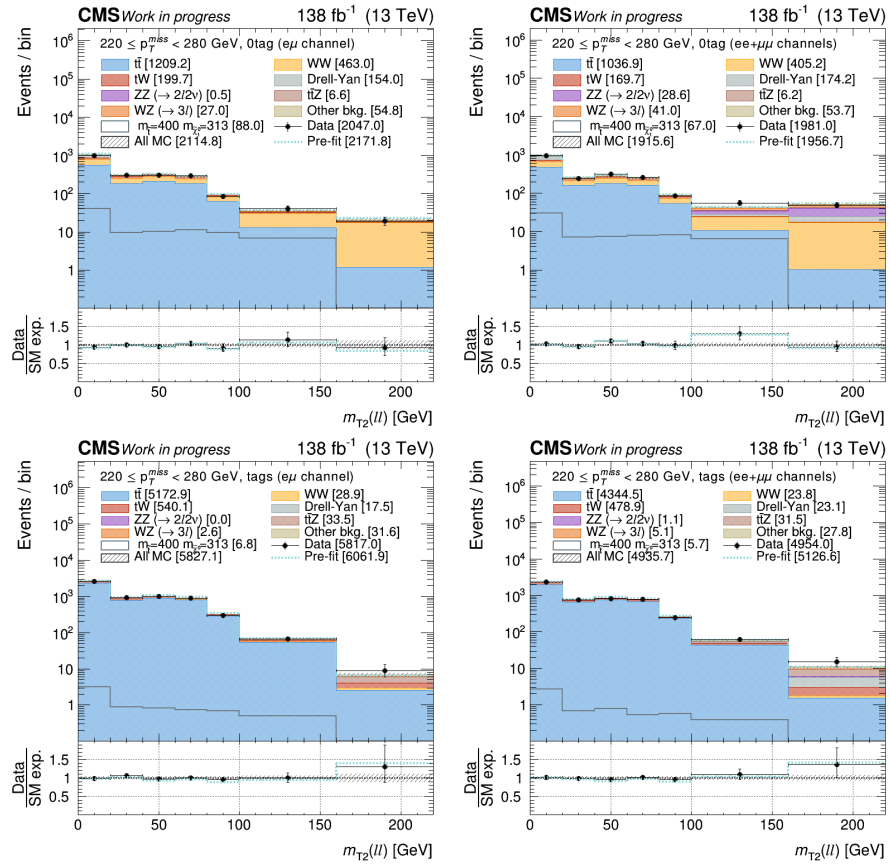


Figure 9.14: Same as for Fig. 9.13 for the SR2.

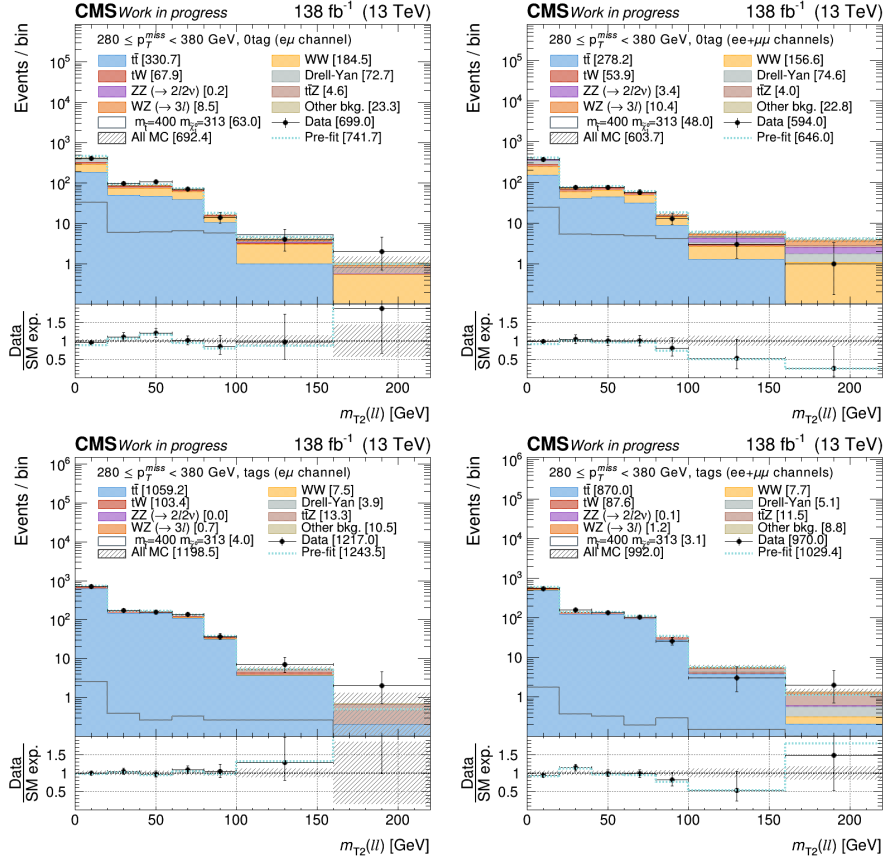


Figure 9.15: Same as for Fig. 9.13 for the SR3.

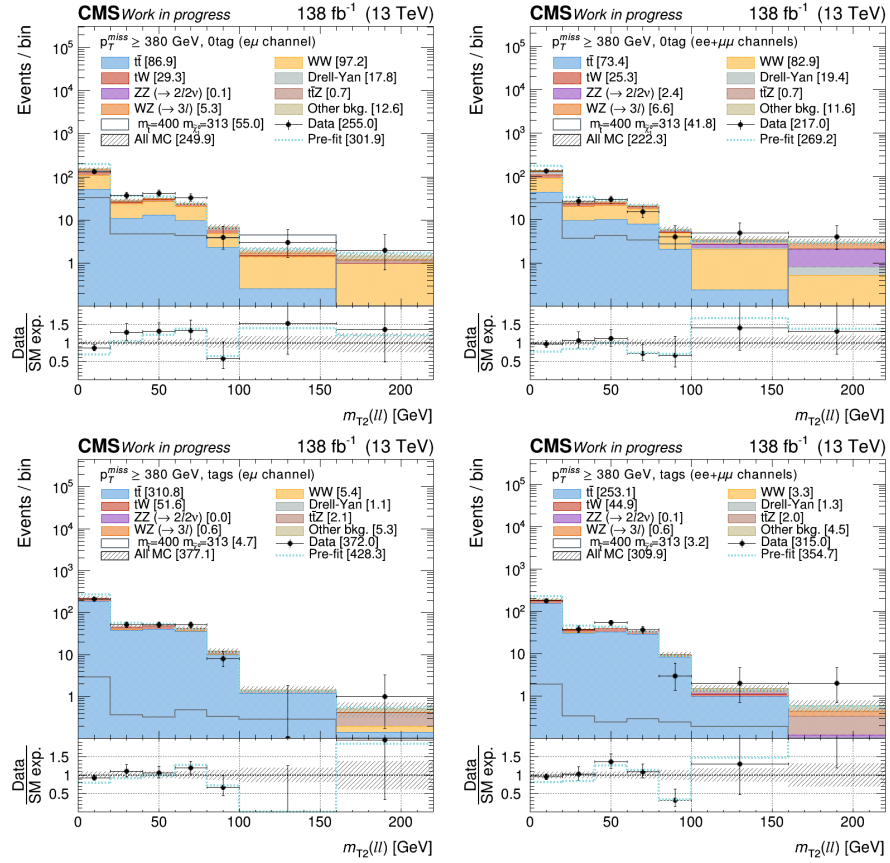


Figure 9.16: Same as for Fig. 9.13 for the SR4.

Table 9.7: Observed and expected yields of DF (upper half) and SF (lower half) events in the SRs for the chargino/slepton search. The quoted uncertainties in the background predictions include statistical and systematic contributions.

$m_{T2}(\ell\ell)$ [GeV]		0-20	20-40	40-60	60-80	80-100	100-160	160-240	240-370	≥ 370
DF events										
SR1 _{0tag} ^{0jet}	SM Processes	97.3 \pm 8.5	64.9 \pm 5.7	77.0 \pm 6.4	87.7 \pm 7.6	50.0 \pm 4.6	48.5 \pm 6.0	11.3 \pm 2.0		
	Data	109	59	70	97	52	47	13		
SR1 _{0tag} ^{1jets}	SM Processes	3469 \pm 55	1148 \pm 19	1388 \pm 22	1380 \pm 19	625 \pm 14	181 \pm 8	15.3 \pm 2.3		
	Data	3545	1099	1368	1397	653	179	9		
SR2 _{0tag} ^{0jet}	SM Processes	19.6 \pm 2.4	12.6 \pm 1.9	13.6 \pm 1.9	11.5 \pm 1.7	4.5 \pm 0.8	5.2 \pm 1.0	6.8 \pm 1.3	1.1 \pm 0.3	
	Data	21	14	12	13	5	7	8	2	
SR2 _{0tag} ^{1jets}	SM Processes	1037 \pm 22	288 \pm 7	311 \pm 8	267 \pm 7	87.7 \pm 3.4	28.5 \pm 2.2	9.4 \pm 1.5	1.3 \pm 0.4	
	Data	982	286	297	278	80	33	9	0	
SR3 _{0tag}	SM Processes	525 \pm 16	124 \pm 4	126 \pm 5	105 \pm 4	27.2 \pm 1.7	10.3 \pm 1.2	7.7 \pm 1.2	6.5 \pm 1.3	
	Data	488	134	142	109	29	8	6	7	
SR4 _{0tag}	SM Processes	173 \pm 8	33.5 \pm 2.4	38.8 \pm 2.4	30.6 \pm 2.2	8.9 \pm 1.0	3.7 \pm 0.6	3.6 \pm 0.7	3.4 \pm 0.9	2.3 \pm 0.9
	Data	154	43	49	35	8	4	2	4	0
SF events										
SR1 _{0tag} ^{0jet}	SM Processes	119 \pm 10	60.4 \pm 5.1	73.2 \pm 6.1	79.1 \pm 6.6	41.9 \pm 3.6	62.3 \pm 5.1	26.4 \pm 2.5		
	Data	118	73	79	82	40	70	31		
SR1 _{0tag} ^{1jets}	SM Processes	3053 \pm 51	999 \pm 17	1185 \pm 19	1153 \pm 17	546 \pm 13	215 \pm 7	64.3 \pm 3.6		
	Data	2992	1002	1142	1202	562	231	68		
SR2 _{0tag} ^{0jet}	SM Processes	19.0 \pm 2.1	12.6 \pm 1.7	13.1 \pm 1.9	12.8 \pm 1.7	4.0 \pm 0.7	6.5 \pm 1.0	11.6 \pm 1.9	2.6 \pm 0.6	
	Data	25	16	10	15	5	10	8	2	
SR2 _{0tag} ^{1jets}	SM Processes	918 \pm 20	248 \pm 6	269 \pm 7	236 \pm 6	83.5 \pm 4.0	35.4 \pm 2.1	25.8 \pm 2.0	9.9 \pm 0.9	
	Data	947	230	303	243	82	46	28	11	
SR3 _{0tag}	SM Processes	461 \pm 14	108 \pm 4	111 \pm 4	86.6 \pm 3.6	26.6 \pm 1.7	15.2 \pm 1.7	16.5 \pm 1.6	15.9 \pm 1.7	
	Data	454	119	118	82	30	15	20	13	
SR4 _{0tag}	SM Processes	158 \pm 8	30.4 \pm 2.2	32.0 \pm 2.1	28.5 \pm 2.4	7.4 \pm 0.8	6.2 \pm 0.8	3.8 \pm 0.6	7.5 \pm 1.1	5.6 \pm 1.0
	Data	159	34	31	25	7	6	4	10	8

9.4 Interpretation of results

No significant excesses above the SM expectations are observed in data. Upper limits at 95% confidence level (CL) are derived on the production cross sections for the different signal models considered, and defined in Section 7.1 of this document. Upper limits on the production of each signal model are calculated utilising the asymptotic approximation of the CLs method [252, 251, 253], calculated through the ML fit previously described in Section 9.3 of this document.

The 95% CL upper limits on the chargino pair production cross sections with the chargino decaying into sleptons are shown in Fig. 9.17a. The $\tilde{\chi}_1^\pm \rightarrow \tilde{\ell}\nu \rightarrow \ell\nu\tilde{\chi}_1^0$ and $\tilde{\chi}_1^\pm \rightarrow \tilde{\ell}\bar{\nu} \rightarrow \ell\nu\tilde{\chi}_1^0$ decay chains are given a branching fraction of 50% each. Likewise, the sleptons are assumed to be degenerate, with a mass equal to the average of the chargino and neutralino masses. By comparing the upper limits with the NLO+NLL $\text{pp} \rightarrow \tilde{\chi}_1^+ \tilde{\chi}_1^-$ production cross sections, observed and expected exclusion regions in the $(m_{\tilde{\chi}_1^\pm}, m_{\tilde{\chi}_1^0})$ plane are also determined. Masses are excluded up to values of about 1120 GeV for the chargino for low neutralino masses; and 490 GeV for the neutralino at a chargino mass of about 850 GeV. These results present a significant improvement on the exclusion region for the chargino mass with respect to the 2016 analysis [44], extending the exclusion mass on the chargino mass by 300 GeV in for low neutralino masses, and the exclusion of the neutralino mass by 150 GeV in the region where $\Delta(m_{\tilde{\chi}_1^\pm}, m_{\tilde{\chi}_1^0})$ is small. These are the most stringent upper limits to date for this signal hypothesis.

The 95% CL upper limits on the chargino pair production cross sections with the chargino decaying into a W boson and the lightest neutralino are presented in Fig. 9.17b. More limited sensitivity is found for this scenario, because of the relatively small branching fraction for the leptonic decay of the W boson.

Table 9.8: Observed and expected yields of DF (upper half) and SF (lower half) events in the SRs for the top squark search. The quoted uncertainties in the background predictions include statistical and systematic contributions.

$m_{T2}(\ell\ell)$ [GeV]		0-20	20-40	40-60	60-80	80-100	100-160	≥ 160
DF events								
SR1 _{tags}	SM Processes	10097 \pm 302	3987 \pm 116	5045 \pm 142	5275 \pm 129	2525 \pm 59	559 \pm 18	9.3 \pm 1.0
	Data	10108	4015	5081	5258	2464	534	6
SR1 _{0tag}	SM Processes	3587 \pm 76	1214 \pm 30	1468 \pm 35	1472 \pm 30	674 \pm 16	230 \pm 9	28.4 \pm 3.1
	Data	3654	1158	1438	1494	705	226	22
SR2 _{tags}	SM Processes	2649 \pm 127	880 \pm 41	1008 \pm 46	900 \pm 41	318 \pm 15	66.0 \pm 4.0	6.9 \pm 0.8
	Data	2628	931	979	902	302	66	9
SR2 _{0tag}	SM Processes	1062 \pm 35	300 \pm 11	324 \pm 12	280 \pm 10	92.8 \pm 4.3	35.1 \pm 2.7	20.5 \pm 2.4
	Data	1003	300	309	291	85	40	19
SR3 _{tags}	SM Processes	709 \pm 40	163 \pm 9	161 \pm 9	125 \pm 8	35.5 \pm 2.7	5.5 \pm 0.7	0.72 \pm 0.61
	Data	707	170	157	137	37	7	2
SR3 _{0tag}	SM Processes	425 \pm 17	89.1 \pm 4.5	87.7 \pm 4.7	69.4 \pm 3.9	16.4 \pm 1.3	4.1 \pm 0.6	1.1 \pm 0.5
	Data	404	99	106	70	14	4	2
SR4 _{tags}	SM Processes	225 \pm 19	46.1 \pm 4.3	48.7 \pm 4.4	42.7 \pm 4.5	12.1 \pm 1.6	1.5 \pm 0.3	0.51 \pm 0.20
	Data	209	51	52	51	8	0	1
SR4 _{0tag}	SM Processes	154 \pm 9	28.7 \pm 2.3	31.9 \pm 2.3	24.6 \pm 2.2	6.9 \pm 0.9	1.9 \pm 0.4	1.5 \pm 0.4
	Data	134	37	42	33	4	3	2
SF events								
SR1 _{tags}	SM Processes	8416 \pm 249	3331 \pm 97	4194 \pm 118	4303 \pm 106	2101 \pm 50	474 \pm 15	20.9 \pm 1.3
	Data	8405	3351	4211	4232	2173	465	25
SR1 _{0tag}	SM Processes	3174 \pm 68	1062 \pm 27	1263 \pm 30	1238 \pm 26	588 \pm 15	277 \pm 9	90.3 \pm 4.3
	Data	3110	1075	1221	1284	602	301	99
SR2 _{tags}	SM Processes	2260 \pm 107	749 \pm 34	844 \pm 38	758 \pm 34	257 \pm 13	57.0 \pm 3.5	10.9 \pm 0.9
	Data	2308	742	811	770	246	62	15
SR2 _{0tag}	SM Processes	942 \pm 29	259 \pm 9	282 \pm 10	250 \pm 9	88.4 \pm 4.6	42.8 \pm 2.3	51.8 \pm 3.5
	Data	972	246	313	258	87	56	49
SR3 _{tags}	SM Processes	573 \pm 32	138 \pm 8	137 \pm 8	105 \pm 6	31.8 \pm 2.4	5.7 \pm 0.7	1.3 \pm 0.2
	Data	542	158	136	103	26	3	2
SR3 _{0tag}	SM Processes	372 \pm 15	73.2 \pm 3.7	76.1 \pm 4.0	57.0 \pm 3.2	16.2 \pm 1.4	5.6 \pm 0.8	3.9 \pm 0.5
	Data	368	76	76	57	13	3	1
SR4 _{tags}	SM Processes	188 \pm 16	36.7 \pm 3.5	39.3 \pm 3.6	33.7 \pm 3.6	9.6 \pm 1.3	1.5 \pm 0.3	0.59 \pm 0.19
	Data	179	38	54	37	3	2	2
SR4 _{0tag}	SM Processes	137 \pm 8	25.5 \pm 2.1	25.8 \pm 1.9	21.0 \pm 2.1	6.1 \pm 0.8	3.6 \pm 0.5	3.0 \pm 0.6
	Data	133	27	29	15	4	5	4

Upper limits are also obtained for the production cross sections of top squark pairs. Figure 9.18 shows the observed and expected 95% CL upper limits for the two SMS considered: Figure 9.18a corresponds to the $\tilde{t}_1 \rightarrow t^* \tilde{\chi}_1^0$ model, and Figure 9.18b to the $\tilde{t}_1 \rightarrow b \tilde{\chi}_1^\pm \rightarrow bW \tilde{\chi}_1^0$ model. The observed and expected exclusion regions when assuming NNLO_{approx}+NNLL top squark pair production cross sections are also presented. In the compressed mass region where the analysis has been optimised, top squark masses are excluded up to about 520 GeV for the $\tilde{t}_1 \rightarrow t^* \tilde{\chi}_1^0$ decay mode. As for the alternative ($\tilde{t}_1 \rightarrow b \tilde{\chi}_1^\pm \rightarrow bW \tilde{\chi}_1^0$) decay model, top squark masses are excluded up to 650 GeV for low neutralino masses, and up to 560 GeV, for $m_{\tilde{t}_1} - m_{\tilde{\chi}_1^0} \approx 2m_W$. These results present an improvement on the exclusion regions for the top squark mass of 100 GeV with respect from the 2016 results [44], and complement other analyses probing for the top squark performed by the CMS Collaboration [174, 173, 176, 177, 187].

Lastly, the 95% CL upper limits on the slepton pair production cross section are shown in Fig. 9.19. By comparing the upper limits with the NLO+NNLL $pp \rightarrow \tilde{\ell}\tilde{\ell}$ production cross section, observed and expected exclusion regions in the $(m_{\tilde{\ell}}, m_{\tilde{\chi}_1^0})$ plane are also determined. Masses are excluded up to values of about 700 GeV for the slepton for low neutralino masses, and up to 360 GeV for the neutralino at a slepton mass of around 600 GeV. The results obtained for this signal hypothesis are found to be competitive with respect to other analyses performed using Run II data, providing additional sensitivity in the region of small $\Delta(m_{\tilde{\ell}}, m_{\tilde{\chi}_1^0})$ [192, 193].

Figure 9.17: Upper limits at 95% CL on the chargino pair production cross section as a function of the chargino and neutralino masses. The thick dashed red line shows the expected exclusion region in the plane $(m_{\tilde{\chi}_1^\pm}, m_{\tilde{\chi}_1^0})$. The thin dashed (dotted) red lines show the $1(2)\sigma$ variation of the expected exclusion region due to the experimental uncertainties. The thick black line shows the observed exclusion region, while the thin black lines show the variation of the observed exclusion region due to the theoretical uncertainties on the production cross section. Limits are shown for a signal model where:

(a) The chargino undergoes a cascade decay via sleptons: $\tilde{\chi}_1^\pm \rightarrow \tilde{\ell} \nu(\ell \tilde{\nu}) \rightarrow \ell \nu \tilde{\chi}_1^0$

(b) the chargino decays into a neutralino and a W boson ($\tilde{\chi}_1^\pm \rightarrow W \tilde{\chi}_1^0$)

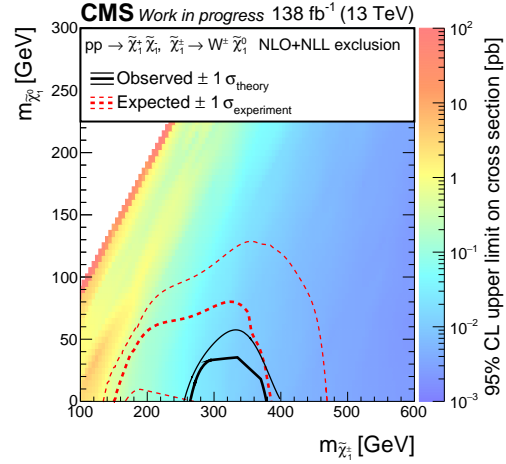
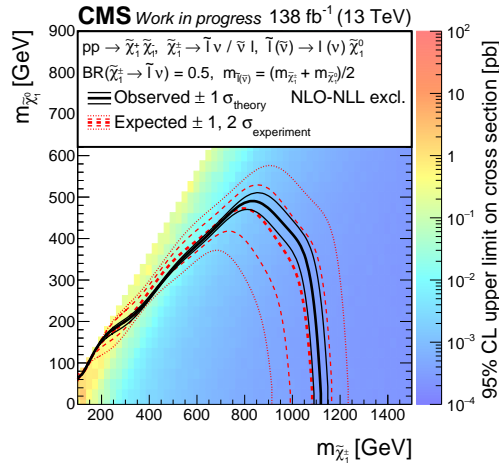
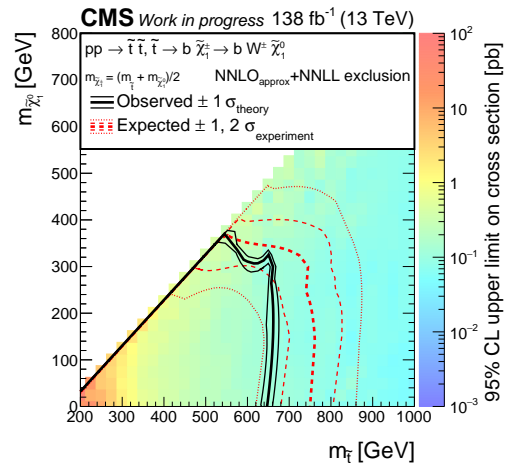
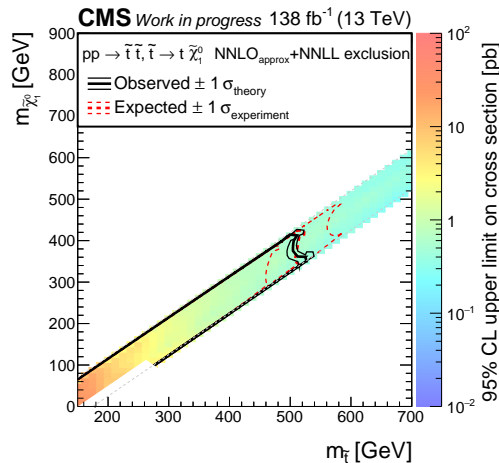


Figure 9.18: Upper limits at 95% CL on the top squark production cross section as a function of the top squark and neutralino masses. The thick dashed red line shows the expected exclusion region in the plane $(m_{\tilde{t}_1}, m_{\tilde{\chi}_1^0})$. The thin dashed (dotted) red lines show the $1(2)\sigma$ variation of the expected exclusion region due to the experimental uncertainties. The thick black line shows the observed exclusion region, while the thin black lines show the variation of the observed exclusion region due to the theoretical uncertainties on the production cross section. Limits are shown for models where:

(a) The top squark decay into a top quark and a neutralino

(b) The top squarks decay into a bottom quark and a chargino, with the latter subsequently decaying into a W boson and a neutralino.



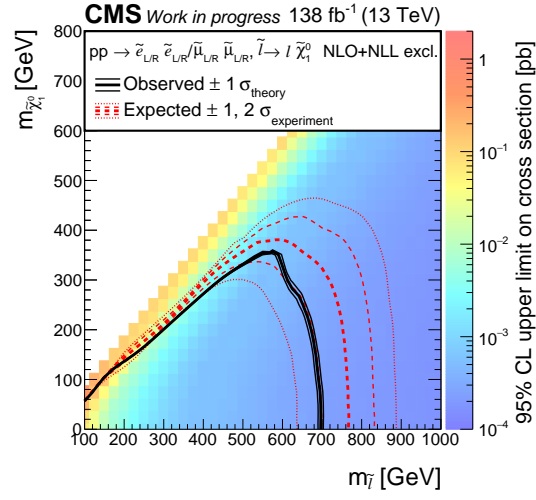


Figure 9.19: Upper limits at 95% CL on the slepton production cross section as a function of the slepton and neutralino masses. The thick dashed red line shows the expected exclusion region in the plane $(m_{\tilde{\ell}}, m_{\tilde{\chi}_1^0})$. The thin dashed (dotted) red lines show the $1(2)\sigma$ variation of the expected exclusion region due to the experimental uncertainties. The thick black line shows the observed exclusion region, while the thin black lines show the variation of the observed exclusion region due to the theoretical uncertainties on the production cross section.

Chapter 10

Conclusions

In this document, a search for several new physics signatures in events with two oppositely charged leptons and large missing transverse momentum has been presented. The obtained results are based on data from pp collision at a centre-of-mass energy of 13 TeV, collected by the CMS experiment at the CERN LHC during the 2016, 2017 and 2018 data-taking years, corresponding to a total integrated luminosity of 138 fb^{-1} . Some of the results presented in this document have already been made public and showcased at international conferences [45], whereas the complete set is currently in the final stage of internal review before publication in a prominent peer-reviewed journal.

No significant evidence for a deviation with respect to the standard model predictions was observed in data. Results have been therefore interpreted in terms of upper limits on the cross sections of supersymmetric particle production for several simplified model spectra. In particular, the pair production of charginos, top squarks or sleptons has been investigated. Chargino pair production has been investigated in two possible decay modes. If the chargino is assumed to undergo a cascade decay through sleptons, an exclusion region in the $(m_{\tilde{\chi}_1^\pm}, m_{\tilde{\chi}_1^0})$ plane is derived, extending to chargino masses of 1120 GeV and neutralino masses of 490 GeV. When the chargino is instead assumed to decay via W bosons, a window of chargino masses between 260 and 380 GeV is excluded for low neutralino masses.

The pair production of top squarks was also probed for two decay scenarios. The main one targets a signal model where the top squark decays into a top quark and a neutralino, and focuses on the case where the mass difference between the top squark and the neutralino lies between the W boson and top quark masses. For this scenario, masses of the top squark are excluded up to 520 GeV. The alternative decay scenario assumes top squark decays into a chargino and a bottom quark, with the chargino subsequently decaying into a W boson and the lightest neutralino. Under these assumptions, top squark masses up to 560 GeV are excluded for $\Delta m \approx 2 m_W$.

Lastly, the production of a pair of sleptons, subsequently decaying into a lepton and a neutralino, has been studied, excluding slepton masses up to 700 GeV and neutralino masses up to 360 GeV.

Bibliography

- [1] Leonardo Carminati and Giovanni Marchiori. *Physics with Photons Using the ATLAS Run 2 Data: Calibration and Identification, Measurement of the Higgs Boson Mass and Search for Supersymmetry in Di-Photon Final State*. Springer Theses. Springer, 2019.
- [2] Siegfried Bethke. Experimental tests of asymptotic freedom. *Prog. Part. Nucl. Phys.*, 58:351–386, 2007.
- [3] Nicolò Trevisani. *Search for Dark Matter Produced in Association with a Higgs Boson in the W^+W^- Fully Leptonic Decay Channel in pp Collisions at $\sqrt{s} = 13$ TeV at the LHC with the CMS Detector*. PhD thesis, Cantabria Inst. of Phys., 2019.
- [4] Y. Gershtein et al. Working Group Report: New Particles, Forces, and Dimensions. In *Snowmass 2013: Snowmass on the Mississippi*, 11 2013.
- [5] Christoph Borschensky, Michael Krämer, Anna Kulesza, Michelangelo Mangano, Sanjay Padhi, Tilman Plehn, and Xavier Portell. Squark and gluino production cross sections in pp collisions at $\sqrt{s} = 13, 14, 33$ and 100 TeV. *Eur. Phys. J. C*, 74(12):3174, 2014.
- [6] Benjamin Fuks, Michael Klasen, David R. Lamprea, and Marcel Rothering. Precision predictions for electroweak superpartner production at hadron colliders with Resummino. *Eur. Phys. J. C*, 73:2480, 2013.
- [7] ATLAS. SUSY August 2023 Summary Plot Update. Technical report, CERN, Geneva, 2023. All figures including auxiliary figures are available at <https://atlas.web.cern.ch/Atlas/GROUPS/PHYSICS/PUBNOTES/ATL-PHYS-PUB-2023-025>.
- [8] Richard D. Ball et al. Parton distributions from high-precision collider data. *Eur. Phys. J. C*, 77(10):663, 2017.
- [9] Tai Sakuma. Cutaway diagrams of CMS detector. <https://cds.cern.ch/record/2665537>, 2019. Accessed: June 14, 2023.
- [10] L. Viliani. CMS tracker performance and readiness for LHC Run II. *Nucl. Instrum. Meth. A*, 824:67–69, 2016.

-
- [11] Giacomo Cucciati. CMS ECAL DAQ monitoring system. *EPJ Web Conf.*, 214:01045, 2019.
- [12] A. Benaglia. The CMS ECAL performance with examples. *JINST*, 9:C02008, 2014.
- [13] Albert M Sirunyan et al. Calibration of the CMS hadron calorimeters using proton-proton collision data at $\sqrt{s} = 13$ TeV. *JINST*, 15(05):P05002, 2020.
- [14] CERN TWiki. CMS Muon DPG Public. <https://twiki.cern.ch/twiki/bin/view/CMSPublic/MuonDPGPublic160729>. Accessed: June 14, 2023.
- [15] A Tapper and Darin Acosta. CMS Technical Design Report for the Level-1 Trigger Upgrade. Technical report, CERN, 2013. Additional contacts: Jeffrey Spalding, Fermilab, Jeffrey.Spalding@cern.ch Didier Contardo, Universite Claude Bernard-Lyon I, dier.claude.contardo@cern.ch.
- [16] CERN Open Data. CMS Monte Carlo Production Overview. <https://opendata.cern.ch/docs/cms-mc-production-overview>. Accessed: June 14, 2023.
- [17] CERN TWiki. CMS Computing Model. <https://twiki.cern.ch/twiki/bin/view/CMSPublic/WorkBookComputingModel>. Accessed: June 14, 2023.
- [18] 1-D plot covering CMS tracker, showing FLUKA simulated 1 MeV neutron equivalent in Silicon including contributions from various particle types. <http://cds.cern.ch/record/2039908>, 2015.
- [19] CERN. Cern document server. <https://cds.cern.ch/record/2120661>, 2015. Accessed: June 14, 2023.
- [20] A. M. Sirunyan et al. Performance of the CMS muon detector and muon reconstruction with proton-proton collisions at $\sqrt{s} = 13$ TeV. *JINST*, 13(06):P06015, 2018.
- [21] Celia Fernandez Madrazo. *Search for long-lived particles decaying into displaced dilepton vertices in proton-proton collisions at $\sqrt{s} = 13$ TeV with the CMS detector*. PhD thesis, 2023, 2023-06-07, Cantabria U., Santander, 6 2023.
- [22] Michael H. Seymour and Marilyn Marx. Monte Carlo Event Generators. In *69th Scottish Universities Summer School in Physics: LHC Physics*, pages 287–319, 4 2013.
- [23] Georges Aad et al. Observation of a new particle in the search for the Standard Model Higgs boson with the ATLAS detector at the LHC. *Phys. Lett. B*, 716:1–29, 2012.
- [24] Serguei Chatrchyan et al. Observation of a New Boson at a Mass of 125 GeV with the CMS Experiment at the LHC. *Phys. Lett. B*, 716:30–61, 2012.
- [25] D. Hanneke, S. Fogwell, and G. Gabrielse. New Measurement of the Electron Magnetic Moment and the Fine Structure Constant. *Phys. Rev. Lett.*, 100:120801, 2008.

-
- [26] Vera C. Rubin and W. Kent Ford, Jr. Rotation of the Andromeda Nebula from a Spectroscopic Survey of Emission Regions. *Astrophys. J.*, 159:379–403, 1970.
- [27] V. C. Rubin, N. Thonnard, and W. K. Ford, Jr. Rotational properties of 21 SC galaxies with a large range of luminosities and radii, from NGC 4605 / $R = 4\text{kpc}/$ to UGC 2885 / $R = 122\text{ kpc}/$. *Astrophys. J.*, 238:471, 1980.
- [28] P. A. R. Ade et al. Planck 2015 results. XIII. Cosmological parameters. *Astron. Astrophys.*, 594:A13, 2016.
- [29] Maxim Markevitch, A. H. Gonzalez, D. Clowe, A. Vikhlinin, L. David, W. Forman, C. Jones, S. Murray, and W. Tucker. Direct constraints on the dark matter self-interaction cross-section from the merging galaxy cluster 1E0657-56. *Astrophys. J.*, 606:819–824, 2004.
- [30] Pierre Ramond. Dual Theory for Free Fermions. *Phys. Rev. D*, 3:2415–2418, 1971.
- [31] Yu. A. Golfand and E. P. Likhtman. Extension of the Algebra of Poincare Group Generators and Violation of p Invariance. *JETP Lett.*, 13:323–326, 1971.
- [32] A. Neveu and J. H. Schwarz. Factorizable dual model of pions. *Nucl. Phys. B*, 31:86–112, 1971.
- [33] D. V. Volkov and V. P. Akulov. Possible universal neutrino interaction. *JETP Lett.*, 16:438–440, 1972.
- [34] J. Wess and B. Zumino. A Lagrangian Model Invariant Under Supergauge Transformations. *Phys. Lett. B*, 49:52, 1974.
- [35] J. Wess and B. Zumino. Supergauge Transformations in Four-Dimensions. *Nucl. Phys. B*, 70:39–50, 1974.
- [36] Pierre Fayet. Supergauge Invariant Extension of the Higgs Mechanism and a Model for the electron and Its Neutrino. *Nucl. Phys. B*, 90:104–124, 1975.
- [37] Hans Peter Nilles. Supersymmetry, Supergravity and Particle Physics. *Phys. Rept.*, 110:1–162, 1984.
- [38] Stephen P. Martin. A Supersymmetry primer. *Adv. Ser. Direct. High Energy Phys.*, 18:1–98, 1998.
- [39] Edward Witten. Dynamical Breaking of Supersymmetry. *Nucl. Phys. B*, 188:513, 1981.
- [40] Savas Dimopoulos and Howard Georgi. Softly Broken Supersymmetry and SU(5). *Nucl. Phys. B*, 193:150–162, 1981.
- [41] Romesh K. Kaul and Parthasarathi Majumdar. Cancellation of Quadratically Divergent Mass Corrections in Globally Supersymmetric Spontaneously Broken Gauge Theories. *Nucl. Phys. B*, 199:36, 1982.

- [42] Glennys R. Farrar and Pierre Fayet. Phenomenology of the Production, Decay, and Detection of New Hadronic States Associated with Supersymmetry. *Phys. Lett. B*, 76:575–579, 1978.
- [43] Gerard Jungman, Marc Kamionkowski, and Kim Griest. Supersymmetric dark matter. *Phys. Rept.*, 267:195–373, 1996.
- [44] Albert M. Sirunyan et al. Searches for pair production of charginos and top squarks in final states with two oppositely charged leptons in proton-proton collisions at $\sqrt{s} = 13$ TeV. *JHEP*, 11:079, 2018.
- [45] Albert M Sirunyan et al. Search for charginos and stops in 2LOS final state (Run 2 legacy). Technical report, CERN, Geneva, 2024.
- [46] Mark Thomson. *Modern particle physics*. Cambridge University Press, New York, 2013.
- [47] F. Halzen and Alan D. Martin. *Quarks and leptons: an introductory course in modern particle physics*. Wiley, 1984.
- [48] R. L. Workman et al. Review of Particle Physics. *PTEP*, 2022:083C01, 2022.
- [49] Fermi National Accelerator Laboratory. What’s a neutrino? <https://neutrinos.fnal.gov/whats-a-neutrino/>, 2024. [Online; accessed 16-January-2024].
- [50] Y. Fukuda et al. Evidence for oscillation of atmospheric neutrinos. *Phys. Rev. Lett.*, 81:1562–1567, 1998.
- [51] Q. R. Ahmad et al. Direct evidence for neutrino flavor transformation from neutral current interactions in the Sudbury Neutrino Observatory. *Phys. Rev. Lett.*, 89:011301, 2002.
- [52] M. Aker et al. Direct neutrino-mass measurement with sub-electronvolt sensitivity. *Nature Phys.*, 18(2):160–166, 2022.
- [53] S. K. Choi et al. Observation of a narrow charmonium-like state in exclusive $B^\pm \rightarrow K^\pm \pi^+ \pi^- J/\psi$ decays. *Phys. Rev. Lett.*, 91:262001, 2003.
- [54] Roel Aaij et al. Observation of $J/\psi p$ Resonances Consistent with Pentaquark States in $\Lambda_b^0 \rightarrow J/\psi K^- p$ Decays. *Phys. Rev. Lett.*, 115:072001, 2015.
- [55] F. Englert and R. Brout. Broken Symmetry and the Mass of Gauge Vector Mesons. *Phys. Rev. Lett.*, 13:321–323, 1964.
- [56] Peter W. Higgs. Broken Symmetries and the Masses of Gauge Bosons. *Phys. Rev. Lett.*, 13:508–509, 1964.
- [57] K. Jimmy Juge, Julius Kuti, and Colin Morningstar. Fine structure of the QCD string spectrum. *Phys. Rev. Lett.*, 90:161601, 2003.

- [58] David J. Gross and Frank Wilczek. Ultraviolet Behavior of Nonabelian Gauge Theories. *Phys. Rev. Lett.*, 30:1343–1346, 1973.
- [59] H. David Politzer. Reliable Perturbative Results for Strong Interactions? *Phys. Rev. Lett.*, 30:1346–1349, 1973.
- [60] Gerard 't Hooft. Renormalization of Massless Yang-Mills Fields. *Nucl. Phys. B*, 33:173–199, 1971.
- [61] J. Goldstone. Field Theories with Superconductor Solutions. *Nuovo Cim.*, 19:154–164, 1961.
- [62] A. B. Balantekin and W. C. Haxton. Neutrino Oscillations. *Prog. Part. Nucl. Phys.*, 71:150–161, 2013.
- [63] Steven Weinberg. A Model of Leptons. *Phys. Rev. Lett.*, 19:1264–1266, 1967.
- [64] Abdus Salam and John Clive Ward. Weak and electromagnetic interactions. *Nuovo Cim.*, 11:568–577, 1959.
- [65] R. Cashmore, L. Maiani, and J. P. Revol, editors. *Prestigious discoveries at CERN: 1973 Neutral currents, 1983 W and Z bosons. Proceedings, Symposium celebrating the anniversary of CERN's discoveries and a look into the future, Geneva, Switzerland, September 16, 2003*, volume 34, 2004.
- [66] J. H. Christenson, J. W. Cronin, V. L. Fitch, and R. Turlay. Evidence for the 2π Decay of the K_2^0 Meson. *Phys. Rev. Lett.*, 13:138–140, 1964.
- [67] Kazuo Abe et al. Observation of large CP violation in the neutral B meson system. *Phys. Rev. Lett.*, 87:091802, 2001.
- [68] Edvige Corbelli and Paolo Salucci. The Extended Rotation Curve and the Dark Matter Halo of M33. *Mon. Not. Roy. Astron. Soc.*, 311:441–447, 2000.
- [69] Douglas Clowe, Marusa Bradac, Anthony H. Gonzalez, Maxim Markevitch, Scott W. Randall, Christine Jones, and Dennis Zaritsky. A direct empirical proof of the existence of dark matter. *Astrophys. J. Lett.*, 648:L109–L113, 2006.
- [70] P. J. E. Peebles and Bharat Ratra. The Cosmological Constant and Dark Energy. *Rev. Mod. Phys.*, 75:559–606, 2003.
- [71] J. Lesgourgues and L. Verde. Neutrinos in cosmology. *Particle Data Group*, 2019.
- [72] Joseph Formaggio et al. Direct neutrino-mass measurement with sub-electronvolt sensitivity. *Nature Physics*, 18(2), 2022.
- [73] H. Georgi and S. L. Glashow. Unity of All Elementary Particle Forces. *Phys. Rev. Lett.*, 32:438–441, 1974.

-
- [74] B. Abi et al. Measurement of the Positive Muon Anomalous Magnetic Moment to 0.46 ppm. *Phys. Rev. Lett.*, 126(14):141801, 2021.
- [75] T. Aoyama et al. The anomalous magnetic moment of the muon in the Standard Model. *Phys. Rept.*, 887:1–166, 2020.
- [76] G. W. Bennett et al. Final Report of the Muon E821 Anomalous Magnetic Moment Measurement at BNL. *Phys. Rev. D*, 73:072003, 2006.
- [77] D. P. Aguillard et al. Measurement of the Positive Muon Anomalous Magnetic Moment to 0.20 ppm. *Phys. Rev. Lett.*, 131(16):161802, 2023.
- [78] Yasmine Sara Amhis et al. Averages of b-hadron, c-hadron, and τ -lepton properties as of 2021. *Phys. Rev. D*, 107(5):052008, 2023.
- [79] F. Abe et al. The CDF Detector: An Overview. *Nucl. Instrum. Meth. A*, 271:387–403, 1988.
- [80] Stephen Holmes, Ronald S. Moore, and Vladimir Shiltsev. Overview of the Tevatron Collider Complex: Goals, Operations and Performance. *JINST*, 6:T08001, 2011.
- [81] T. Aaltonen et al. High-precision measurement of the W boson mass with the CDF II detector. *Science*, 376(6589):170–176, 2022.
- [82] Georges Aad et al. Improved W boson Mass Measurement using 7 TeV Proton-Proton Collisions with the ATLAS Detector. Technical report, CERN, Geneva, 2023. All figures including auxiliary figures are available at <https://atlas.web.cern.ch/Atlas/GROUPS/PHYSICS/CONFNOTES/ATLAS-CONF-2023-004>.
- [83] Roel Aaij et al. Measurement of the W boson mass. *JHEP*, 01:036, 2022.
- [84] Albert M Sirunyan et al. Measurement of the W boson mass in proton-proton collisions at $\sqrt{s} = 13$ TeV. Technical report, CERN, Geneva, 2024.
- [85] Savas Dimopoulos and Howard Georgi. Softly Broken Supersymmetry and $SU(5)$. *Nucl. Phys. B*, 193:150–162, 1981.
- [86] Joseph Gerard Polchinski. *String theory, volume I: An introduction to the bosonic string*. Cambridge university press Cambridge, 1998.
- [87] H. Nishino et al. Search for Proton Decay via $p \rightarrow e^+ \pi^0$ and $p \rightarrow \mu^+ \pi^0$ in a Large Water Cherenkov Detector. *Phys. Rev. Lett.*, 102:141801, 2009.
- [88] Takehiko Asaka, Koji Ishiwata, and Takeo Moroi. Right-handed sneutrino as cold dark matter of the universe. *Phys. Rev. D*, 75:065001, 2007.

- [89] Stephen P. Martin. A Supersymmetry primer. *Advanced Series on Directions in High Energy Physics*, 18:1, 2016.
- [90] Rolf-Dieter Heuer. CERN and 60 years of science for peace. *AIP Conf. Proc.*, 1645(1):430–436, 2015.
- [91] Joachim Mnich. Cern status and news. Technical report, CERN, 2022.
- [92] CERN. Le cern inaugure le portail de la science, son nouveau centre de communication grand public pour l’éducation scientifique. <https://home.cern/fr/news/press-release/cern/cern-inaugurates-science-gateway-its-new-outreach-centre-science-education>, 2023. Accessed: 2024-01-22.
- [93] Summer student programme. <https://home.cern/summer-student-programme>. Accessed: 2024-01-22.
- [94] Stephen Myers. *The LEP Collider, from design to approval and commissioning*. John Adams’ memorial lecture. CERN, Geneva, 1991. Delivered at CERN, 26 Nov 1990.
- [95] J. Alcaraz et al. A Combination of preliminary electroweak measurements and constraints on the standard model, 12 2006.
- [96] S. Abachi et al. Observation of the top quark. *Phys. Rev. Lett.*, 74:2632–2637, 1995.
- [97] The T. E. V. N. P. H. Working Group. Combined CDF and D0 Upper Limits on Standard Model Higgs-Boson Production with up to 6.7 fb^{-1} of Data. In *35th International Conference on High Energy Physics*, 7 2010.
- [98] G. Aad et al. The ATLAS Experiment at the CERN Large Hadron Collider. *JINST*, 3:S08003, 2008.
- [99] A. Augusto Alves, Jr. et al. The LHCb Detector at the LHC. *JINST*, 3:S08005, 2008.
- [100] K. Aamodt et al. The ALICE experiment at the CERN LHC. *JINST*, 3:S08002, 2008.
- [101] R Alemany-Fernandez, E Bravin, L Drosdal, A Gorzawski, V Kain, M Lamont, A Macpherson, G Papotti, M Pojer, L Ponce, S Redaelli, G Roy, M Solfaroli Camillocci, W Venturini, and J Wenninger. Operation and Configuration of the LHC in Run 1. Technical report, CERN, 2013.
- [102] J. T. Boyd. LHC Run-2 and future prospects. *CERN Yellow Rep. School Proc.*, 5:247, 2022.
- [103] V Karimäki, M Mannelli, P Siegrist, H Breuker, A Caner, R Castaldi, K Freudenreich, G Hall, R Horisberger, M Huhtinen, and A Cattai. *The CMS tracker system project: Technical Design Report*. Technical design report. CMS. CERN, Geneva, 1997.

-
- [104] W. Adam et al. The CMS Phase-1 Pixel Detector Upgrade. *JINST*, 16(02):P02027, 2021.
- [105] Walaa Elmetenawee. CMS track reconstruction performance during Run 2 and developments for Run 3. *PoS*, ICHEP2020:733, 2021.
- [106] CMS. *The CMS electromagnetic calorimeter project: Technical Design Report*. Technical design report. CMS. CERN, Geneva, 1997.
- [107] CMS. *The CMS hadron calorimeter project: Technical Design Report*. Technical design report. CMS. CERN, Geneva, 1997. The following files are from http://uscms.fnal.gov/pub/hcal_tdr and may not be the version as printed, please check the printed version to be sure.
- [108] CMS. *The CMS magnet project: Technical Design Report*. Technical design report. CMS. CERN, Geneva, 1997.
- [109] A. M. Sirunyan et al. Searches for pair production of charginos and top squarks in final states with two oppositely charged leptons in proton-proton collisions at $\sqrt{s} = 13$ TeV. *JHEP*, 11:079, 2018.
- [110] J. G. Layter. *The CMS muon project: Technical Design Report*. Technical design report. CMS. CERN, Geneva, 1997.
- [111] Vardan Khachatryan et al. The CMS trigger system. *JINST*, 12(01):P01020, 2017.
- [112] S. Dasu et al. *CMS TriDAS project: Technical Design Report, Volume 1: The Trigger Systems*. Technical design report. CMS. CERN, 2000.
- [113] Sergio Cittolin, Attila Rácz, and Paris Sphicas. *CMS The TriDAS Project: Technical Design Report, Volume 2: Data Acquisition and High-Level Trigger. CMS trigger and data-acquisition project*. Technical design report. CMS. CERN, Geneva, 2002.
- [114] CMS Public Luminosity Results. https://twiki.cern.ch/twiki/bin/view/CMSPublic/LumiPublicResults#Run_1_charts_of_luminosity.
- [115] Alfredo Ferrari, Paola R. Sala, Alberto Fasso, and Johannes Ranft. FLUKA: A multi-particle transport code (Program version 2005). Technical report, CERN, 10 2005.
- [116] CERN RD50 Collaboration. Rd50 - radiation hard semiconductor devices for very high luminosity colliders. <http://rd50.web.cern.ch/>, 2023. Accessed: 29-09-2023.
- [117] M. Glaser, F. Ravotti, and M. Moll. Dosimetry assessments in the irradiation facilities at the CERN-PS accelerator. *IEEE Trans. Nucl. Sci.*, 53:2016–2022, 2006.
- [118] M. Moll, E. Fretwurst, and G. Lindstrom. Leakage current of hadron irradiated silicon detectors - material dependence. *Nucl. Instrum. Meth. A*, 426:87–93, 1999.

-
- [119] Pablo Matorras Cuevas. An automatic method to analyze the Capacity-Voltage and Current-Voltage curves of a sensor. <http://cds.cern.ch/record/2281851>, 2017.
- [120] DESY Particle Physics. Test beams at desy. https://particle-physics.desy.de/test_beams_at_desy/, 2023. Accessed: 2023-09-29.
- [121] CMS. Particle-Flow Event Reconstruction in CMS and Performance for Jets, Taus, and MET. Technical report, CERN, Geneva, 2009.
- [122] Serguei Chatrchyan et al. Performance of CMS Muon Reconstruction in pp Collision Events at $\sqrt{s} = 7$ TeV. *JINST*, 7:P10002, 2012.
- [123] R. E. Kalman. A New Approach to Linear Filtering and Prediction Problems. *Journal of Basic Engineering*, 82(1):35–45, 03 1960.
- [124] R. Fruhwirth. Application of Kalman filtering to track and vertex fitting. *Nucl. Instrum. Meth. A*, 262:444–450, 1987.
- [125] CMS Collaboration. Muon Identification and Isolation for Run 2. <https://twiki.cern.ch/twiki/bin/view/CMS/SWGuideMuonIdRun2>, 2019. CMS Muon POG Recommendations, accessed on October 8, 2024.
- [126] Albert M Sirunyan et al. Electron and photon reconstruction and identification with the CMS experiment at the CERN LHC. *JINST*, 16(05):P05014, 2021.
- [127] Wolfgang Adam, R Frühwirth, Are Strandlie, and T Todor. Reconstruction of Electrons with the Gaussian-Sum Filter in the CMS Tracker at the LHC. Technical report, CERN, Geneva, 2005.
- [128] H. Bethe and W. Heitler. On the Stopping of fast particles and on the creation of positive electrons. *Proc. Roy. Soc. Lond. A*, 146:83–112, 1934.
- [129] Albert M Sirunyan et al. Electron and photon reconstruction and identification with the CMS experiment at the CERN LHC. *JINST*, 16(05):P05014, 2021.
- [130] Andreas Hocker, Peter Speckmayer, Jorg Stelzer, Jan Therhaag, Eckhard von Toerne, Helge Voss, Moritz Backes, Tancredi Carli, Or Cohen, Asen Christov, Domikik Dannheim, Krzysztof Danielowski, S. Henrot-Versille, M. Jachowski, Kamil Kraszewski, Jr. Krasznahorkay, A., Maciej Kruk, Y. Mahalalel, Rustem Ospanov, X. Prudent, Arnaud Robert, Doug Schouten, F. Tegenfeldt, Alexander Voight, K. Voss, Marcin Wolter, and Andrzej Zemla. TMVA - Toolkit for Multivariate Data Analysis with ROOT: Users guide. TMVA - Toolkit for Multivariate Data Analysis. Technical report, CERN, Geneva, 2007. TMVA-v4 Users Guide: 135 pages, 19 figures, numerous code examples and references.
- [131] Albert M. Sirunyan et al. Measurements of properties of the Higgs boson decaying to a W boson pair in pp collisions at $\sqrt{s} = 13$ TeV. *Phys. Lett. B*, 791:96, 2019.
- [132] Matteo Cacciari, Gavin P. Salam, and Gregory Soyez. The anti- k_t jet clustering algorithm. *JHEP*, 04:063, 2008.

-
- [133] Tilman Plehn, Gavin P. Salam, and Michael Spannowsky. Fat Jets for a Light Higgs. *Phys. Rev. Lett.*, 104:111801, 2010.
- [134] Garvita Agarwal. Jet Energy Scale and Resolution Measurements in CMS. *PoS, ICHEP2022*:652, 2022.
- [135] A. M. Sirunyan et al. Identification of heavy-flavour jets with the CMS detector in pp collisions at 13 TeV. *JINST*, 13(05):P05011, 2018.
- [136] Emil Bols, Jan Kieseler, Mauro Verzetti, Markus Stoye, and Anna Stakia. Jet Flavour Classification Using DeepJet. *JINST*, 15(12):P12012, 2020.
- [137] Huilin Qu and Loukas Gouskos. ParticleNet: Jet Tagging via Particle Clouds. *Phys. Rev. D*, 101(5):056019, 2020.
- [138] Huilin Qu, Congqiao Li, and Sitian Qian. Particle Transformer for Jet Tagging, 2 2022.
- [139] A. M. Sirunyan et al. Performance of reconstruction and identification of τ leptons decaying to hadrons and ν_τ in pp collisions at $\sqrt{s} = 13$ TeV. *JINST*, 13(10):P10005, 2018.
- [140] Serguei Chatrchyan et al. Missing transverse energy performance of the CMS detector. *JINST*, 6:P09001, 2011.
- [141] K. Mavrokoridis, F. Ball, J. Carroll, M. Lazos, K. J. McCormick, N. A. Smith, C. Touramanis, and J. Walker. Optical Readout of a Two Phase Liquid Argon TPC using CCD Camera and THGEMs. *JINST*, 9:P02006, 2014.
- [142] Nicholas Metropolis and Stanislaw Ulam. The monte carlo method. *Journal of the American statistical association*, 44(247):335–341, 1949.
- [143] Dirk P Kroese, Tim Brereton, Thomas Taimre, and Zdravko I Botev. Why the monte carlo method is so important today. *Wiley Interdisciplinary Reviews: Computational Statistics*, 6(6):386–392, 2014.
- [144] S. Agostinelli et al. GEANT4—a simulation toolkit. *Nucl. Instrum. Meth. A*, 506:250–303, 2003.
- [145] J. de Favereau, C. Delaere, P. Demin, A. Giammanco, V. Lemaître, A. Mertens, and M. Selvaggi. DELPHES 3, A modular framework for fast simulation of a generic collider experiment. *JHEP*, 02:057, 2014.
- [146] J. Alwall, R. Frederix, S. Frixione, V. Hirschi, F. Maltoni, O. Mattelaer, H. S. Shao, T. Stelzer, P. Torrielli, and M. Zaro. The automated computation of tree-level and next-to-leading order differential cross sections, and their matching to parton shower simulations. *JHEP*, 07:079, 2014.
- [147] Simone Alioli, Paolo Nason, Carlo Oleari, and Emanuele Re. A general framework for implementing NLO calculations in shower Monte Carlo programs: the POWHEG BOX. *JHEP*, 06:043, 2010.

-
- [148] Rikkert Frederix and Stefano Frixione. Merging meets matching in MC@NLO. *JHEP*, 12:061, 2012.
- [149] T. Gleisberg, Stefan. Hoeche, F. Krauss, M. Schonherr, S. Schumann, F. Siegert, and J. Winter. Event generation with SHERPA 1.1. *JHEP*, 02:007, 2009.
- [150] Torbjörn Sjöstrand, Stefan Ask, Jesper R. Christiansen, Richard Corke, Nishita Desai, Philip Ilten, Stephen Mrenna, Stefan Prestel, Christine O. Rasmussen, and Peter Z. Skands. An introduction to PYTHIA 8.2. *Comput. Phys. Commun.*, 191:159–177, 2015.
- [151] Johannes Bellm et al. Herwig 7.0/Herwig++ 3.0 release note. *Eur. Phys. J. C*, 76(4):196, 2016.
- [152] Bo Andersson, G. Gustafson, and B. Soderberg. A General Model for Jet Fragmentation. *Z. Phys. C*, 20:317, 1983.
- [153] B. R. Webber. Fragmentation and hadronization. *Int. J. Mod. Phys. A*, 15S1:577–606, 2000.
- [154] A first look at early 2022 proton-proton collisions at $\sqrt{s} = 13.6$ TeV for heavy-flavor jet tagging, 2023.
- [155] A. M. Sirunyan et al. Identification of heavy-flavour jets with the CMS detector in pp collisions at 13 TeV. *JINST*, 13(05):P05011, 2018.
- [156] Armen Tumasyan et al. A new calibration method for charm jet identification validated with proton-proton collision events at $\sqrt{s} = 13$ TeV. *JINST*, 17(03):P03014, 2022.
- [157] A. M. Sirunyan et al. Performance of the CMS muon detector and muon reconstruction with proton-proton collisions at $\sqrt{s} = 13$ TeV. *JINST*, 13(06):P06015, 2018.
- [158] Vardan Khachatryan et al. Searches for electroweak production of charginos, neutralinos, and sleptons decaying to leptons and W, Z, and Higgs bosons in pp collisions at 8 TeV. *Eur. Phys. J. C*, 74:3036, 2014.
- [159] Armen Tumasyan et al. Search for electroweak production of charginos and neutralinos at $\sqrt{s} = 13$ TeV in final states containing hadronic decays of WW, WZ, or WH and missing transverse momentum. *Phys. Lett. B*, 842:137460, 2023.
- [160] Georges Aad et al. Search for direct production of charginos, neutralinos and sleptons in final states with two leptons and missing transverse momentum in pp collisions at $\sqrt{s} = 8$ TeV with the ATLAS detector. *JHEP*, 05:071, 2014.
- [161] Georges Aad et al. Search for the direct production of charginos, neutralinos and staus in final states with at least two hadronically decaying taus and missing transverse momentum in pp collisions at $\sqrt{s} = 8$ TeV with the ATLAS detector. *JHEP*, 10:096, 2014.
- [162] Georges Aad et al. Search for the electroweak production of supersymmetric particles in $\sqrt{s} = 8$ TeV pp collisions with the ATLAS detector. *Phys. Rev. D*, 93:052002, 2016.

-
- [163] M. Aaboud et al. Search for the direct production of charginos and neutralinos in final states with tau leptons in $\sqrt{s} = 13$ TeV pp collisions with the ATLAS detector. *Eur. Phys. J. C*, 78:154, 2018.
- [164] M. Aaboud et al. Search for electroweak production of supersymmetric states in scenarios with compressed mass spectra at $\sqrt{s} = 13$ TeV with the ATLAS detector. *Phys. Rev. D*, 97:052010, 2018.
- [165] M. Aaboud et al. Search for electroweak production of supersymmetric particles in final states with two or three leptons at $\sqrt{s} = 13$ TeV with the ATLAS detector. *Eur. Phys. J. C*, 78(12):995, 2018.
- [166] Georges Aad et al. Search for direct pair production of sleptons and charginos decaying to two leptons and neutralinos with mass splittings near the W-boson mass in $\sqrt{s} = 13$ TeV pp collisions with the ATLAS detector. *JHEP*, 06:031, 2023.
- [167] Georges Aad et al. Search for electroweak production of charginos and sleptons decaying into final states with two leptons and missing transverse momentum in $\sqrt{s} = 13$ TeV pp collisions using the ATLAS detector. *Eur. Phys. J. C*, 80(2):123, 2020.
- [168] Georges Aad et al. Search for direct production of electroweakinos in final states with one lepton, jets and missing transverse momentum and in pp collisions at $\sqrt{s} = 13$ TeV with the ATLAS detector. Technical report, CERN, Geneva, 2022. All figures including auxiliary figures are available at <https://atlas.web.cern.ch/Atlas/GROUPS/PHYSICS/CONFNOTES/ATLAS-CONF-2022-059>.
- [169] Georges Aad et al. Search for electroweak production of supersymmetric particles in final states with two τ -leptons in $\sqrt{s} = 13$ TeV pp collisions with the ATLAS detector. *JHEP*, 05:150, 2024.
- [170] Georges Aad et al. Search for direct production of electroweakinos in final states with one lepton, jets and missing transverse momentum in pp collisions at $\sqrt{s} = 13$ TeV with the ATLAS detector. *JHEP*, 12:167, 2023.
- [171] Georges Aad et al. A statistical combination of ATLAS Run 2 searches for charginos and neutralinos at the LHC. *Submitted to Physics Reports*, 2 2024.
- [172] Georges Aad et al. The quest to discover supersymmetry at the ATLAS experiment. Technical report, CERN, 3 2024.
- [173] Albert M Sirunyan et al. Search for top squark pair production using dilepton final states in pp collision data collected at $\sqrt{s} = 13$ TeV. *Eur. Phys. J. C*, 81(1):3, 2021.
- [174] Albert M Sirunyan et al. Search for direct top squark pair production in events with one lepton, jets, and missing transverse momentum at 13 TeV with the CMS experiment. *JHEP*, 05:032, 2020.
- [175] A. M. Sirunyan et al. Search for direct production of supersymmetric partners of the top quark in the all-jets final state in proton-proton collisions at $\sqrt{s} = 13$ TeV. *JHEP*, 10:005,

- 2017.
- [176] Albert M Sirunyan et al. Search for top squark production in fully-hadronic final states in proton-proton collisions at $\sqrt{s} = 13$ TeV. *Phys. Rev. D*, 104(5):052001, 2021.
- [177] Armen Tumasyan et al. Search for top squarks decaying via the four-body mode in single-lepton final states from Run 2 of the LHC. Technical report, CERN, Geneva, 2022.
- [178] A. M. Sirunyan et al. General search for supersymmetric particles in scenarios with compressed mass spectra using proton-proton collisions at $\sqrt{s} = 13$ TeV, 2024.
- [179] Armen Tumasyan et al. Search for top squark pair production in a final state with at least one hadronically decaying tau lepton in proton-proton collisions at $\sqrt{s} = 13$ TeV. *JHEP*, 07:110, 2023.
- [180] M. Aaboud et al. Search for a scalar partner of the top quark in the jets plus missing transverse momentum final state at $\sqrt{s} = 13$ TeV with the ATLAS detector. *JHEP*, 12:085, 2017.
- [181] Morad Aaboud et al. Search for top-squark pair production in final states with one lepton, jets, and missing transverse momentum using 36fb-1 of $\sqrt{s} = 13$ TeV pp collision data with the ATLAS detector. *JHEP*, 06:108, 2018.
- [182] M. Aaboud et al. Search for direct top squark pair production in final states with two leptons in $\sqrt{s} = 13$ TeV pp collisions with the ATLAS detector. *Eur. Phys. J. C*, 77:898, 2017.
- [183] Georges Aad et al. Search for a scalar partner of the top quark in the all-hadronic $t\bar{t}$ plus missing transverse momentum final state at $\sqrt{s} = 13$ TeV with the ATLAS detector. *Eur. Phys. J. C*, 80(8):737, 2020.
- [184] Georges Aad et al. Search for new phenomena with top quark pairs in final states with one lepton, jets, and missing transverse momentum in pp collisions at $\sqrt{s} = 13$ TeV with the ATLAS detector. *JHEP*, 04:174, 2021.
- [185] Georges Aad et al. Search for new phenomena in events with two opposite-charge leptons, jets and missing transverse momentum in pp collisions at $\sqrt{s} = 13$ TeV with the ATLAS detector. *JHEP*, 04:165, 2021.
- [186] Georges Aad et al. Search for new phenomena with top-quark pairs and large missing transverse momentum using 140 fb $^{-1}$ of pp collision data at $\sqrt{s} = 13$ TeV with the ATLAS detector. *JHEP*, 2403:139, 2024. All figures including auxiliary figures are available at <https://atlas.web.cern.ch/Atlas/GROUPS/PHYSICS/PAPERS/SUSY-2023-22/>.
- [187] A.M. Sirunyan et al. Search for top squarks in final states with many light flavor jets and 0, 1, or 2 leptons in proton-proton collisions at $\sqrt{s} = 13$ TeV. Technical report, CERN, Geneva, 2024.
- [188] Georges Aad et al. A search for top-squark pair production, in final states containing a

- top quark, a charm quark and missing transverse momentum, using the 139 fb^{-1} of pp collision data collected by the ATLAS detector. Technical report, CERN, 2 2024.
- [189] A. M. Sirunyan et al. Search for supersymmetric partners of electrons and muons in proton-proton collisions at $\sqrt{s} = 13 \text{ TeV}$. *Phys. Lett. B*, 790:005, 2019.
- [190] Armen Tumasyan et al. Search for supersymmetry in final states with two or three soft leptons and missing transverse momentum in proton-proton collisions at $\sqrt{s} = 13 \text{ TeV}$. *JHEP*, 04:091, 2022.
- [191] Albert M Sirunyan et al. Search for supersymmetry in final states with two oppositely charged same-flavor leptons and missing transverse momentum in proton-proton collisions at $\sqrt{s} = 13 \text{ TeV}$. *JHEP*, 04:123, 2021.
- [192] Aram Hayrapetyan et al. Combined search for electroweak production of winos, binos, higgsinos, and sleptons in proton-proton collisions at $\sqrt{s}=13 \text{ TeV}$. *Phys. Rev. D*, 109(11):112001, 2024.
- [193] G. Aad et al. Search for electroweak production of charginos and sleptons decaying into final states with two leptons and missing transverse momentum in $\sqrt{s} = 13 \text{ TeV}$ pp collisions using the ATLAS detector. *Eur. Phys. J. C*, 80:123, 2020.
- [194] Paolo Nason. A New method for combining NLO QCD with shower Monte Carlo algorithms. *JHEP*, 11:040, 2004.
- [195] Stefano Frixione, Paolo Nason, and Carlo Oleari. Matching NLO QCD computations with Parton Shower simulations: the POWHEG method. *JHEP*, 11:070, 2007.
- [196] Simone Alioli, Paolo Nason, Carlo Oleari, and Emanuele Re. A general framework for implementing NLO calculations in shower Monte Carlo programs: the POWHEG BOX. *JHEP*, 06:043, 2010.
- [197] Michal Czakon and Alexander Mitov. Top++: A program for the calculation of the top-pair cross-section at hadron colliders. *Comput. Phys. Commun.*, 185:2930, 2014.
- [198] E. Re. Single-top Wt-channel production matched with parton showers using the POWHEG method. *Eur. Phys. J. C*, 71:1547, 2011.
- [199] Kidonakis, N. NNLL threshold resummation for top-pair and single-top production. *Phys. Part. Nucl.*, 45:714, 2014.
- [200] Melia, T. and Nason, P. and Rontsch, R. and Zanderighi, G. W^+W^- , WZ and ZZ production in the POWHEG BOX. *JHEP*, 11:078, 2011.
- [201] P. Nason and G. Zanderighi. W^+W^- , WZ and ZZ production in the POWHEG-BOX-V2. *Eur. Phys. J. C*, 74:2702, 2014.
- [202] T. Gehrmann, M. Grazzini, S. Kallweit, P. Maierhöfer, A. von Manteuffel, S. Pozzorini, D. Rathlev, and L. Tancredi. W^+W^- production at hadron colliders in NNLO QCD. *Phys.*

- Rev. Lett.*, 113:212001, 2014.
- [203] A. M. Sirunyan et al. Measurements of properties of the Higgs boson decaying into the four-lepton final state in pp collisions at $\sqrt{s} = 13$ TeV. *JHEP*, 11:047, 2017.
- [204] J. M. Campbell and R. K. Ellis. MCFM for the Tevatron and the LHC. *Nucl. Phys. Proc. Suppl.*, 205:10, 2010.
- [205] F. Caola, K. Melnikov, R. Rtsch, and L. Tancredi. QCD corrections to W^+W^- production through gluon fusion. *Phys. Lett. B*, 754:275, 2016.
- [206] R. Gavin, Y. Li, F. Petriello, and S. Quackenbush. FEWZ 2.0: A code for hadronic Z production at next-to-next-to-leading order. *Comput. Phys. Commun.*, 182:2388, 2011.
- [207] M. V. Garzelli, A. Kardos, C. G. Papadopoulos, and Z. Trocsanyi. $t\bar{t}W^\pm$ and $t\bar{t}Z$ hadroproduction at NLO accuracy in QCD with parton shower and hadronization effects. *JHEP*, 11:056, 2012.
- [208] LHC Higgs Cross Section Working Group. Handbook of LHC Higgs cross sections: 3. Higgs Properties. *CERN*, 2013.
- [209] Simone Alioli, Paolo Nason, Carlo Oleari, and Emanuele Re. NLO higgs boson production via gluon fusion matched with shower in POWHEG. *JHEP*, 04:002, 2009.
- [210] Paolo Nason and Carlo Oleari. NLO higgs boson production via vector-boson fusion matched with shower in POWHEG. *JHEP*, 02:037, 2010.
- [211] Richard D. Ball et al. Parton distributions from high-precision collider data. *Eur. Phys. J. C*, 77:663, 2017.
- [212] Torbjörn Sjöstrand, Stefan Ask, Jesper R. Christiansen, Richard Corke, Nishita Desai, Philip Ilten, Stephen Mrenna, Stefan Prestel, Christine O. Rasmussen, and Peter Z. Skands. An Introduction to PYTHIA 8.2. *Comput. Phys. Commun.*, 191:159, 2015.
- [213] A. M. Sirunyan et al. Extraction and validation of a new set of cms pythia8 tunes from underlying-event measurements. *Eur. Phys. J. C*, 80:4, 2020.
- [214] W. Beenakker, M. Klasen, M. Kramer, T. Plehn, M. Spira, and P. M. Zerwas. Production of charginos, neutralinos, and sleptons at hadron colliders. *Phys. Rev. Lett.*, 83:3780, 1999.
- [215] Benjamin Fuks, Michael Klasen, David R. Lamprea, and Marcel Rothering. Gaugino production in proton-proton collisions at a center-of-mass energy of 8 TeV. *JHEP*, 10:081, 2012.
- [216] Benjamin Fuks, Michael Klasen, David R. Lamprea, and Marcel Rothering. Precision predictions for electroweak superpartner production at hadron colliders with RESUMMINO. *Eur. Phys. J. C*, 73:2480, 2013.

-
- [217] Benjamin Fuks, Michael Klasen, David R. Lamprea, and Marcel Rothering. Revisiting slepton pair production at the Large Hadron Collider. *JHEP*, 01:168, 2014.
- [218] W. Beenakker, R. Hopker, M. Spira, and P. M. Zerwas. Squark and gluino production at hadron colliders. *Nucl. Phys. B*, 492:51, 1997.
- [219] A. Kulesza and L. Motyka. Threshold resummation for squark-antisquark and gluino-pair production at the LHC. *Phys. Rev. Lett.*, 102:111802, 2009.
- [220] A. Kulesza and L. Motyka. Soft gluon resummation for the production of gluino-gluino and squark-antisquark pairs at the LHC. *Phys. Rev. D*, 80:095004, 2009.
- [221] Wim Beenakker, Silja Brensing, Michael Kramer, Anna Kulesza, Eric Laenen, and Irene Niessen. Soft-gluon resummation for squark and gluino hadroproduction. *JHEP*, 12:041, 2009.
- [222] W. Beenakker, S. Brensing, M. n Kramer, A. Kulesza, E. Laenen, L. Motyka, and I. Niessen. Squark and gluino hadroproduction. *Int. J. Mod. Phys. A*, 26:2637, 2011.
- [223] Christoph Borschensky, Michael Krämer, Anna Kulesza, Michelangelo Mangano, Sanjay Padhi, Tilman Plehn, and Xavier Portell. Squark and gluino production cross sections in pp collisions at $\sqrt{s} = 13, 14, 33$ and 100 TeV. *Eur. Phys. J. C*, 74:3174, 2014.
- [224] Wim Beenakker, Silja Brensing, Michael Kramer, Anna Kulesza, Eric Laenen, and Irene Niessen. NNLL resummation for squark-antisquark pair production at the LHC. *JHEP*, 01:076, 2012.
- [225] Wim Beenakker, Tim Janssen, Susanne Lepoeter, Michael Krämer, Anna Kulesza, Eric Laenen, Irene Niessen, Silja Thewes, and Tom Van Daal. Towards NNLL resummation: hard matching coefficients for squark and gluino hadroproduction. *JHEP*, 10:120, 2013.
- [226] Wim Beenakker, Christoph Borschensky, Michael Krämer, Anna Kulesza, Eric Laenen, Vincent Theeuwes, and Silja Thewes. NNLL resummation for squark and gluino production at the LHC. *JHEP*, 12:023, 2014.
- [227] Wim Beenakker, Christoph Borschensky, Michael Krämer, Anna Kulesza, and Eric Laenen. NNLL-fast: predictions for coloured supersymmetric particle production at the LHC with threshold and Coulomb resummation. *JHEP*, 12:133, 2016.
- [228] W. Beenakker, M. Kramer, T. Plehn, M. Spira, and P. M. Zerwas. Stop production at hadron colliders. *Nucl. Phys.*, B515:3, 1998.
- [229] Wim Beenakker, Silja Brensing, Michael Kramer, Anna Kulesza, Eric Laenen, and Irene Niessen. Supersymmetric top and bottom squark production at hadron colliders. *JHEP*, 08:098, 2010.
- [230] Wim Beenakker, Christoph Borschensky, Raphael Heger, Michael Krämer, Anna Kulesza, and Eric Laenen. NNLL resummation for stop pair-production at the LHC. *JHEP*, 05:153, 2016.

- [231] S. Agostinelli et al. GEANT4—a simulation toolkit. *Nucl. Instrum. Meth. A*, 506:250, 2003.
- [232] S. Abdullin, P. Azzi, F. Beaudette, P. Janot, and A. Perrotta. The Fast Simulation of the CMS detector at LHC. In *J. Phys. Conf. Ser.*, volume 331, page 032049, 2011.
- [233] CMS Collaboration. Cut-Based Electron Identification in Run 2. <https://twiki.cern.ch/twiki/bin/view/CMS/CutBasedElectronIdentificationRun2>, 2023. Accessed: July 8, 2023.
- [234] CMS Collaboration. Missing et uncertainty prescription for 2017 data. https://twiki.cern.ch/twiki/bin/viewauth/CMS/MissingETUncertaintyPrescription#Instructions_for_2017_data_with, 2024. Accessed: 2024-10-18.
- [235] C. G. Lester and D. J. Summers. Measuring masses of semiinvisibly decaying particles pair produced at hadron colliders. *Phys. Lett. B*, 463:99, 1999.
- [236] A.M. Sirunyan et al. WW boson pair production in proton-proton collisions at $\sqrt{s} = 13$ TeV. *Phys. Rev. D*, 102:092001, 2020.
- [237] Prerit Jaiswal and Takemichi Okui. An explanation of the WW excess at the LHC by jet-veto resummation. *Phys. Rev. D*, 90:073009, 2014.
- [238] Pier Francesco Monni and Giulia Zanderighi. On the excess in the inclusive $W^+W^- \rightarrow l^+l^- \nu\bar{\nu}$ cross section. *JHEP*, 05:013, 2015.
- [239] A. M. Sirunyan et al. Precision luminosity measurement in proton-proton collisions at $\sqrt{s} = 13$ TeV in 2015 and 2016 at CMS. *Eur. Phys. J. C*, 81:800, 2021.
- [240] CMS Collaboration. CMS luminosity measurements for the 2017 data-taking period at $\sqrt{s} = 13$ TeV. CMS Physics Analysis Summary CMS-PAS-LUM-17-004, CERN, 2018.
- [241] CMS Collaboration. CMS luminosity measurement for the 2018 data-taking period at $\sqrt{s} = 13$ TeV. CMS Physics Analysis Summary CMS-PAS-LUM-18-002, CERN, 2019.
- [242] CMS Collaboration. Pileup json file for data: Recommended cross section. https://twiki.cern.ch/twiki/bin/viewauth/CMS/PileupJSONFileforData#Recommended_cross_section, 2024. Accessed: 2024-10-18.
- [243] Vardan Khachatryan et al. Jet energy scale and resolution in the CMS experiment in pp collisions at 8 TeV. *JINST*, 12(02):P02014, 2017.
- [244] A. M. Sirunyan et al. Identification of heavy-flavour jets with the CMS detector in pp collisions at 13 TeV. *JINST*, 13(05):P05011, 2018.
- [245] Jon Butterworth et al. PDF4LHC recommendations for LHC Run II. *J. Phys. G*, 43:023001, 2016.

-
- [246] Vardan Khachatryan et al. Measurement of differential cross sections for top quark pair production using the lepton+jets final state in proton-proton collisions at 13 TeV. *Phys. Rev. D*, 95:092001, 2017.
- [247] Vardan Khachatryan et al. Measurement of the differential cross section for top quark pair production in pp collisions at $\sqrt{s} = 8$ TeV. *Eur. Phys. J. C*, 75:542, 2015.
- [248] Vardan Khachatryan et al. Measurement of the $t\bar{t}$ production cross section in the all-jets final state in pp collisions at $\sqrt{s} = 8$ TeV. *Eur. Phys. J. C*, 76:128, 2016.
- [249] J. S. Conway. Incorporating Nuisance Parameters in Likelihoods for Multisource Spectra. In *PHYSTAT 2011*, pages 115–120, 2011.
- [250] CMS Collaboration. Higgs analysis combined limit tool. <http://cms-analysis.github.io/HiggsAnalysis-CombinedLimit/>, 2024. Accessed: 2024-10-18.
- [251] Thomas Junk. Confidence level computation for combining searches with small statistics. *Nucl. Instrum. Meth. A*, 434:435, 1999.
- [252] Alexander L. Read. Presentation of search results: The CL_s technique. *J. Phys. G*, 28:2693, 2002.
- [253] Glen Cowan, Kyle Cranmer, Eilam Gross, and Ofer Vitells. Asymptotic formulae for likelihood-based tests of new physics. *Eur. Phys. J. C*, 71:1554, 2011. [Erratum: *Eur.Phys.J.C* 73, 2501 (2013)].

Appendix A

Resumen en español

En este documento se ha presentado una búsqueda de varios modelos de nueva física, examinando eventos con dos leptones de cargas opuestas y alto momento transversal perdido. Los resultados obtenidos se basan en datos recogidos por el experimento CMS durante los años de toma de datos 2016, 2017 y 2018, con una energía en el centro de masa de 13 TeV, lo que representa una luminosidad integrada total de 138 fb^{-1} . Se han considerado cinco modelos simplificados diferentes, todos ellos en busca de compañeros Supersimétricos de las partículas del Modelo Estándar. Se han estudiado dos modelos de desintegración para la producción de pares de charginos, incluyendo su desintegración en cascada a través de sleptones, y un modelo alternativo donde el chargino se desintegra a través de bosones W. Asimismo, se han explorado dos modelos más que sondan la producción de squarks de top, los principales objetivos son un modelo de señal donde el squark de top se desintegra en un quark top y un neutralino, optimizado para desintegraciones comprimidas, mientras que el modelo alternativo busca el squark de top desintegrándose en un chargino y un quark bottom, donde cada chargino se desintegra posteriormente en un bosón W y un neutralino. Por último, se ha estudiado un modelo donde se investiga la producción de un par de sleptones, donde cada slepton se desintegra en un leptón y un neutralino.

El documento comienza con una revisión del Modelo Estándar, explicando tanto las partículas fundamentales que lo forman como las interacciones que describe. Se enfatizan sus logros, como la predicción y descubrimiento del bosón de Higgs, así como sus limitaciones, como la incapacidad de explicar la materia oscura, la energía oscura y las masas de los neutrinos. Posteriormente, se introduce la supersimetría como una extensión teórica que intenta resolver estas limitaciones. El documento entonces se centra en explicar el fundamento teórico Modelo Estándar Supersimétrico Mínimo (MSSM), describiendo las nuevas partículas y conceptos que propone, como el rompimiento suave de supersimetría y los candidatos a materia oscura.

En la sección experimental, se describe en detalle la infraestructura utilizada para la investigación. Esto incluye el gran colisionador de hadrones (LHC, por sus siglas en inglés), un acelerador de partículas que colisiona protones a energías extremadamente altas; y el detector CMS, diseñado para observar las partículas resultantes de estas colisiones. Se describen en detalle cada uno de los componentes principales del detector, como el detector de trazas, los calorímetros electromagnético y hadrónico, el sistema de detección de muones o el mismo electroimán. Seguidamente, se presentan los métodos que se utilizaron para la reconstrucción e identificación de los objetos físicos utilizados en este análisis, como muones, electrones, o jets, así como el tratamiento seguido para aquellas partículas que solamente interactúan débilmente y, por tanto, no son detectadas directamente por CMS, como los neutrinos. Asimismo, se presentan las simulaciones de eventos Monte Carlo, fundamentales para modelar tanto procesos estándar como supersimétricos y para validar los resultados experimentales.

Posteriormente, el documento aborda en detalle el fundamento teórico de los principales fondos que contribuyen a las señales analizadas en la búsqueda de partículas supersimétricas. Estos fondos, generados por procesos estándar del Modelo Estándar, incluyen la producción de quarks top ($t\bar{t}$), los bosones Z y W , combinaciones de múltiples bosones (dibosones y tribosones), así como el bosón de Higgs.

Una vez todos los objetos e instrumentos han sido definidos, esta memoria se centra en explicar las estrategias de búsqueda y análisis de datos. Aquí, se define el diseño de regiones de señal y fondo, así como la optimización de dichas regiones de señal, con el fin de maximizar el número de posibles eventos de producción de partículas supersimétricas, manteniendo los eventos de fondo al mínimo posible. Se detalla la selección de eventos, así como el tratamiento de problemas técnicos que afectaron la toma de datos durante diferentes periodos de funcionamiento del LHC. Además, se discute el enfoque para estimar y modelar los procesos de fondo previamente presentados, mostrando las distribuciones utilizadas para tal fin.

Finalmente, después de haber descrito las principales fuentes de incertidumbres que contribuyen en el análisis, se presenta un capítulo de resultados, donde se explica en detalle las características del ajuste de máxima verosimilitud utilizado, y se presentan las distribuciones obtenidas para las regiones de señal tanto antes como después de haber realizado dicho ajuste. El análisis incluye la interpretación de resultados tanto observados como esperados, destacando las implicaciones para la física más allá del Modelo Estándar.

Los resultados obtenidos no encuentran ninguna evidencia significativa de una desviación con respecto a la predicción del modelo estándar en los datos. Por lo tanto, los resultados se interpretan en términos de límites superiores en la sección eficaz de cada uno de los espectros del modelo simplificado supersimétrico mencionado. Si se asume que el chargino sufre una desintegración en cascada a través de sleptones, se ha derivado una región de exclusión en el plano $(m_{\tilde{\chi}_1^\pm}, m_{\tilde{\chi}_1^0})$, extendiéndose a masas de charginos de 1120 GeV y masas de neutralinos de 490 GeV. Estos resultados representan una mejora significativa en la región de exclusión de la masa del chargino con respecto al análisis de 2016 [44], y extienden la exclusión de la masa del chargino en 300 GeV para masas del neutralino bajas; y la exclusión de la masa del neutralino en 150 GeV en la región donde $\Delta(m_{\tilde{\chi}_1^\pm}, m_{\tilde{\chi}_1^0})$ es pequeña. Estos son los mayores límites superiores hasta la fecha para esta hipótesis de señal.

También se ha sondeado la producción de un par de squarks de top, con un enfoque en modos de desintegración comprimidos. Se ha considerado un modelo con el squark de top desintegrándose en un quark top y un neutralino. En la región donde $m_W < m_{\tilde{t}_1} - m_{\tilde{\chi}_1^0} \lesssim m_t$, los límites se extienden hasta 500 GeV para la masa del squark de top. Se ha considerado también un modelo alternativo, donde el squark de top se desintegra en un chargino y un quark bottom, con el chargino desintegrándose posteriormente en un bosón W y el neutralino más ligero. De manera similar, se han excluido masas de squark de top hasta 560 GeV para $\Delta m \approx 2m_W$. Estos resultados presentan una mejora en las regiones de exclusión para la masa del squark top de 100 GeV respecto a los resultados de 2016 [44], y complementan otros análisis en busca del squark top realizados por la Colaboración CMS [174, 173, 176, 177, 187].

Por último, se ha considerado la producción de pares de sleptones, excluyendo masas de sleptones hasta 700 GeV y masas de neutralinos hasta 360 GeV. Los resultados obtenidos para esta hipótesis de señal son competitivos con respecto a otros análisis realizados utilizando datos de Run II, proporcionando una sensibilidad adicional en la región de pequeña $\Delta(m_{\tilde{\tau}}, m_{\tilde{\chi}_1^0})$ [192, 193].

Appendix B

Triggers

B.1 Trigger paths

The trigger paths used in this analysis are listed in Tables B.1 to B.4.

Table B.1: Trigger paths used to select events for the 2016 pre-VFP data-taking period.

Data set	Run range	HLT path
MuonEG	[271036,278272]	HLT_Mu8_TrkIsoVVL_Ele23_CaloIdL_TrackIdL_IsoVL_v*
		HLT_Mu23_TrkIsoVVL_Ele12_CaloIdL_TrackIdL_IsoVL_v*
	[278273,278807]	HLT_Mu12_TrkIsoVVL_Ele23_CaloIdL_TrackIdL_IsoVL_DZ_v*
		HLT_Mu23_TrkIsoVVL_Ele12_CaloIdL_TrackIdL_IsoVL_DZ_v*
DoubleMuon	[271036,278807]	HLT_Mu17_TrkIsoVVL_Mu8_TrkIsoVVL_v*
		HLT_Mu17_TrkIsoVVL_TkMu8_TrkIsoVVL_v*
DoubleEG	[271036,278807]	HLT_Ele23_Ele12_CaloIdL_TrackIdL_IsoVL_DZ_v*
SingleMuon	[271036,278807]	HLT_IsoMu24_v*
		HLT_IsoTkMu24_v*
SingleElectron	[271036,278807]	HLT_Ele27_WPTight_Gsf_v*
		HLT_Ele25_eta2p1_WPTight_Gsf_v*

Table B.2: Trigger paths used to select events for the 2016 post-VFP data-taking period.

Data set	Run range	HLT path
MuonEG	[278769,284044]	HLT_Mu12_TrkIsoVVL_Ele23_CaloIdL_TrackIdL_IsoVL_DZ_v*
		HLT_Mu23_TrkIsoVVL_Ele12_CaloIdL_TrackIdL_IsoVL_DZ_v*
DoubleMuon	[278769,281612]	HLT_Mu17_TrkIsoVVL_Mu8_TrkIsoVVL_v*
		HLT_Mu17_TrkIsoVVL_TkMu8_TrkIsoVVL_v*
	[281613,284044]	HLT_Mu17_TrkIsoVVL_Mu8_TrkIsoVVL_DZ_v*
		HLT_Mu17_TrkIsoVVL_TkMu8_TrkIsoVVL_DZ_v*
DoubleEG	[278769,284044]	HLT_Ele23_Ele12_CaloIdL_TrackIdL_IsoVL_DZ_v*
SingleMuon	[278769,284044]	HLT_IsoMu24_v*
		HLT_IsoTkMu24_v*
SingleElectron	[278769,284044]	HLT_Ele27_WPTight_Gsf_v*
		HLT_Ele25_eta2p1_WPTight_Gsf_v*

Table B.3: Trigger paths used to select events for the 2017 data-taking period.

Data set	Run range	HLT path
MuonEG	[297046,299329]	HLT_Mu12_TrkIsoVVL_Ele23_CaloIdL_TrackIdL_IsoVL_DZ_v*
		HLT_Mu23_TrkIsoVVL_Ele12_CaloIdL_TrackIdL_IsoVL_DZ_v*
	[299368,306462]	HLT_Mu12_TrkIsoVVL_Ele23_CaloIdL_TrackIdL_IsoVL_DZ_v*
		HLT_Mu23_TrkIsoVVL_Ele12_CaloIdL_TrackIdL_IsoVL_v*
DoubleMuon	[297046,299329]	HLT_Mu17_TrkIsoVVL_Mu8_TrkIsoVVL_DZ_v*
	[299368,306462]	HLT_Mu17_TrkIsoVVL_Mu8_TrkIsoVVL_DZ_Mass8_v*
DoubleEG	[297046,306462]	HLT_Ele23_Ele12_CaloIdL_TrackIdL_IsoVL_v*
SingleMuon	[297046,306462]	HLT_IsoMu27_v*
SingleElectron	[297046,306462]	HLT_Ele35_WPTight_Gsf_v*

Table B.4: Trigger paths used to select events for the 2018 data-taking period.

Data set	Run range	HLT path
MuonEG	[315252,325175]	HLT_Mu12_TrkIsoVVL_Ele23_CaloIdL_TrackIdL_IsoVL_DZ_v*
		HLT_Mu23_TrkIsoVVL_Ele12_CaloIdL_TrackIdL_IsoVL_v*
DoubleMuon	[315252,325175]	HLT_Mu17_TrkIsoVVL_Mu8_TrkIsoVVL_DZ_Mass3p8_v*
EGamma	[315252,325175]	HLT_Ele23_Ele12_CaloIdL_TrackIdL_IsoVL_v*
		HLT_Ele32_WPTight_Gsf_v*
SingleMuon	[315252,325175]	HLT_IsoMu24_v*

B.2 Measurement of the trigger efficiencies

We measure the efficiencies of the triggers with respect to events passing our baseline selection by using events that fired a set of cross triggers from the p_T^{miss} primary dataset. The efficiencies are computed as the fraction of events firing the cross triggers and passing the baseline selection that also fire the triggers used in the analysis. The efficiencies are measured as a function of the p_T of the leading and trailing leptons, for the ee , $e\mu$, and $\mu\mu$ channels and for each data-taking years. Trigger efficiencies for the 2016 pre-VFP and post-VFP data-taking periods are presented in Fig. B.1, with the equivalent figures but for 2017 and 2018 data-taking years shown in Fig. B.2. The quoted uncertainties are statistical only. An additional 2% systematic uncertainty is set to cover possible correlations between the cross triggers and the analysis triggers.

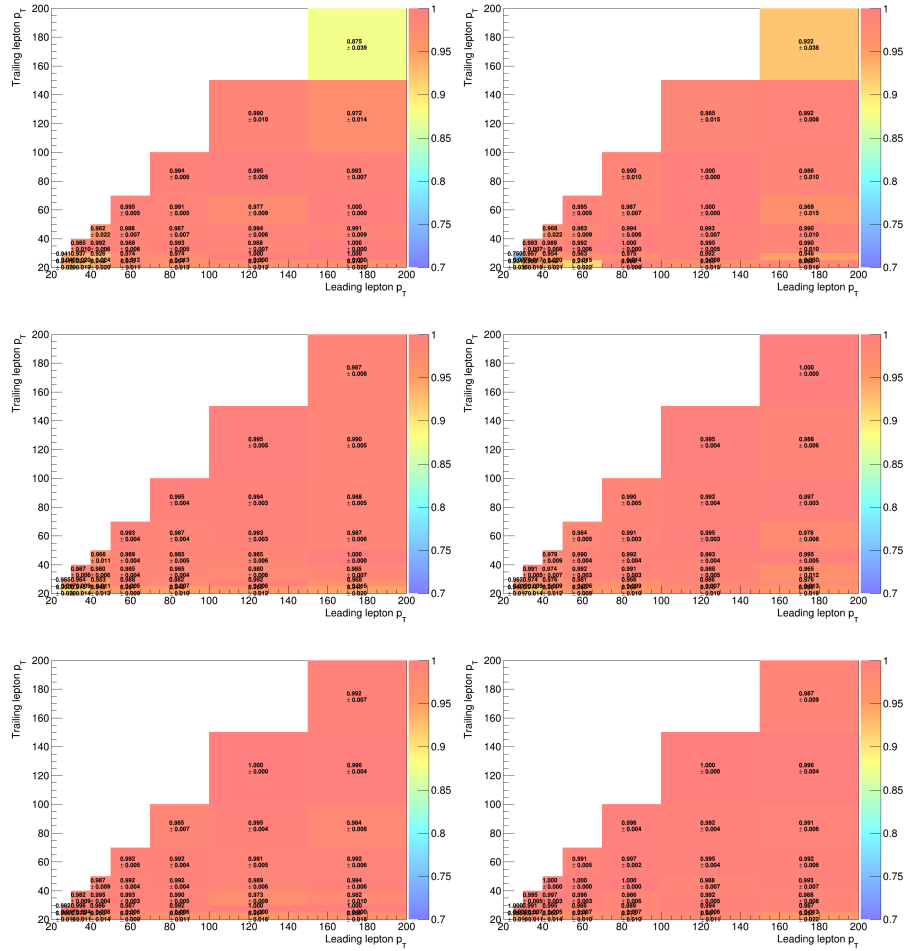


Figure B.1: Efficiencies for a selected event in the ee (top plots), $e\mu$ (middle) and $\mu\mu$ (bottom) channel to pass the trigger requirements in the data-taking year 2016 for the pre-VFP (left) and post-VFP (right) periods, as a function of the leading and trailing lepton's p_T . The quoted uncertainties are statistical only.

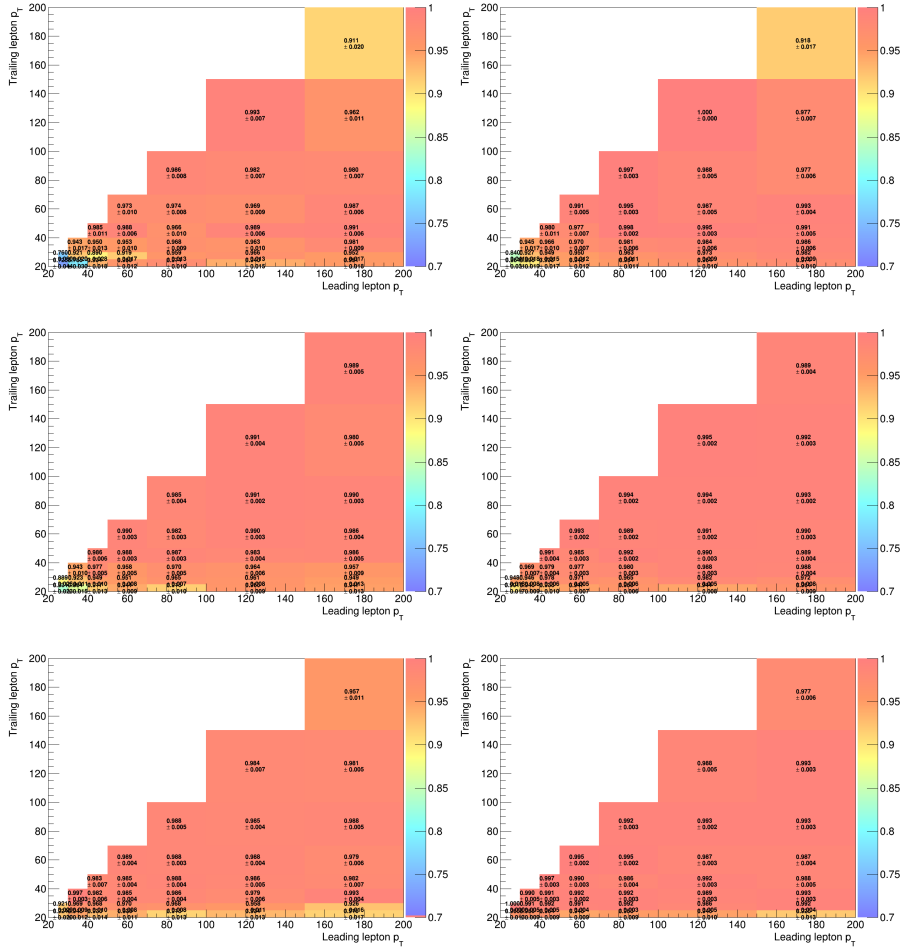


Figure B.2: Efficiencies for a selected event in the ee (top plots), $e\mu$ (middle) and $\mu\mu$ (bottom) channel to pass the trigger requirements in the data-taking years 2017 (left) and 2018 (right), as a function of the leading and trailing lepton p_T 's. The quoted uncertainties are statistical only.

Appendix C

Scale factors for additional requirements on lepton selection

The selection of the leptons used in the search described in this document is based on POG-recommended working points plus some additional quality requirements on the associated track impact parameters and number of missing hits, as detailed in Section 8.1. In this Appendix, measurements of dedicated scale factors for these additional requirements, computed with respect to leptons satisfying the POG-recommended working points are presented.

A tag&probe method is used, based on Drell–Yan events from data and MC simulations. Events collected from single lepton triggers are used. A pair of oppositely charged same-flavour leptons is required. One lepton (tag) is required to match the trigger primitive and to pass all the lepton requirements used for the analysis. Its presence in the event assures a high purity of the selected event sample in pairs of prompt leptons from Z boson decays. The other lepton (probe) is required to pass the corresponding POG working point requirements. The efficiencies are measured as the fraction of probe leptons passing the additional requirements.

The details of the event selection and of the requirements applied on the tag and probe leptons are summarised in Table C.1. The efficiencies measured in data and MC simulations are shown in terms of the lepton p_T and pseudorapidity η in Figs. C.1 and C.2 for electrons and muons, respectively, while the derived scale factors, defined as the ratio between the efficiencies measured in data and MC simulations, are shown in Fig. C.3. The systematic uncertainties on the scale factors are determined by the change in the scale factor values when varying alternately the event selection and tag lepton requirements, as presented in Table C.1. The measured scale factors are typically in the range $[0.9, 1.05]$. Some variations are observed, especially in the high- p_T high- η bins, which are nonetheless covered by the statistical uncertainties.

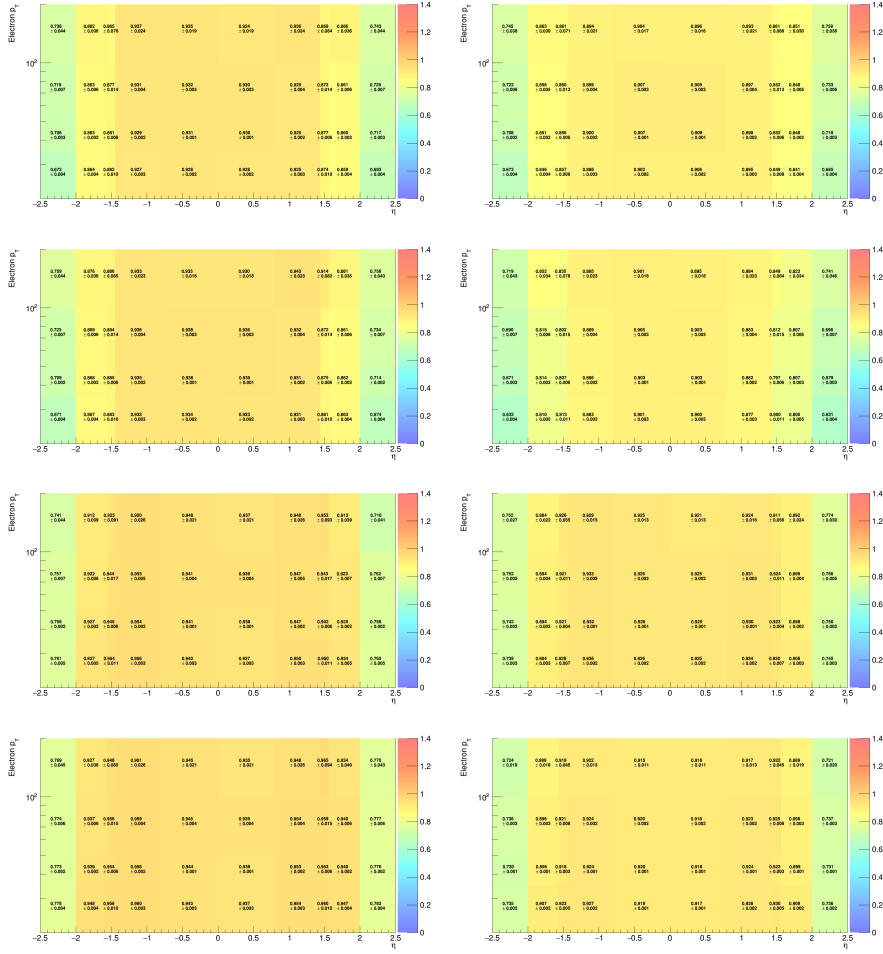


Figure C.1: Efficiencies for an electron satisfying the cut-based medium ID to pass the additional requirements on the track impact parameters and number of missing hits as a function of its p_T and super-cluster (SCs) η . From top to bottom, the plots correspond to the pre-VFP 2016, post-VFP 2016, 2017, and 2018 data-taking year, for Drell-Yan simulated events (left) and data from single electron triggers (right).

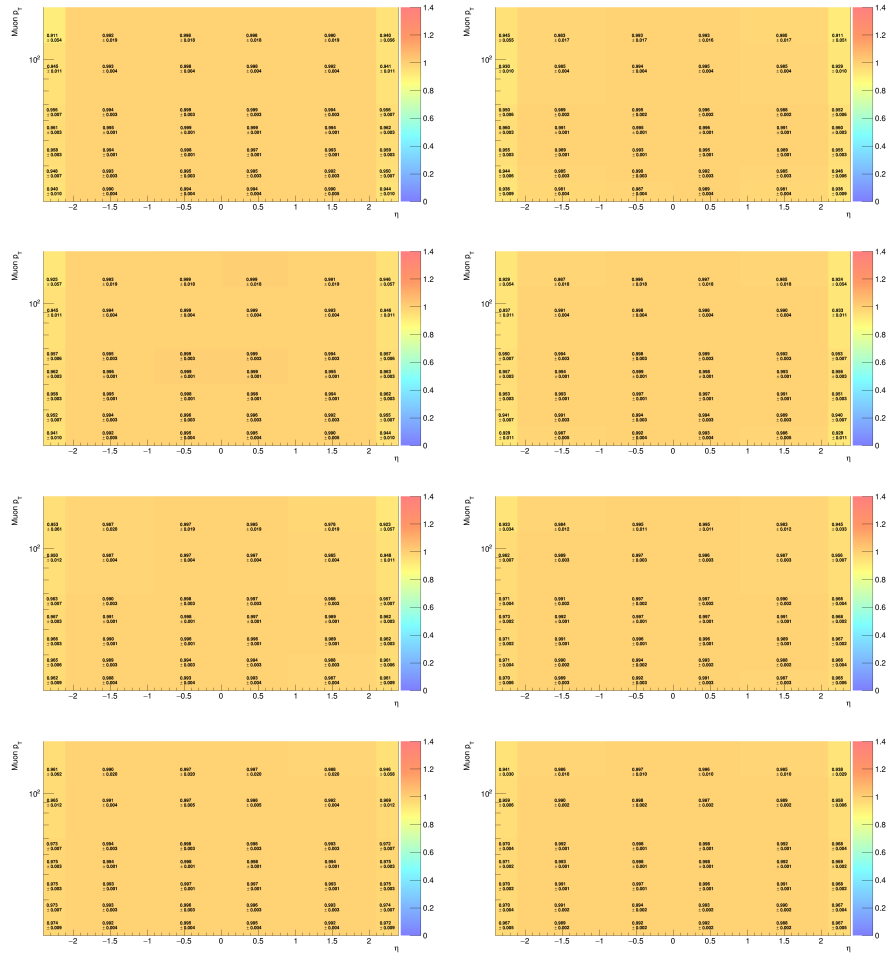


Figure C.2: Same as in Fig. C.1 for muons satisfying the medium ID and $I_{\text{rel}} < 0.15$ requirements.

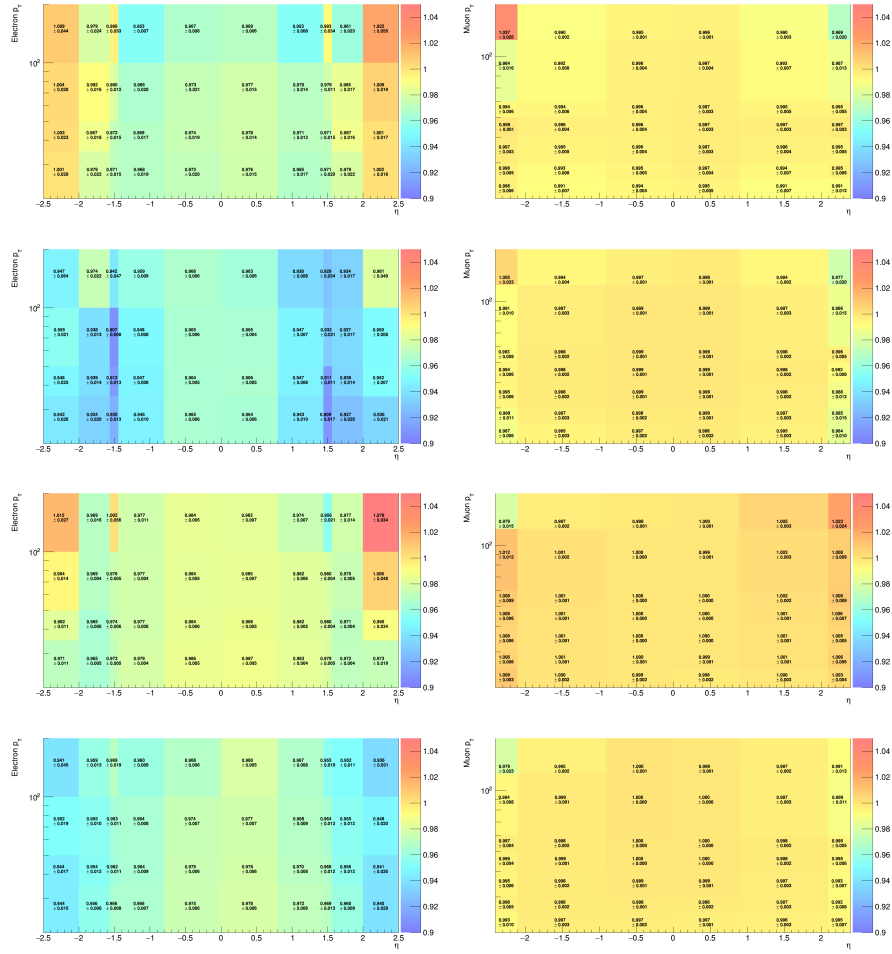


Figure C.3: Scale factors for the leptons, defined as the ratio between the efficiencies for data and simulations shown in Fig. C.1 and Fig. C.2, for electrons (left) and muons (right). From top to bottom, the plots correspond to pre-VFP 2016, post-VFP 2016, 2017, and 2018 data-taking year.

Table C.1: Summary of the event selection and of the requirements on the tag and probe leptons used in the measurements of the scale factors for the additional requirements on the leptons used in the analysis.

	Electrons	Muons
Event selection	$60 < m_{\ell\ell} < 120 \text{ GeV}$ $p_T^{e1} = 35 \text{ GeV}, p_T^{e2} = 27 \text{ GeV},$	$70 < m_{\ell\ell} < 130 \text{ GeV}$ $p_T^{\mu1} = 27 \text{ GeV}, p_T^{\mu2} = 24 \text{ GeV},$
Tag lepton	analysis electron match trigger primitive	analysis muon match trigger primitive
Probe lepton	cut based medium ID	medium ID and $I_{\text{rel}} < 0.15$
Cuts to probe	$ d_0 < 0.05\text{cm}, d_z < 0.10\text{cm},$ $S_{3D}^d < 4, N_{\text{miss. hits}}^{\text{inn.tracker}} = 0$	$ d_0 < 0.05\text{cm}, d_z < 0.10\text{cm},$ $S_{3D}^d < 4$
Varying cuts for systematics	tag MVA Iso wp90 ID $p_T^{\text{miss}} < 50 \text{ GeV}$ $N_{\text{jets}} = 0$	tag $I_{\text{rel}} < 0.1, I_{\text{rel}} < 0.3$ $p_T^{\text{miss}} < 50 \text{ GeV}$ $N_{\text{jets}} = 0$ $75 < m_{\ell\ell} < 140 \text{ GeV}, 65 < m_{\ell\ell} < 120 \text{ GeV}$

Appendix D

FULLSIM/FASTSIM correction factors for lepton selection efficiencies

We derive correction factors to match the lepton selection efficiencies found in signal samples simulated by FASTSIM to the ones expected in samples simulated with the full detector simulation (FULLSIM). We estimate the efficiencies in Drell–Yan simulated events, following the same tag&probe approach used to compute the efficiencies of the additional requirements on the lepton selection (C). The results are shown in Figs. D.1 and D.2 for electrons and muons, respectively. We study the dependence of the FULLSIM/FASTSIM correction factors on the event topology by repeating the procedure using $t\bar{t}$ simulated samples. The measured correction factors are shown in Fig. D.3. Based on the agreement between the results in Drell–Yan and $t\bar{t}$ events, a systematic uncertainty of 2% is set on the FULLSIM/FASTSIM correction factors.

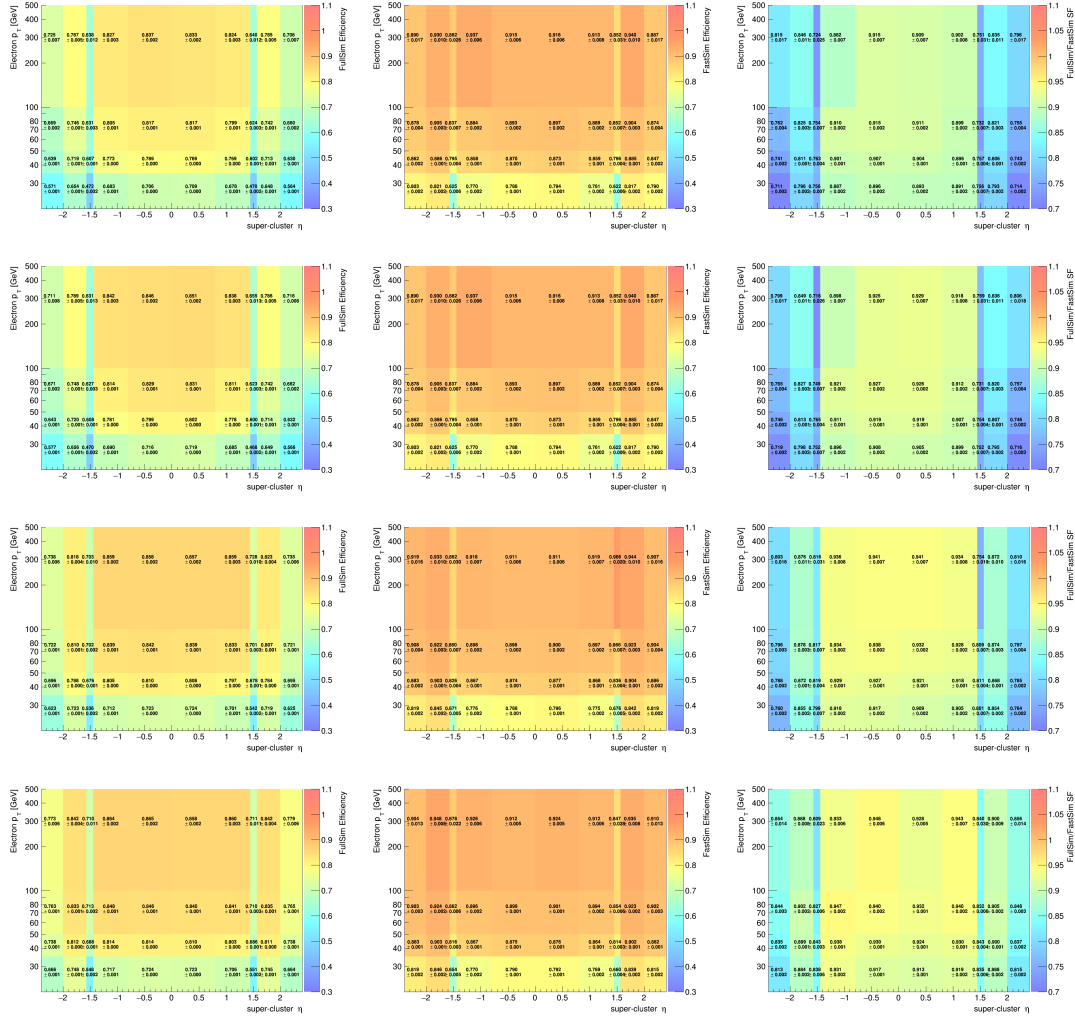


Figure D.1: Upper: the left and middle plots show the efficiencies for an electron to pass our selection requirements as a function of its p_T and supercluster η in 2016 pre-VFP FULLSIM and FASTSIM Drell–Yan events, respectively; the right plot shows the FULLSIM/FASTSIM correction factors, derived as the ratio of the two sets of efficiencies. Uncertainties are statistical only. Second row: same for 2016 post-VFP FULLSIM and FASTSIM Drell–Yan events. Third row: same for 2017 FULLSIM and FASTSIM Drell–Yan events. Lower: same for 2018 FULLSIM and FASTSIM Drell–Yan events.

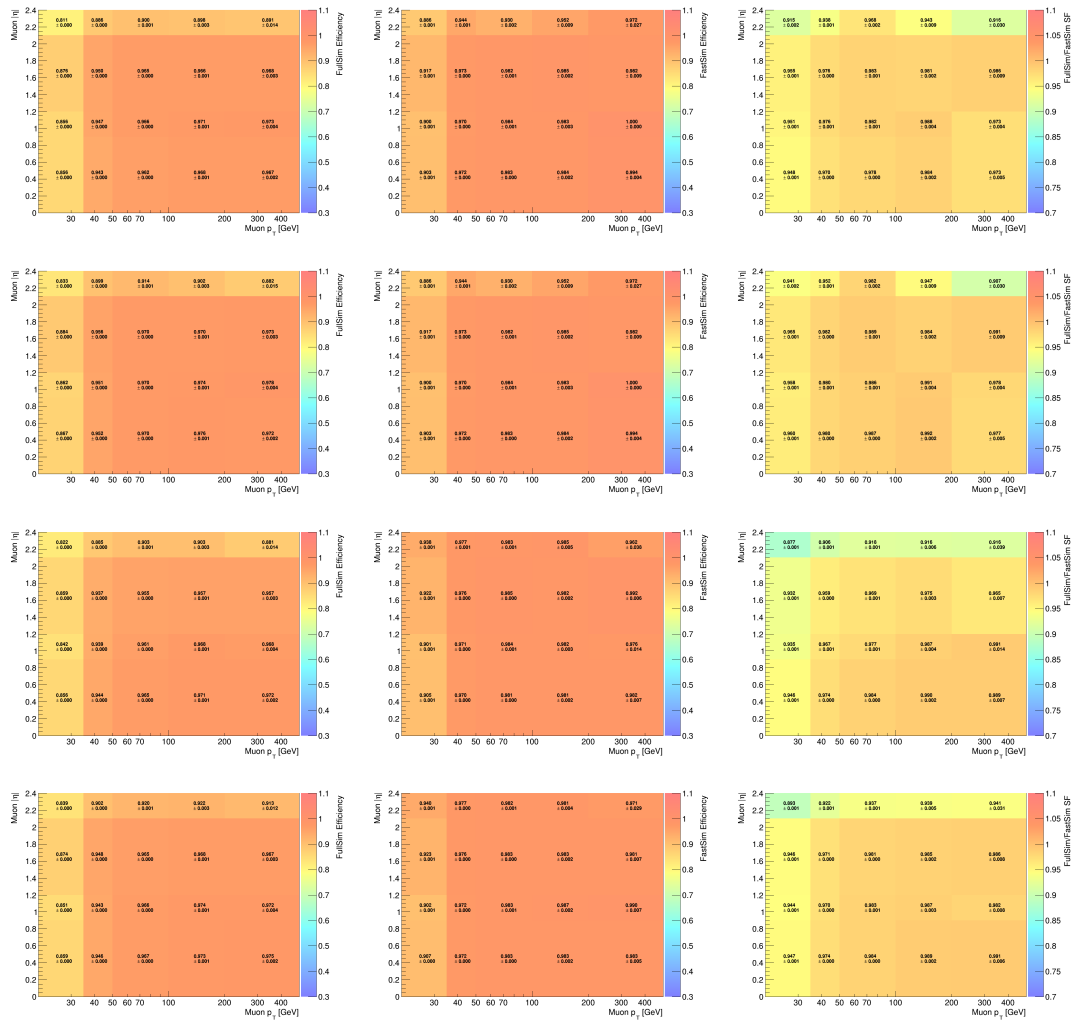


Figure D.2: Same as in Fig. D.1 for muons.

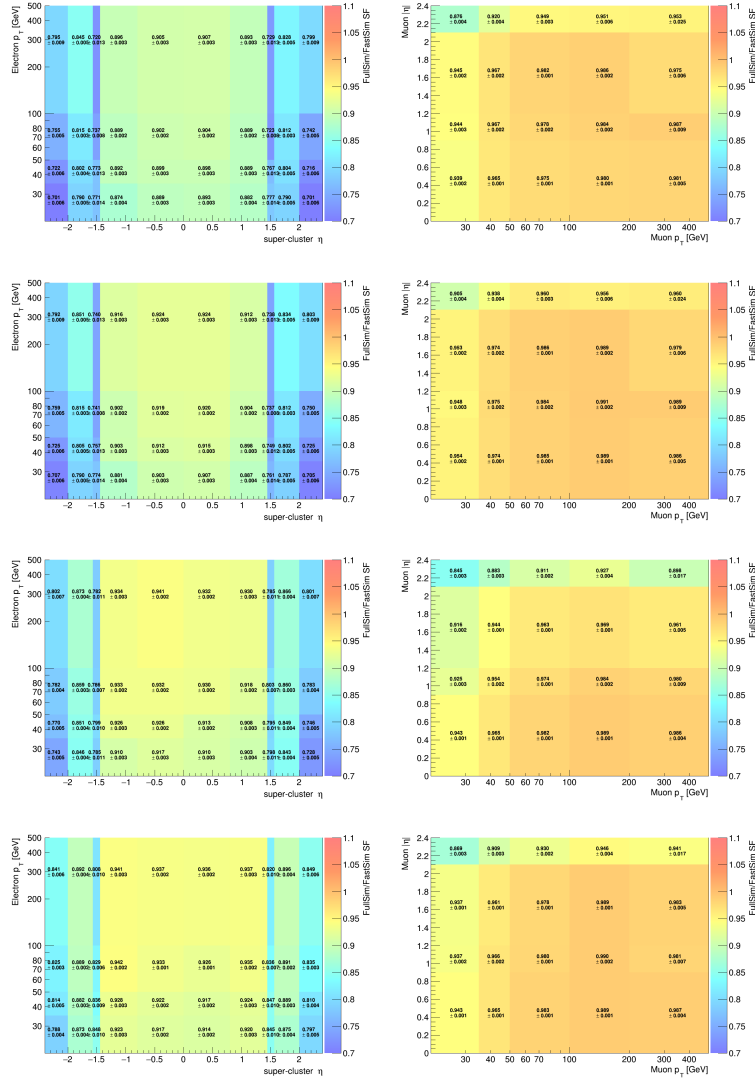


Figure D.3: FULLSIM/FASTSIM correction factors measured in $t\bar{t}$ events for electrons (left) and muons (right). Upper to lower plots show the results for 2016 pre-VFP to 2018 simulated samples.

D.1 Effect of the correction factors on top squark signal samples

In order to ensure the effect of the aforementioned correction factors, we compare the kinematic distributions for the leptons in events of top squark pair production simulated with FULLSIM and in FASTSIM, both before and after applying the FULLSIM/FASTSIM corrections. Comparisons are shown for the leading and trailing leptons' p_T and η in Fig. D.4 for 2016 samples, Fig. D.5 for 2017 samples, and Fig. D.6 for 2018 samples. The corrections are found to greatly improve the agreement between the distributions in FULLSIM and FASTSIM simulated events.

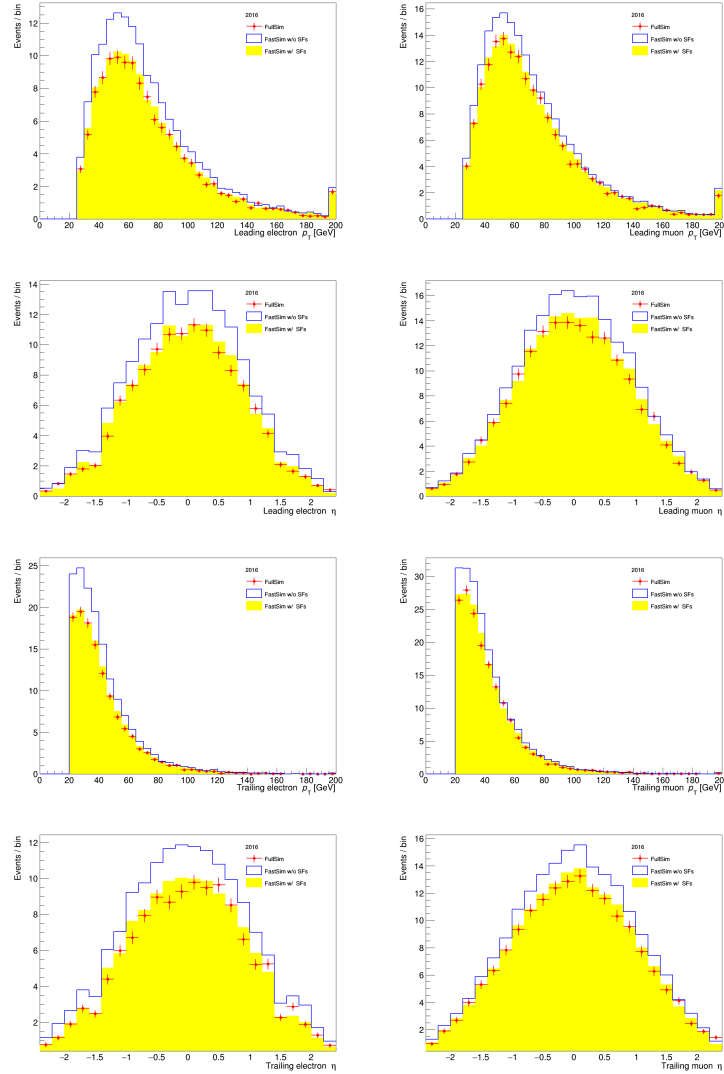


Figure D.4: Comparison of the kinematic distributions for the leptons in top squark pair production events simulated with the 2016 setting of FULLSIM (red solid points) and FASTSIM before (blue lines) and after (yellow solid histogram) applying the FULLSIM/FASTSIM correction factors. Left (right) plots are for electron (muon) distributions. Upper to lower, the panels show the leading lepton p_T , leading lepton η , trailing lepton p_T , and trailing lepton η .

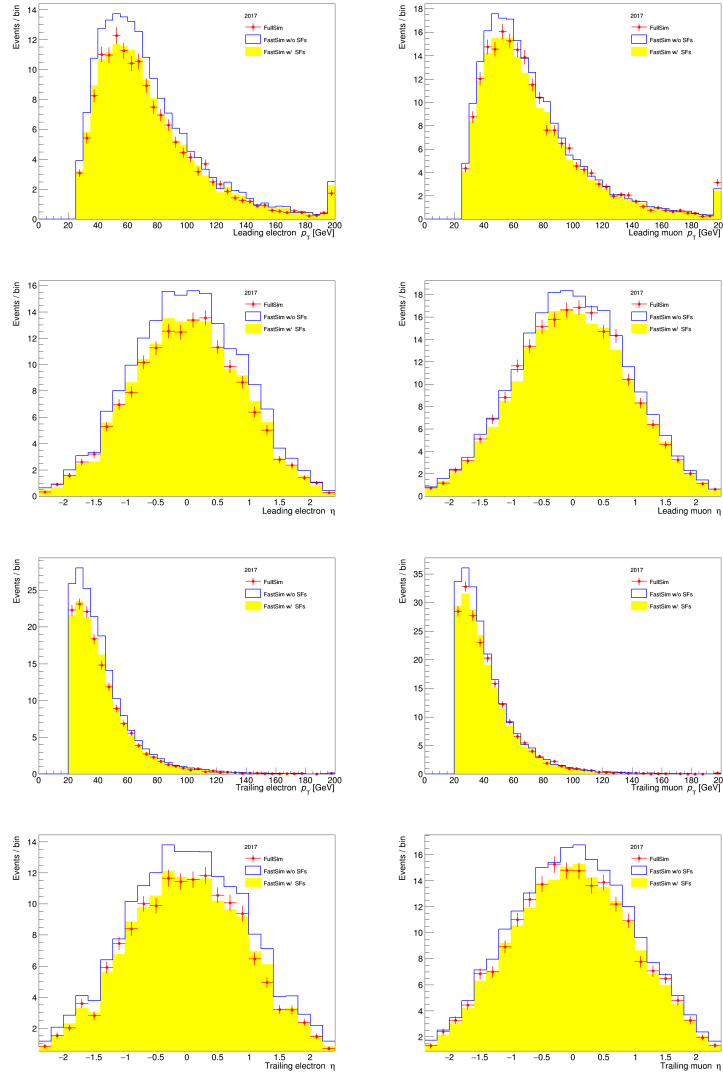


Figure D.5: Same as in Fig. D.4 for 2017 samples.

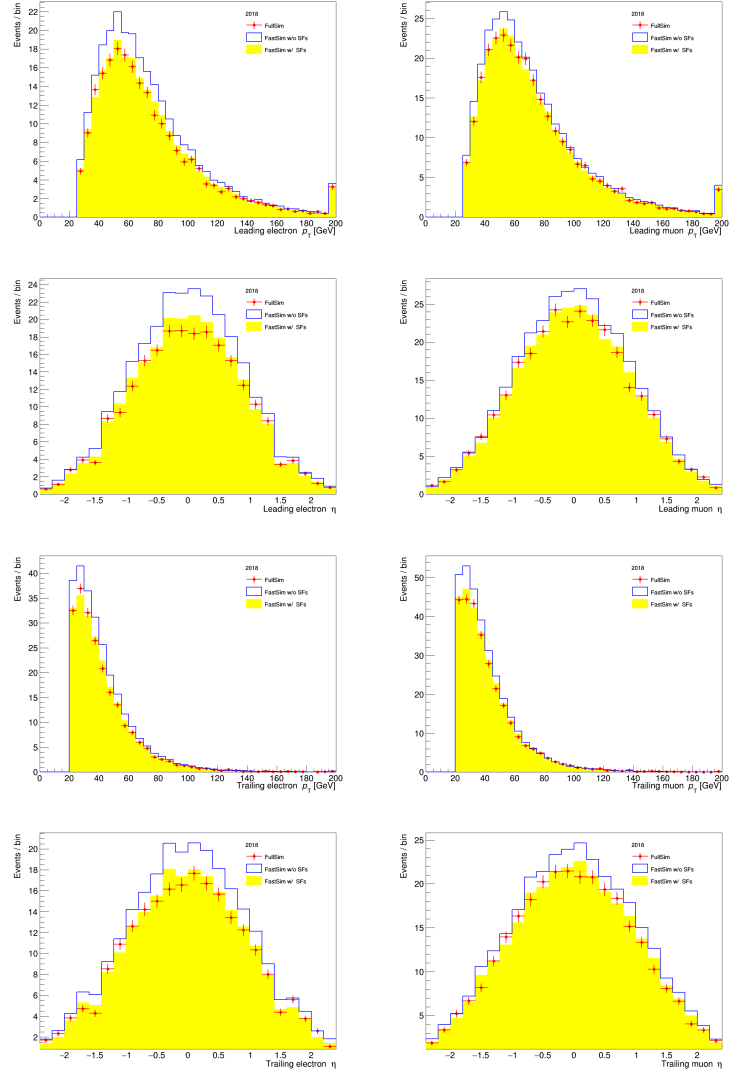


Figure D.6: Same as in Fig. D.4 for 2018 samples.

Appendix E

Test of the ML fit in events with $100 \leq p_T^{\text{miss}} < 140 \text{ GeV}$

In this Appendix, The results of a ML fit to the CR with $100 \leq p_T^{\text{miss}} < 140 \text{ GeV}$ are presented. Post-fit distributions of the $m_{T2}(\ell\ell)$ observables in 2016 data and simulated events are shown in Figs. E.1. Figures E.2 and E.3 show the pulls of the nuisances used in the fit. Figures E.4 to E.6 and Figs. E.7 to E.9 show the equivalent plots for the 2017 and 2018 data-taking years, respectively. We observe good post-fit agreement between observed events and SM expectations. In general, the most pulled nuisances are the one describing the uncertainties on the jet energy scale and resolution, and the rate parameter associated to the normalization of the WW production process.

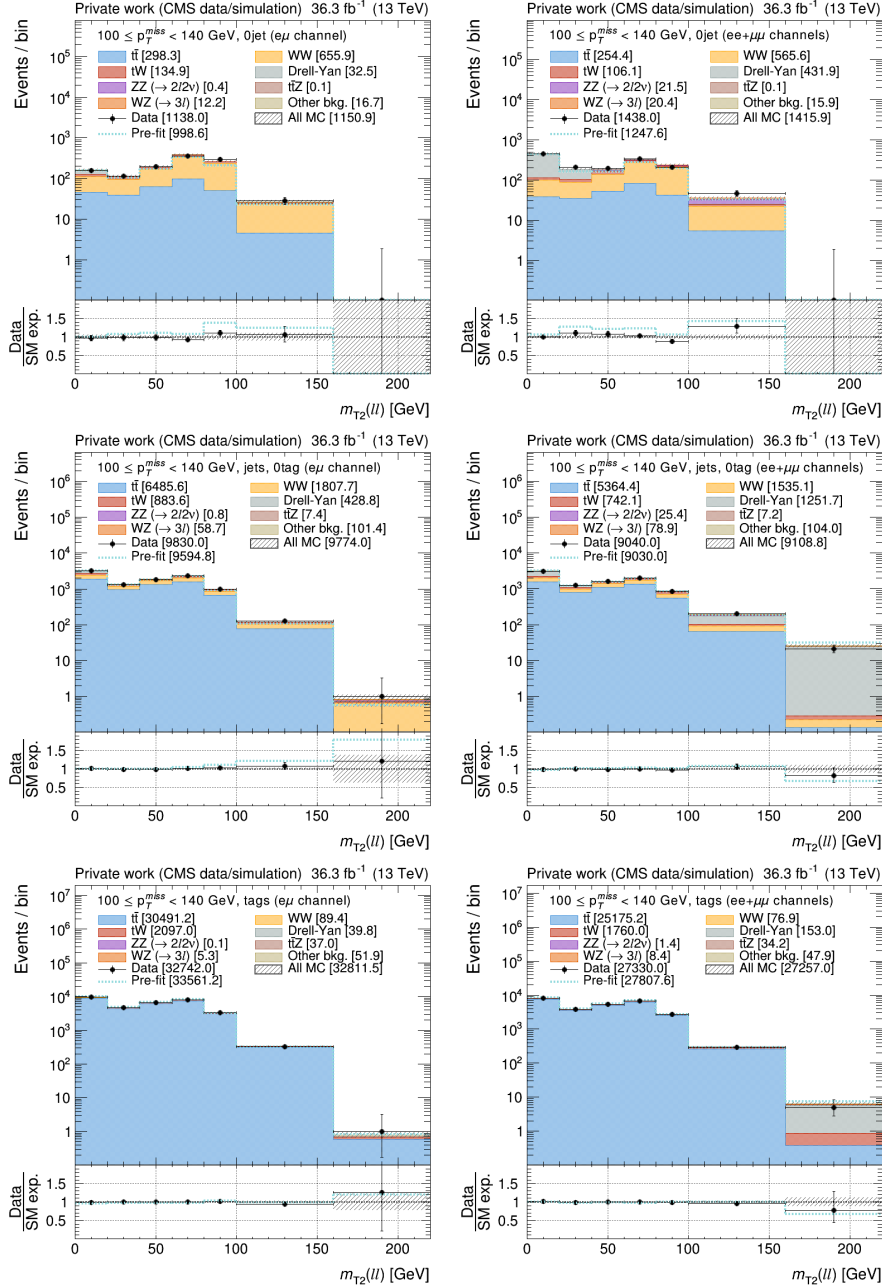


Figure E.1: Distributions of $m_{T2}(\ell\ell)$ after the fit to 2016 data in the CR with $100 \leq p_T^{\text{miss}} < 140 \text{ GeV}$. The distributions are shown in events with no jets (upper plots), jets but no b-tagged jets (middle), and b-tagged jets (lower) for the DF (left plots) and SF (right) channels. The dark blue dashed line represents the expected total SM contributions before the fit. The last bin includes the overflow entries. In the bottom panel, the ratio of data and SM expectations is shown for the expected total SM contribution after the fit using the background-only hypothesis (black dots) and before any fit (dark blue dashed line). The hatched band represents the total uncertainty after the fit.

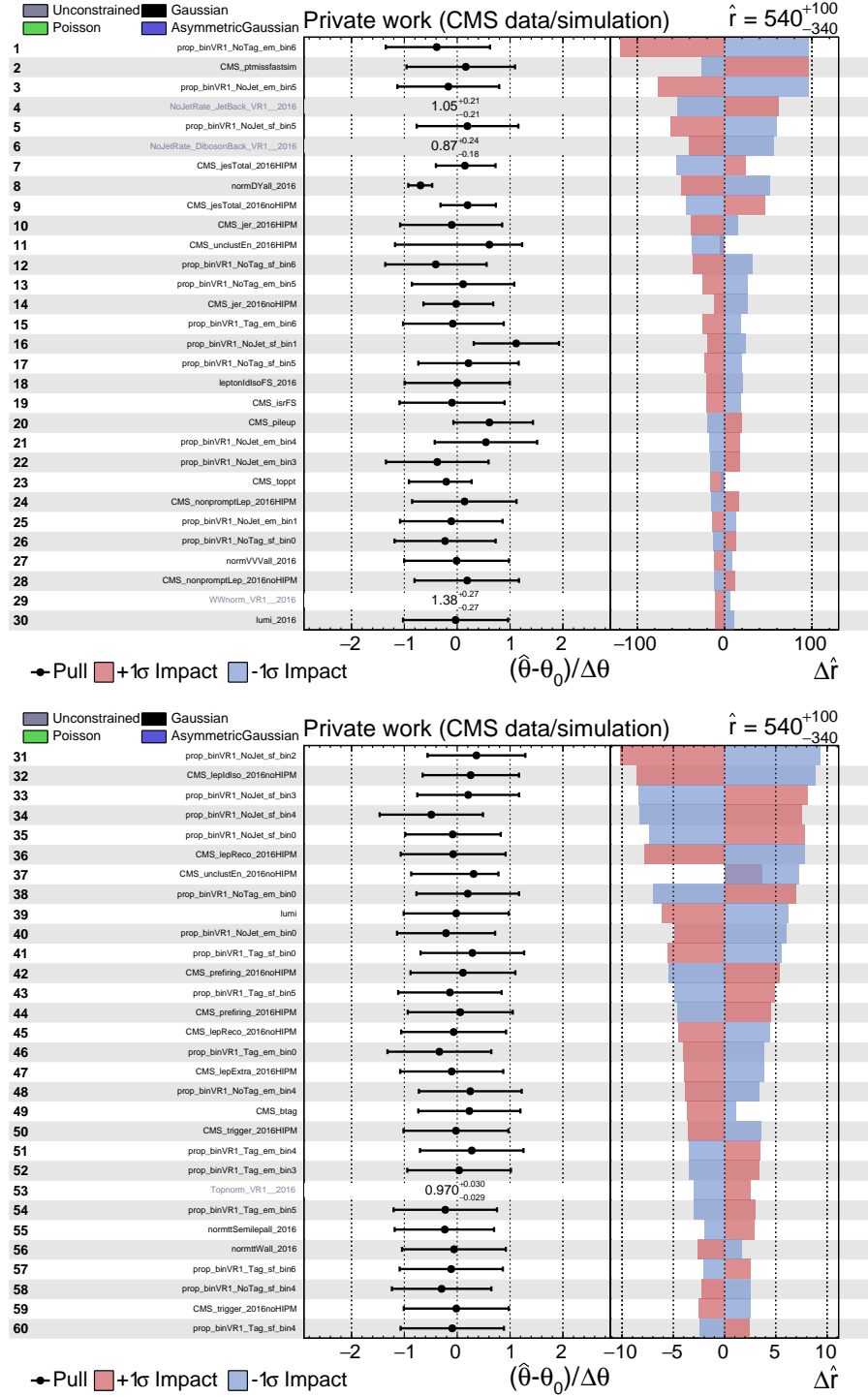


Figure E.2: Pulls of the nuisance parameters for the fit to 2016 data in the CR with $100 \leq p_T^{\text{miss}} < 140 \text{ GeV}$ (page 1).

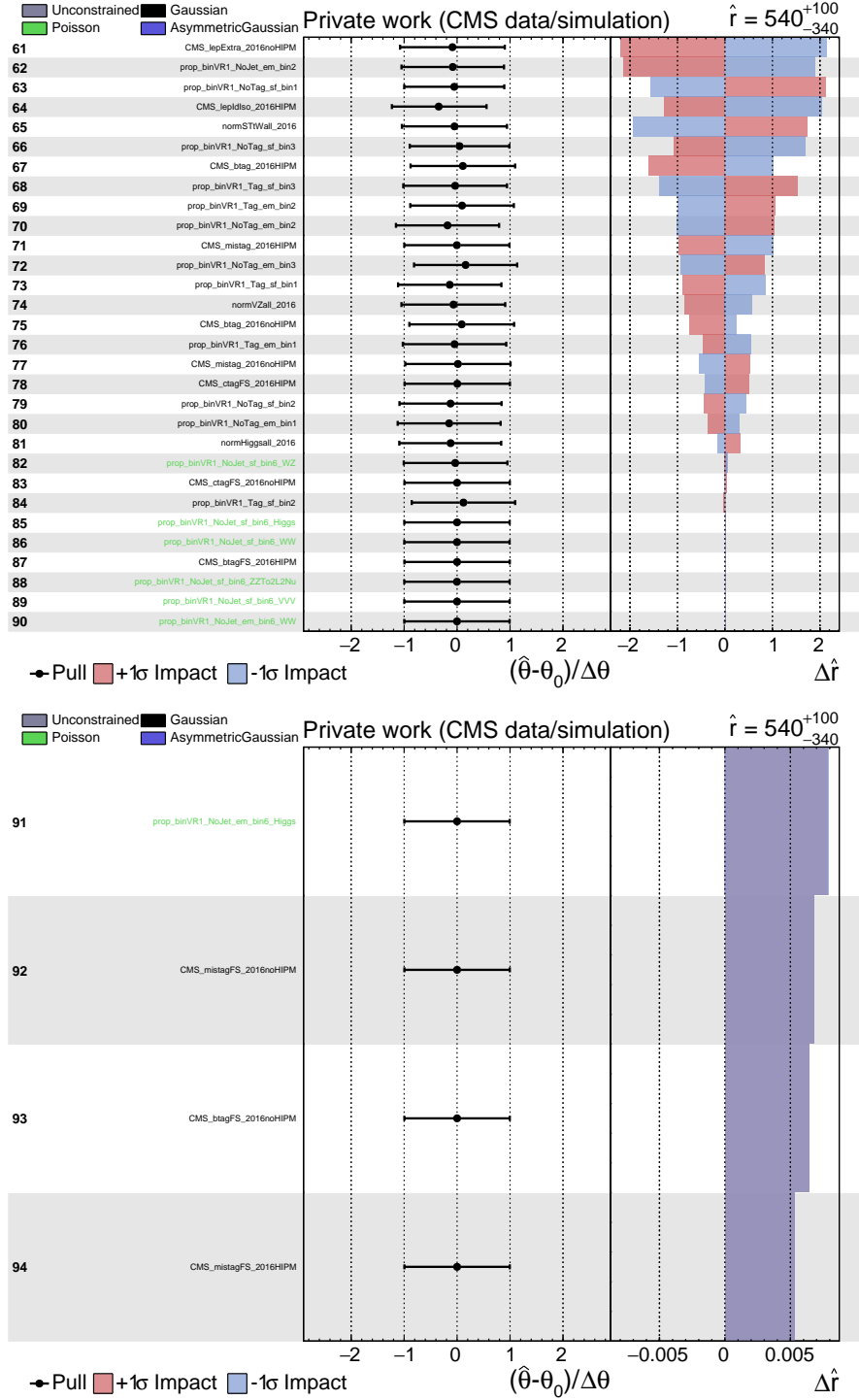


Figure E.3: Pulls of the nuisance parameters for the fit to 2016 data in the CR with $100 \leq p_T^{\text{miss}} < 140$ GeV (page 2).

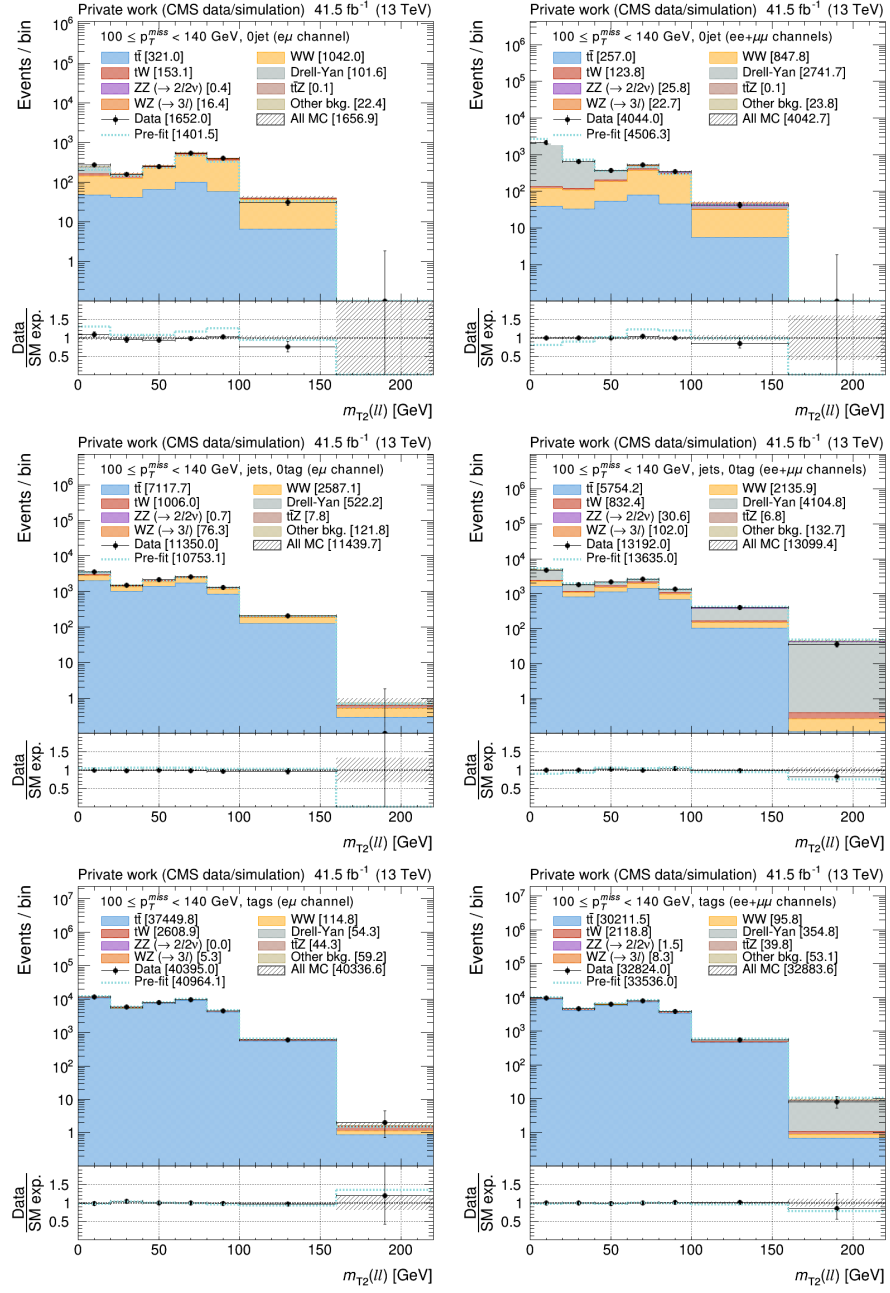


Figure E.4: Same as Fig. E.1, but for 2017 data.

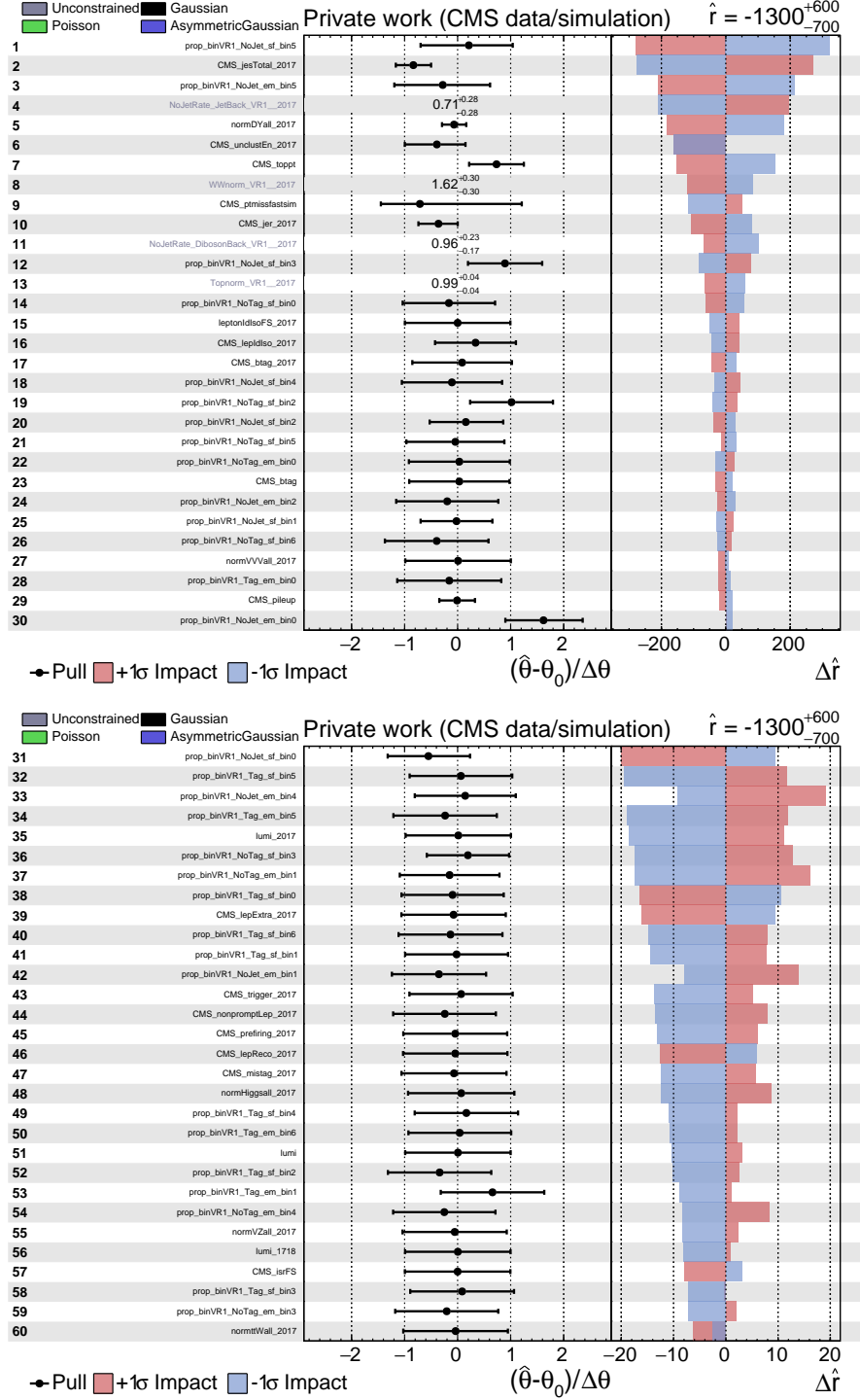


Figure E.5: Pulls of the nuisance parameters for the fit to 2017 data in the CR with $100 \leq p_T^{\text{miss}} < 140 \text{ GeV}$ (page 1).

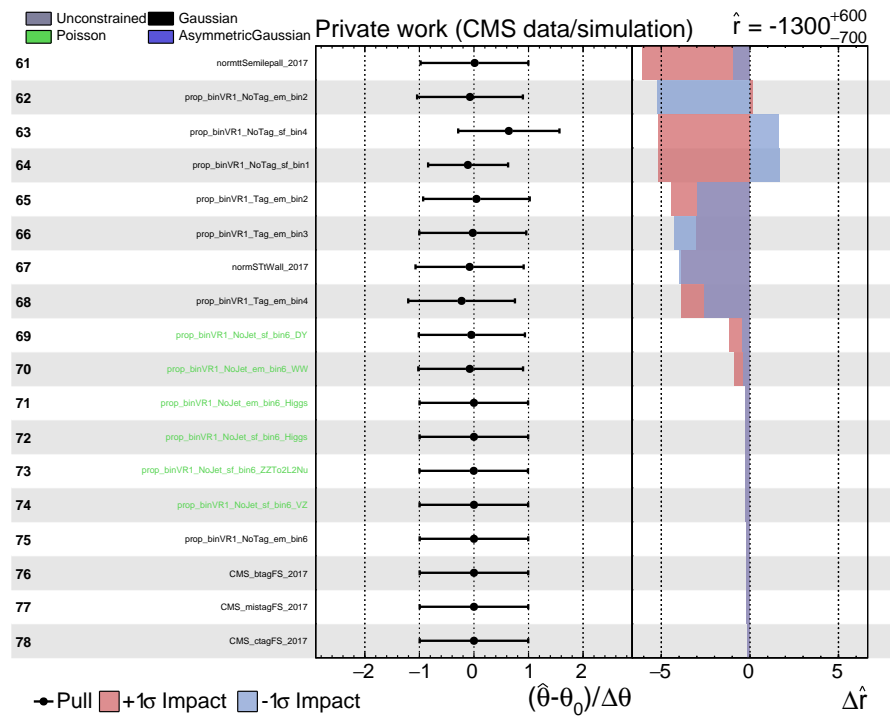


Figure E.6: Pulls of the nuisance parameters for the fit to 2017 data in the CR with $100 \leq p_T^{\text{miss}} < 140 \text{ GeV}$ (page 2).

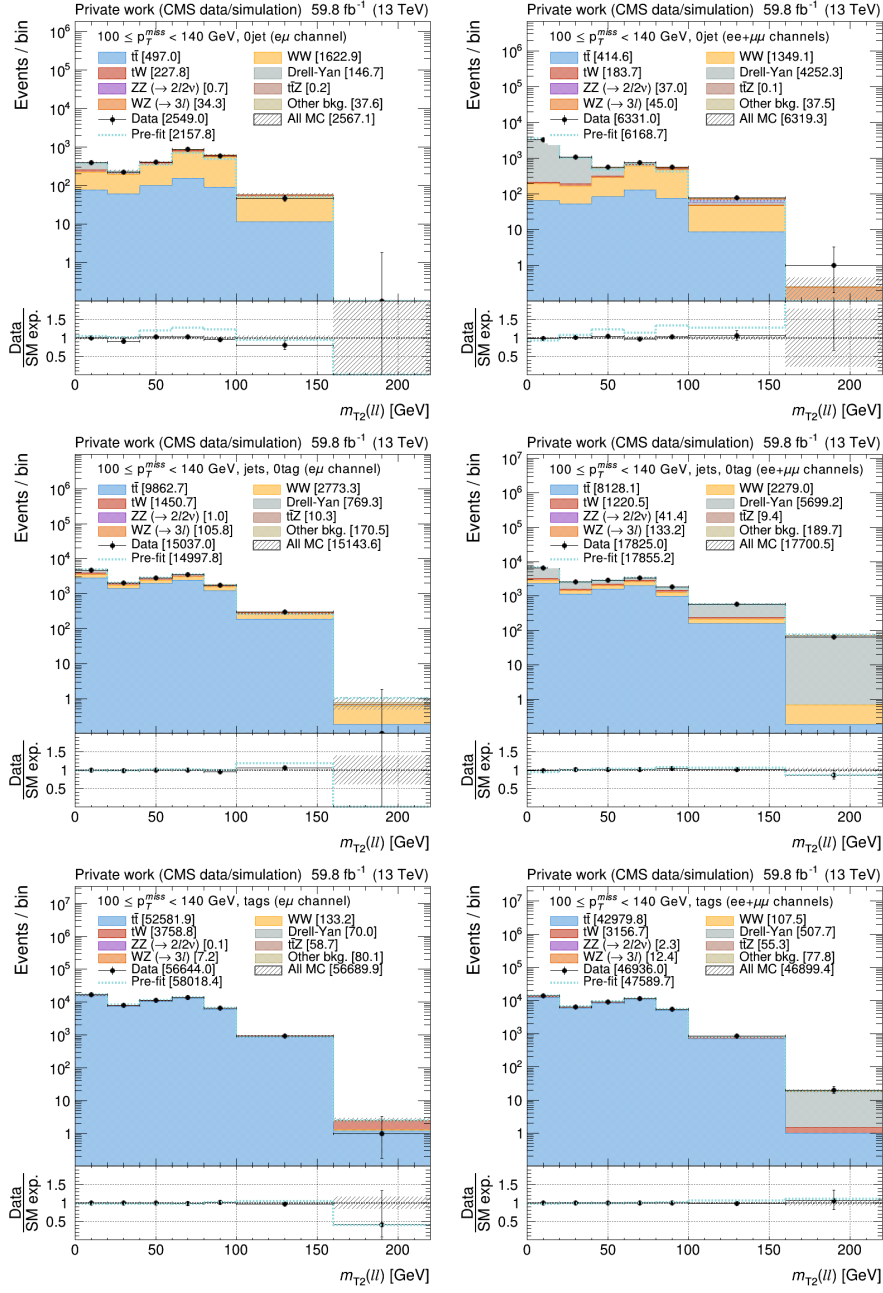


Figure E.7: Same as Fig. E.1, but for 2018 data.

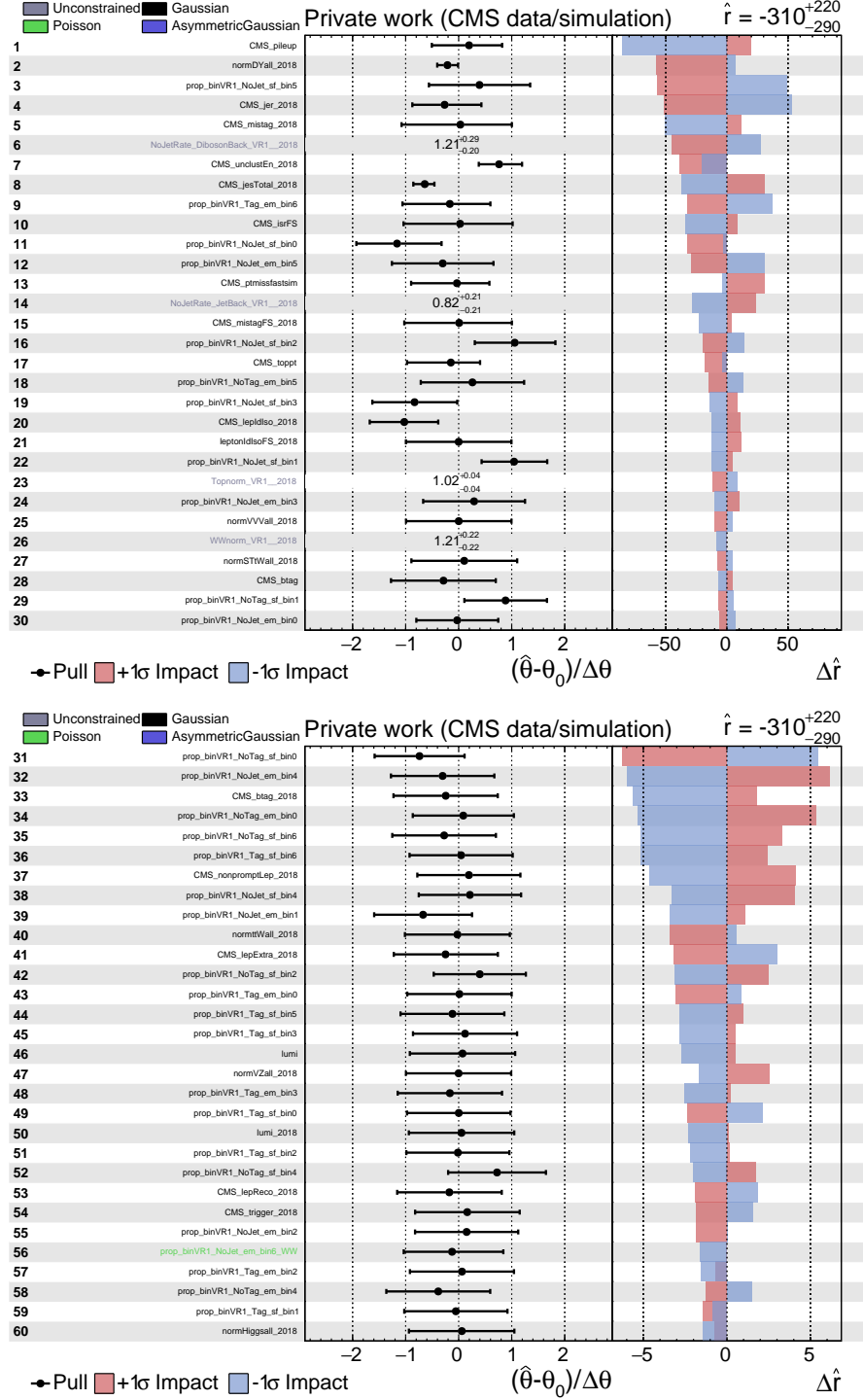


Figure E.8: Pulls of the nuisance parameters for the fit to 2018 data in the CR with $100 \leq p_T^{\text{miss}} < 140 \text{ GeV}$ (page 1).

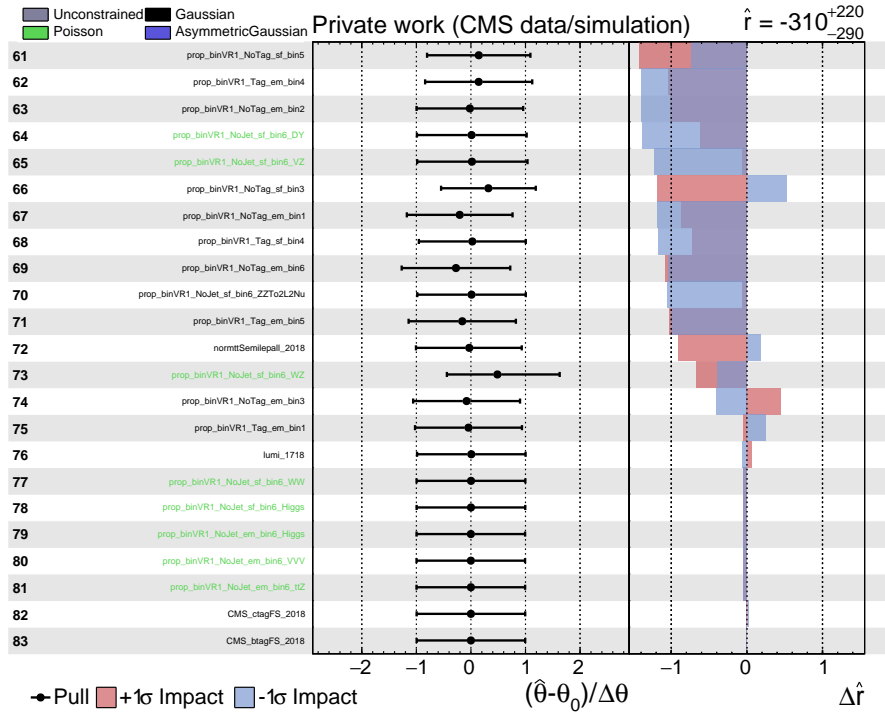


Figure E.9: Pulls of the nuisance parameters for the fit to 2018 data in the CR with $100 \leq p_T^{\text{miss}} < 140 \text{ GeV}$ (page 2).

Appendix F

Smoothing of shape variations for uncertainties in JES, JER, and unclustered energy

We developed a smoothing procedure of the shape variations for the uncertainties in JES, JER, and unclustered energy along these lines:

- ◆ We start computing the variations by merging the signal regions with the same “jet selection” (multiplicity of jets and of b-tagged jets) across the p_T^{miss} bins and lepton flavours since the variations of $m_{T2}(\ell\ell)$ (and p_T^{miss}) for JES, JER, and unclustered energy uncertainties are naturally expected to be very sensitive to this selection.
- ◆ In order to obtain the variations for events with a specific jet selection and p_T^{miss} bin, we take the merged variations for the corresponding jet selection computed above, and correct them by the ratio of the variations for all events in the considered p_T^{miss} bin (merged across jet selection and lepton flavours) to the variations in all events (merged across all the signal regions). This amounts to assuming that residual dependencies of the variations on the jet selection would factorize in the ratio across the p_T^{miss} bins. While this is of course an approximation, we leave to the subsequent comparison of the original MC variations to the smoothed ones to decide if it is accurate enough for our purposes.
- ◆ Drell–Yan variations for JER and unclustered energy are found to behave differently than the ones for other backgrounds and are taken out of the smoothing procedure.
- ◆ Adjacent bins of merged $m_{T2}(\ell\ell)$ distributions with a statistical uncertainty greater than 10% are merged, and a smoothing of outliers is applied at the end of the procedure.

This smoothing procedure is generally found to reproduce well the original MC variations for bins with small statistical uncertainties (an example is given in Fig. F.1 for events with $160 \leq p_T^{\text{miss}} < 220$ GeV, at least one jet but no b-tagged jets in 2018 simulated data sets), while providing a reasonably smooth and accurate modelling of the variations for bins with large statistical uncertainties (as exemplified in Fig. F.2 for events with $p_T^{\text{miss}} \geq 380$ GeV and veto on b-tagged jets in 2018 simulated data sets). The comparison of blinded exclusion regions obtained when using original MC variations and the smoothed ones shows that the smoothing procedure has a negligible impact both for the chargino and top squark pair production models (Fig. F.3). This confirms that the impact of the details in JES, JER, and unclustered energy variations is

shadowed in the fit when the statistical uncertainties are large. We propose to use the smoothed variations for the regions where the $m_{T2}(\ell\ell)$ shape variations for the uncertainties in JES, JER, and unclustered energy become smaller than the statistical uncertainties.

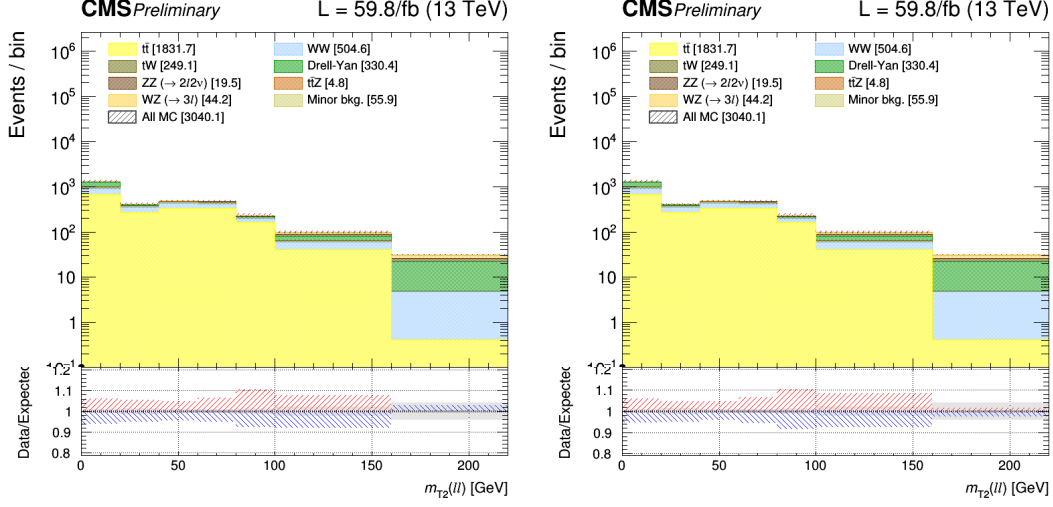


Figure F.1: Distributions of $m_{T2}(\ell\ell)$ for events with $160 \leq p_T^{\text{miss}} < 220$ GeV, at least one jet but no b-tagged jets in 2018 simulated data sets. The last bin includes the overflow entries. In the bottom panel, the uncertainties in the expected yields of the SM processes are shown: the gray band represents the statistical uncertainty, while the red (blue) band shows the variation in the $m_{T2}(\ell\ell)$ distribution when varying the JES up (down) by its uncertainty. In the left plot, original MC variations are used, while in the right one, the smoothed variations are shown.

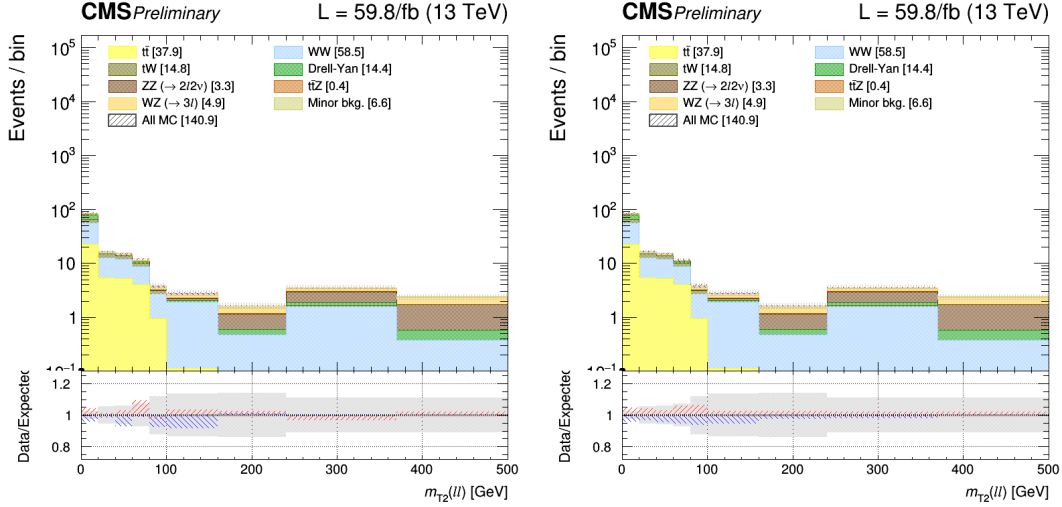


Figure F.2: Same as in Fig. F.1 for events with $p_T^{\text{miss}} \geq 380$ GeV and veto on b-tagged jets in 2018 simulated data sets.

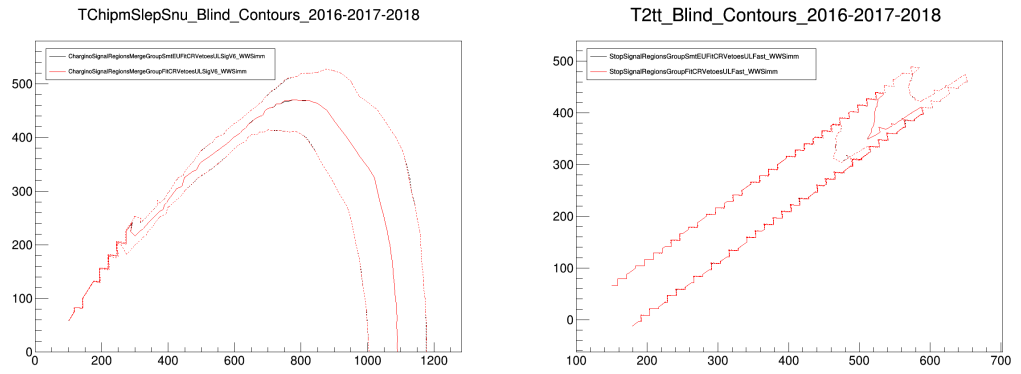


Figure F.3: Comparison of blinded exclusion regions obtained when using the original MC variations (red curve) and the smoothed ones (black) for chargino (left plot) and top squark (right) pair production.

Appendix G

Signal and control regions after performing the ML fit by year

In this Appendix, the year by year distributions after performing the ML fit are presented. The appendix is split into two sections. Section G.1 depicts the year by year post fit distributions are shown for relevant mass hypotheses on both the chargino and top squark signal regions. Likewise, Section G.2 show the observed and expected $m_{T2}(\ell\ell)$ distributions in the CRs for both of the both searches after performing a background-only fit.

G.1 Post fit distributions in the signal regions

G.1.1 Chargino search regions

The $m_{T2}(\ell\ell)$ distributions after a background-only fit to the data in the chargino pair production SRs, as defined in the top part of Table 8.2, are presented in Figs. G.1 to G.7, for each of the data taking years of Run II. The expected $m_{T2}(\ell\ell)$ distributions for a signal hypothesis with a chargino mass of 800 GeV and a neutralino mass of 200 GeV are also shown as a reference.

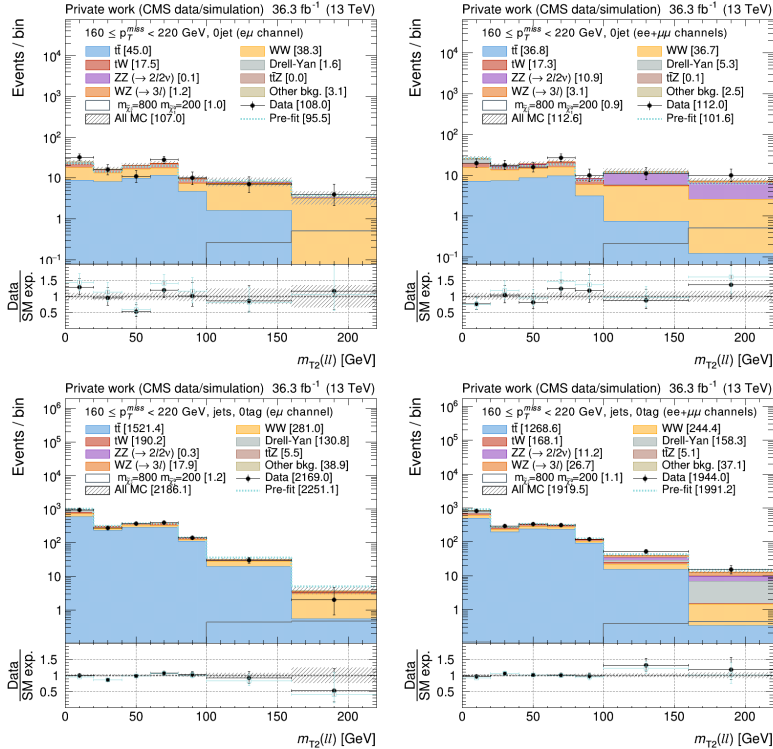


Figure G.1: Observed and expected $m_{T2}(\ell\ell)$ distributions for SM processes in the SR1 after a background-only fit to the data in the chargino SRs for 2016 data. The $m_{T2}(\ell\ell)$ distributions for a signal hypothesis with a chargino mass of 800 GeV and a neutralino mass of 200 GeV are also shown. The distributions in the SR1 with no jets are shown at the top, and the ones in the SR1 with jets but no b-tagged jets are shown at the bottom, with the plots on the left corresponding to different flavour events and the ones on the right to same flavour events, respectively. In the bottom panel, the ratio of data and SM expectations is shown. The hatched band represents the total uncertainty, including the sources discussed in Section 8.5.

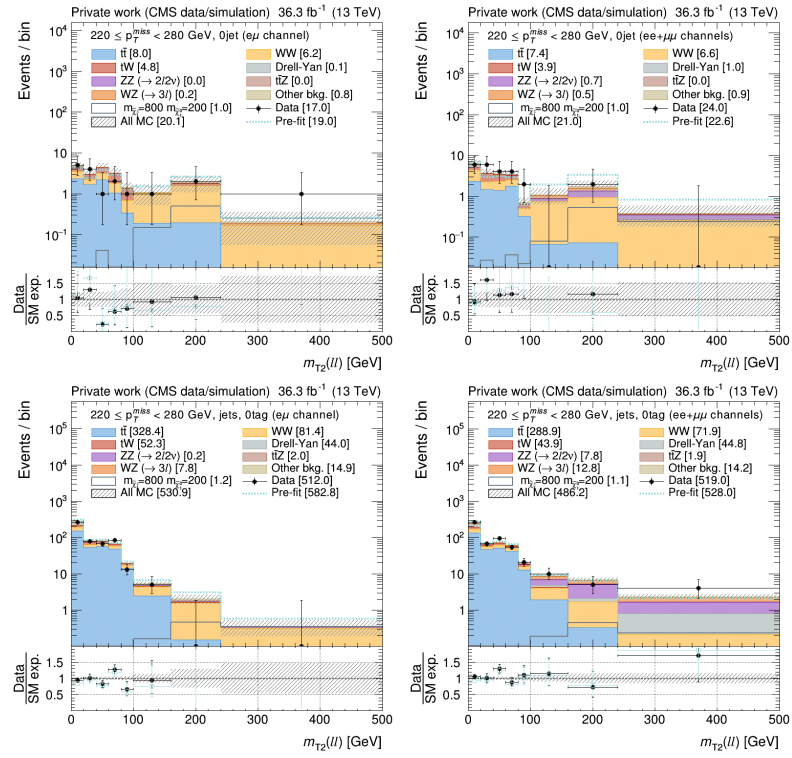


Figure G.2: Same as for Fig. G.1 but for the SR2.

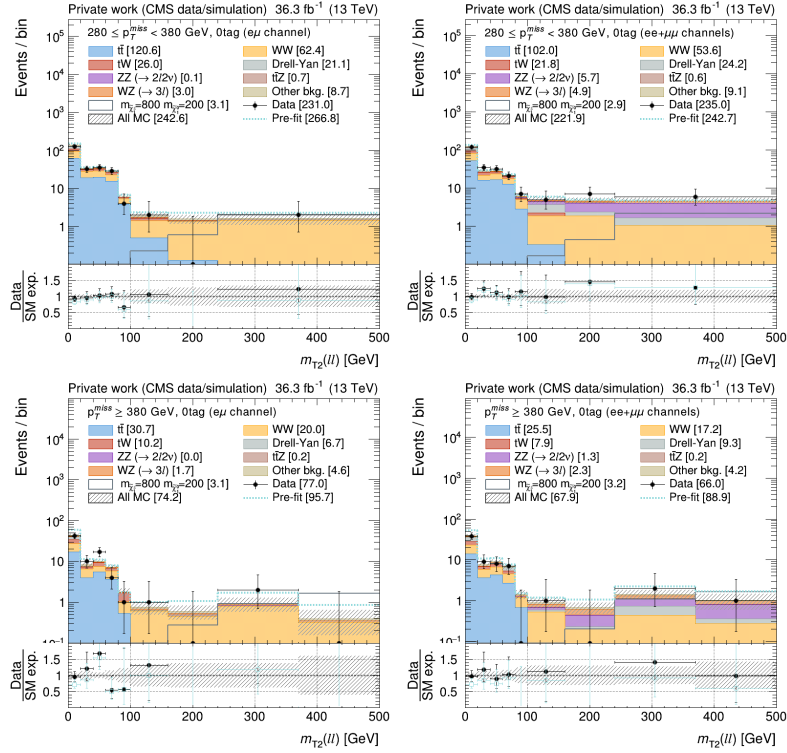


Figure G.3: Observed and expected $m_{T2}(\ell\ell)$ distributions for SM processes in the SR3 and SR4 after a background-only fit to the data in the chargino SRs for 2016 data. The $m_{T2}(\ell\ell)$ distributions for a signal hypothesis with a chargino mass of 800 GeV and a neutralino mass of 200 GeV are also shown. The distributions in the SR3 are shown at the top, and the ones in the SR4 are shown at the bottom, with the plots on the left corresponding to different flavour events and the ones on the right to same flavour events, respectively. In the bottom panel, the ratio of data and SM expectations is shown. The hatched band represents the total uncertainty, including the sources discussed in Section 8.5.

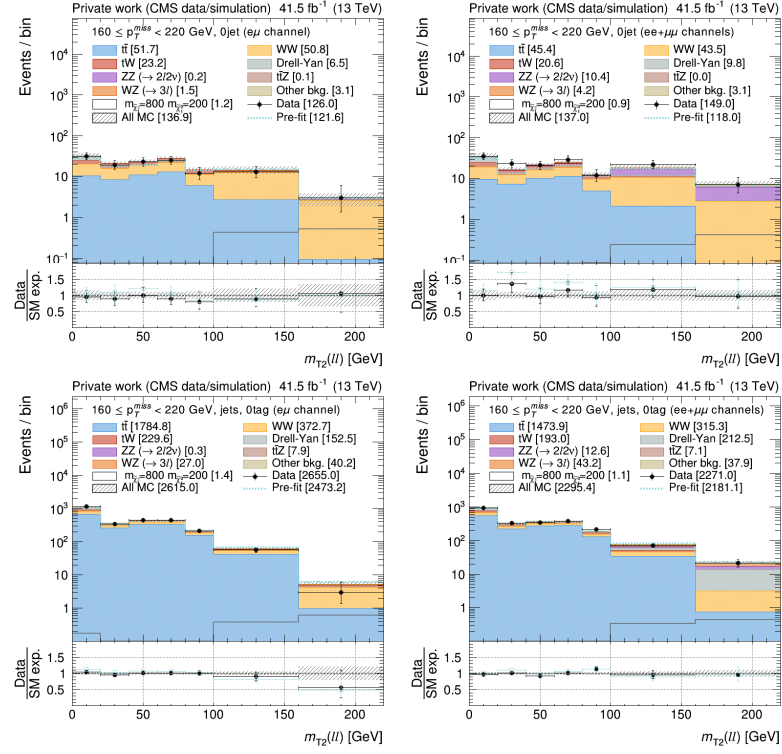


Figure G.4: Same as for Fig. G.1 but for 2017 data.

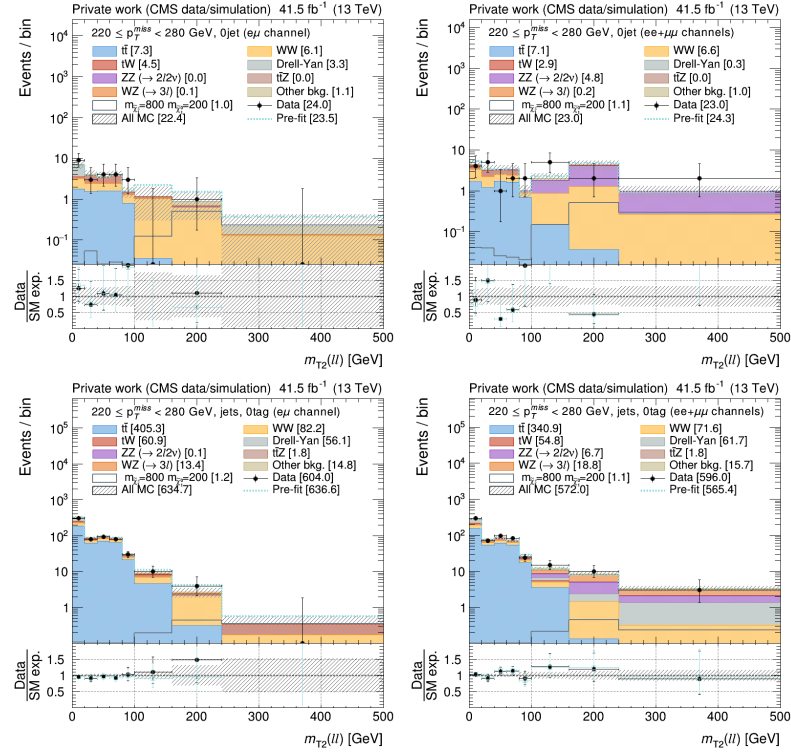


Figure G.5: Same as for Fig. G.4 but for the SR2 and 2017 data.

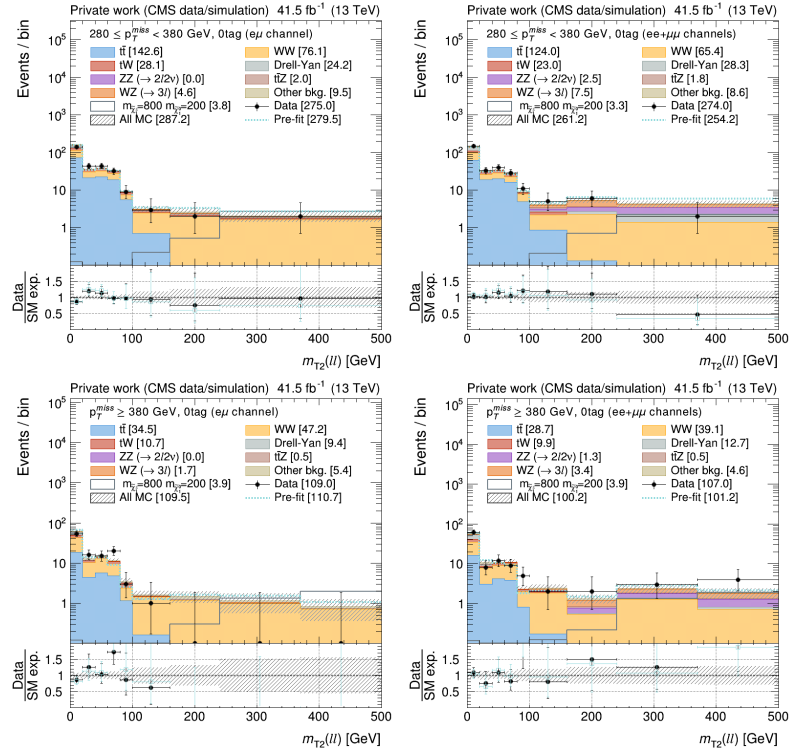


Figure G.6: Same as for Fig. G.3 but for 2017 data.

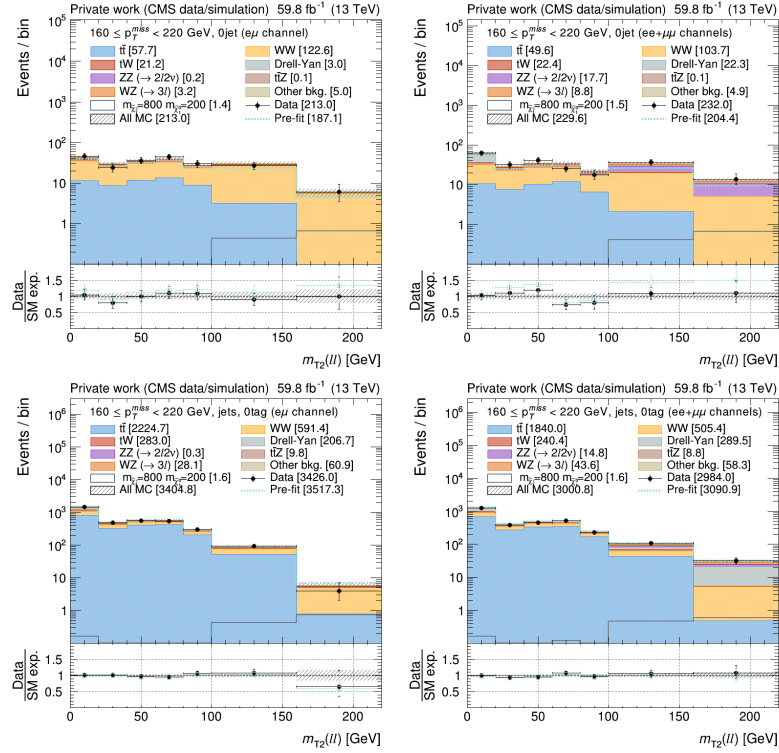


Figure G.7: Same as for Fig. G.1 but for 2018 data.

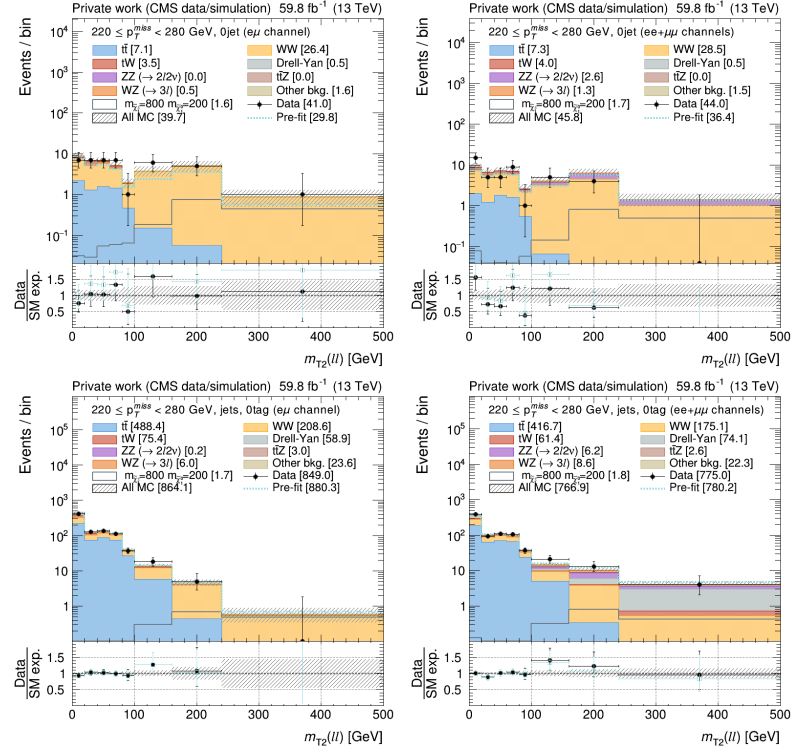


Figure G.8: Same as for Fig. G.1 but for the SR2 and 2018 data.

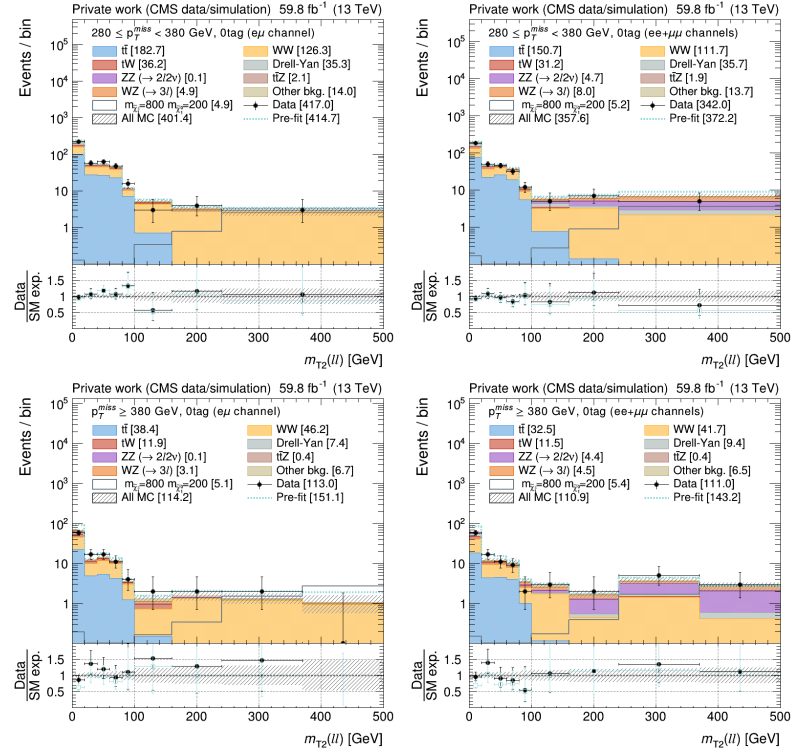


Figure G.9: Same as for Fig. G.3 but for 2018 data.

G.1.2 Top squark search regions

The $m_{T2}(\ell\ell)$ distributions after a background-only fit to the data in the top squark pair production SRs, defined in the bottom part of Table 8.2, are depicted in Figs. G.10 and G.21, similarly to chargino signal regions previously shown. The signal hypothesis with a top squark mass of 400 GeV and a neutralino mass of 313 GeV is also shown.

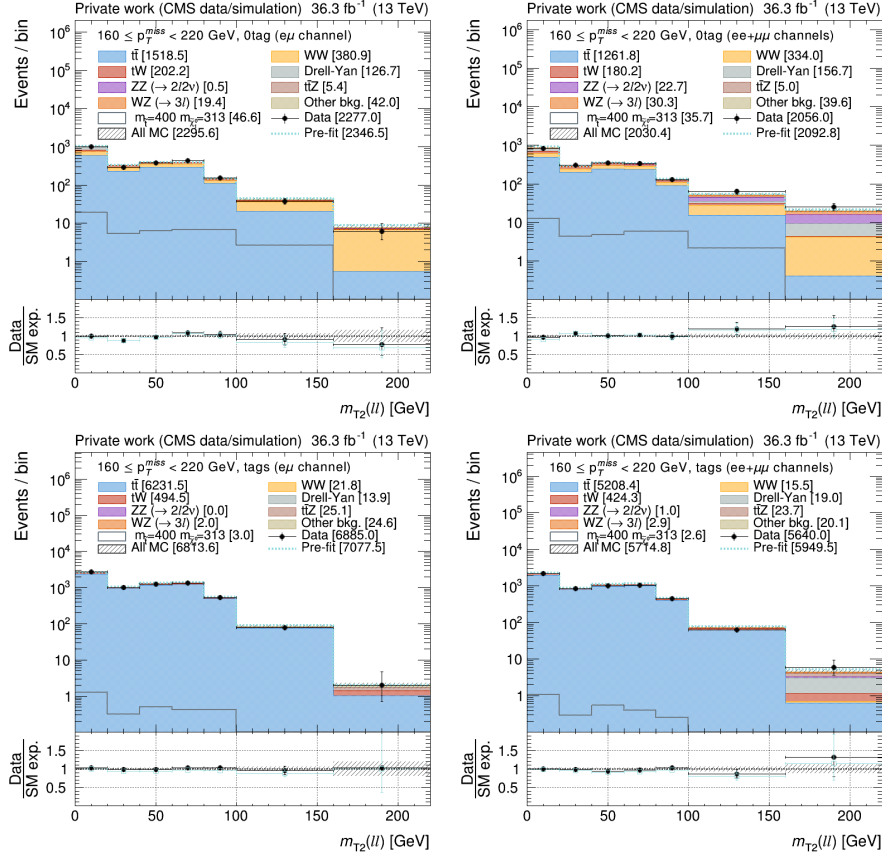


Figure G.10: Observed and expected $m_{T2}(\ell\ell)$ distributions for SM processes in the SR1 after a background-only fit to the data in the top squark SRs for 2016 data. The $m_{T2}(\ell\ell)$ distributions for a signal hypothesis with a top squark mass of 400 GeV and a neutralino mass of 313 GeV are also shown. Top plots are for DF (left) and SF (right) events with no b-tagged jets. Bottom plots are for DF (left) and SF (right) events with at least one b-tagged jets. In the bottom panel, the ratio of data and SM expectations is shown. The hatched band represents the total uncertainty, including the sources discussed in Section 8.5.

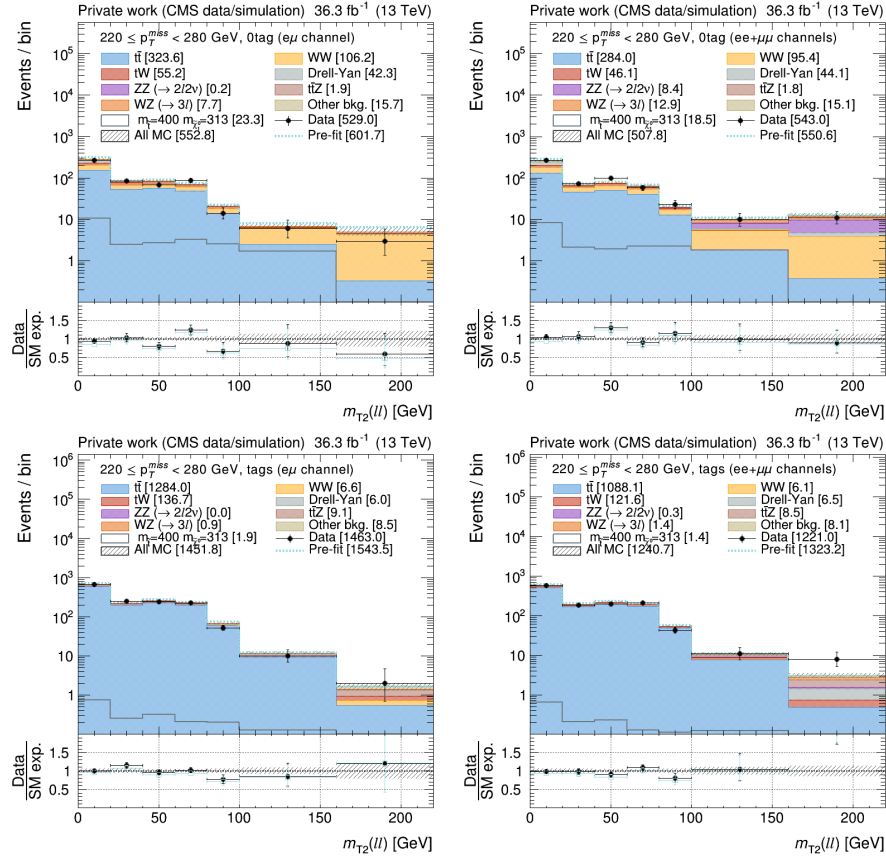


Figure G.11: Same as for Fig. G.10 for the SR2.

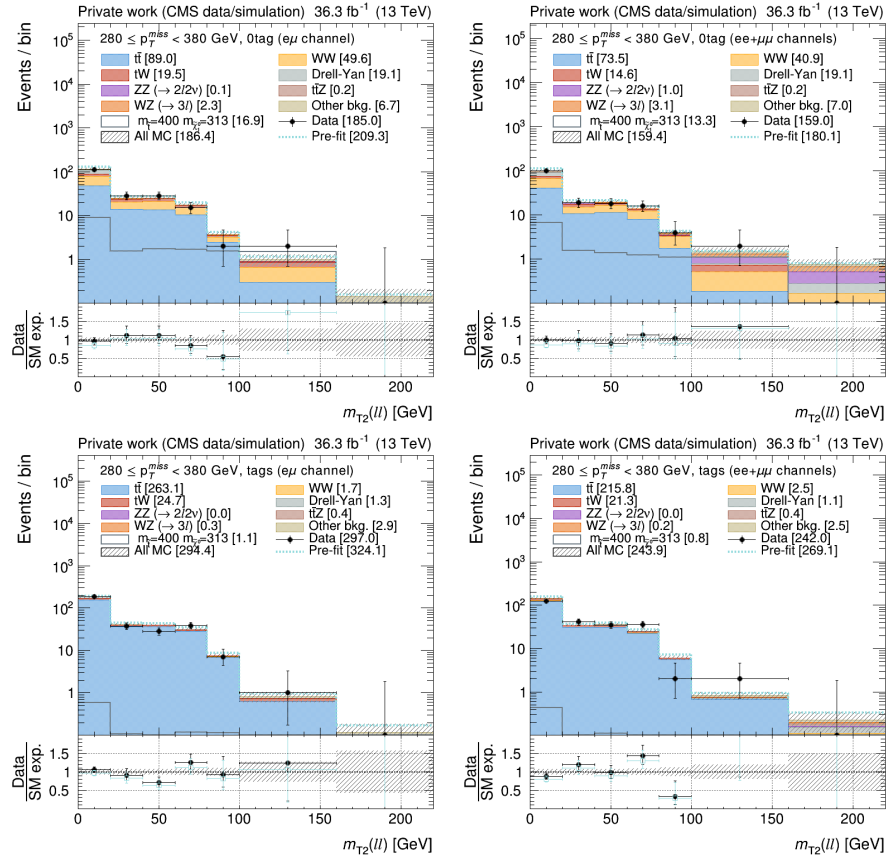


Figure G.12: Same as for Fig. G.10 for the SR3.

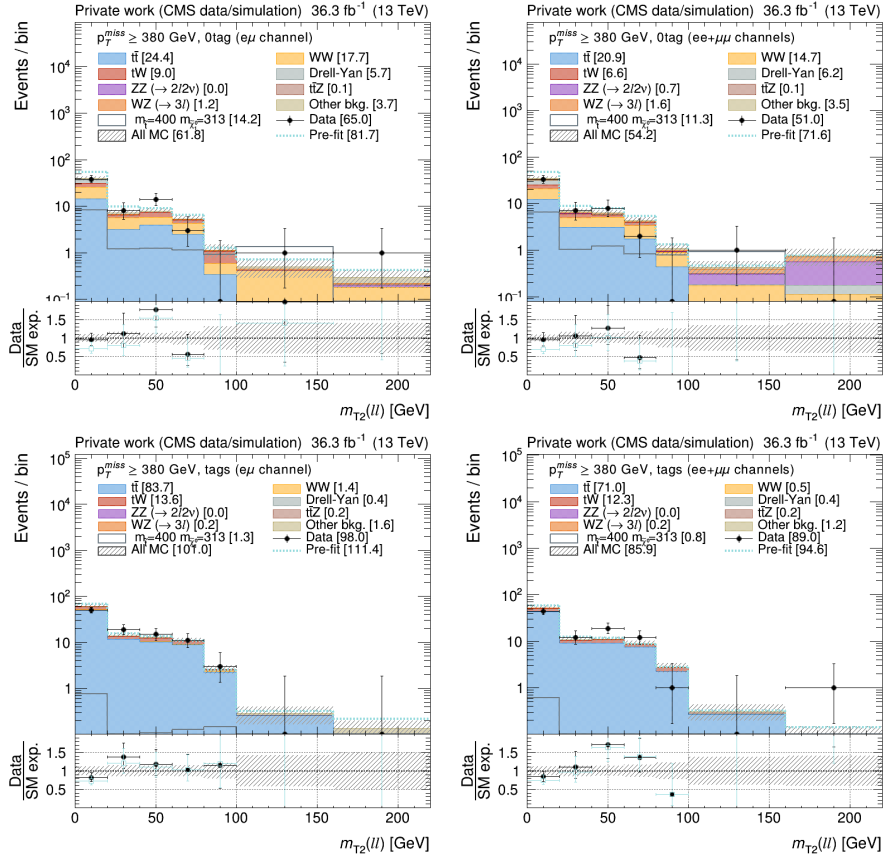


Figure G.13: Same as for Fig. G.10 for the SR4.

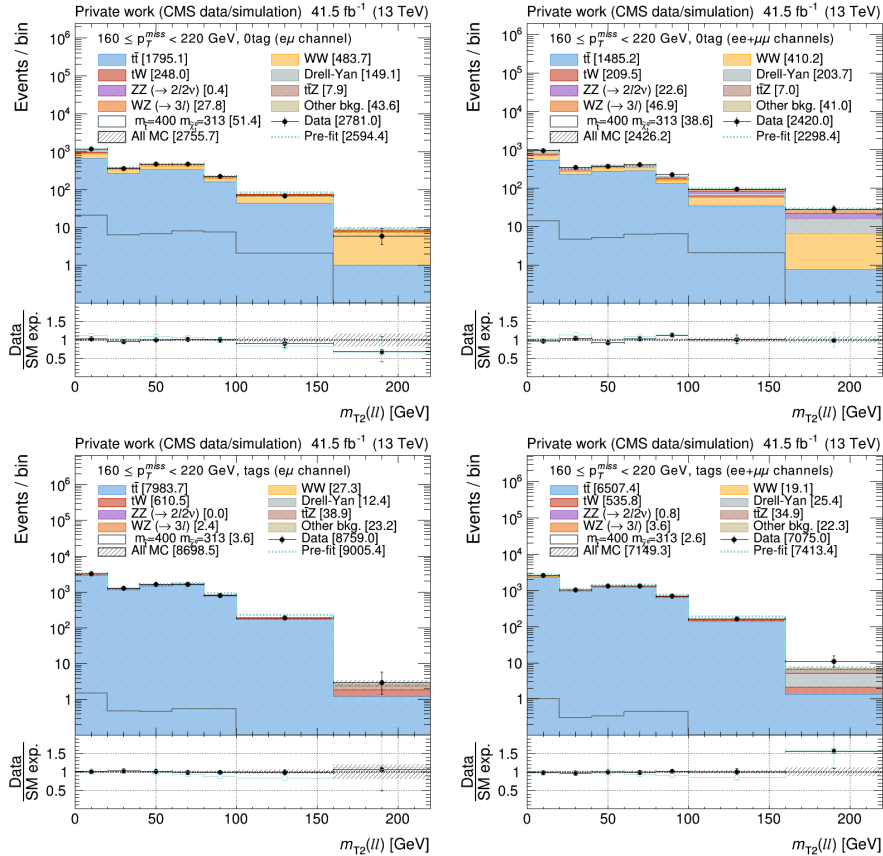


Figure G.14: Same as for Fig. G.10 for the 17 data.

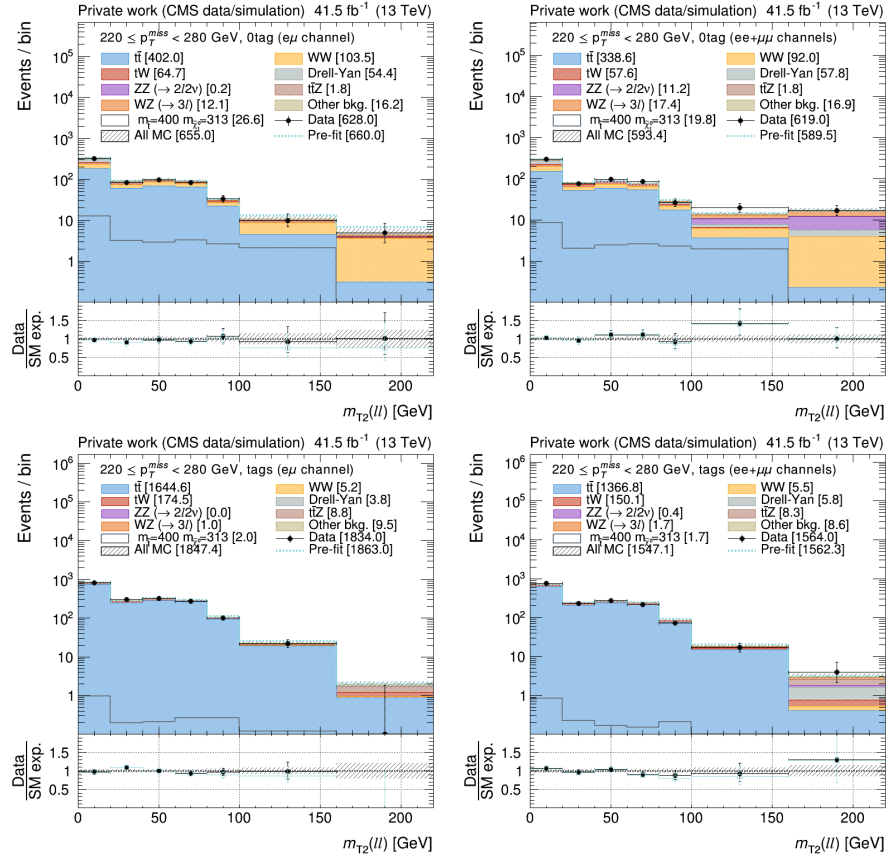


Figure G.15: Same as for Fig. G.10 for the SR2 and 2017 data.

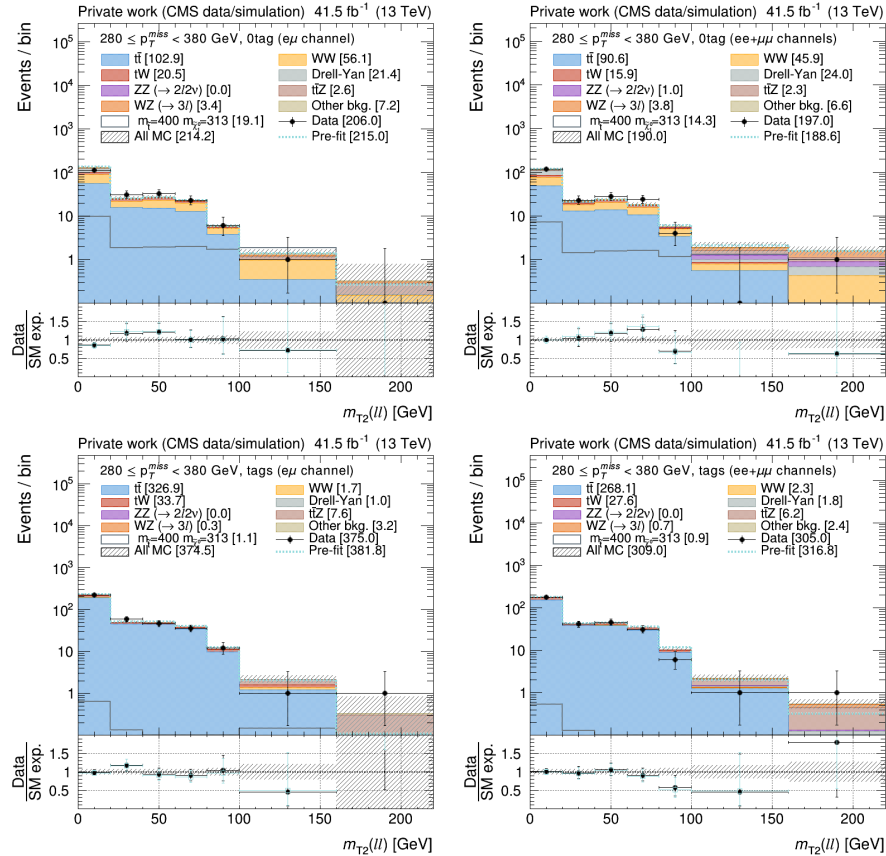


Figure G.16: Same as for Fig. G.10 for the SR3 and 2017 data.

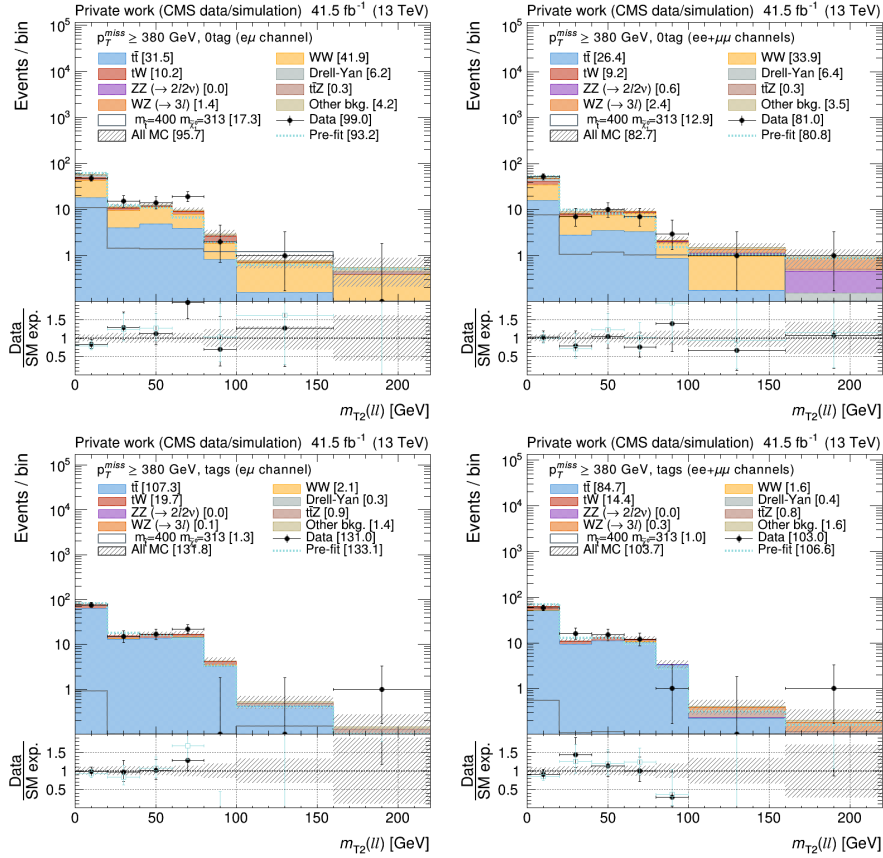


Figure G.17: Same as for Fig. G.10 for the SR4 and 2017 data.

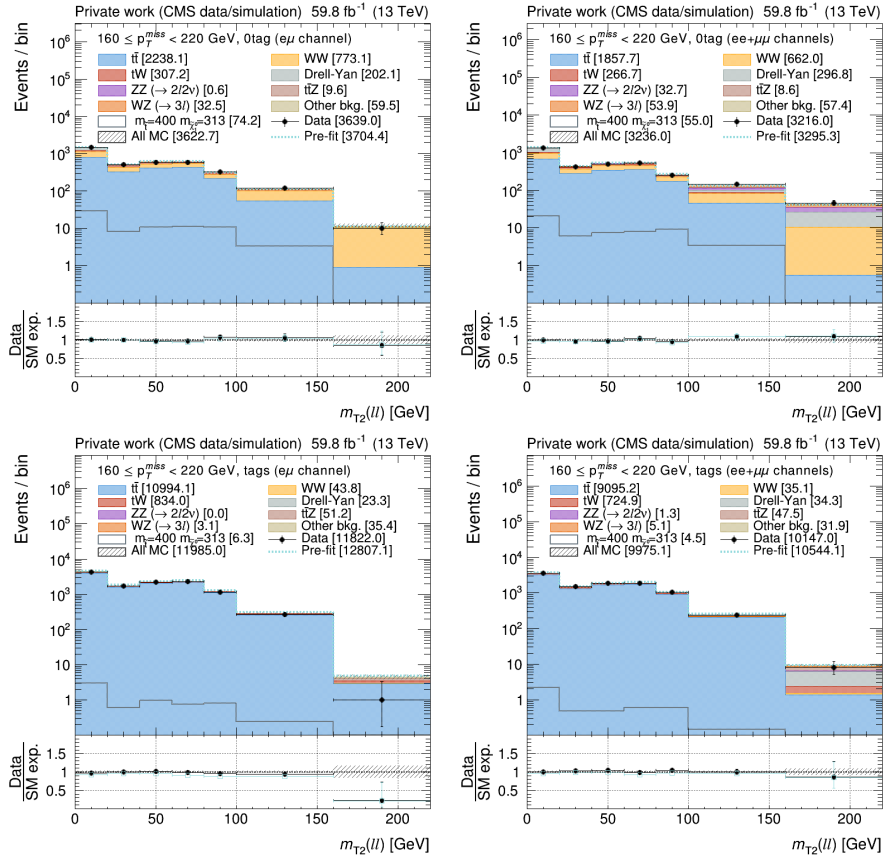


Figure G.18: Same as for Fig. G.10 for the 2018 data.

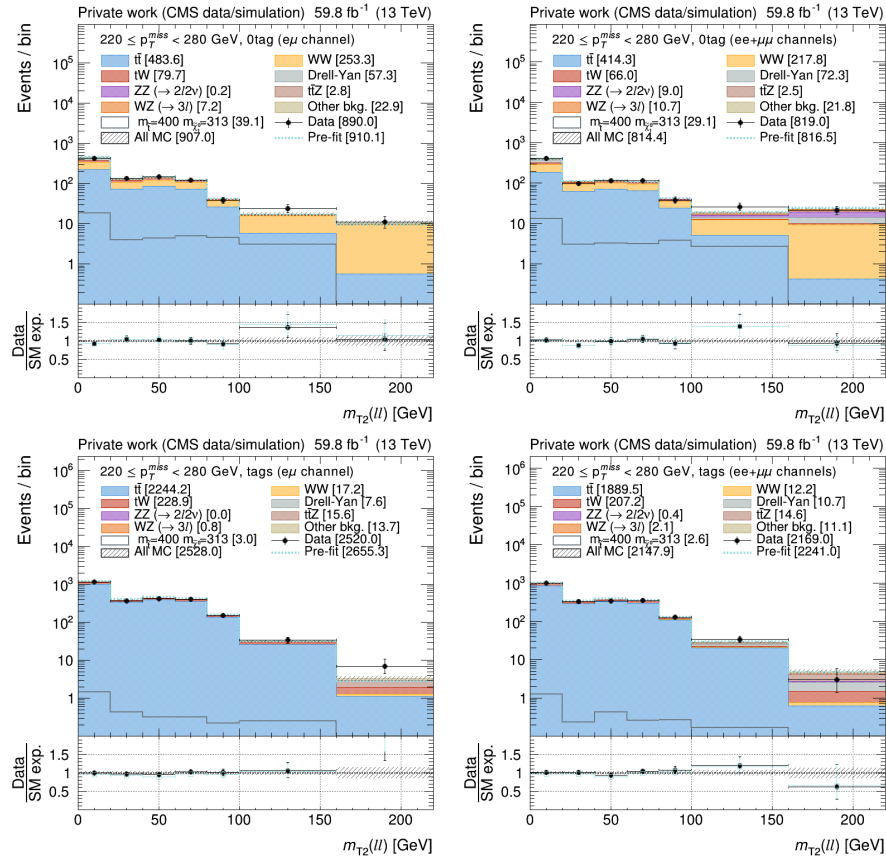


Figure G.19: Same as for Fig. G.10 for the SR2 and 2018 data.

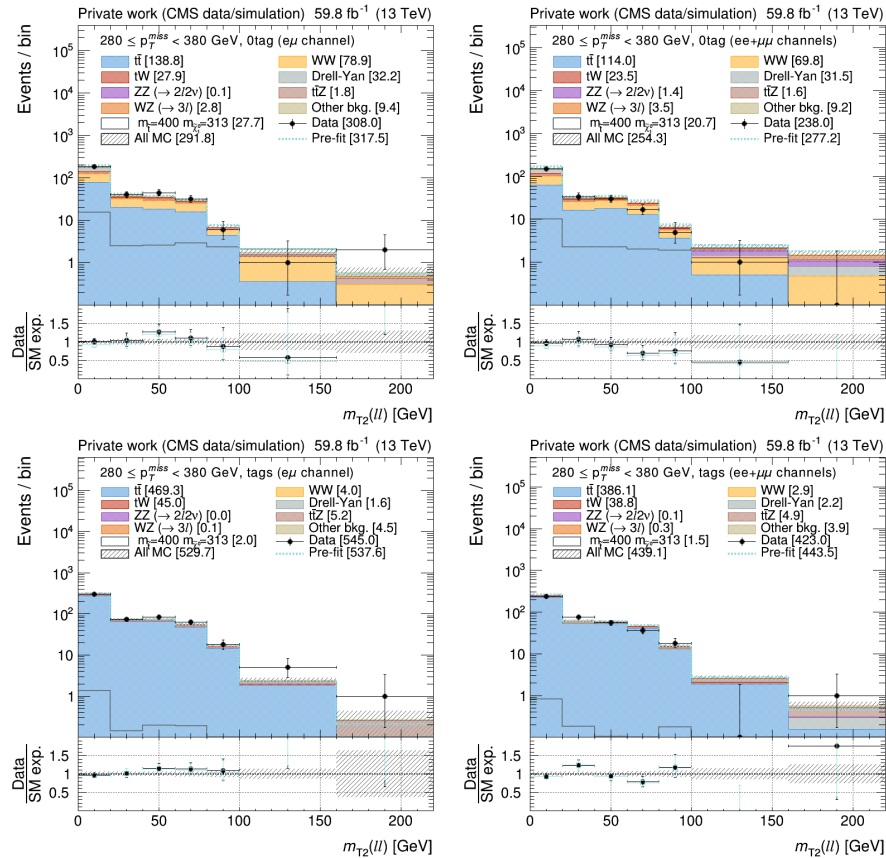


Figure G.20: Same as for Fig. G.10 for the SR3 and 2018 data.

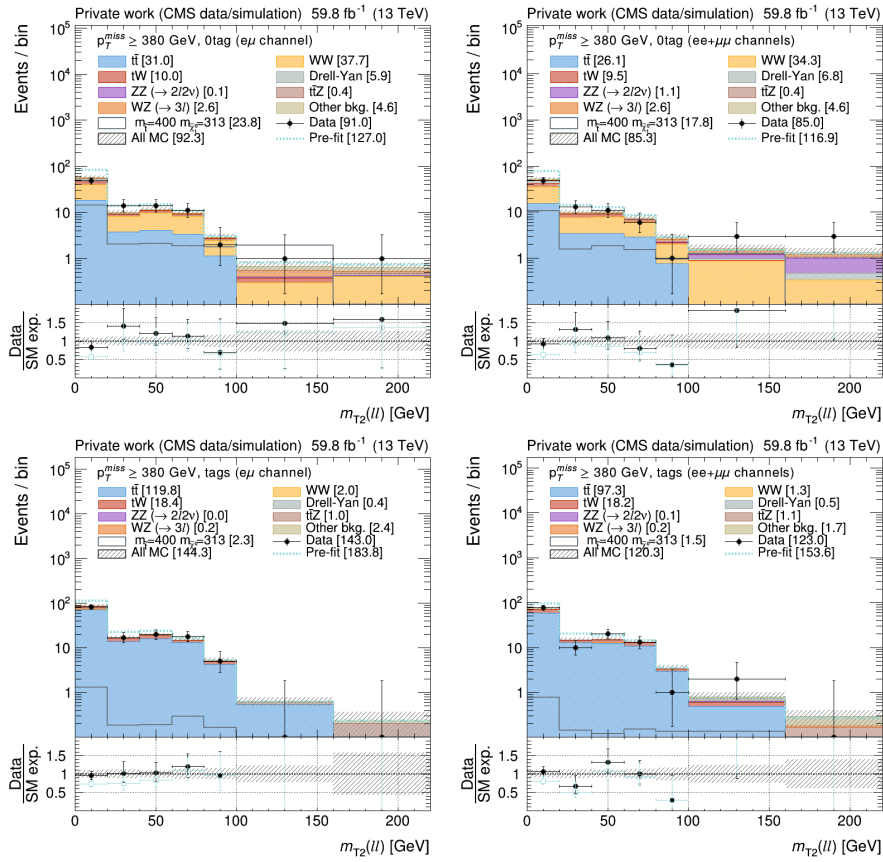


Figure G.21: Same as for Fig. G.10 for the SR4 and 2018 data.

G.2 Post fit distributions in the control regions

Figures G.22 to G.36 show the observed and expected $m_{T2}(\ell\ell)$ distributions in the CRs for the chargino/slepton search after a background-only fit. Figures G.37 to G.45 do the same for the top squark search.

G.2.1 Control regions for chargino/slepton ML fits in 2016 data

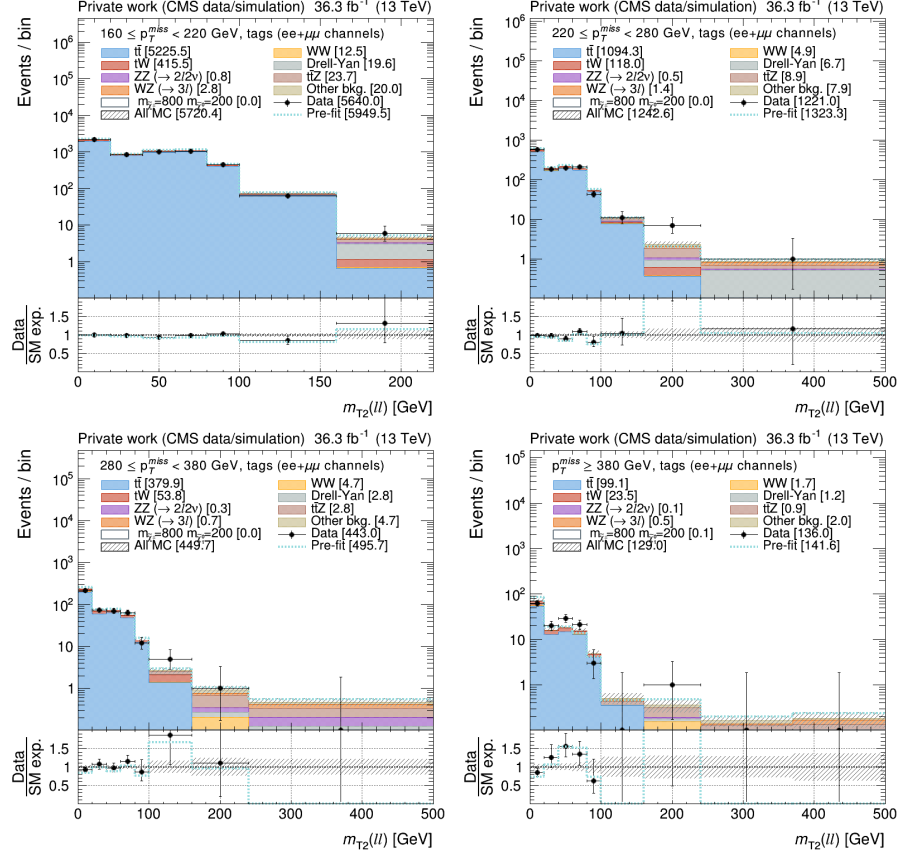


Figure G.22: Observed and expected yields of events in the CRs for the normalization of the top background in 2016 data after a background-only ML fit to the chargino/slepton SRs. From top-left clockwise, the SF events in CR1_{tags}, CR2_{tags}, CR4_{tags}, and CR3_{tags} are shown. In the bottom panel, the ratio of data and SM expectations is shown. The hatched band represents the total uncertainty after the fit.

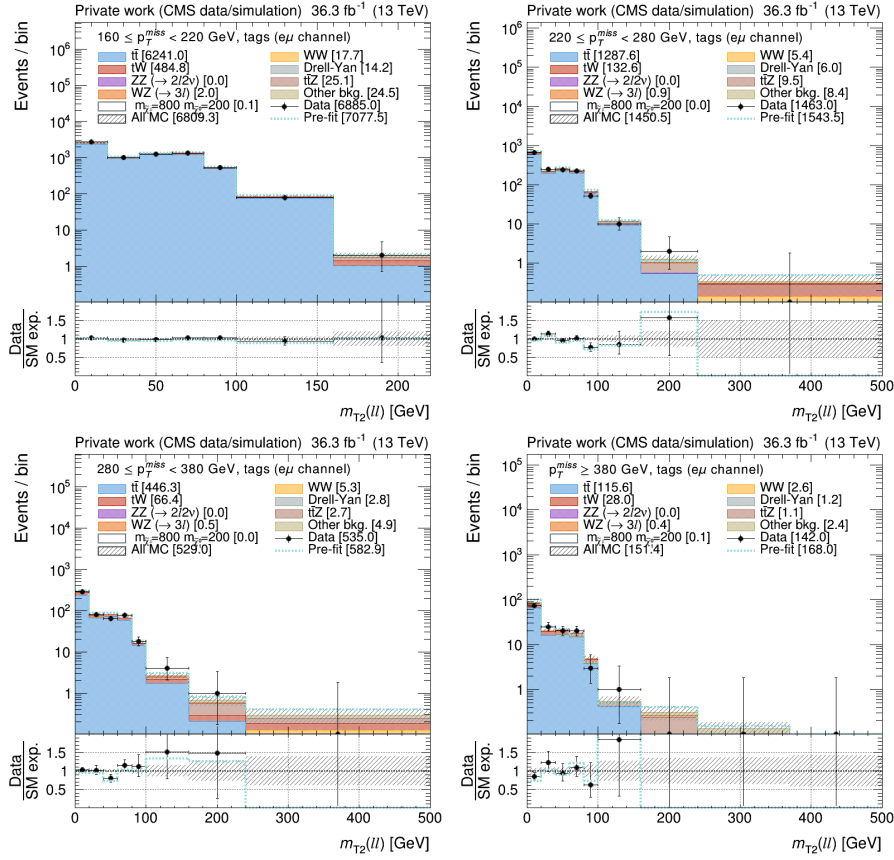


Figure G.23: Observed and expected yields of events in the CRs for the normalization of the top background in 2016 data after a background-only ML fit to the chargino/slepton SRs. From top-left clockwise, the DF events in CR1_{tags}, CR2_{tags}, CR4_{tags}, and CR3_{tags} are shown. In the bottom panel, the ratio of data and SM expectations is shown. The hatched band represents the total uncertainty after the fit.

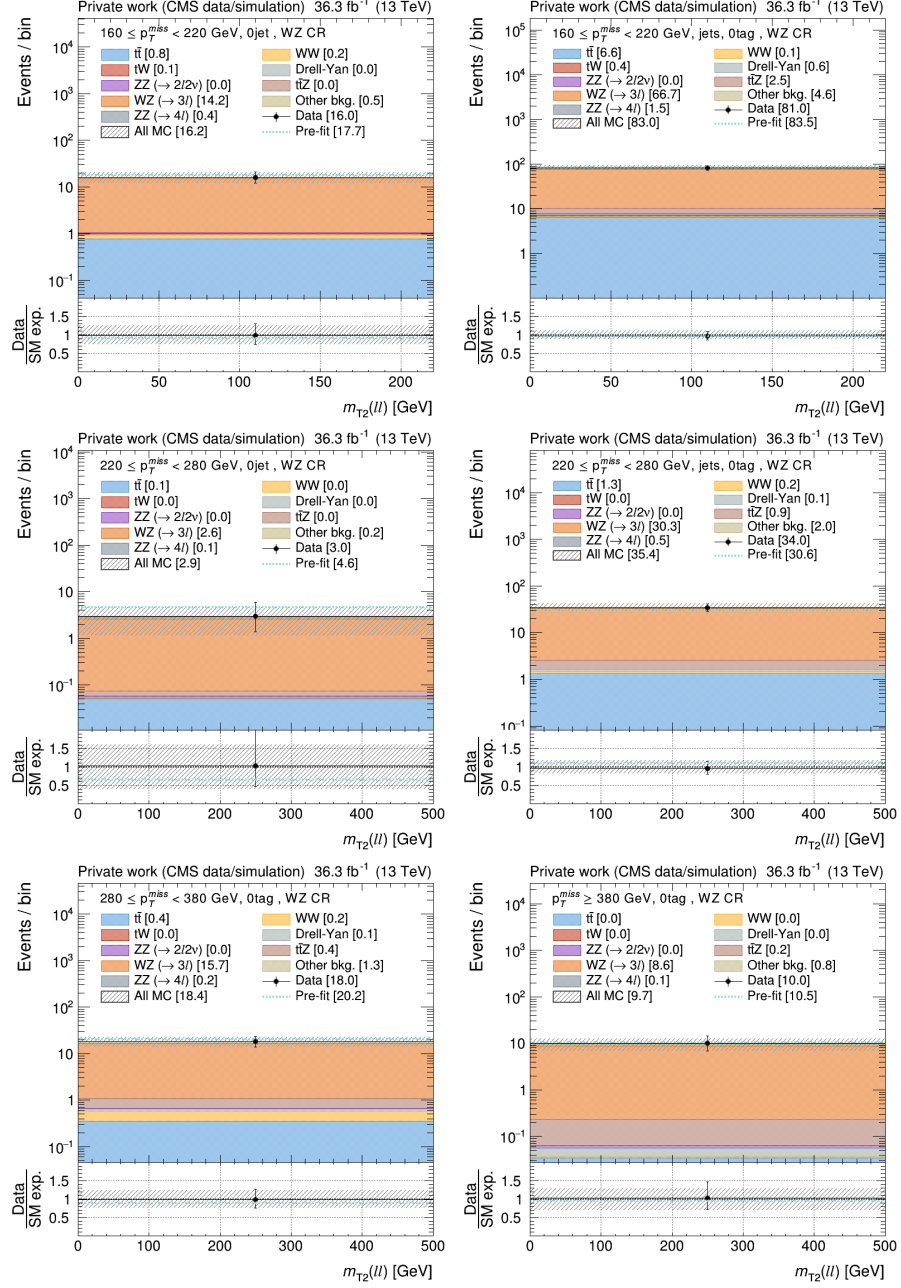


Figure G.24: Observed and expected yields of events in the CRs for the normalization of the WZ background in 2016 data after a background-only ML fit to the chargino/slepton SRs (Table 8.5). Top row shows the events with $160 < p_T^{\text{miss}} < 220$ GeV and no jets (left) or at least one jet but no b-tagged jets (right). The middle row shows the same but for events with $220 < p_T^{\text{miss}} < 280$ GeV. Bottom row shows events with $280 < p_T^{\text{miss}} < 380$ GeV (left) with $p_T^{\text{miss}} > 380$ GeV (right), both with no b-tagged jets. In the bottom panel, the ratio of data and SM expectations is shown. The hatched band represents the total uncertainty after the fit.

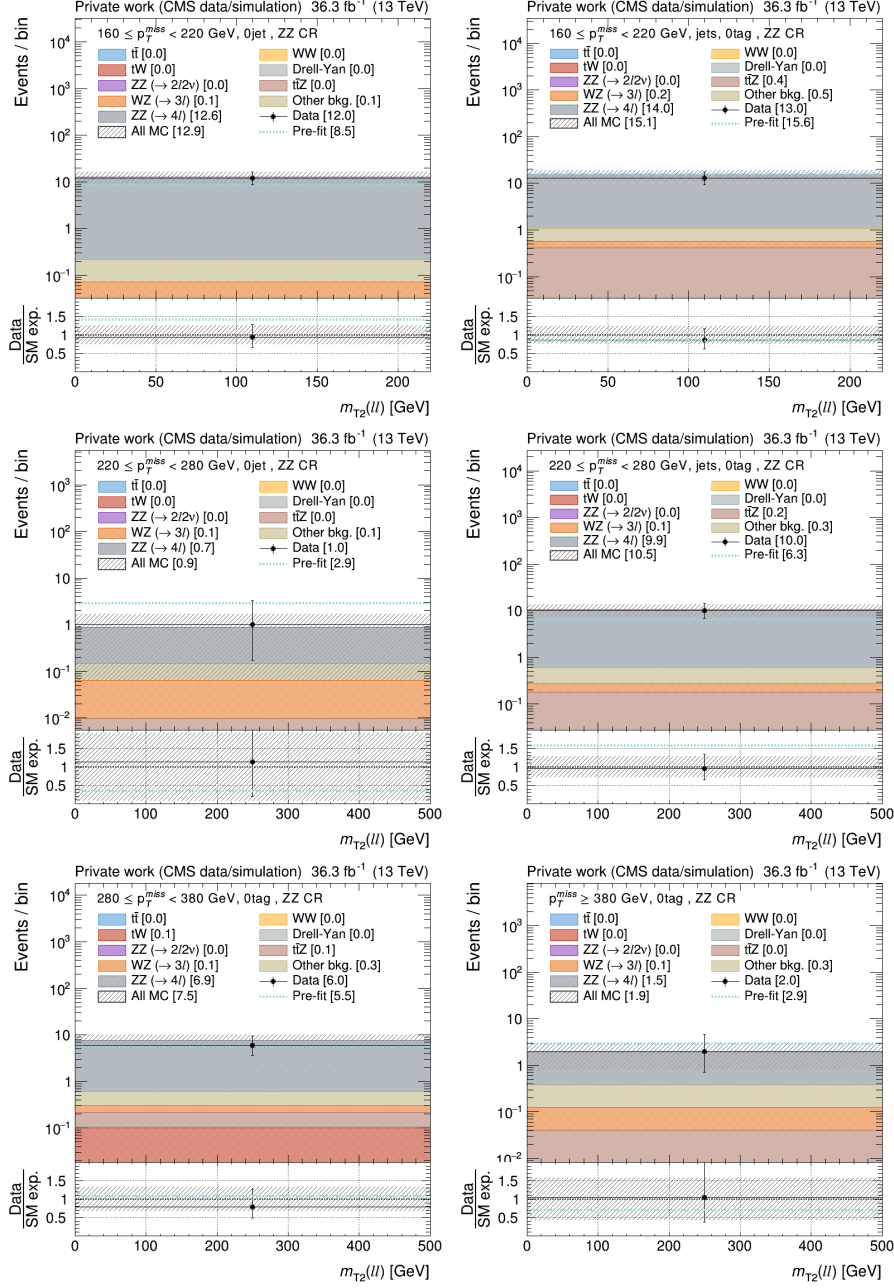


Figure G.25: Observed and expected yields of events in the CRs for the normalization of the ZZ background in 2016 data after a background-only ML fit to the chargino/slepton SRs (Table 8.5). Top row shows the events with $160 < p_T^{\text{miss}} < 220$ GeV and no jets (left) or at least one jet but no b-tagged jets (right). The middle row shows the same but for events with $220 < p_T^{\text{miss}} < 280$ GeV. Bottom row shows events with $280 < p_T^{\text{miss}} < 380$ GeV (left) with $p_T^{\text{miss}} > 380$ GeV (right), both with no b-tagged jets. In the bottom panel, the ratio of data and SM expectations is shown. The hatched band represents the total uncertainty after the fit.

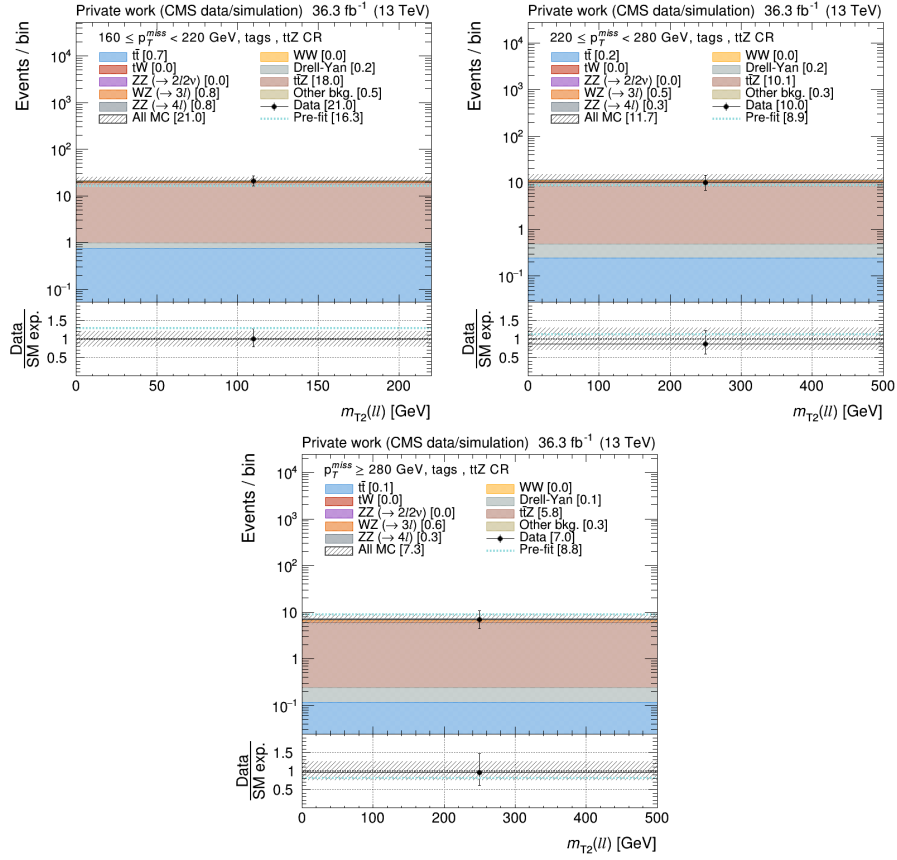


Figure G.26: Observed and expected yields of events in the CRs for the normalization of the $t\bar{t}Z$ background in 2016 data after a background-only ML fit to the chargino/slepton SRs (Table 8.5). From top-left clockwise, the events with $160 < p_T^{\text{miss}} < 220$ GeV, $220 < p_T^{\text{miss}} < 280$ GeV, and $p_T^{\text{miss}} > 280$ GeV are shown. In the bottom panel, the ratio of data and SM expectations is shown. The hatched band represents the total uncertainty after the fit.

G.2.2 Control regions for chargino/slepton ML fits in 2017 data

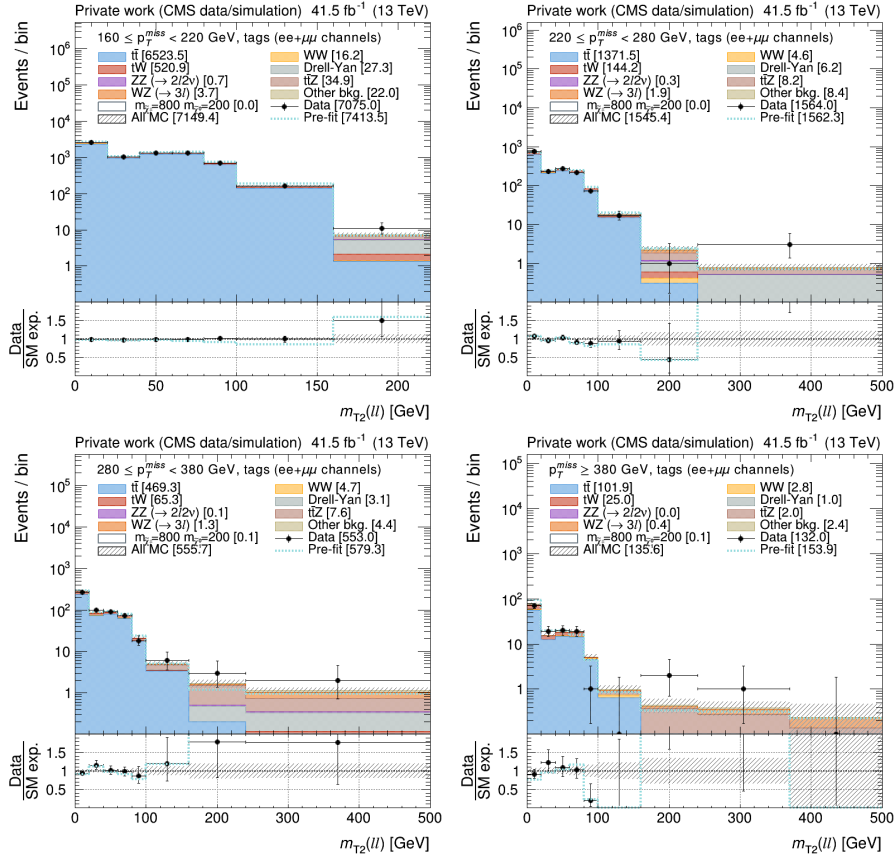


Figure G.27: Observed and expected yields of events in the CRs for the normalization of the top background in 2017 data after a background-only ML fit to the chargino/slepton SRs. From top-left clockwise, the SF events in CR1_{tags}, CR2_{tags}, CR4_{tags}, and CR3_{tags} are shown. In the bottom panel, the ratio of data and SM expectations is shown. The hatched band represents the total uncertainty after the fit.

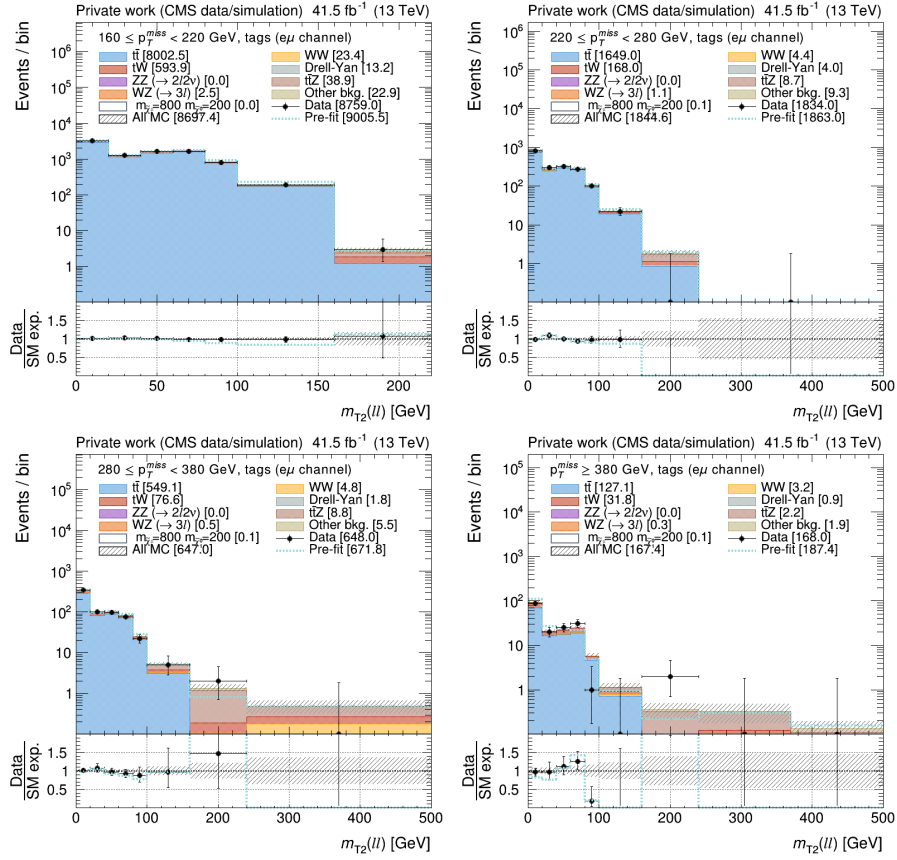


Figure G.28: Observed and expected yields of events in the CRs for the normalization of the top background in 2017 data after a background-only ML fit to the chargino/slepton SRs. From top-left clockwise, the DF events in CR_{1tags}, CR_{2tags}, CR_{4tags}, and CR_{3tags} are shown. In the bottom panel, the ratio of data and SM expectations is shown. The hatched band represents the total uncertainty after the fit.

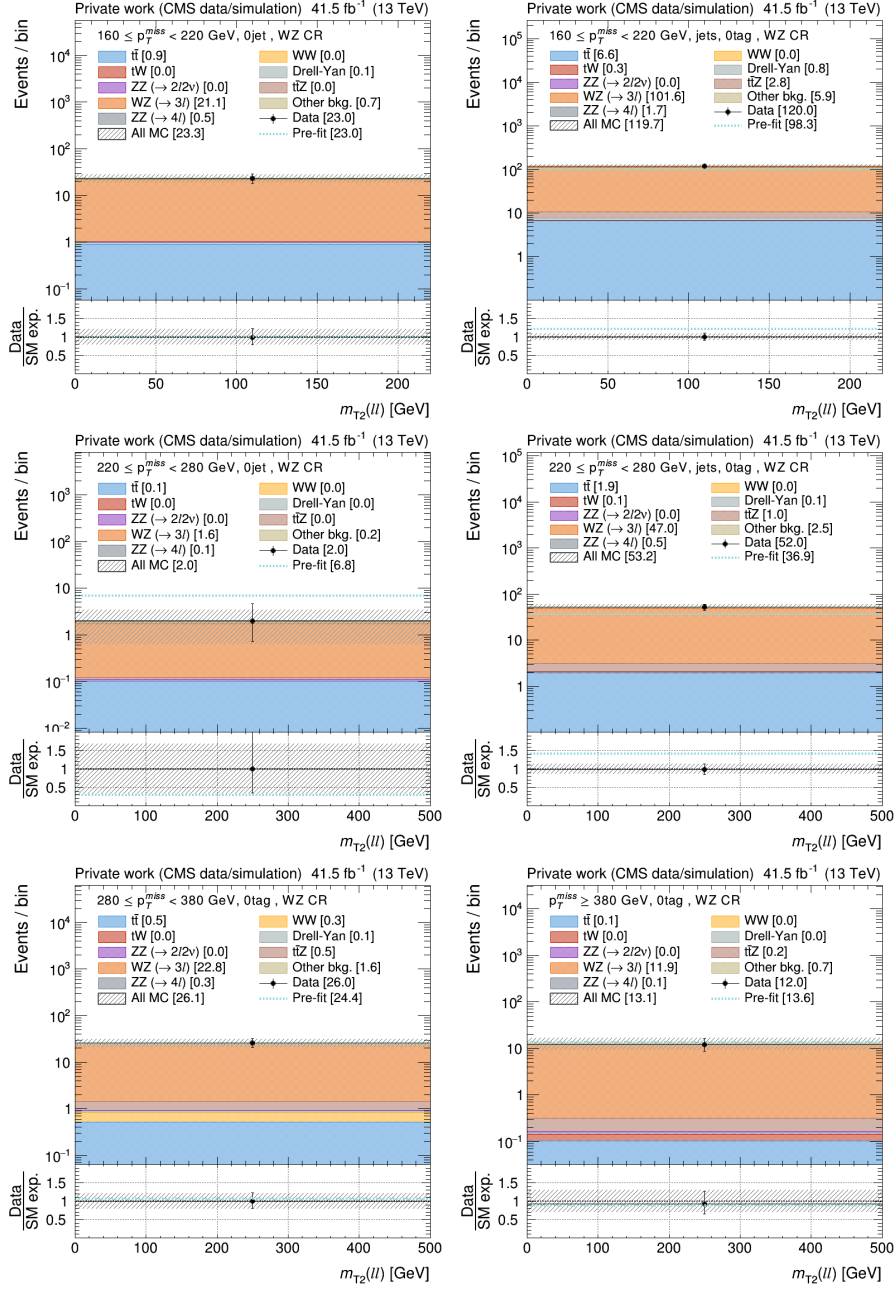


Figure G.29: Observed and expected yields of events in the CRs for the normalization of the WZ background in 2017 data after a background-only ML fit to the chargino/slepton SRs (Table 8.5). Top row shows the events with $160 < p_T^{\text{miss}} < 220$ GeV and no jets (left) or at least one jet but no b-tagged jets (right). The middle row shows the same but for events with $220 < p_T^{\text{miss}} < 280$ GeV. Bottom row shows events with $280 < p_T^{\text{miss}} < 380$ GeV (left) with $p_T^{\text{miss}} > 380$ GeV (right), both with no b-tagged jets. In the bottom panel, the ratio of data and SM expectations is shown. The hatched band represents the total uncertainty after the fit.

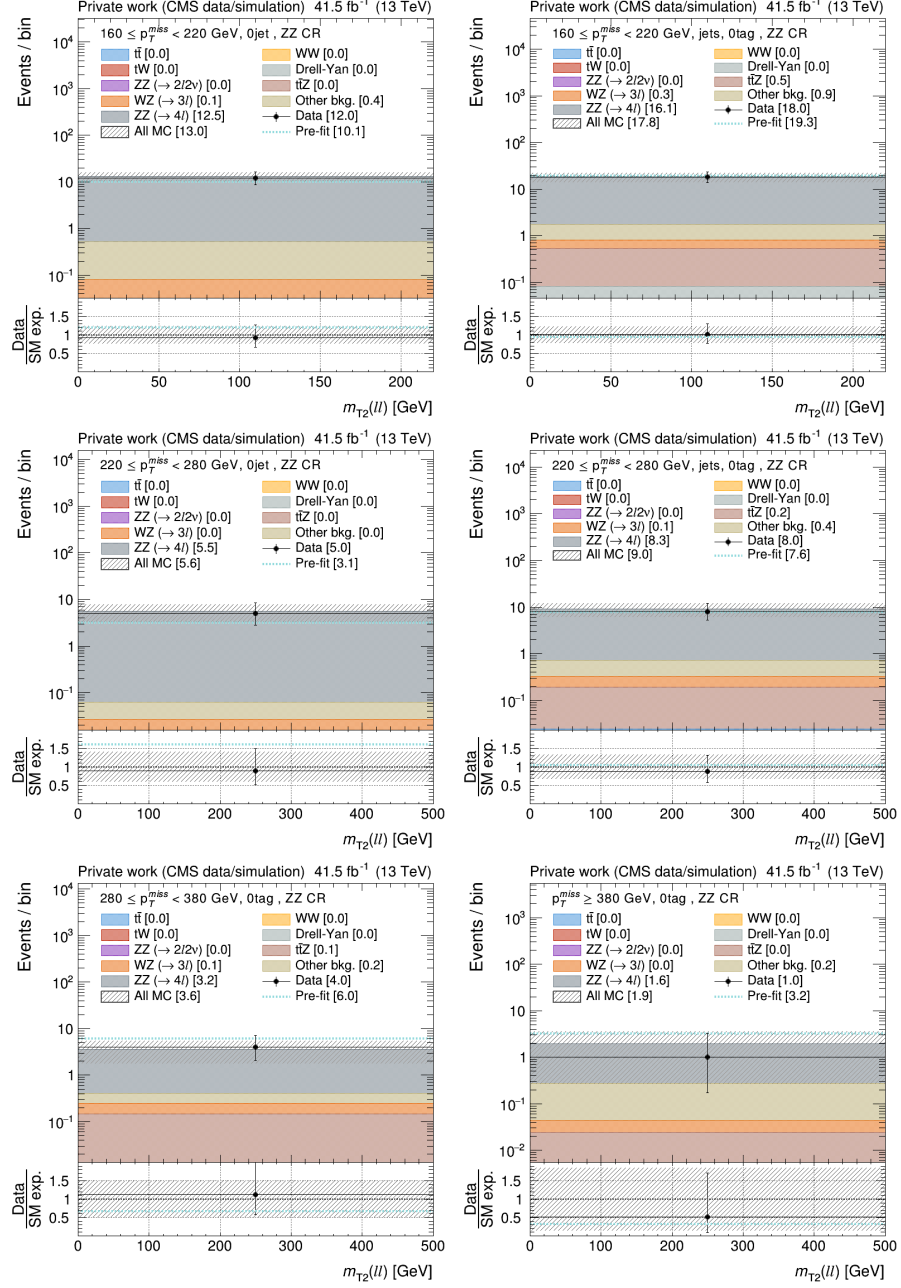


Figure G.30: Observed and expected yields of events in the CRs for the normalization of the ZZ background in 2017 data after a background-only ML fit to the chargino/slepton SRs (Table 8.5). Top row shows the events with $160 < p_T^{\text{miss}} < 220$ GeV and no jets (left) or at least one jet but no b-tagged jets (right). The middle row shows the same but for events with $220 < p_T^{\text{miss}} < 280$ GeV. Bottom row shows events with $280 < p_T^{\text{miss}} < 380$ GeV (left) with $p_T^{\text{miss}} > 380$ GeV (right), both with no b-tagged jets. In the bottom panel, the ratio of data and SM expectations is shown. The hatched band represents the total uncertainty after the fit.

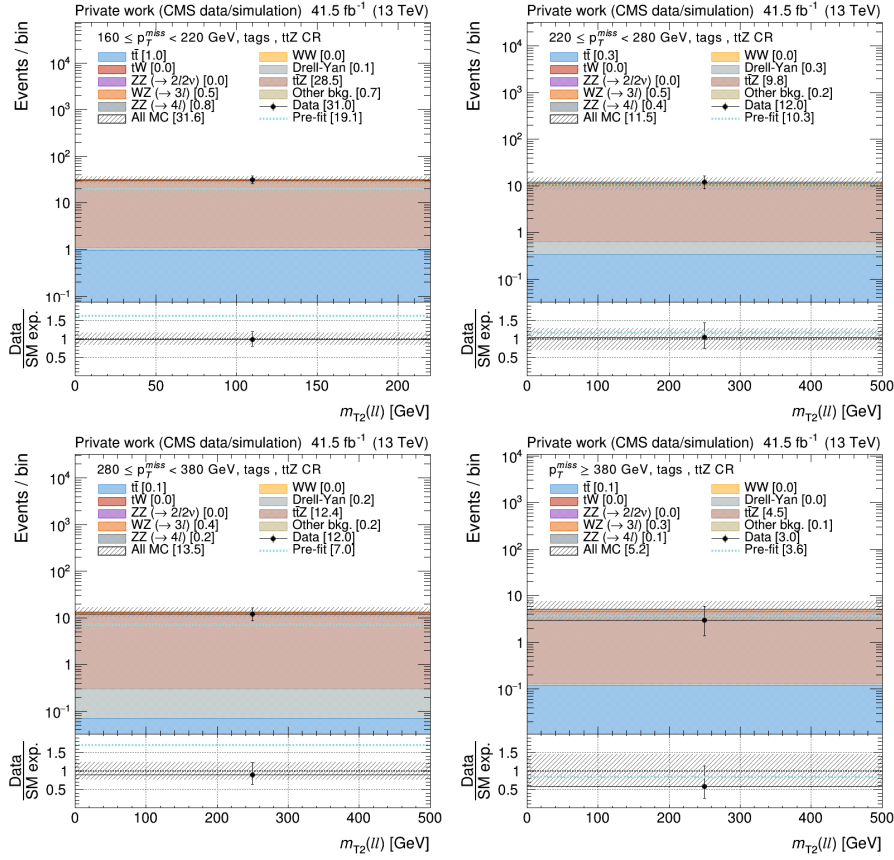


Figure G.31: Observed and expected yields of events in the CRs for the normalization of the $t\bar{t}Z$ background in 2017 data after a background-only ML fit to the chargino/slepton SRs (Table 8.5). From top-left clockwise, the events with $160 < p_T^{\text{miss}} < 220$ GeV, $220 < p_T^{\text{miss}} < 280$ GeV, $p_T^{\text{miss}} > 380$ GeV, and $280 < p_T^{\text{miss}} < 380$ GeV are shown. In the bottom panel, the ratio of data and SM expectations is shown. The hatched band represents the total uncertainty after the fit.

G.2.3 Control regions for chargino/slepton ML fits in 2018 data

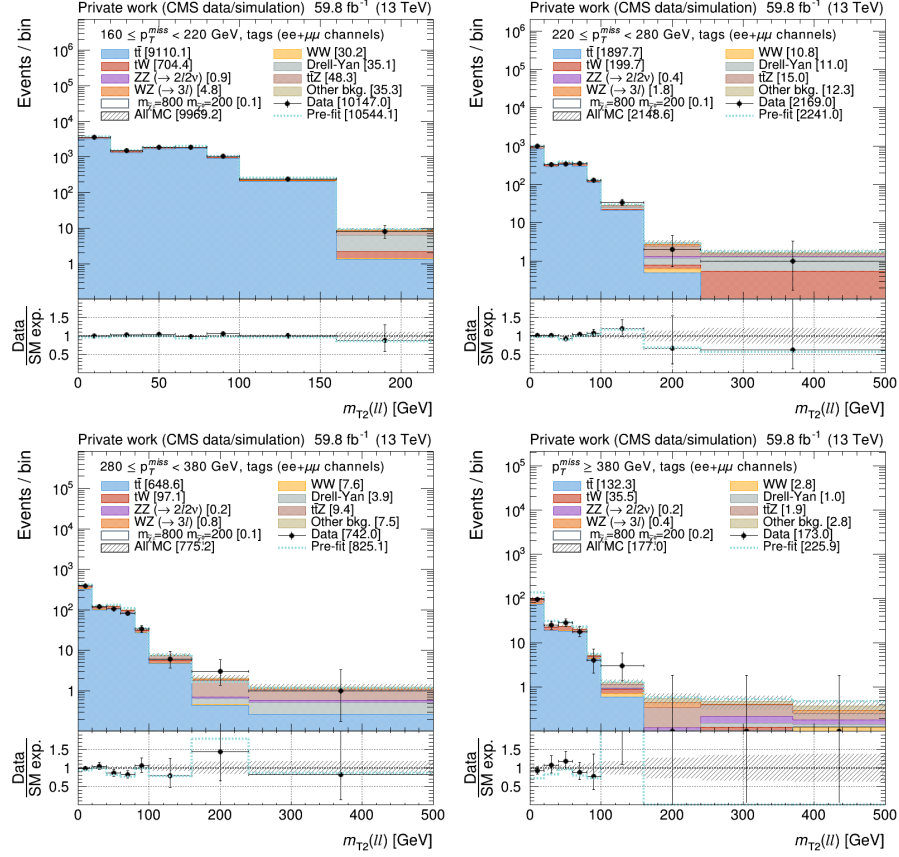


Figure G.32: Observed and expected yields of events in the CRs for the normalization of the top background in 2018 data after a background-only ML fit to the chargino/slepton SRs. From top-left clockwise, the SF events in CR1_{tags}, CR2_{tags}, CR4_{tags}, and CR3_{tags} are shown. In the bottom panel, the ratio of data and SM expectations is shown. The hatched band represents the total uncertainty after the fit.

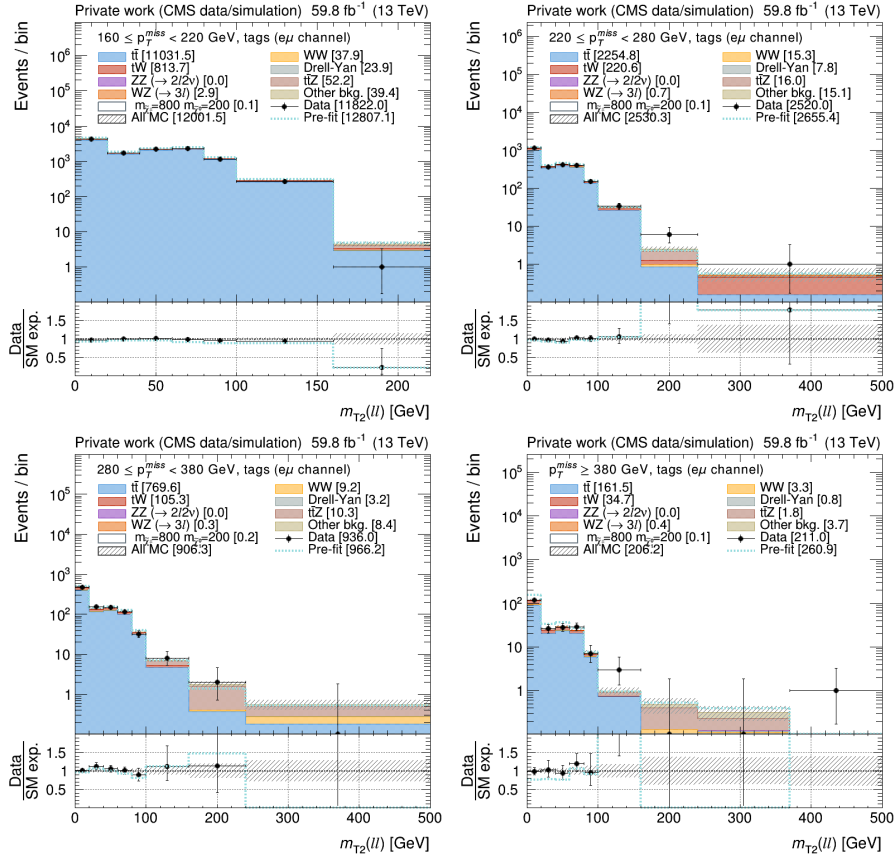


Figure G.33: Observed and expected yields of events in the CRs for the normalization of the top background in 2018 data after a background-only ML fit to the chargino/slepton SRs. From top-left clockwise, the DF events in CR1_{tags}, CR2_{tags}, CR4_{tags}, and CR3_{tags} are shown. In the bottom panel, the ratio of data and SM expectations is shown. The hatched band represents the total uncertainty after the fit.

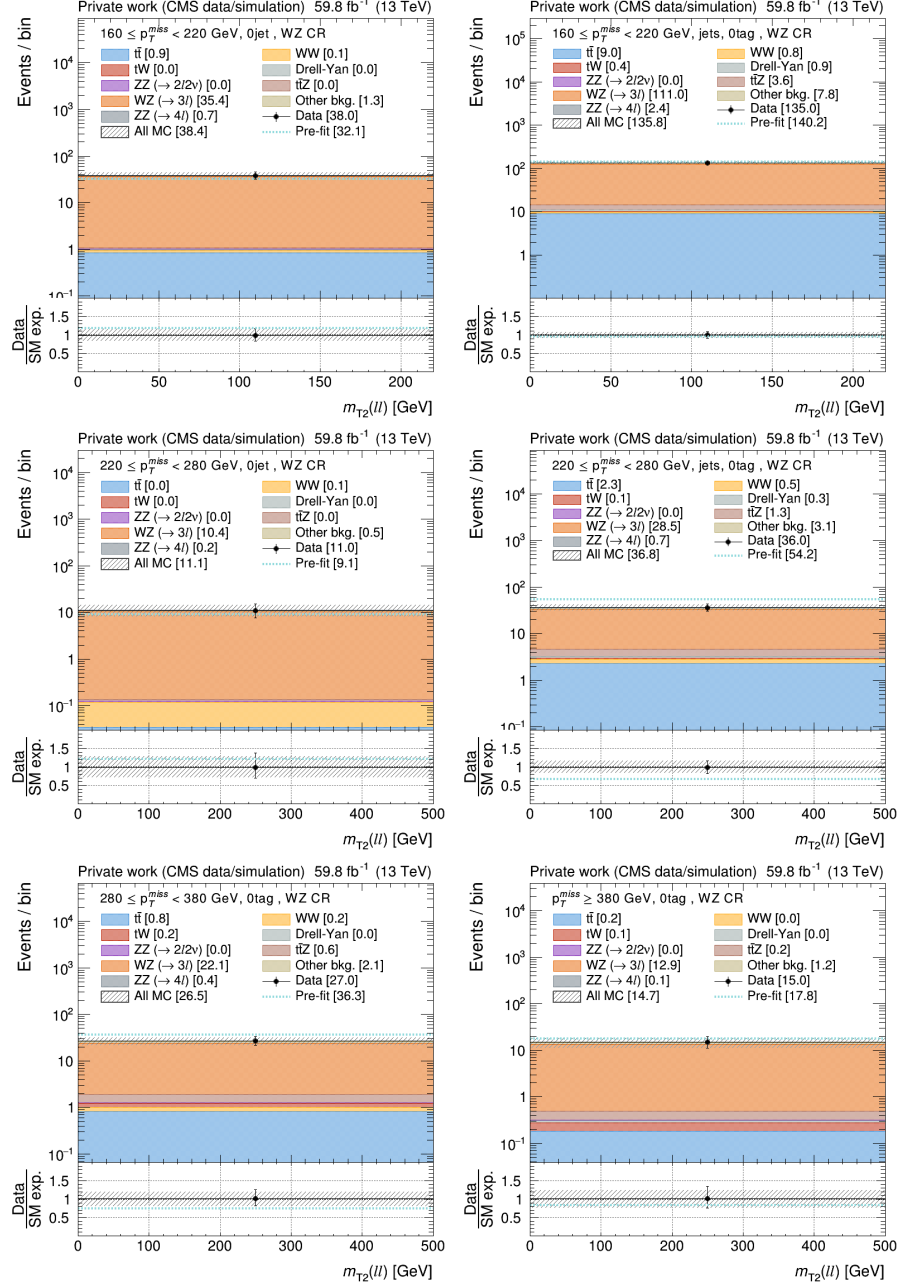


Figure G.34: Observed and expected yields of events in the CRs for the normalization of the WZ background in 2018 data after a background-only ML fit to the chargino/slepton SRs (Table 8.5). Top row shows the events with $160 < p_T^{\text{miss}} < 220$ GeV and no jets (left) or at least one jet but no b-tagged jets (right). The middle row shows the same but for events with $220 < p_T^{\text{miss}} < 280$ GeV. Bottom row shows events with $280 < p_T^{\text{miss}} < 380$ GeV (left) with $p_T^{\text{miss}} > 380$ GeV (right), both with no b-tagged jets. In the bottom panel, the ratio of data and SM expectations is shown. The hatched band represents the total uncertainty after the fit.

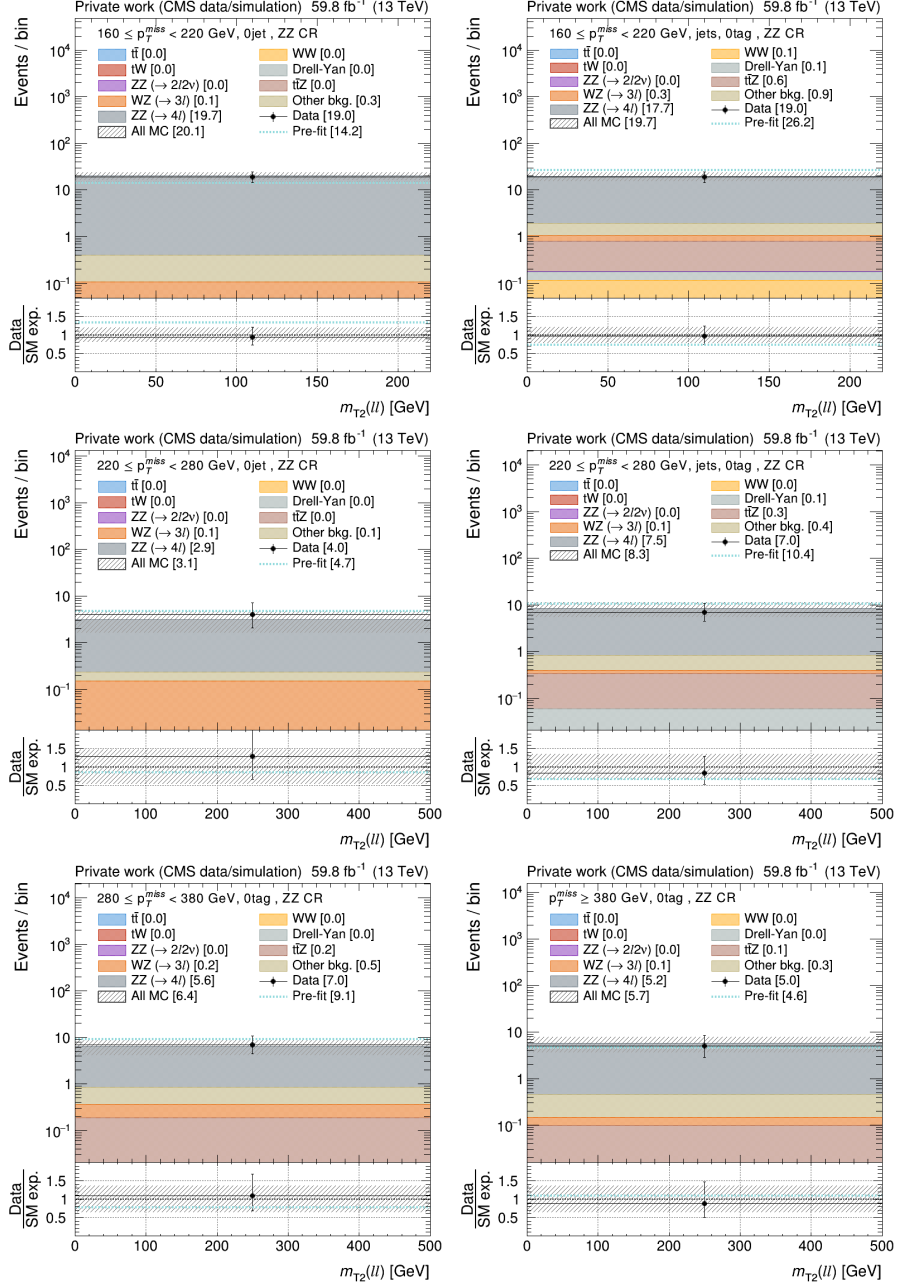


Figure G.35: Observed and expected yields of events in the CRs for the normalization of the ZZ background in 2018 data after a background-only ML fit to the chargino/slepton SRs (Table 8.5). Top row shows the events with $160 < p_T^{\text{miss}} < 220$ GeV and no jets (left) or at least one jet but no b-tagged jets (right). The middle row shows the same but for events with $220 < p_T^{\text{miss}} < 280$ GeV. Bottom row shows events with $280 < p_T^{\text{miss}} < 380$ GeV (left) with $p_T^{\text{miss}} > 380$ GeV (right), both with no b-tagged jets. In the bottom panel, the ratio of data and SM expectations is shown. The hatched band represents the total uncertainty after the fit.

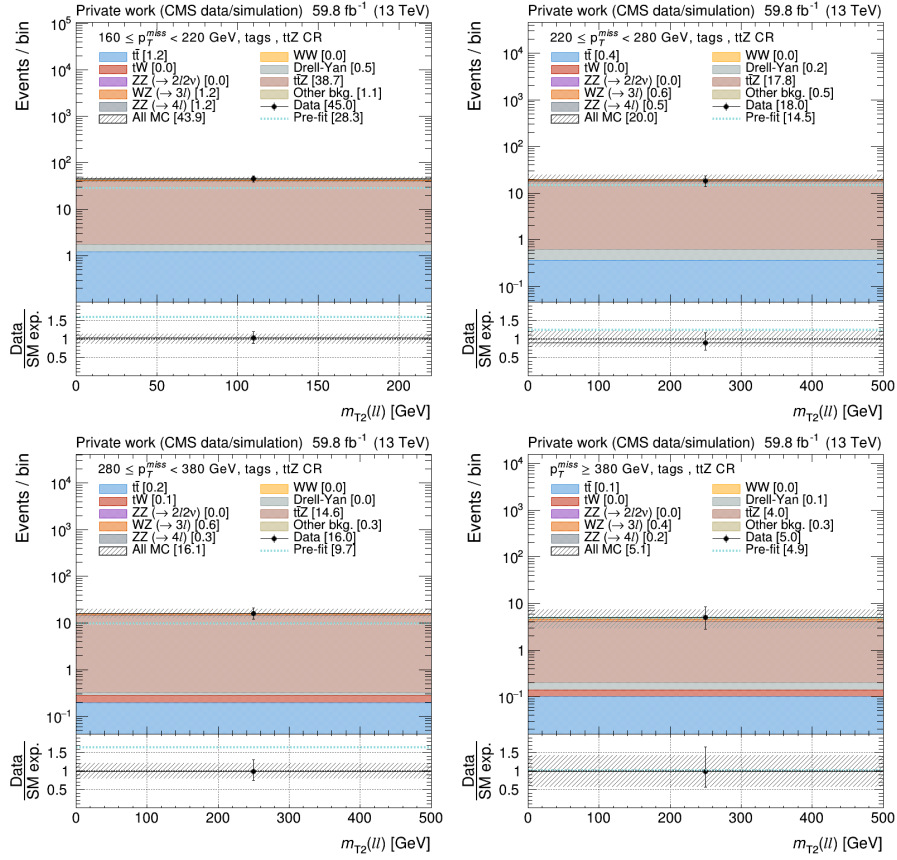


Figure G.36: Observed and expected yields of events in the CRs for the normalization of the $t\bar{t}Z$ background in 2018 data after a background-only ML fit to the chargino/slepton SRs (Table 8.5). From top-left clockwise, the events with $160 < p_T^{\text{miss}} < 220$ GeV, $220 < p_T^{\text{miss}} < 280$ GeV, $p_T^{\text{miss}} > 380$ GeV, and $280 < p_T^{\text{miss}} < 380$ GeV are shown. In the bottom panel, the ratio of data and SM expectations is shown. The hatched band represents the total uncertainty after the fit.

G.2.4 Control regions for top squark ML fits in 2016 data

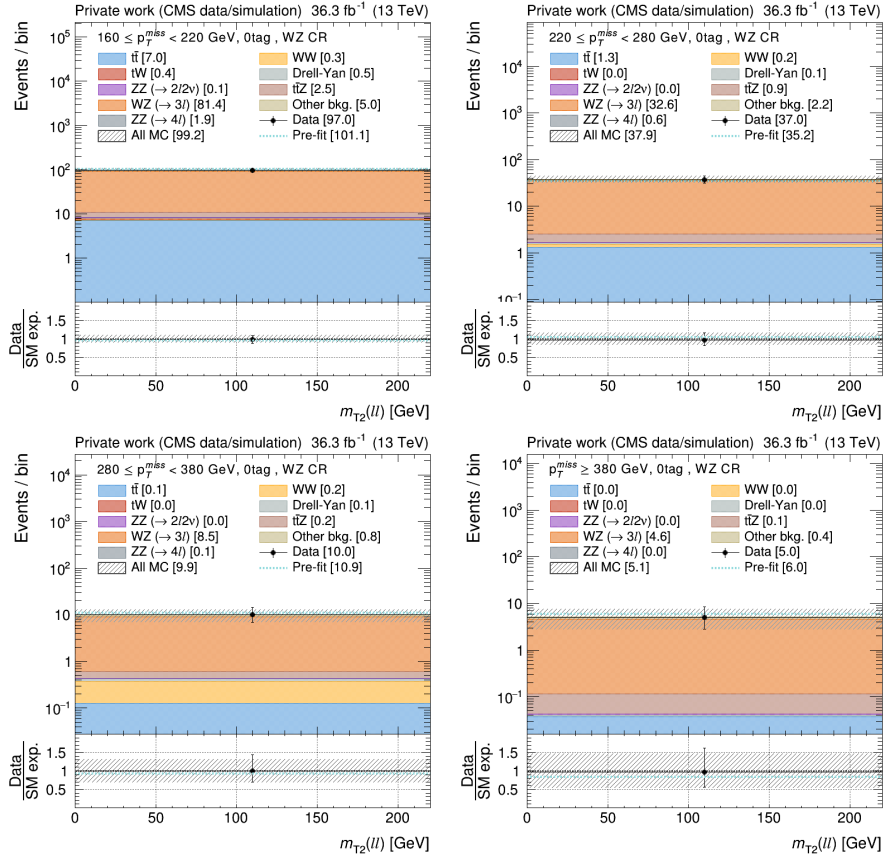


Figure G.37: Observed and expected yields of events in the CRs for the normalization of the WZ background in 2016 data after a background-only ML fit to the top squark SRs (Table 8.5). From top-left clockwise, the events with $160 < p_T^{\text{miss}} < 220$ GeV, $220 < p_T^{\text{miss}} < 280$ GeV, $p_T^{\text{miss}} > 380$ GeV, and $280 < p_T^{\text{miss}} < 380$ GeV are shown. In the bottom panel, the ratio of data and SM expectations is shown. The hatched band represents the total uncertainty after the fit.

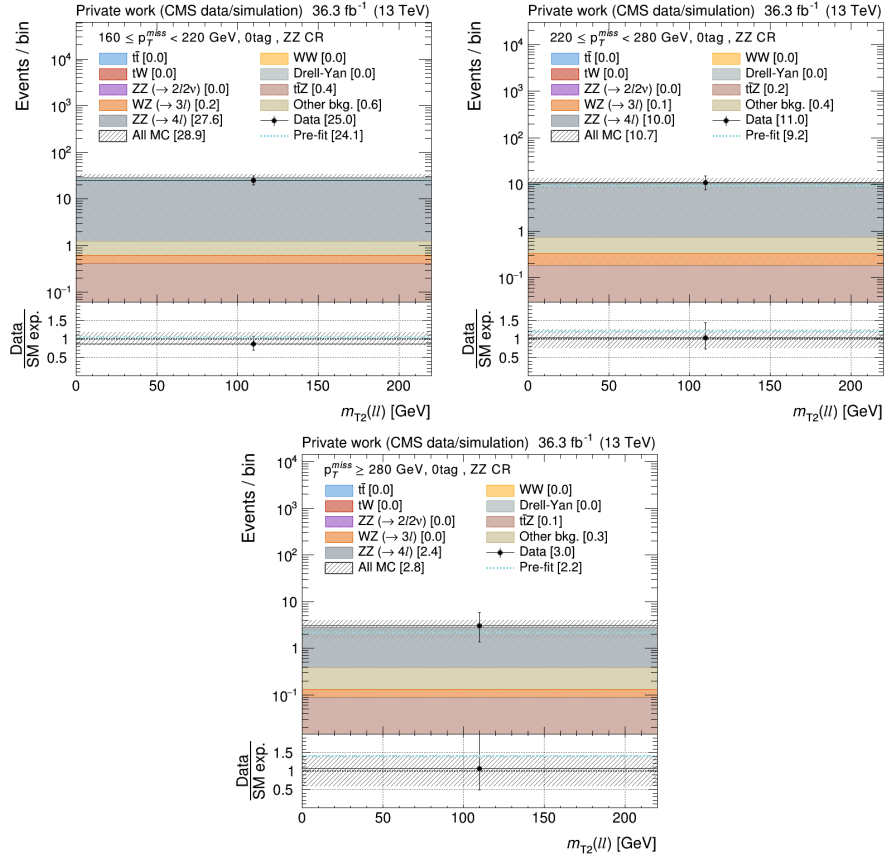


Figure G.38: Observed and expected yields of events in the CRs for the normalization of the ZZ background in 2016 data after a background-only ML fit to the top squark SRs (Table 8.5). From top-left clockwise, the events with $160 < p_T^{\text{miss}} < 220$ GeV, $220 < p_T^{\text{miss}} < 280$ GeV, and $p_T^{\text{miss}} > 280$ GeV are shown. In the bottom panel, the ratio of data and SM expectations is shown. The hatched band represents the total uncertainty after the fit.

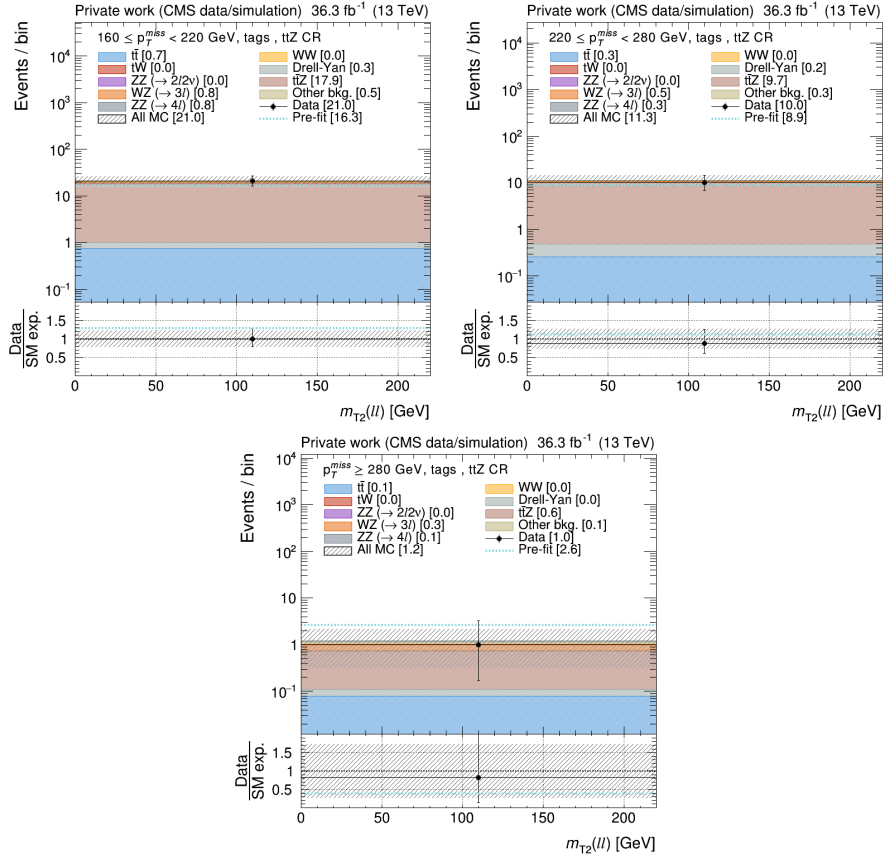


Figure G.39: Observed and expected yields of events in the CRs for the normalization of the $t\bar{t}Z$ background in 2016 data after a background-only ML fit to the top squark SRs (Table 8.5). From top-left clockwise, the events with $160 < p_T^{\text{miss}} < 220$ GeV, $220 < p_T^{\text{miss}} < 280$ GeV, and $p_T^{\text{miss}} > 280$ GeV are shown. In the bottom panel, the ratio of data and SM expectations is shown. The hatched band represents the total uncertainty after the fit.

G.2.5 Control regions for top squark ML fits in 2017 data

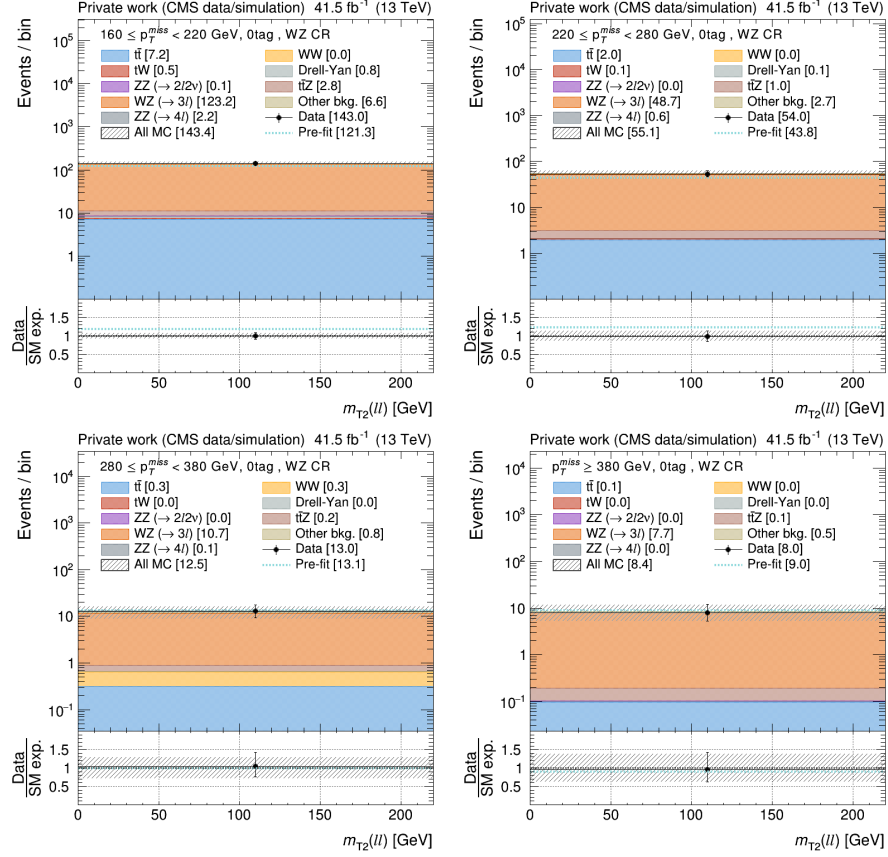


Figure G.40: Observed and expected yields of events in the CRs for the normalization of the WZ background in 2017 data after a background-only ML fit to the top squark SRs (Table 8.5). From top-left clockwise, the events with $160 < p_T^{\text{miss}} < 220$ GeV, $220 < p_T^{\text{miss}} < 280$ GeV, $p_T^{\text{miss}} > 380$ GeV, and $280 < p_T^{\text{miss}} < 380$ GeV are shown. In the bottom panel, the ratio of data and SM expectations is shown. The hatched band represents the total uncertainty after the fit.

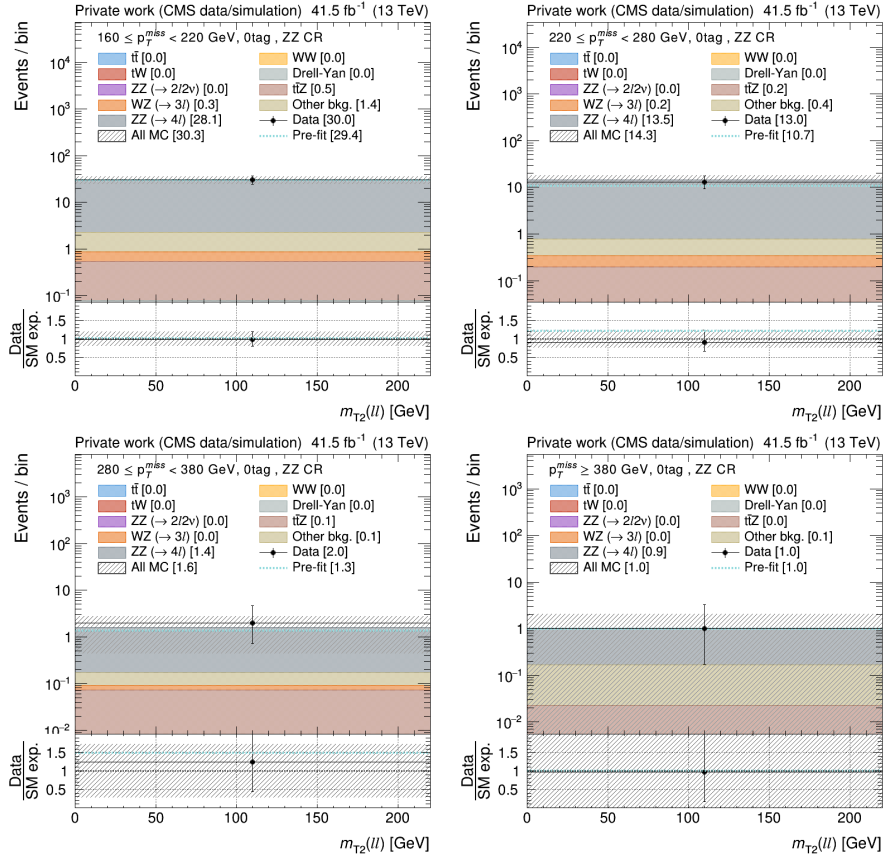


Figure G.41: Observed and expected yields of events in the CRs for the normalization of the ZZ background in 2017 data after a background-only ML fit to the top squark SRs (Table 8.5). From top-left clockwise, the events with $160 < p_T^{\text{miss}} < 220$ GeV, $220 < p_T^{\text{miss}} < 280$ GeV, $p_T^{\text{miss}} > 380$ GeV, and $280 < p_T^{\text{miss}} < 380$ GeV are shown. In the bottom panel, the ratio of data and SM expectations is shown. The hatched band represents the total uncertainty after the fit.

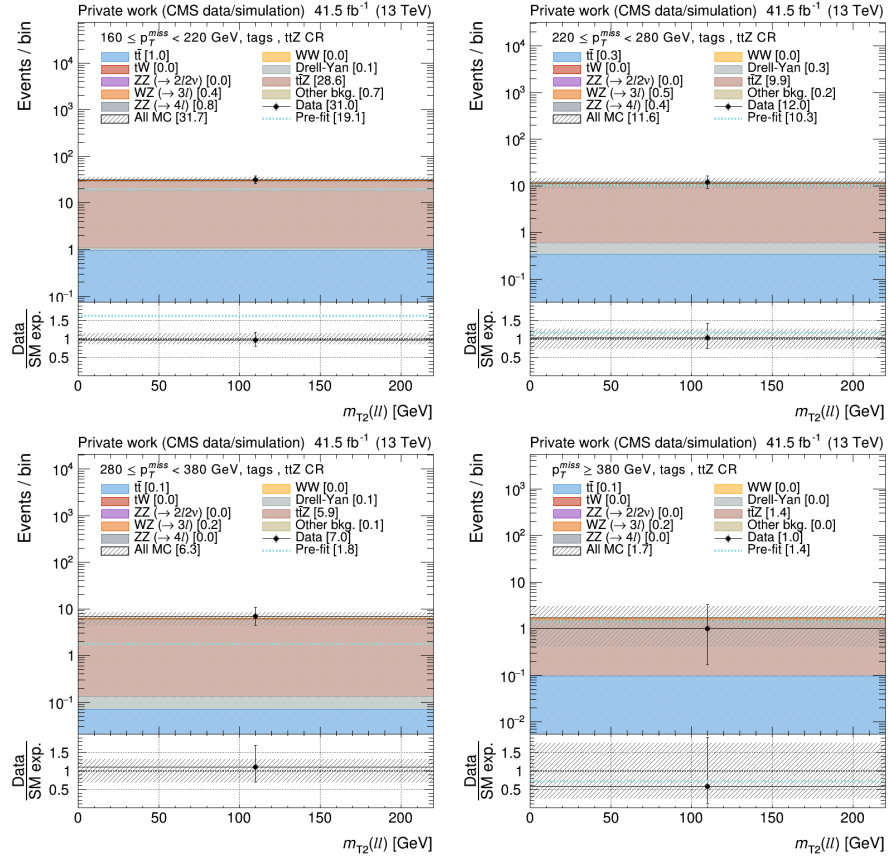


Figure G.42: Observed and expected yields of events in the CRs for the normalization of the $t\bar{t}Z$ background in 2017 data after a background-only ML fit to the top squark SRs (Table 8.5). From top-left clockwise, the events with $160 < p_T^{\text{miss}} < 220$ GeV, $220 < p_T^{\text{miss}} < 280$ GeV, $p_T^{\text{miss}} > 380$ GeV, and $280 < p_T^{\text{miss}} < 380$ GeV are shown. In the bottom panel, the ratio of data and SM expectations is shown. The hatched band represents the total uncertainty after the fit.

G.2.6 Control regions for top squark ML fits in 2018 data

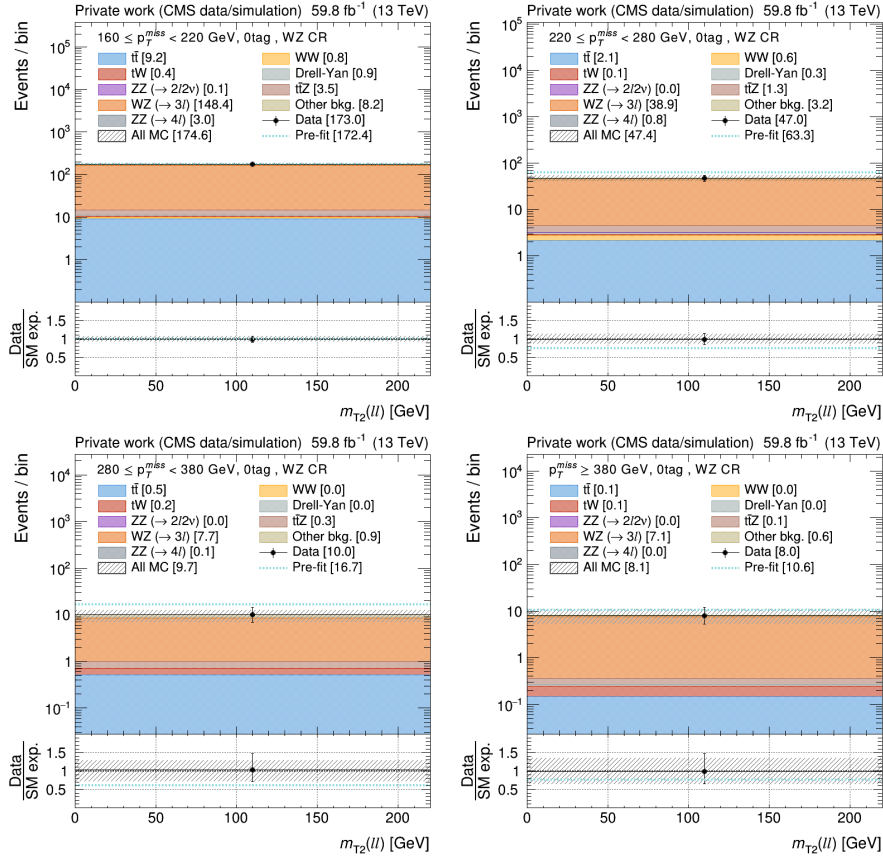


Figure G.43: Observed and expected yields of events in the CRs for the normalization of the WZ background in 2018 data after a background-only ML fit to the top squark SRs (Table 8.5). From top-left clockwise, the events with $160 < p_T^{\text{miss}} < 220$ GeV, $220 < p_T^{\text{miss}} < 280$ GeV, $p_T^{\text{miss}} > 380$ GeV, and $280 < p_T^{\text{miss}} < 380$ GeV are shown. In the bottom panel, the ratio of data and SM expectations is shown. The hatched band represents the total uncertainty after the fit.

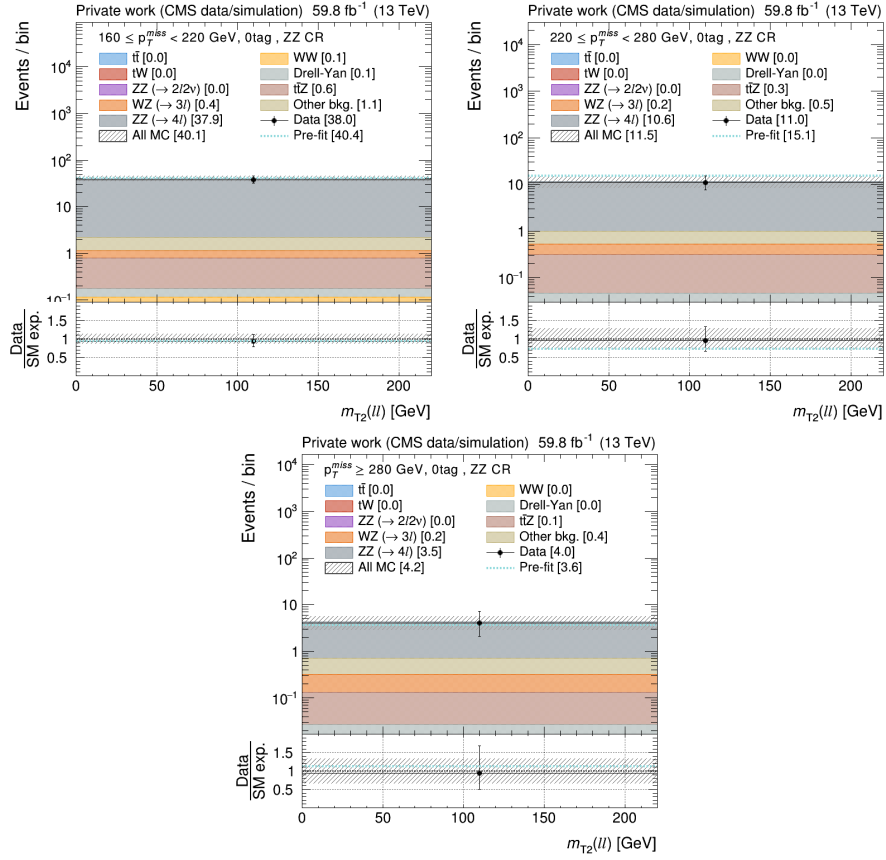


Figure G.44: Observed and expected yields of events in the CRs for the normalization of the ZZ background in 2018 data after a background-only ML fit to the top squark SRs (Table 8.5). From top-left clockwise, the events with $160 < p_T^{\text{miss}} < 220$ GeV, $220 < p_T^{\text{miss}} < 280$ GeV, and $p_T^{\text{miss}} > 280$ GeV are shown. In the bottom panel, the ratio of data and SM expectations is shown. The hatched band represents the total uncertainty after the fit.

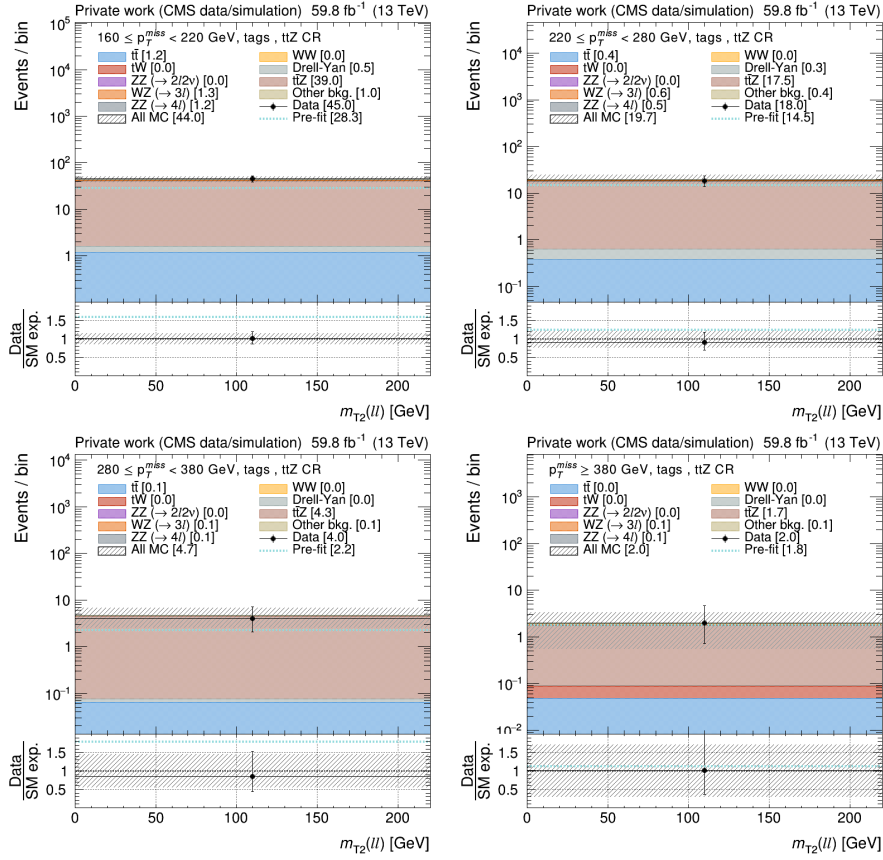


Figure G.45: Observed and expected yields of events in the CRs for the normalization of the $t\bar{t}Z$ background in 2018 data after a background-only ML fit to the top squark SRs (Table 8.5). From top-left clockwise, the events with $160 < p_T^{\text{miss}} < 220$ GeV, $220 < p_T^{\text{miss}} < 280$ GeV, $p_T^{\text{miss}} > 380$ GeV, and $280 < p_T^{\text{miss}} < 380$ GeV are shown. In the bottom panel, the ratio of data and SM expectations is shown. The hatched band represents the total uncertainty after the fit.